Max-Planck-Institut für Astrophysik

Nucleosynthesis and Hydrodynamic Instabilities in Core Collapse Supernovae

Konstantinos Kifonidis

Nucleosynthesis and Hydrodynamic Instabilities in Core Collapse Supernovae

Konstantinos Kifonidis
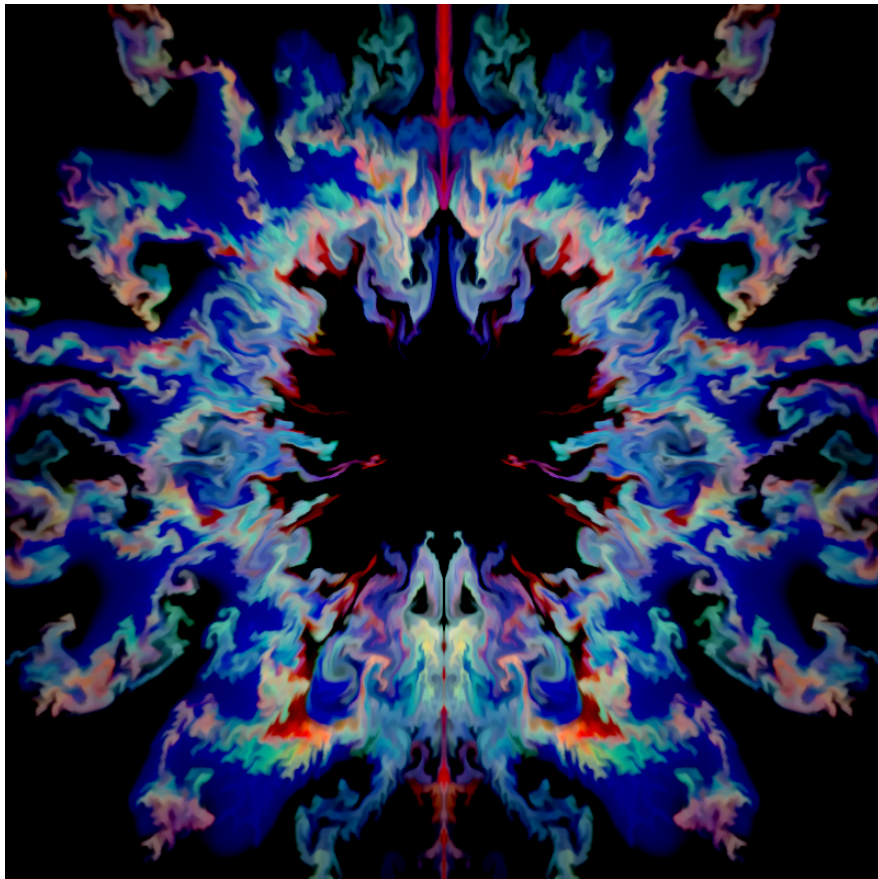
Zusammenfassung

Massereiche Sterne beenden ihre Millionen Jahre andauernde Entwicklung in gewaltigen Supernovaexplosionen. Durch den gravitativen Kollaps ihres zentralen Eisenkerns werden riesige Energiemengen freigesetzt und der größte Teil der Sternmasse in den interstellaren Raum geschleudert. Nur ein kleiner Teil der Masse bleibt als zentraler Neutronenstern oder als schwarzes Loch zurück. Supernovae sind von zentraler Bedeutung in der Astrophysik, da unter den extremen Bedingungen, die während der ersten Sekunde in ihrem Inneren vorliegen, schwere Elemente durch thermonukleare Reaktionen synthetisiert werden. Trotz ihrer enormen physikalischen Bedeutung sind diese Ereignisse bislang nur unzureichend verstanden. Inbesondere die Frage nach dem Explosionsmechanismus ist bislang unbeantwortet geblieben. Die derzeit akzeptierte Vorstellung geht davon aus, daß die durch den Kollaps freiwerdende Energie vorwiegend in Form von Neutrinos emittiert wird. Durch schwache Wechselwirkung mit den dichten Sternschichten hinter der beim Kollaps enstehenden Stoßwelle, können die Neutrinos etwa 1% ihrer Energie auf die Stoßfront übertragen und hierdurch den Einsturz der äußeren Sternschichten in eine Explosion verwandeln.

Beobachtungen der nahen Supernova SN 1987 A in der großen Magellanschen Wolke sowie einiger anderer extragalaktischer Supernovae haben Hinweise dafür erbracht, daß hydrodynamische Instabilitäten und Mischvorgänge eine wichtige Rolle im Explosionsmechanismus spielen, indem sie die Effizienz des Neutrinoheizens erhöhen. Als beobachtete Manifestation dieser Effekte gelten die gemessenen hohen Expansionsgeschwindigkeiten von Elementen der Eisengruppe ($v_{\exp} \leq 4000\,\mathrm{km/s}$), die während der Explosion in Klumpen von Schichten nahe des kollabierten Kerns bis in die äußere Wasserstoffhülle des Sterns geschleudert worden sind. Alle bislang durchgeführten mehrdimensionalen hydrodynamischen Rechnungen der Spätphasen der Explosion, die jedoch keine detaillierte Behandlung des Explosionsmechanismus selbst enthielten, konnten diese Geschwindigkeiten nicht reproduzieren.

Die vorliegende Arbeit stellt den ersten Versuch dar, durch konsistente mehrdimensionale Rechnungen, eine Brücke zwischen der Theorie des neutrinogetriebenen Explosionsmechanismus und den Beobachtungen zu schlagen. Beginnend zu einer Zeit von 20 ms nach dem Kernkollaps wird die gesamte hydrodynamische Entwicklung der Explosion inklusive der Nukleosynthese und konvektiver Instabilitäten konsistent über den Zeitpunkt des Ausbruchs der Stoßfront durch die Sternoberfäche hinaus verfolgt. Die sich aus den Rechnungen ergebenden Geschwindigkeitsverteilungen sowie das Ausmaß des Mischens neusynthetisierter Elemente werden mit Beobachtungsdaten verglichen. Die Ergebnisse zeigen, daß Beobachtungen von sogenannten Typ Ib und Typ Ic Supernovae, d.h. Explosionen in Sternen ohne dichter Wasserstoff-, bzw. Heliumhülle, zwanglos im Rahmen des neutrinogetriebenen Mechanismus erklärt werden können. Bereits während der ersten Minute der Explosion bilden sich durch Rayleigh-Taylor-Instabilitäten schnelle, mit neusynthetisierten Eisengruppenelementen angereicherte Klumpen, die durch einen Großteil der Heliumschale des Sterns geschleudert werden. Dieses Hinausmischen radioaktiver Isotope in die Supernovaphotosphäre ist bei Typ Ib und einigen Typ Ic Ereignissen seit geraumer Zeit aus spektroskopischen Untersuchungen bekannt und in der vorliegenden Arbeit zum ersten Mal in einer konsistenten Rechnung bestätigt worden.

Die Übereinstimmung mit Beobachtungen von Typ II Supernovae (d.h. Explosionen in Sternen mit einer massiven Wasserstoffhülle) erweist sich dagegen als weniger

befriedigend. Insbesondere können die hohen Nickel- und Eisengeschwindigkeiten in SN 1987 A nicht reproduziert werden, da die in der Wasserstoffhülle abbremsende Stoßwelle eine Dichte Schale am Kompositionssprung zum Heliumkern des Sterns hinterlässt. In dieser Schale werden die Klumpen von Geschwindigkeiten über $3000\,\mathrm{km/s}$ auf unter $2000\,\mathrm{km/s}$ abgebremst. Die Diskrepanz zwischen den Rechnungen und Beobachtungen dieser Supernova kann auf Besonderheiten in der Explosion von SN 1987 A, Unsicherheiten in heutigen Sternmodellen, der Beschränkung der vorliegenden Rechnungen auf zwei Raumdimensionen, oder unverstandene Physik im Explosionsmechanismus selbst deuten.

Contents

Chapter 1

Introduction

1.1   The supernova phenomenon

The cataclysmic death of an evolved star in a gigantic supernova explosion is one of natures greatest spectacles. Within seconds a supernova releases about 10^{51} ergs as kinetic and internal energy of expanding debris and (depending on its type) a few 10^{53} ergs in form of neutrino radiation and is thus among the most energetic events in the present day universe, second probably only to the mysterious gamma-ray bursts. It would take our sun with its luminosity of 3.85×10^{33} ergs/s about 10 billion years to emit the energy typically stored in a supernova's ejecta and about 200 times the age of the universe to radiate the 10^{53} ergs imparted to the neutrinos. "It is a feat that stretches even the well-stretched minds of astronomers" as Woosley & Weaver (1989) remark impressed. Accompanying the explosion is an enormous outburst of electromagnetic radiation which typically releases 10^{49} ergs over several hundred days and, with peak luminosities in the optical wavelength range of about 10^{43} ergs/s, makes the supernova as bright as its entire host galaxy.

Due to this intrinsic brightness, galactic supernovae have been observed since almost two millenia. At least as early as 185 A.D., Chinese astronomers have recorded them as "guest stars", i.e. stars that suddenly appeared in the sky, were visible for several months or even a few years, and then faded away. An excellent discussion of the fascinating observational accounts found in Chinese but also in Korean, Japanese, Arabic and medieval European records and the deduced association of present day supernova remnants with these historical supernovae is given by Clark & Stephenson (1977). To date, long-term search programs have led to the detection of around 1000 extragalactic supernovae (Bartunov & Tsvetkov 1997) with about 100 being discovered per year.

The importance of supernovae reaches far beyond the different branches of astrophysics. It is under these extreme conditions that substantial amounts of heavy elements are produced and together with the products of the star's previous hydrostatic burning phases are expelled to interstellar space, thereby enriching the interstellar medium with elements heavier than helium, the prerequisites of life. In this respect supernovae play also a second, equally important role. Since they represent the major source of energy input into the Galaxy they can directly trigger gravitational collapse of interstellar clouds from which new stars and planetary systems can form.

Since the early work of Minkowski (1941), supernovae have been classified into two basic types: Type I events which show no hydrogen Balmer lines in their spectra and

Type II where hydrogen lines are clearly present. Both types also differ in their absolute magnitudes at peak light and in the shapes of their light curves. While typical light curves of both types start with a rise in luminosity, which extends over a week or two, Type I events show peaks which are fairly narrow while the peak of Type II is broad. About 80% of all Type I light curves are nearly identical, while there is a significant spread in light curve shapes within Type II.

The differences within the two classes led to a sub-classification. Type II supernovae are subdivided into Type II-L and Type II-P depending on whether their light curve shows a linear decline of the bolometric magnitude (i.e. an exponential decline of the *luminosity*) after maximum light or the appearance of a marked plateau, respectively. Type I supernovae on the other hand are subdivided *spectroscopically* into Type Ia events which show the marked Si II $\lambda6355$ Å absorption feature, blue-shifted to $\lambda6150$ Å in their spectra during peak light, and Types Ib and Ic which do not. The presence of helium lines, especially He I $\lambda5876$ Å in turn distinguishes Type Ib from Type Ic (Wheeler & Harkness 1986, Harkness et al. 1987, Fillipenko 1997 and references therein).

Information on the progenitor systems can be inferred from the types of the host galaxies as well as the locations of the supernovae within them. Type Ia supernovae occur in all types of galaxies including ellipticals and show no preference for spiral arms when they occur in spiral galaxies. This indicates that they are connected to low-mass, old-population stars. It is nowadays widely believed that they originate from the thermonuclear explosion (and complete disruption) of white dwarfs which exceed the Chandrasekhar mass owing to mass transfer in a binary system (Hoyle & Fowler 1960, but see e.g. Livne & Arnett 1995 and Woosley & Weaver 1994 for sub-Chandrasekhar mass scenarios). Consistent with this picture is their intrinsic brightness which requires that rather large amounts (more than about 0.5 $M_\odot$) of radioactive ^{56}Ni have to be synthesized during the explosion in order to power the light curve. Since Chandrasekhar mass white dwarfs represent a rather homogeneous class of objects, Type Ia supernovae are regarded as "standard candles". They are of significant importance for cosmology since they allow to determine the distances of remote galaxies and thereby measure the Hubble constant and the deceleration parameter of the Universe.

Type II as well as Type Ib/c supernovae on the other hand have only been observed in spiral galaxies later than Hubble type S0. They show a strong preference for spiral arms and H II regions which indicates massive Population I stars as progenitors. Indeed, evidence that the progenitors and the explosion mechanism of Types Ib/c must be quite distinct from Type Ia supernovae can also be found in spectroscopic data. Spectra of Type Ib/c explosions taken later than about a month after maximum light are dominated by strong O I emission. In contrast, Type Ia spectra of the same age display various Fe and Co lines but no oxygen. Furthermore, both Type Ib and Ic supernovae have been detected by radio observations (Weiler & Sramek 1988), while Type Ia has not. Since radio emission is expected to result from the interaction of the supernova's ejecta with circumstellar material, this lends further support to the hypothesis that Types Ib and Ic originate from massive stars which show an appreciable amount of mass loss. Thus, the majority of supernova types (i.e. Ib, Ic, II-L, II-P etc.) is nowadays thought to originate from the collapse of the iron cores of evolved massive stars with zero age main sequence masses $M > 8\,M_\odot$. While Type II supernovae are explosions of stars with a massive hydrogen envelope, Types Ib and Ic are obviously connected to progenitors which have lost their hydrogen and in case of Type Ic possibly also (a part

of) their He envelope (Swartz et al. 1993; Nomoto et al. 1995, 1997). There is no general agreement, however, on whether Type Ic should be regarded as a separate fundamental class. The excitation of the $1s2p\,^3\mathrm{P^o}$ state responsible for the characteristic He I $\lambda5876$ Å absorption line which distinguishes Type Ib from Type Ic depends sensitively on the amount of newly synthesized radioactive ^{56}Ni which is mixed up to the supernova photosphere from layers near the collapsed core (Lucy 1991; Woosley & Eastman 1997). This could imply that the amount of mixing is the primary difference between Types Ib and Ic and that a smooth transition between both could exist (but see the discussion in Lucy 1991 for possible problems arising in this scenario).

Unfortunately, the large distances of extragalactic supernovae (up to several 100 Mpc) usually preclude a direct identification of the progenitor stars and render truly detailed observations impossible, which could be used to test the current theoretical models. One can therefore understand the excitement prevailing in the astrophysical community when on February 23rd 1987, SN 1987 A, a Type II supernova, exploded in the Large Magellanic Cloud at a distance of merely 50 kpc from the sun. For the first time ever it became possible to identify the progenitor star of a supernova with the $\sim 18\,\mathrm{M_\odot}$ blue supergiant Sk $-69°\,202$ and to detect neutrinos from the collapse of its core to a compact object (Hirata et al. 1987; Bionta et al. 1987), presumably a neutron star. Though surprise was initially great, that a blue and not a red supergiant (as favored by most stellar evolutionary calculations) had exploded, the fundamental predictions of supernova theory were impressively confirmed. Throughout the rest of this work we will be concerned exclusively with core collapse supernovae and in particular with models of Type II explosions.

1.2 The quest for an explosion mechanism

Already in 1934, Baade & Zwicky speculated on the existence of extremely compact stars consisting predominantly of neutrons and proposed that the gravitational binding energy released during the formation of such a neutron star from an ordinary star is the energy source of supernovae. Observational confirmation of this hypothesis came with the detection of pulsars, i.e. rapidly rotating neutron stars with strong magnetic fields ($\sim 10^{12}$ G), in the Crab (Staelin & Reifenstein 1968; Cocke et al. 1969; Richards & Comella 1969) and Vela (Large et al. 1968; Wallace et al. 1977) supernova remnants. However, the details of the explosion mechanism still remain elusive. Even nearly forty years of theoretical and numerical work have not led to definite conclusions on how the collapse is reversed to yield the observable explosion. This dismal state is largely due to the fact that realistic supernova modeling represents a challenge in nearly every respect, starting with fundamental uncertainties in our knowledge of weak interaction and dense matter physics, the difficulties introduced by an accurate treatment of neutrino transport in time-dependent hydrodynamic simulations, the multidimensional nature of the problem and the extreme non-linearity of the resulting equations of reactive, self-gravitating, radiation-hydrodynamic fluid flow, and ending with the importance of general relativistic effects.

The current standard scenario begins when a star with an initial mass on the main sequence of more than about $8\,\mathrm{M_\odot}$, after having proceeded through subsequent phases of central thermonuclear burning, has built up an onion-shell like internal structure with a central iron core. The core is surrounded by shells consisting of Si+S, O+Ne+Mg, C+O, and He, respectively, the products of the previous burning phases, and (in case

of Type II supernova progenitors) an envelope of hydrogen and helium.

Since iron-group nuclei have the largest binding energy per nucleon, it is not possible to gain energy neither from their fusion nor from their fission and the core, unable to support its pressure against copious neutrino cooling, becomes unstable to gravitational collapse. At the onset of collapse central densities $\rho_c \approx 10^{10}\,\mathrm{g\,cm^{-3}}$, temperatures $T_c \approx 8-10 \times 10^9\,\mathrm{K}$ and rather low entropies per nucleon of around $1\,k_B$ are encountered. Under these conditions the pressure, p, is dominated by relativistic, degenerate electrons and the adiabatic index $\gamma = (\partial \ln p / \partial \ln \rho)_{|Y_e, S}$ (with ρ denoting the density, Y_e the ratio between the electron and the baryon density and S the entropy) is close to the critical value of $4/3$. In addition, strong and electromagnetic interactions are in equilibrium with each other, i.e. (local) nuclear statistical equilibrium (NSE) is established, and the composition of the matter is determined by the Saha equation. The instability sets in because for temperatures in the given range, NSE starts to favor alpha particles and free nucleons rather than iron-group nuclei, so that photodisintegration of the iron nuclei by energetic photons sets in. Since this is an endothermic process it saps pressure support from the core. Furthermore, electron captures on protons, which become important at high densities, reduce the electron fraction Y_e and thus the Chandrasekhar mass

$$M_{\mathrm{Ch}} = 1.457(2Y_e)^2 \mathrm{M}_\odot, \qquad (1.1)$$

above which the core cannot be stabilized against its own gravity by the pressure of its degenerate electron gas. Since the mass of the core is continuously growing due to silicon shell burning, it must eventually exceed the Chandrasekhar mass. Within about one tenth of a second, the core, several thousand kilometers in size, collapses to a configuration with a radius of only $\sim 50\,\mathrm{km}$, the proto neutron star. The gravitational binding energy released during collapse is of the order of

$$E \approx 3 \times 10^{53} \left(\frac{M}{\mathrm{M}_\odot} \right)^2 \left(\frac{R}{10\,\mathrm{km}} \right)^{-1}\,\mathrm{ergs} \qquad (1.2)$$

and more than adequate to explain the kinetic energy of the ejecta of $\sim 10^{51}$ ergs. For a long time it was hoped that a sufficiently large fraction of this energy could be converted into outward momentum of the stellar envelope by a purely hydrodynamic mechanism and thus lead to a "prompt" explosion, i.e. an explosion which evolves on the collapsed core's dynamical time scale of a few milliseconds. This hope has not been fulfilled by detailed core collapse calculations. Nowadays, a second mechanism found by Wilson (1985), discussed by Bethe & Wilson (1985) and further tested by Wilson et al. (1986) and Wilson & Mayle (1993), appears to be more promising. It makes use of the fact that nearly all of the released gravitational binding energy is initially stored as internal energy of degenerate leptons in the proto neutron star and radiated away by neutrinos on its cooling time scale of several seconds. A conversion of only about 1% of the energy carried away by the neutrinos into kinetic energy of the stellar envelope is sufficient to generate a "delayed" explosion (typically occuring on a time scale of a few hundred ms as opposed to the few ms in case of a prompt explosion) and to explain the supernova outburst. In the following we will discuss some of the problems inherent to these two basic explosion paradigms, already noting that for the moment we intentionally leave out multidimensional effects caused by rotation and hydrodynamic instabilities which in general lead to significant adjustments of the standard picture.

1.2.1 The prompt mechanism

According to the self-similar solutions of Yahil & Lattimer (1982) and Yahil (1983), who extended the earlier work of Goldreich & Weber (1980), the core separates during collapse into a homologously ($v(r) \propto r$) and subsonically collapsing inner core and a supersonically collapsing outer core. As long as densities in the core are relatively low, neutrinos produced by electron captures on free protons can leak out which leads to a deleptonization of the core, i.e. the electron fraction, Y_e, decreases. For densities larger than about $10^{12} \, \mathrm{g \, cm^{-3}}$, however, the mean free path of neutrinos decreases to such low values that the neutrino diffusion time scale becomes larger than the collapse time scale and the neutrinos become trapped interior to the so-called "neutrino sphere" defined as the surface where the neutrinos' (energy dependent!) optical depth reaches values between 2/3 and unity.

The collapse proceeds until the inner core reaches and exceeds nuclear saturation density. At such densities, the incompressibility of nuclear matter abruptly increases the adiabatic index γ to values above 2 and causes the inner core to rebound. Starting at the center of the core successive mass shells are stopped while pressure waves move outwards in radius and steepen into a strong shock wave near the inner core's outer edge. The shock starts to propagate through the still infalling outer core and, if it is sufficiently energetic, reverses the infall and ejects the entire envelope of the star giving rise to the supernova.

Analytical estimates as well as numerical simulations show that the shock which forms at a mass coordinate of about $0.8 \, \mathrm{M_\odot}$ has an initial energy of $E_{\mathrm{shock}}^{\mathrm{ini}} = (4-10) \times 10^{51} \mathrm{ergs}$. However, prior to the shock's passage, the matter in the outer core consists of tightly bound iron-group nuclei, supersonically falling toward the shock with maximum velocities close to a quarter of the speed of light. In propagating through the outer core the shock must dissociate these nuclei to free nucleons and alpha particles due to the high post-shock temperatures of several MeV. Since 8.8 MeV are required to unbind a nucleon from an iron nucleus, the shock looses an energy of about $E_{\mathrm{loss}} = 1.7 \times 10^{51} \mathrm{ergs}$ per $0.1 \, \mathrm{M_\odot}$ of core material dissociated. Note that once the shock succeeds to emerge from the iron core it does *not* suffer further energy losses due to photodisintegration, because all outer layers of the star consist of elements with (substantially) smaller binding energies per nucleon than iron. The strong and electromagnetic reactions which occur during explosive silicon, oxygen, neon and carbon "burning" (e.g. Thielemann et al. 1998) transform these light nuclei into heavier elements and therefore lead to a net *release* of nuclear energy.

Considering only the energy loss due to photodisintegration of iron-group nuclei an upper limit to the mass of the outer core for a successful prompt explosion can be derived which amounts to about $0.45 \, \mathrm{M_\odot}$. In order to avoid stalling, the shock thus has to form quite far out in the core, i.e. the inner core has to be very large. As numerical simulations including realistic neutrino interactions and transport show, this is precluded by the deleptonization from which the inner core suffers during infall. With an inner core mass in the range 0.8–$0.9 \, \mathrm{M_\odot}$ as found in these calculations this implies that the prompt mechanism may work, if at all, only for iron cores with masses smaller than $1.35 \, \mathrm{M_\odot}$. However, the photodissociation of iron nuclei has also a second adverse effect on the shock. Huge amounts of electron neutrinos are produced by electron captures on the protons thus released. As long as the shock is moving through material still within the (electron) neutrino sphere these neutrinos are trapped. However, once the shock crosses

the neutrino sphere, the neutrinos can escape (almost) freely and thus cool the post-shock matter. The combined energy losses are so severe, that in all modern simulations the shock stagnates still within the outer core and becomes an accretion shock at a radius of about 100 km within only a few tens of milliseconds after bounce.

1.2.2 The delayed mechanism

The idea that neutrinos might generate supernova explosions dates back to Colgate & White (1966). Though the calculations in this pioneering work lacked a realistic treatment of neutrino energy transfer to the matter by simply depositing half the thermal energy of the inner core into the surrounding stellar layers (see the critique of Arnett 1996, p. 382), they inspired more realistic simulations of core collapse in which an accurate modeling of neutrino/matter interactions is a key ingredient. The result of such calculations performed by Wilson (1985) is the modern explosion paradigm, in which neutrino heating can generate delayed neutrino driven explosions by reviving an otherwise failing prompt shock. The main reactions by which this is accomplished are

$$\nu_e + n \quad \rightarrow \quad e^- + p \tag{1.3}$$

$$\bar{\nu}_e + p \quad \rightarrow \quad e^+ + n. \tag{1.4}$$

Considering the situation behind the stalling shock in a collapsed stellar core it is essential to realize that reactions (1.3) and (1.4), which are important at radii of about 100-200 km, are *not* in local thermodynamic equilibrium since the neutrinos originating at radii of around $R_\nu = 10 - 60$ km from the electron neutrino sphere (which shrinks with time due to the deleptonization and contraction of the proto neutron star) are nearly freely streaming farther outside. In the semitransparent layers outside the neutrinosphere the heating rate due to reactions (1.3) and (1.4) can be written as

$$Q^+_{\nu_e,\bar{\nu}_e} \cong 110 \cdot \frac{L_{\nu,52} \langle \epsilon^2_{\nu,15} \rangle}{r_7^2 \langle \mu \rangle} \cdot \left\{ \begin{array}{c} Y_n \\ Y_p \end{array} \right\} \quad \left[\frac{\text{MeV}}{\text{s} \cdot \text{nucleon}} \right] \tag{1.5}$$

(Janka 1993). Here $Y_n = n_n/n_b$ and $Y_p = n_p/n_b$ are the number fractions of free neutrons and protons, respectively, (with n_b denoting the baryon density), $L_{\nu,52}$ is the (electron) neutrino or antineutrino luminosity in units of 10^{52} ergs s^{-1}, $\langle \epsilon^2_{\nu,15} \rangle$ the average of the squared neutrino energy measured in units of $(15 \text{ MeV})^2$, r_7 the radius from the central neutrino source in units of 10^7 cm and $\langle \mu \rangle$ the angular dilution factor of the neutrino radiation field. The latter quantities are defined in cgs units as

$$L_\nu \quad = \quad 4\pi r^2 \frac{2\pi c}{(hc)^3} \int d\epsilon_\nu d\mu_\nu \epsilon^3_\nu \mu_\nu f, \tag{1.6}$$

$$\langle \epsilon^2_\nu \rangle \quad = \quad \frac{\int d\epsilon_\nu d\mu_\nu \epsilon^5_\nu f}{\int d\epsilon_\nu d\mu_\nu \epsilon^3_\nu f}, \tag{1.7}$$

$$\langle \mu \rangle \quad = \quad \frac{\int d\epsilon_\nu d\mu_\nu \epsilon^3_\nu \mu_\nu f}{\int d\epsilon_\nu d\mu_\nu \epsilon^3_\nu f} \tag{1.8}$$

$$= \quad \frac{L_\nu}{4\pi r^2 c u_\nu}, \tag{1.9}$$

and thus depend on the neutrino distribution function, $f(r, t, \mu_\nu, \epsilon_\nu)$, which is itself a function of the spatial coordinate, r, the neutrino direction cosine, μ_ν, the neutrino energy, ϵ_ν and the time t. The angular dilution factor $\langle \mu \rangle$ connects the neutrino flux

$F_\nu = L_\nu/(4\pi r^2)$ with the neutrino energy density u_ν and varies between about 0.25 at the neutrinosphere and 1 for radially streaming neutrinos far out (Yamada et al. 1999; Messer et al. 1998; Janka & Müller 1996). The dependence of Eq. (1.5) on Y_n and Y_p indicates that zones for which the heating is expected to work, must be inside the shock radius. Matter outside the shock still consists of heavy nuclei which do not interact with the neutrinos as readily as protons and neutrons.

The cooling rates due to the inverse reactions of (1.3) and (1.4) are given by

$$Q^-_{\nu_e, \bar{\nu}_e} \cong 2.4 \left(\frac{T}{1\mathrm{MeV}} \right)^6 \cdot \left\{ \begin{array}{c} Y_p \\ Y_n \end{array} \right\} \left[\frac{\mathrm{MeV}}{\mathrm{s} \cdot \mathrm{nucleon}} \right] \tag{1.10}$$

(Janka 1993). Assuming a Fermi energy distribution for the neutrinos at an effective neutrino Temperature T_ν and zero chemical potential it can be shown, that the net heating rate outside of the neutrino sphere can be written as

$$Q_{\mathrm{net}} = Q^+_{\nu_e, \bar{\nu}_e} - Q^-_{\nu_e, \bar{\nu}_e} = \mathrm{const} \left[T^6_\nu (R_\nu/2r)^2 - T^6 \right] \tag{1.11}$$

(Wilson & Mayle 1993). This makes clear that neutrino heating can only deposit energy in layers which are not too hot, otherwise the T^6 term in (1.11) will dominate and matter will cool by neutrino emission instead of being heated. Because the temperature gradient between neutrino sphere and shock is negative, a surface must exist at which cooling by neutrino emission is balanced by the heating due to neutrino absorption. This surface is called the gain radius. Inside the gain radius neutrino cooling dominates whereas in the region between gain radius and shock net heating occurs. It is this heating which eventually allows the stalling shock to finally overcome the ram pressure of the infalling outer core and lead to the supernova explosion.

So far, however, only Wilson (1985), Wilson et al. (1986) and Wilson & Mayle (1993) have found explosions in their one-dimensional supernova models while other groups (Hillebrandt 1987; Bruenn 1993; Bruenn et al. 1995) could not reproduce these results. The success of the mechanism depends very sensitively on the value of the product $L_\nu \langle \epsilon^2_\nu \rangle$. Indeed, Wilson & Mayle (1993) obtained explosions only if they took into account convection inside the proto neutron star and its effect on the neutrino luminosities. Numerical studies by Janka & Müller (1996) confirm that for given neutrino spectra there exists a well-defined minimum neutrino luminosity for a model to explode and that only small changes in the luminosities around this value, e.g. caused by the still uncertain neutrino opacities (Reddy & Prakash 1997; Reddy et al. 1998; Keil et al. 1995, and the references therein), can lead to qualitatively different outcomes. Similarly, it is known that hard neutrino spectra help in producing explosions (e.g. Wilson & Mayle 1988; Mezzacappa et al. 1998b). Furthermore, the currently widely employed flux-limited diffusion schemes for neutrino transport tend to enforce $\langle \mu \rangle \to 1$ too quickly with increasing radius and thus tend to underestimate the heating rate in the gain region (Yamada et al. 1999; Messer et al. 1998; Janka 1992). All this emphasizes the importance of an accurate modeling of neutrino transport during the shock reheating phase which in general requires that the full Boltzmann transport equation has to be solved in step with the hydrodynamics, a task which is computationally extremely expensive (M. Rampp & H.-Th. Janka, private communication). Until very recently, a coupled solution of the Boltzmann and the hydrodynamic equations had only been accomplished for the core collapse phase (Mezzacappa & Bruenn 1993b,a). New calculations of Mezzacappa et al. (2000) and Rampp & Janka (2000), which have succeeded to cover also the shock revival phase, confirm that Boltzmann neutrino transport indeed yields larger heating rates. However, while in the calculations of Mezzacappa et al.

(2000) the energy deposition is sufficient in order to cause a (weak) explosion of a $13\,M_\odot$ star with an iron core of $1.17\,M_\odot$, Rampp & Janka (2000) do not obtain an explosion for a $15\,M_\odot$ star with an $1.28\,M_\odot$ core.

The failure of the unassisted "delayed" mechanism has recently renewed interest in hydrodynamic instabilities during the explosion which could lead to higher values of $L_\nu \langle \epsilon_\nu^2 \rangle$ than the usual spherically symmetric models predict (e.g. Epstein 1979; Wilson & Mayle 1993). Alternatively the efficiency of the mechanism may be enhanced by increasing the amount of matter which is heated by neutrinos if material is cycled between gain region and stalling shock by bulk convective motions (Bethe 1990; Herant et al. 1992; Herant et al. 1994). Indeed it has been widely recognized within the last few years that in contrast to the "standard scenarios" which were described above and are all based on calculations under the assumption of spherical symmetry, any realistic model of a core collapse supernova has to be multidimensional in nature. The observational evidence for the occurrence of hydrodynamic instabilities as well as the complications introduced by these multidimensional effects are the subject of Chapter 2.

Chapter 2

Hydrodynamic Instabilities in Core Collapse Supernovae

2.1 Observations requiring non-spherical models

2.1.1 SN 1987 A

The by far most important clues to extensive mixing during the explosion of core collapse supernovae were provided by SN 1987 A, the nearest supernova since centuries. Numerous independent observations of this event indicate that the expanding envelope of the progenitor star $Sk -69° \, 202$ must have substantially fragmented shortly after core collapse (for a complete and more detailed account of all relevant observational data than the one that can be given here, the reader is referred to the reviews of Hillebrandt & Höflich 1989, Arnett et al. 1989a, Wooden 1997 and Müller 1998. In the following we will only discuss the results of some representative and more recent works).

Already around March 15th, i.e. three weeks after the explosion, when the supernova's photosphere was located still inside the hydrogen envelope, the "Bochum event" appeared (Hanuschik & Dachs 1987; Hanuschik et al. 1988), an asymmetry in the Hα and other hydrogen line profiles which suggests enhanced heating of the envelope, presumably due to radioactive ^{56}Ni (Lucy 1988; Phillips & Heathcote 1989). As one-dimensional explosion models show, this isotope is synthesized by complete (explosive) silicon burning[1] in the innermost layers of the ejecta. Buried under more than 10 solar masses of overlying material it should not have been observable until about one year after the explosion. Utrobin et al. (1995) have computed synthetic Hα profiles of the "Bochum event" phase and concluded that the fine structure feature visible in the red wing of the line is consistent with the presence of a fast-moving ($v_{\mathrm{exp}} = 4700 \pm 500$ km/s), large ($\sim 10^{-3}$ M$_\odot$) ^{56}Ni clump on the rear side of the expanding hydrogen envelope. Furthermore, Wooden (1997) argues that the time evolution of the blue shifted features of the Hα line suggests that also several "fingers" of ^{56}Ni were ejected in the explosion toward the observer with high velocities.

^{56}Co, the decay product of ^{56}Ni, was directly seen for the first time in August 1987, i.e. six months after the discovery of the supernova, when hard X-rays originating

---

[1]Regardless of the initial composition, we will denote by the term "incomplete silicon burning" the nucleosynthesis in zones which experience peak temperatures of $(4 - 5) \times 10^9$ K. Zones which attain temperatures above 5×10^9 K (required for ^{56}Ni production) are said to undergo "complete silicon burning". See the discussion in Section 3.6 for details on the nomenclature.

from scattered 847 keV and 1238 keV γ-photons from the decay of ^{56}Co to ^{56}Fe were detected (Dotani et al. 1987; Sunyaev et al. 1987), and finally the Doppler-broadened γ-ray lines themselves were measured (Matz et al. 1988). These detections occurred half a year earlier than spherically symmetric explosion models had predicted, and could be accounted for by one-dimensional explosion models in which the ^{56}Co was mixed artificially into the hydrogen envelope (Pinto & Woosley 1988a,b; Kumagai et al. 1989).

Further spectroscopic evidence for very high velocities of iron-group elements was provided by infrared Fe, Co and Ni lines showing extremely broad wings, which could be observed after the ejecta became optically thin in the infrared at about day 150. The importance of these measurements is twofold:

1. They directly and independently confirm that iron-group elements were mixed from the slower moving inner regions of the ejecta into outer layers which were expanding with up to 4000 km/s

2. They show an unresolved emission feature in the profiles of the 17.94 and 25.99 μm Fe II line (Haas et al. 1990; Colgan et al. 1994) that can be interpreted as a high-velocity clump moving with ≥ 3000 km/s and containing about 3% of the total iron mass, i.e. about 2×10^{-3} M$_\odot$.

Li et al. (1993) in analyzing the light curves of several Fe, Co and Ni infrared lines found that the observations for 150 days $\leq t \leq 2$ yrs can be explained if these elements were mixed outward macroscopically and inhomogeneously in about 60 to 100 identical clumps. From studies of the "sawtooth profile" of the [O I] $\lambda\lambda 6300, 6363$ lines, Stathakis et al. (1991) concluded that also the [O I] emitting material is clumpy while Chugai (1994) estimated that 1.2–1.5 M$_\odot$ of oxygen are present in the ejecta which are distributed in about 2000 clumps.

That not only oxygen and iron-group elements were mixed outward during the explosion but also hydrogen mixed into the metal core to velocities as low as ~ 700 km/s is indicated by the narrow central peak of the Hα line at about day 800 after the explosion (Phillips et al. 1990) and by synthetic spectra of Kozma & Fransson (1998). These findings are in agreement with the observed smoothness of the light curve. Light curve modeling (Arnett 1988; Woosley 1988; Shigeyama et al. 1988; Shigeyama & Nomoto 1990) has shown that besides mixing of ^{56}Co as well as Si, S, C and O into the hydrogen envelope, also deep mixing of H and He into the metal core is required. The combined effects of early radioactive heating and the time-spread in the energy release due to hydrogen recombination, which can be obtained in this way, enable one to fit the position and shape of the broad light-curve peak which otherwise cannot be reproduced satisfactorily using one-dimensional explosion models (Shigeyama & Nomoto 1990).

Fassia & Meikle (1999) have recently used observations of He I 10830 Å to probe the extent of the ^{56}Ni mixing at very early times. The presence of He I 10830 Å later than about day 10 after the explosion implies re-ionization of the He-rich ejecta, which is attributed to upward mixing of radioactive material. Fassia & Meikle (1999) demonstrate that a good fit to the He I line profile as well as the γ-ray light curves can be obtained when a mixed version of the one-dimensional model 10H of Woosley (1988) is used to model the explosion. Moreover, their estimate that about 3–4% of the total ^{56}Ni mass expanded faster than 3,000 km/s appears to be consistent with the iron-group velocities deduced from the infrared line profiles (Haas et al. 1990) as well as the conclusions of Utrobin et al. (1995) from the Hα data. As Fassia & Meikle (1999) note, however, the

microscopic mixing employed in their models is most likely not a good approximation to the real situation in which clumps of material interpenetrate the different stellar layers. It is thus certainly not possible to confirm the existence of a single large ^{56}Ni clump (Utrobin et al. 1995) from the He I 10830 Å data. The spread in the numbers and sizes of clumps found by Utrobin et al. (1995), Li et al. (1993) and Chugai (1994) is also uncomfortably large and difficult to understand on theoretical grounds if one assumes that a single physical mechanism (i.e. a hydrodynamic instability) is responsible for their formation.

2.1.2   Other supernovae and supernova remnants

Recently observational evidence is growing which indicates that hydrodynamic instabilities are apparently generic in core collapse supernovae and that the mixing found in SN 1987 A is by no means an exception. The [O I] lines at 6300 and 6363 Å have again proved to be particularly useful in this respect. Using an analysis similar to the one employed by Stathakis et al. (1991) for SN 1987 A, Filippenko & Sargent (1989) have found evidence that the ejecta of SN 1987 F, a Type Ib supernova, were also clumped. Spyromilio (1991) and Spyromilio (1994) as well as Wang & Hu (1994) came to similar conclusions for SN 1988 A (Type II), and SN 1993 J (Type IIb), respectively. The latter supernova is generally attributed to the explosion of a 15 M$_\odot$ red supergiant which has lost most of its hydrogen envelope. Iwamoto et al. (1997) could only fit its light curve peak by mixing ^{56}Ni throughout the inner 2.2 M$_\odot$ of the star, i.e. throughout more than half of the helium core.

Fassia et al. (1998) have found late-time He I 10830 Å emission in the Type II-P SN 1995 V, which, as in the case of SN 1987 A, requires the presence of a reionizing energy source. They concluded that upward mixing of ^{56}Ni, with $\sim 10^{-5}$ of the total nickel mass reaching above the helium photosphere was needed in order to fit the line profile. Similar consequences of ^{56}Ni mixing have apparently been noted in optical spectra of Type Ib supernovae at least as early as the work of Harkness et al. (1987). Using synthetic spectra to identify He lines in these objects, Harkness et al. (1987) had to overpopulate excited states of He I by factors of $\sim 10^4$ relative to local thermodynamic equilibrium (LTE) conditions in order to reproduce the observed strong lines. Lucy (1991) has computed synthetic Type Ib spectra and has shown that the presence of the He I lines and the implied departures from LTE can be understood in terms of impact excitations and ionizations by nonthermal electrons, presumed to originate from collisions with the high-energy electrons resulting from Compton-scattering of the γ-rays from ^{56}Co decay (see also the discussion in Woosley & Eastman 1997).

It is well-known from work on galactic supernova remnants that fast moving clumps of material enriched in metals exist in Vela (Aschenbach et al. 1995), Cas A (Anderson et al. 1994) and Puppis A (Winkler & Kirshner 1985). Particularly intriguing are the recent high-resolution observations of the Cas A remnant by the Chandra X-ray observatory. Hughes et al. (2000) interpret the varying spectral characteristics of the different filaments and knots in Cas A as being indicative for the spatial distribution of the products of explosive oxygen and silicon burning. They find a spatial separation between Fe and Si-rich material with the Fe-rich gas being located at the outermost edge of the ejecta, preceding the Si-knots. Arguing against projection effects, they conclude that the ejecta must have undergone a spatial inversion, since the stellar zones which experience explosive silicon burning are originally located interior to the oxygen

burning regions. In addition, they emphasize that this macroscopic mixing obviously did not lead to a homogenization of the composition.

Finally, further possible evidence for substantial macroscopic mixing in core collapse supernovae is provided by the discovery of several types of circumstellar dust grains which were preserved in primitive meteorites at the time the solar system has formed. Among these, a small fraction of the presolar SiC grains (called grains X) as well as some low-density graphite grains show isotopic ratios with marked deviations from the solar values, which were interpreted as hinting toward a supernova origin of these grains (Amari et al. 1992; Zinner et al. 1995; Nittler et al. 1996; Travaglio et al. 1999). In particular, Nittler et al. (1996) report on large excesses of ^{44}Ca relative to the solar ^{44}Ca/^{40}Ca ratio in X and graphite grains from the Murchison meteorite which they attribute to in situ decay of ^{44}Ti. Current (one-dimensional) core collapse supernova models, which take into account the explosive nucleosynthesis, predict that this short-lived isotope ($T_{1/2} = 58$ yrs) is produced in the innermost layers of the ejecta, which experience an α-rich freezeout from nuclear statistical equilibrium (Thielemann et al. 1996; Woosley & Weaver 1995). Its synthesis depends strongly on the details of the explosion mechanism. In addition, ^{44}Ti is also produced in sub-Chandrasekhar mass models of Type Ia explosions (Woosley & Weaver 1995; Woosley et al. 1986; Woosley & Weaver 1994). Bearing in mind the uncertainties of the current models and assuming that the grains indeed condensed in the ejecta of a core collapse supernova, as Nittler et al. (1996) suggest, the presence of ^{44}Ti (and ^{28}Si) in material which had a C/O abundance-ratio > 1 (required for graphite and SiC formation) might be interpreted as an indication for (macroscopic) mixing of the innermost stellar layers with material from the regions near the C/He interface of the star. It should be noted, though, that certain isotopic ratios of the grains can only be explained if, in addition, substantial *microscopic* mixing of the composition is assumed (Amari et al. 1995; Travaglio et al. 1999).

2.2   Rayleigh-Taylor instabilities in supernova envelopes

2.2.1   Models for the mixing in SN 1987 A

Early analytic and numerical work (Falk & Arnett 1973; Chevalier 1976; Chevalier & Klein 1978; Bandiera 1984) had already pointed out the possible occurence of substantial mixing due to Rayleigh-Taylor instabilities during the expansion of a supernova's ejecta into an (inhomogeneous) circumstellar medium. However, with the advent of SN 1987 A direct evidence was obtained that large-scale mixing *during the explosion itself* had occured. Today there is general agreement among supernova theorists that the observed mixing is a consequence of Rayleigh-Taylor instabilities which grew behind the outward sweeping shock wave even before the latter reached the surface of the star about 2 hours after core bounce.

As the theory of adiabatic point-blast explosions (Sedov 1959) shows, the propagation speed of the shock depends sensitively on the density gradient of the ambient medium. The shock accelerates whenever the density declines with radius steeper than $\sim r^{-3}$ while it must decelerate when the density profile is shallower than $\sim r^{-3}$. All realistic stellar evolution models for the progenitor of SN 1987 A (Woosley et al. 1988; Woosley 1988; Arnett 1987, 1988; Nomoto et al. 1988) share the basic feature that rather pronounced density jumps occur at the interfaces which separate the shells of varying

composition. Thus, whenever the outward moving shock encounters a composition interface in the progenitor star, the steep drop in density leads to an initial acceleration of the shock which is followed by a deceleration once it enters the region behind the interface where the density usually decreases with radius slower than $\sim r^{-3}$. This unsteady propagation speed of the shock leads to the formation of density inversions at the composition interfaces which themselves give rise to the instability. The criterion for instability derived from a linear stability analysis (for the case of incompressible flows) has been given by Chevalier (1976) as

$$\frac{d\rho}{dr}\frac{dp}{dr} < 0, \qquad (2.1)$$

i.e. layers with density and pressure gradients of opposite sign are unstable and interpenetration of the material in this region must be expected. Bandiera (1984) has performed a linear stability analysis for compressible flows and shown that in this case the criterion for instability is the well-known Schwarzschild criterion for convection (Kippenhahn & Weigert 1994). Ebisuzaki et al. (1989) as well as Benz & Thielemann (1990) have applied the incompressible and compressible instability criteria, respectively, to the problem of shock propagation in a progenitor model of SN 1987 A computed by Nomoto et al. (1988) and concurred in that instabilities must be expected to grow at the C+O/He and He/H composition interfaces. In order to gain a more detailed insight into the problem, multidimensional numerical simulations were required due to the non-linearity of the hydrodynamic equations. Numerous calculations of shock propagation and Rayleigh-Taylor mixing in models of blue-supergiant stars were thus performed. In the following we will give an overview of these calculations, not considering the very early simulations of Nagasawa et al. (1988), Müller et al. (1989) and Benz & Thielemann (1991) which used polytropic stellar models as initial conditions and which are nowadays only of academic interest since they do not give a realistic picture of the explosion of the progenitor of SN 1987 A.

It must be emphasized that due to computational reasons, *all* these investigations have excluded the explosion mechanism itself from the study, i.e. they assumed that the late-time propagation of the shock could be followed independently of its creation. According to the different methods which were adopted in order to initiate the explosion, the calculations can be divided into two main groups. In addition, different numerical schemes of varying sophistication were employed by the different workers in the field. We will describe the results of these simulations in some detail since they provide significant motivation for the calculations in this thesis.

Models using point-like explosions

In these studies, a shock wave was created artificially by depositing the explosion energy near the center of a pre-collapse progenitor model. The propagation of the resulting shock was subsequently followed in one spatial dimension until it had reached the He/H interface. The 1D models were then mapped to a 2D grid and the rest of the evolution computed with a multidimensional code after seed perturbations were applied to the radial velocity field in order to break the spherical symmetry of the problem and to trigger the growth of the instability. Calculations of this kind, were performed by Arnett et al. (1989b), Fryxell et al. (1991) and Müller et al. (1991b) for a 15 $M_\odot$ progenitor model (Arnett 1987), by Hachisu et al. (1990) for a 16 $M_\odot$ progenitor model which originated from a 20 $M_\odot$ zero-age-main-sequence model (Nomoto et al. 1988;

Shigeyama & Nomoto 1990), and by Herant & Benz (1991) and Herant & Benz (1992) using several progenitors from different authors.

All of these studies found that Rayleigh-Taylor instabilities indeed grow within the first hours after shock formation and lead to macroscopic mixing of different stellar layers. The first of these works (Arnett et al. 1989b) clearly showed that the He/H interface becomes unstable after the passage of the shock wave, and that narrow, dense, mushroom-capped fingers of helium form, which penetrate into the hydrogen envelope while hydrogen is mixed into the He-core in large low-density bubbles. Arnett et al. (1989b) used the PROMETHEUS code which is an implementation of the direct Eulerian Piecewise Parabolic Method (PPM) of Colella & Woodward (1984), a scheme which still represents the state of the art in numerical fluid dynamics of compressible flows. The later computations of this group (Fryxell et al. 1991; Müller et al. 1991b) with improved resolution succeeded in proving that also a second instability develops at the C+O/He interface of the stellar model of Arnett (1987) and interacts with the one at the He/H interface, thus transporting metals through the He-fingers into the hydrogen envelope. This result was also confirmed in subsequent calculations by Müller et al. (1991a) who employed moving cylindrical and spherical grids of up to 700×700 and 800×400 zones, respectively. The radial resolution of these calculations was equivalent to that of a fixed, spherical grid covering the whole star with up to 4000 equidistant radial zones.

Using the progenitor of Nomoto et al. (1988) and a Lax-Wendroff as well as a Roe-type scheme Hachisu et al. (1990) and Hachisu et al. (1992), respectively, found only the instability at the He/H interface. While Müller et al. (1991b) pointed out that the discrepancies may be partly due to differences in the numerics, resolution, and the treatment of the equation of state employed by the two groups, Smoothed Particle Hydrodynamics (SPH) calculations of Herant & Benz (1991) and Herant & Benz (1992) using the progenitor models of both, Hachisu et al. (1990) and Fryxell et al. (1991), suggest that the differences stem mainly from the structure of the progenitors.

While all these calculations were successful in qualitatively explaining the main features of the mixing observed in SN 1987 A, they failed to quantitatively reproduce the high observed cobalt and iron velocities. As Table 2.1 shows, Müller et al. (1991b), Müller et al. (1991a) as well as Hachisu et al. (1990) obtained maximum ^{56}Ni velocities of ≤ 2000 km/s. Müller et al. (1991a) noted that, compared to their earlier lower resolution simulations, in their moving-grid calculations the Rayleigh-Taylor "fingers" gave way to a smaller "turbulent" mixing layer consisting of bent mushrooms. This result, which was due to a better resolution of the Kelvin-Helmholtz instability between the protruding "fingers" and the ambient medium, did not have appreciable effects on the velocity distribution of the elements, though. Having exhausted a possible numerical origin of the small nickel velocities, Müller et al. (1991a) as well as Hachisu et al. (1990) speculated that the energy released by the decay of ^{56}Ni to ^{56}Co may boost these velocities to values more in line with the observations. The potential importance of this effect was already pointed out by Woosley (1988) as well as Arnett (1988). Calculations exploring this hypothesis were performed by Herant & Benz (1991) using SPH. While one must note that despite the Lagrangian nature of SPH their numerical resolution (between 3000 and 60,000 particles) appears to be hardly sufficient to confidently follow the evolution over the first three months (although the authors claim otherwise), their result was that nickel and cobalt decay indeed increased the peak velocities of ^{56}Ni and its decay products by about 40% from 1400 to 1900 km/s for the progenitor of Nomoto

	method	pert.	res.	note	progenitor	time	Explosion energy [10^{51} ergs]		
							1.0	1.0[a]	2.0[a]
Herant & Benz (1992)	SPH	5%; rand.	~ 23000	cyl. coor.	20 $M_\odot$ N88	~ 24000 s	1100	2350	3000
					15 $M_\odot$ A87		750	–	–
Hachisu et al. (1990)	Lax-Wendroff	5%; rand.	1793×1793	cyl. coor.	20 $M_\odot$ N88	1000 s	1880[b]	–	–
Fryxell et al. (1991)	PPM	1%–10%; rand.	500×500	cyl. coor.	15 $M_\odot$ A87	~ 13000 s	2000[c]	–	–
Müller et al. (1991b)	PPM	10%; rand.	1000×1000	cyl. coor.	15 $M_\odot$ A87	~ 12600 s	1500	–	–
Müller et al. (1991a)	PPM	10%; rand.	700×180	spher. coor.; moving grid	15 $M_\odot$ A87	~ 12600 s	1500	–	–
Nagataki et al. (1998b)	Roe	0%	2000×100	spher. coor.;	20 $M_\odot$ N88	5000 s	1500	–	–
		5%		Model A1		5000 s	1800	–	–
		30%				5000 s	2300	–	–

Table 2.1: Maximum ^{56}Ni velocities obtained from some representative 2D hydrodynamic models of Rayleigh-Taylor mixing in SN 1987 A. All the calculations covered a quadrant of the entire star ($0° \leq \theta \leq 90°$) except for the work of Herant & Benz (1992) who used a 60° wedge which was centered around the equator. The amplitudes of the initial radial velocity perturbations are also given. In the column for the resolution, the number of particles is given for the SPH runs and the number of zones in the first and second grid dimension in all other cases. a: models with premixing, b: value estimated from tracer particles initially placed at O/Si interface, c: No explicit tracking of ^{56}Ni mass fraction, value estimated from ^{24}Mg mass fraction. A87: Arnett (1987), N88: Nomoto et al. (1988), rand: random perturbation.

et al. (1988). Yet the magnitude of this effect was too small to explain the high-velocity wings of the Fe lines which extend to 3500–4000 km/s. When heated by the radioactive energy release, the nickel expanded in all directions forming a large, hot bubble, since the paths of least resistance were not directed outward along the fingers but rather inward and sideways.

Herant & Benz (1992) presented a more extensive set of calculations with different progenitor models, initial perturbations, explosion energies and (assumed) ^{56}Ni distributions which included also a three-dimensional computation. As the simulations of Herant & Benz (1991) these newer calculations suffered from the same problems regarding resolution and the high intrinsic level of noise of SPH, which Herant et al. (1992) (in a different context) found to be "largely sufficient to seed the instabilities [without adding seed perturbations]". Yet, the authors concluded that using high explosion energies (2×10^{51} ergs) in conjunction with "premixing" of the ^{56}Ni it is possible to explain the high nickel velocities. Their simulations, which did not cover the first 300 seconds of evolution, required that the ^{56}Ni was mixed out to mass coordinates of 1.5 M$_\odot$ above the Fe/Si interface (i.e. throughout 75% of the metal core of the progenitor model of Nomoto et al. 1988) by some "early" instability. Herant & Benz (1992) identified this instability with neutrino-driven convection during the first second of the explosion. So far no other group has attempted to verify these claims.

A possibility to obtain higher ^{56}Ni velocities which has not yet been studied extensively is the influence of three-dimensional effects on the growth and propagation of the high-density Rayleigh-Taylor fingers. Since the fingers and mushrooms which are found in two-dimensional calculations are in fact tori exhibiting axial symmetry around the polar axis, one should expect that the instability will develop differently in two and three dimensions. Preliminary three-dimensional calculations with an angular resolution of 0.9° were done by Müller et al. (1991c) for the 15 M$_\odot$ progenitor of Arnett (1987) using PROMETHEUS. They found pronounced instabilities that formed genuine three-dimensional clumpy structures with a density which was higher than in the surrounding medium by a factor of ten. Yet, the overall appearance of the instability qualitatively resembled coarse two-dimensional results on grids with similar angular and radial resolution.

In an interesting recent work, Kane et al. (2000) compare the growth of Rayleigh-Taylor instabilities at the C+O/He and He/H interfaces of a 20 M$_\odot$ progenitor in 2D and 3D computations using PROMETHEUS. They show that in the rest frame of an unperturbed (one-dimensional) interface a three-dimensional single-mode perturbation grows 30%–35% faster than a corresponding two-dimensional perturbation. Although their highest resolution 3D calculations do not seem to be converged yet, they also indicate that the Rayleigh-Taylor fingers penetrate further in 3D than in 2D, a result which is consistent with analytic and experimental work on single-mode perturbations of incompressible fluids in planar geometries. Still, however, as Kane et al. (2000) note, the differences are not sufficient to account for the discrepancy between the observed ^{56}Ni velocities and the results of the previous 2D hydrodynamic calculations.

Models using aspherical shocks

A somewhat different, two-dimensional, approach was chosen in calculations belonging to the second group of numerical studies. These were also started from realistic progenitors but initiated the explosion using a parameterized, aspherical shock wave. The

recent calculations of Nagataki et al. (1998b) belong to this class. They represent an improvement upon earlier models of Yamada & Sato (1990, 1991) with respect to the numerics (second order Roe scheme compared to a first order donor-cell scheme) and by computing the nucleosynthesis in the early stages of the explosion using a marker particle approximation (Nagataki et al. 1997). However, besides neglecting the complications introduced by the explosion mechanism itself, with only 10 angular zones and 500 marker particles the spatial resolution in the calculations of Nagataki et al. (1997) is much too low to allow for detailed conclusions about the spatial distribution and yields of the newly synthesized nuclei. Judging from the results of Fryxell et al. (1991) and Müller et al. (1991b) which are given in Table 2.1, the angular resolution in the subsequent Rayleigh-Taylor calculations of Nagataki et al. (1998b), who covered a quadrant of the entire star with 2000×100 zones, appears to be also too low in order to obtain approximately converged results. Nonetheless, Nagataki et al. (1998b) believe that spherical explosion models cannot reproduce ^{56}Ni velocities as high as 3000 km/s even if the amplitude of the initial radial velocity perturbations is as high as 30% and that aspherical (i.e. axisymmetric) shock waves are required in order to reproduce the observed line profiles.

2.2.2 Models for Rayleigh-Taylor mixing in other core collapse supernovae

Though SN 1987 A has naturally received most of the attention of supernova modelers, several studies of Rayleigh-Taylor mixing in other core collapse supernovae exist. As in all works dealing with the mixing in SN 1987 A an ad hoc deposition of the explosion energy in conjunction with an assumed spectrum of seed perturbations was employed.

Simulations of the instability in the explosion of red supergiants were performed by Herant & Woosley (1994), Shigeyama et al. (1996) and Iwamoto et al. (1997) while Hachisu et al. (1991) and Hachisu et al. (1994) have done a very useful parameter study of the mixing in Type Ib supernova progenitors. The main result of these latter two works (Hachisu et al. 1991, 1994) was that Rayleigh-Taylor instabilities grow at the C+O/He interfaces of helium core models of between 3 and 6 $M_\odot$ and might lead to large-scale mixing which can possibly account for the mixing of ^{56}Ni into the helium envelope required to model the fast decline of the light-curves of Type Ib/Ic supernovae (Shigeyama et al. 1990). Hachisu et al. (1991) also demonstrated that the instability is more violent for progenitors of smaller mass in which the mass ratio between the helium envelope and the metal core (excluding the neutron star) is usually larger[2], which leads to a stronger deceleration of the core.

Hachisu et al. (1994) found that the extent of the mixing (the "mixing width") is strongly dependent on the amplitude of the initial seed perturbations. Moreover, radial velocity perturbations exceeding 5% were needed at the time the shock passes the C+O/He interface, in order to obtain such strong mixing as light-curve calculations require. For seed perturbations larger than $\sim 1\%$ the mixing width could be determined almost independently of the mesh resolution since it was mainly determined by the (resolved) large scale mushroom structures.

We will show in a later chapter of this thesis that these results are consistent with ours and that the neutrino-driven convection discussed in the following section, nat-

---

[2]For 3.3, 4, 6 and 8 $M_\odot$ helium core models, Nomoto et al. (1991) give this ratio as, 2.5, 2.7, 1.0, and 0.45, respectively

urally explains the origin of the large seed perturbations required by Hachisu et al. (1994).

2.3   Convective instabilities in the delayed explosion mechanism

Facing the failure of the Rayleigh-Taylor calculations to explain the high iron velocities in SN 1987 A and the nagging problem of the explosion mechanism, the focus of supernova theorists has recently shifted toward hydrodynamic instabilities in the explosion mechanism itself. Indeed, several convective instabilities are nowadays known to eventually develop immediately after core bounce in the epoch of shock reheating, i.e. within the first $\sim 100\,\text{ms}$ of the explosion. These are

1. Ledoux convection inside the proto neutron star,

2. neutron finger convection inside the proto neutron star,

3. neutrino driven convection between gain radius and stalling shock

Though their existence and their importance for the explosion mechanism is still vividly debated, it has been realized that they might provide the key for an understanding of the observations of SN 1987 A.

Post collapse models of stellar cores usually show a complex variation of the entropy, S, the electron fraction, Y_e, and the temperature, T, with radius (see Figure 2.1). The entropy and temperature profiles depend on the history of the collapse and are further influenced by the formation and propagation of the shock wave. All realistic models show a positive entropy gradient which is situated at mass coordinates between 0.4 $\text{M}_\odot$ and 1.0 $\text{M}_\odot$ and is produced by the strengthening shock as it absorbs pressure waves generated by the rebounding inner core immediately after core bounce. Correspondingly, the temperature gradient is positive, too. Outside this region, in layers just below the electron neutrinosphere, the entropy gradient (as well as the temperature gradient) is negative, exhibiting the effects of the weakening of the shock. The electron fraction shows a deep trough due to the increasing mean free path of the escaping neutrinos which causes a strong deleptonization of these regions. Still farther outward, in regions somewhat outside the gain radius, an entropy maximum exists, which is caused by heating due to neutrinos. Finally, the entropy chops off towards the shock.

2.3.1   Ledoux convection inside the proto neutron star

In the Ledoux approximation, convective instabilities arise when a displaced fluid element of constant entropy and electron fraction, maintaining pressure equilibrium with its surroundings, expierences buoyancy forces which tend to amplify its displacement. In this case the criterion for convective instability is given by

$$\frac{\text{d}S}{\text{d}r}\left(\frac{\partial \rho}{\partial S}\right)_{Y_\text{e},P} + \frac{\text{d}Y_\text{e}}{\text{d}r}\left(\frac{\partial \rho}{\partial Y_\text{e}}\right)_{S,P} > 0. \tag{2.2}$$

Since for realistic equations of state $(\partial\rho/\partial S)_{Y_\text{e},P}$ and $(\partial\rho/\partial Y_\text{e})_{S,P}$ are usually negative for values of the thermodynamic variables which are of interest for the supernova
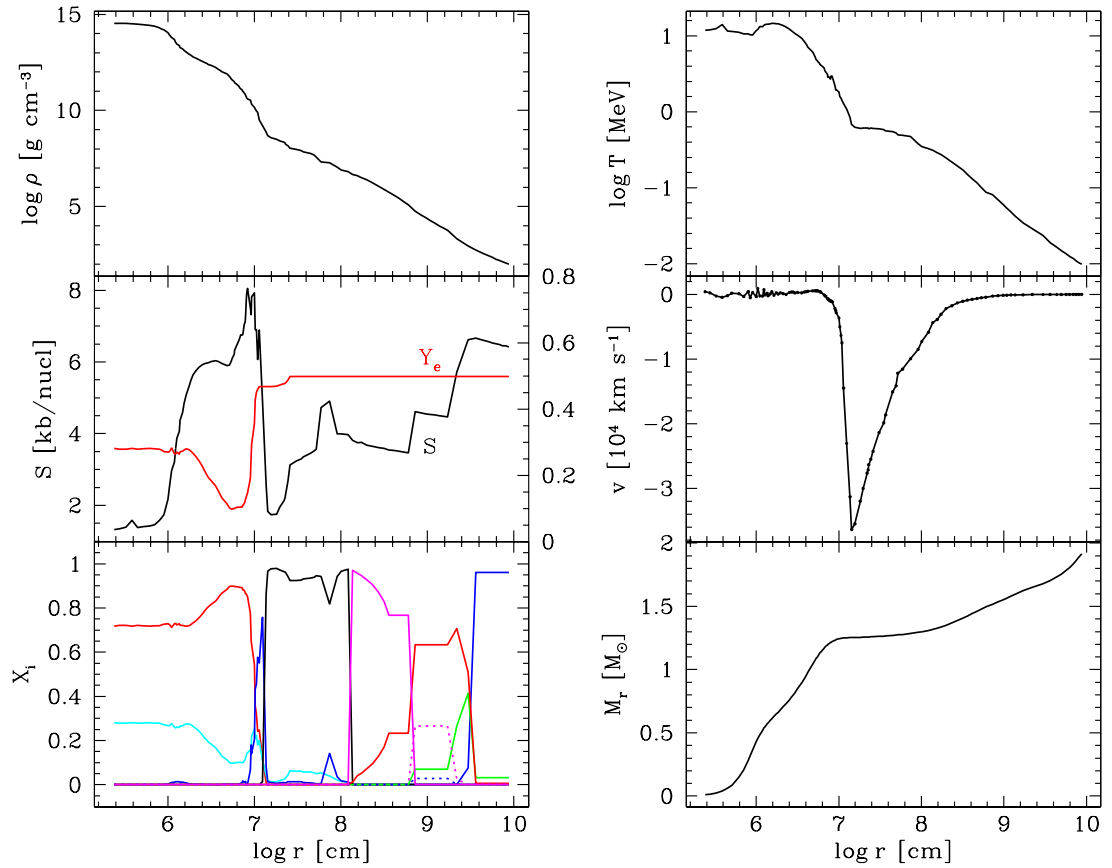
Figure 2.1: Post-collapse model WPE15 ls (180) of Bruenn (1993). The accretion shock can best be discerned in the plot of the (radial) velocity. Behind the shock matter is almost in hydrostatic equilibrium. Going from the center outwards, the entropy shows a pronounced positive gradient which becomes negative for $6.575 \leq \log(r \, [\mathrm{cm}]) \leq 6.65$. In this region Ledoux-convection can be expected to grow because there exists also a negative gradient of the electron fraction Y_e in the "deleptonization trough" just below the neutrinospheres. Farther outward a zone with positive S and Y_e gradients separates the region unstable to entropy-driven convection (caused by neutrino heating) from the proto neutron star.
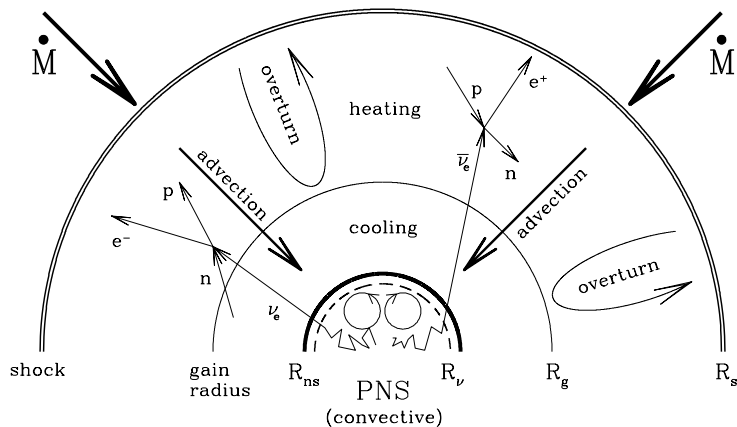
Figure 2.2: Schematic representation of the processes occuring in the delayed explosion mechanism (from Janka & Keil 1997). The radius of the electron neutrinosphere (assumed to be identical for ν_e and $\bar{\nu}_e$) is denoted by R_ν, the radius of the proto neutron star (PNS) by R_{ns}.

problem (but see also Janka & Keil 1997 and the references therein), the presence of negative gradients of S and Y_e is a sufficient condition for the onset of the instability. If only one of the gradients is negative, convection may still develop, but its growth will depend on the magnitude of the stabilizing gradient as well as on the thermodynamic derivatives.

Inside the proto neutron star, Ledoux convection, which is also referred to as "prompt" convection, occurs in regions near and below the electron neutrino sphere (see Figure 2.2). It may initially develop due to the negative entropy gradient which is left behind in these layers by the dying prompt shock. Because convective motions will tend to flatten out this gradient by mixing high and low entropy material and because the gradient is not sustained over time by other processes, *entropy* driven convection in this region can be expected to cease after some time. However, shortly after the shock breaks through the electron neutrinosphere a convectively unstable stratification in this region can be sustained by the negative lepton gradient which forms due to the ν_e losses.

The main effect of Ledoux-type proto neutron star convection on the explosion mechanism is an increase of the ν_e and $\bar{\nu}_e$ luminosities and mean neutrino energies, which may help to boost $L_\nu \langle \epsilon_\nu^2 \rangle$ just above the critical value required for an explosion (see Section 1.2.2 as well as Janka & Müller 1996). There is currently no consensus among different groups on the importance of this convection. This is mainly due to the fact that inside the nascent neutron star energy and lepton number exchange of the convective elements with their surroundings are usually not negligible. Thus the criterion for instability Eq. (2.2) is only an approximation (Janka & Keil 1997) and multidimensional calculations including neutrino transport are required. Keil et al. (1996) who have followed proto neutron star cooling in two-dimensional calculations for more than 1 s find vigorous ("Quasi-Ledoux") convection which engulfs the entire neutron star. Burrows & Fryxell (1993) reported on a "convective trigger", i.e. a convective enhancement of the neutrino luminosities which caused an explosion, while in a later work Burrows et al. (1995) characterize proto neutron star convection as being weak. Finally, Bruenn et al. (1995) and Mezzacappa et al. (1998a) find proto neutron star

convection to be unimportant.

2.3.2 Neutron finger convection

Neutron finger convection is a doubly diffusive instability. It may arise in a collapsed stellar core when heat and composition diffuse at different rates. As alluded to earlier, the deleptonization of the matter near and below the electron neutrinosphere results in a negative Y_e gradient in the core[3]. Material in the innermost layers of the proto neutron star is thus less neutron rich than the matter near the neutrinosphere. In addition, positive entropy and temperature gradients exist in the deeper layers of the core. When a blob of hot neutron-rich material begins to sink towards the center of the star (always maintaining pressure equilibrium with its environment), collisions with neutrinos of all types will tend to bring it into thermal and chemical equilibrium with its surroundings. If the blob can attain thermal equilibrium faster than chemical equilibrium it will find itself being denser than its surroundings which consist of material with a higher electron fraction and therefore will continue to sink toward the center in a finger like fashion.

Neutron finger convection was proposed by Wilson & Mayle (1988, 1993) and included into their one-dimensional calculations using a mixing-length type scheme. Wilson & Mayle (1993) emphasized that this convection is essential for triggering an explosion by mixing lepton-rich material from the center outwards thus enhancing the electron neutrino luminosities. However, Bruenn et al. (1995) in investigating neutron finger convection for a variety of typical conditions in post-collapse cores reached contradictory results. In particular they found, that counter-intuitively, lepton equilibration which is only mediated by two neutrino types (ν_e, $\bar{\nu}_e$) is not slower than energy equilibration which is mediated by all six neutrino types. Bruenn et al. (1995) therefore concluded that matter below the neutrinospheres is at no time unstable to neutron finger convection and that the latter plays no role in the supernova mechanism.

2.3.3 Neutrino driven convection between gain radius and shock

Convection between gain radius and shock is driven by the negative entropy gradient in the region of neutrino heating outside the gain radius. Since this gradient is continuously maintained by neutrino matter interactions one also refers to this convective mode as "neutrino driven convection". In contrast to the other two types, neutrino driven convection has only a minimal effect on the neutrino luminosities, since the matter between gain radius and shock is nearly transparent to neutrinos.

However, this convection transports energy in form of large high-entropy bubbles of gas from layers close to the gain radius, where the heating is strongest, near to the stalling shock (Figure 2.2). Thus the post-shock pressure is increased and work is performed on matter accreted through the shock. In addition, cool post-shock material is transported to the layers of maximum heating deeper inside and after absorbing energy in turn rises toward the shock. Neutrino driven convection therefore increases the *efficiency* of neutrino energy deposition for *given* neutrino luminosities. This typically leads to higher explosion energies in multidimensional models computed for the same neutrino luminosities as their one dimensional analogues (Janka & Müller 1996).

---

[3]Note that, more precisely, in the dense inner regions of the proto neutron star, where the neutrinos are trapped, they can attain equilibrium with respect to weak-interaction processes, and the electron fraction Y_e should be replaced by the total lepton fraction Y_L

Though all groups agree on its existence, the importance of neutrino driven convection for the explosion mechanism is debated. Herant et al. (1992) and Herant et al. (1994), based on results of SPH calculations, have advanced the view that it is *the* key to the supernova mechanism and always leads to "robust" explosions. However, the results of three independent groups employing accurate multidimensional PPM hydrodynamics and very different neutrino transport schemes agree in that this does not appear to be the case (Mezzacappa et al. 1998b; Janka & Müller 1996; Burrows et al. 1995). Janka & Müller (1996) have demonstrated that the effects of neutrino-driven convection are particularly important only within a narrow window of luminosities close to the critical luminosities for a successful explosion. In this case, neutrino driven convection can indeed lead to *qualitative* evolutionary differences, turning unsuccessful one-dimensional models into exploding ones in multidimensional calculations.

Regardless of its role in triggering the explosion itself, because of its occurrence in the immediate post-shock layers, neutrino driven convection has been repeatedly suggested to influence the spatial distribution and the expansion velocities of the products of the explosive nucleosynthesis and to provide the perturbations needed to seed the Rayleigh-Taylor instabilities, which later develop at the composition interfaces of the stellar envelope (Herant & Benz 1992; Herant et al. 1994; Burrows et al. 1995; Janka & Müller 1996). It is thus of crucial importance for an understanding of the mixing in core collapse supernovae.

2.4   Aims and further structure of this work: Towards a more coherent picture

From what has been said above it is clear that there exists a considerable discrepancy in the results of recent calculations of core collapse explosions. Indeed, not only the details of the explosion mechanism are nowadays debated but there also exists a variety of partly contradicting results for the subsequent phase of shock propagation through the envelope. This is only in part due to uncertainties in the presupernova models. Parameter-free, successful, fully self-consistent, high-resolution, multidimensional calculations which cover the entire evolution within the first crucial hours of the explosion are still lacking. Thus, a number of long standing questions in supernova research which are e.g. connected to the actual location of the mass cut in the ejecta and the amount and composition of material that falls back onto the central remnant in the late stages of the explosion, cannot be reliably answered nowadays.

Consistent calculations are also urgently required in order to put constraints on the different explosion paradigms. Though the amount of observational data which has been collected in recent years is impressive, it has not allowed to resolve the question whether the prompt or the delayed mechanism are responsible for the explosion of massive stars. Most of the observable properties of a supernova, like its light curve and spectra, are not very sensitive to the explosion mechanism, but require only that about 10^{51} ergs are released near the center of the star. The mere 19 neutrinos which were detected from SN 1987 A in the water tanks of the Kamiokande 2 and IMB detectors do not allow to draw detailed conclusions about the neutrino spectra and the evolution of the neutrino luminosities which could be used to strongly constrain delayed explosion models. This will only change with the next galactic core collapse supernova. Current and planned neutrino detectors should be able to measure several thousand neutrinos

from such an event (Beacom 1999; Vogel 1999).

In the mean time, the *only* available probe to the explosion mechanism is provided by the clues to extensive mixing of newly synthesized iron-group elements into the outer envelope of SN 1987 A and other extragalactic supernovae. The still unresolved problem of the high ^{56}Ni velocities in SN 1987 A indicates that our current understanding of supernova explosions is at best incomplete, and that a detailed understanding of the problem of nucleosynthesis and mixing is required to gain further insight into the explosion mechanism. Multidimensional nucleosynthesis calculations in core collapse supernovae have just begun to be performed and are nowadays confined to preliminary, parameterized attempts (Nagataki et al. 1997) with rather coarse numerical resolution. In particular, no work to connect the nucleosynthesis to the explosion mechanism has yet been attempted. It is thus a major aim of this thesis to study explosive nucleosynthesis in multidimensional calculations of delayed neutrino-driven explosions, and to explore its dependence upon the early convective instabilities.

The second major goal of this work is to illuminate the impact of neutrino driven convection upon the Rayleigh-Taylor mixing. While both types of fluid dynamic instabilities have been studied in the context of core collapse supernovae in a number of investigations, no attempt has been made yet in numerical work to study their interaction, although it has been suggested that this might be the origin of the high ^{56}Ni velocities in SN 1987 A (e.g. Herant & Benz 1992). The calculations which we have conducted for this purpose are the first which cover the entire evolution of the supernova during the first hours in more than one spatial dimension and explicitly include a detailed modeling of the explosion mechanism itself. Thus, the present study represents the first attempt to provide the link between the theory of delayed explosions and observations. At the same time, it is a first step toward the long-term goal of obtaining fully consistent multidimensional supernova models.

The reason why, despite their importance, calculations of this kind have not yet been performed is twofold. Firstly, the range of physical processes involved during the early stages following core collapse is so broad that it is very difficult and extremely expensive in terms of computer time to take them all into account in a multidimensional calculation without introducing specific approximations. Secondly, the widely differing time and length scales of the problem do not allow to follow the revival and propagation of the shock up to the stellar surface and the development of the associated Rayleigh-Taylor instabilities with sufficient spatial resolution. As Figure 2.3 illustrates a range of spatial scales of $r/\Delta r \approx 10^7$ is encountered from the moment of shock formation until the break-out of the shock through the stellar photosphere while starting from nuclear time scales of $\Delta t_{\mathrm{nuc}} \approx 10^{-14}\,\mathrm{s}$ and ending with the shock propagation time through the star $t_{\mathrm{Shock}} \approx 10^4\,\mathrm{s}$ a formidable range of time scales spanning 18 orders of magnitude has to be covered. Though the problem's physics allows for some crucial simplifications it is nevertheless clear that the use of conventional numerical techniques and/or computational resources cannot be expected to yield solutions in a manageable amount of computer time.

In what follows we will describe a two-step approach to the problem. In the first step, we have extended earlier one and two-dimensional work on the explosion mechanism (Janka & Müller 1996) by including a treatment of the nucleosynthesis during explosive silicon and oxygen burning and by improving upon the numerics used in this former study which has turned out to influence the character of the neutrino driven convection under certain circumstances. For the reasons mentioned above, no attempt was made
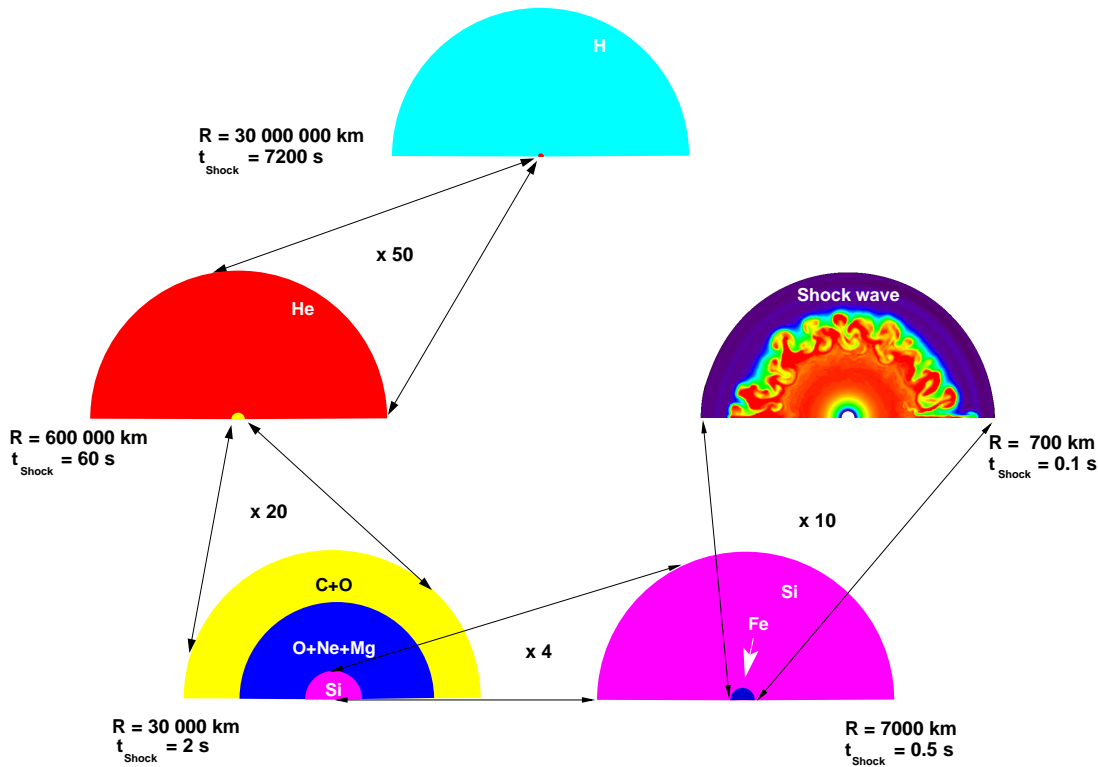
Figure 2.3: Schematic representation of the location of composition interfaces and the range of spatial scales encountered in an exploding $15\,M_\odot$ blue supergiant progenitor, comparable to the progenitor of SN 1987 A. From top left to top right one has to zoom into the exploding star by a factor of $40\,000$ in order to discern the shock wave about $100\,\mathrm{ms}$ after core-bounce and the neutrino-driven convection behind it. The radii of the major interfaces as well as the time it takes the shock to arrive at each of these are also noted. Within each panel the shells of differing composition are drawn to scale. Note that in order to resolve the surface of the proto neutron star one still needs a numerical resolution of $r/\Delta r \approx 1000$ in the simulation shown in the last panel at top right.

to obtain a fully consistent treatment of the explosion, including all phases from core collapse to shock stagnation and revival, which would have required a detailed treatment of neutrino transport. In the spirit of Janka & Müller (1996) we have used models with a simplified treatment of the neutrino physics to illuminate trends instead, and to clearly separate the influence of the various physical as well as numerical effects on the computed explosion models. This is the subject of Chapter 3. Starting with a discussion of the implemented physics we successively present first one-dimensional explosion models in Section 3.7 which include the explosive nucleosynthesis and already exhibit the gross evolutionary features of the flow. Thereafter, we discuss two-dimensional simulations in Section 3.9 and highlight the important effects of neutrino driven convection using the one-dimensional models as a reference for comparison.

In a second step, we have used the explosion models described in Chapter 3 to follow the subsequent evolution of the young supernova until well after the phase of shock break-out through the stellar envelope. In order to do so, a new numerical tool, which is based on recent advances in numerical mathematics and algorithmics, was adapted to the modeling of core collapse supernovae and applied in a first exploratory study

to the problem of mixing in SN 1987 A. In Chapter 4 we describe the computational setup that was adopted for these calculations and discuss their results in detail using the same philosophy of comparing one and two-dimensional models to illuminate the physics of the problem as done previously in Chapter 3.

Chapter 5 finally summarizes the main results of this thesis. Implications of the observational data of SN 1987 A for further theoretical modeling are discussed in the light of our new results, and an outlook on necessary future work is given.

In two appendices we address some of the physical and technical foundations upon which the present work builds. Appendix A discusses the equations of self-gravitating, reactive fluid flow. Appendix B describes the computer codes which we have developed and used to obtain the results presented in Chapters 3 and 4. After giving an overview of the basic hydrodynamics scheme employed, we focus on a description of the code which we have used to study the Rayleigh-Taylor instability in Chapter 4. This code is an extended version of the AMRA Adaptive Mesh Refinement (AMR) code of Plewa & Müller (2000), and implements the mesh refinement strategy for hyperbolic equations first suggested by Berger & Oliger (1984) and later reformulated by Berger & Colella (1989) for hyperbolic systems of conservation laws. In its latter form the AMR algorithm takes explicit advantage of the conservative, high-resolution shock capturing schemes nowadays used successfully for a wide range of problems involving supersonic flows. Additions to the basic scheme, which were necessary in order to compute self-gravitating, reactive flows with a realistic equation of state, are also described and examples of test calculations are given.

Chapter 3

The "inner problem": Nucleosynthesis and neutrino driven convection

3.1 The initial model

Since no attempt is made in this work to compute the evolution from the onset of collapse and since this phase sets the stage for what follows, we have started our calculations 20 ms after core bounce from model WPE15 ls (180) of Bruenn (1993) (see Figure 2.1 for the detailed structure of this model) who has followed core collapse in the 15 $M_\odot$ progenitor model of Woosley et al. (1988). Already shortly after the appearance of SN 1987 A, Woosley et al. (1988) had concluded that a 15 $M_\odot$ blue supergiant progenitor model was able to account for the observational data of the supernova obtained until April 1987 (i.e. six weeks after the explosion). Although later studies have corrected the progenitor mass to values of $19 \pm 3\,M_\odot$ (Woosley 1988) the lack of adequate progenitor models which have been evolved consistently through core collapse in calculations including a realistic treatment of the neutrino physics as well as the possibility to compare our results with the earlier calculations of Janka & Müller (1996) have led us to adopt the Woosley et al. (1988) progenitor for all further investigations. Bruenn (1993) has followed the evolution of this model for more than 800 ms after bounce in his 1D calculations and did not obtain an explosion. After an initial expansion to a radius of 200 km the bounce-shock had retreated again to become a stationary accretion shock at a radius of about 100 km.

Bruenn's models were obtained with a one-dimensional, Lagrangian, general relativistic hydrodynamics code using the equation of state of Lattimer & Swesty (1991) and a multi-group, flux-limited diffusion transport scheme for all neutrino types (Bruenn 1985; Bruenn & Haxton 1991). At the time of writing these models were still the most realistic post-bounce models available for progenitors comparable to the one of SN 1987 A, although their spatial resolution is somewhat coarse in the outermost zones that cover the layers of the outer C/O-core and the inner He-shell. This region, though not particularly interesting for a modeling of the shock-revival phase, is of special importance for the onset of the Rayleigh-Taylor instability (see Chapter 4).

3.2   Hydrodynamics

For all calculations described in this chapter we have used the version of the HER-AKLES code which is described in Appendix B.1. HERAKLES solves the multidimensional reactive (Euler) equations of hydrodynamics with the direct Eulerian version of the Piecewise Parabolic Method (PPM, Colella & Woodward 1984). Special provisions were made to minimize numerical diffusion of the composition, to guarantee exact conservation of nuclear species and to suppress the "odd-even-decoupling" phenomenon (see Quirk 1994), a numerical defect which we will discuss in Section 3.11 and which appears to affect most multidimensional supernova models calculated to date with PPM. Besides an incorporation of the additional physics which is described below, the code allows for the use of general equations of state according to the algorithm of Colella & Glaz (1985) and a moving grid (see e.g. Müller et al. 1991a).

3.3   Neutrino source terms and equation of state

The description of the neutrino physics and the equation of state which is used in the present work is the same as the one of Janka & Müller (1996). A light-bulb approximation is adopted for the neutrinos in which initial luminosities L_ν^0 for ν_e, ν_μ, $\bar{\nu}_\mu$, ν_τ and $\bar{\nu}_\tau$ are prescribed at the inner boundary of the computational domain somewhat below the neutrinosphere (at a mass coordinate of $M_{ic} = 0.848\,M_\odot$, initially corresponding to a radius of 3.17×10^6 cm, see Section 3.4), with the relation $L_{\nu_\mu}^0 = L_{\bar{\nu}_\mu}^0 = L_{\nu_\tau}^0 = L_{\bar{\nu}_\tau}^0 \equiv L_{\nu_x}^0$ being fulfilled. The luminosities are held constant with radius and decay exponentially with time according to

$$L_{\nu_i} = L_{\nu_i}^0 \exp\left(-t/t_L\right) \qquad (\nu_i \equiv \nu_e, \bar{\nu}_e, \nu_x, \text{ where } \nu_x = \nu_\mu, \bar{\nu}_\mu, \nu_\tau, \bar{\nu}_\tau). \qquad (3.1)$$

The initial $\bar{\nu}_e$ luminosity as well as the decay time scale, t_L, are functions of the total energy loss, $\Delta\varepsilon\,M_\odot c^2\,e^{\phi(r_{ib})}$, and lepton loss, $\Delta Y_L N_A M_{ic}$, of the inner iron core. Here $\Delta\varepsilon$ and ΔY_L (the average reduction of the lepton fraction of the inner core with mass M_{ic}) are parameters of the calculation and $\phi(r_{ib})$ denotes the *tt*-component of the metric that measures the gravitational redshift from the inner boundary r_{ib} to the observer at infinity (see Janka & Müller 1996).

   Since the luminosities were prescribed and not computed from a full transport calculation, a single neutrinosphere radius could be assumed for all neutrino types, which is a simplification of the real situation in which μ and τ-neutrinos and antineutrinos, which interact with the neutron star matter only via neutral currents, decouple in deeper layers than the electron-neutrino types. Furthermore the $\bar{\nu}_e$-sphere is located at somewhat smaller radii than the ν_e-sphere because, due to the high neutron abundances, the optical depth for the ν_e is larger in the outer layers of the proto neutron star. The effects of different decoupling depths, however, are taken into account in the prescription of the spectra which are Fermi-Dirac like in shape with effective temperature and degeneracy parameters. These parameters were obtained from fits to data of detailed Monte-Carlo simulations of neutrino transport in proto neutron stars performed by Janka (1991). Both parameters differ for each neutrino species while the temperatures also vary with time in order to simulate the evolution of the spectra from the cooling neutron star. Fit relations obtained from the Monte-Carlo simulations were also used in order to prescribe the angular dilution factor of the neutrino field which enters the heating rate (see Eq. 1.5) and the variable Eddington factor which was needed to transform the

properties of the neutrino field from the observers rest frame into the comoving frame of the stellar medium in order to compute the reaction rates (see below). We refer the reader to the original work of Janka & Müller (1996) for further details and note that the approximations described above neglect

i) the neutrino luminosities due to accretion of matter onto the neutron star and

ii) the effects that convection below the neutrinospheres will have upon the luminosities and spectra.

The interaction of neutrinos with the matter in the semi-transparent stellar layers outside the neutrinosphere is taken into account by source terms for the energy and lepton number in the hydrodynamic equations according to the formulae derived in Janka (1991) and further discussed in Janka (1993). The following processes were included in the computation of these terms:

- neutrino and antineutrino absorption on free nucleons; electron and positron capture on free nucleons

$$\nu_e + n \;\rightleftharpoons\; e^- + p \tag{3.2}$$
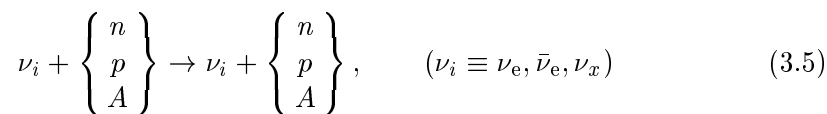$$\bar{\nu}_e + p \;\rightleftharpoons\; e^+ + n. \tag{3.3}$$

These are the dominant reactions for the energy balance of the stellar gas. The heating and cooling rates resulting from these reactions were given in Chapter 1.
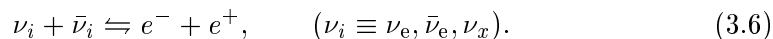
- neutrino scattering off electrons and positrons

$$\nu_i + e^\pm \rightarrow \nu_i + e^\pm, \qquad (\nu_i \equiv \nu_e, \bar{\nu}_e, \nu_x). \tag{3.4}$$
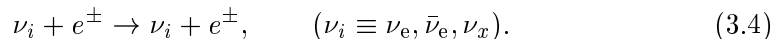
- neutrino-nucleon and neutrino-nucleus scattering

$$\nu_i + \left\{ \begin{matrix} n \\ p \\ A \end{matrix} \right\} \rightarrow \nu_i + \left\{ \begin{matrix} n \\ p \\ A \end{matrix} \right\}, \qquad (\nu_i \equiv \nu_e, \bar{\nu}_e, \nu_x) \tag{3.5}$$

- neutrino-antineutrino pair annihilation; electron-positron annihilation with ν-pair production

$$\nu_i + \bar{\nu}_i \rightleftharpoons e^- + e^+, \qquad (\nu_i \equiv \nu_e, \bar{\nu}_e, \nu_x). \tag{3.6}$$

The equation of state includes contributions from four nuclear species (protons, neutrons, α-particles, and a representative heavy nucleus of the iron group) which are all treated as ideal non-relativistic Boltzmann gases, since we do not include the innermost regions of the neutron star with densities $\gtrsim 3 \times 10^{12}\,\mathrm{g\,cm^{-3}}$ (see below) where nucleon interactions and nucleon degeneracy become important. The abundances are computed from nuclear statistical equilibrium for $T > 5 \times 10^9$ K. Electrons and positrons are taken into account as arbitrarily degenerate and arbitrarily relativistic Fermi gases and contributions from photons in thermodynamic equilibrium with the matter are included.

3.4   Numerical grid, boundary conditions and seed perturbations

The high sound speed in the proto neutron star renders it computationally expensive to follow the evolution of the entire stellar core with an explicit hydrodynamics code over time scales of seconds. The innermost $0.848\,M_\odot$ of the core are therefore cut out and replaced by a point mass. Spherical coordinates are adopted and the inner boundary of the computational domain is placed somewhat below the electron neutrinosphere at a radius of 3.17×10^6 cm. The outer radial boundary is located at $r = 1.7 \times 10^9$ cm, well inside the C+O-core of the star. In the case of one-dimensional models between 400 and 6400 non-equidistant radial zones are used. The lower resolution is chosen to be identical to the one employed in the 2D computations, in order to enable a meaningful comparison. In our two-dimensional models 180 or 192 angular zones are distributed uniformly between $0 \le \theta \le \pi$ and axial symmetry around the polar axis (i.e. for $0 < \varphi \le 2\pi$) is assumed. We have chosen not to adopt smaller angular wedges since the results of Janka & Müller (1996) indicated that the bubbles formed by neutrino driven convection may grow to angular sizes of more than $\sim 40°$ and their growth as well as the explosion timescale may be substantially influenced by smaller angular grids.

With this setup, the time-step resulting from the Courant-Friedrichs-Lewy stability condition (Courant et al. 1928; see also LeVeque 1998) is typically of the order of a few 10^{-5} s in one-dimensional calculations, and several 10^{-6} s in two-dimensional simulations. In order to simulate the contraction of the cooling and deleptonizing proto neutron star, the inner boundary is moved inwards during the course of the computations according to the movement of the corresponding mass shell in Bruenn's one-dimensional calculations. This is achieved by making use of the moving grid implemented in our code (cf. Janka & Müller 1996, for details). Free outflow is allowed for across the outer radial boundary and reflecting boundaries are chosen for $\theta = 0$ and $\theta = \pi$.

Except where otherwise noted, in all two-dimensional computations a random initial seed perturbation is added to the velocity field on the entire grid with a modulus of 10^{-3} of the (radial) velocity of Bruenn's post-collapse model. In the immediate upstream region of the accretion shock, this corresponds to velocity perturbations with a modulus of $\sim 5 \times 10^{-3}$ of the local sound speed, while further outward this value decreases with the decreasing infall velocities to $\sim 10^{-3}$. Starting at 20 ms after core bounce the computations are continued until about $800 - 900$ ms, when the explosion energy has saturated and all nuclear reactions have frozen out (see also Sect. 3.7).

3.5   Self-gravity

Janka & Müller (1996) have observed that the mapping of Bruenn's post-collapse model, which was obtained with a general relativistic code, to their PPM hydrodynamics code which employed Newtonian gravity led to an initial force imbalance within the first 10-20 ms of their calculations which was caused by the shallower Newtonian potential. In this transient phase, the shock moves out in radius, subsequently oscillates around a reference position and finally comes to rest at a distance of about 200 km from the center. We have observed similar oscillations in calculations using Newtonian gravity which resulted in slight changes of the entropy profile behind the shock. These artifacts can be eliminated if general relativistic corrections to the gravitational potential as

described by Keil (1997) are included. The starting point in this approach is the one-dimensional Newtonian hydrostatic equation

$$\frac{1}{\rho_0}\frac{\partial P}{\partial r} = -\frac{GM_r}{r^2} = -\boldsymbol{\nabla}\Phi_{1D}^N, \tag{3.7}$$

where M_r is the enclosed baryonic mass. The one-dimensional general relativistic generalization of this equation is the Tolman-Oppenheimer-Volkoff equation

$$\frac{1}{\rho}\frac{\partial P}{\partial r} = -\frac{G\tilde{m}}{r^2}\left(1 + \frac{4\pi r^3 P}{\tilde{m}c^2}\right)\frac{1}{\Gamma^2}\left(1 + \frac{P}{\rho c^2}\right), \tag{3.8}$$

where $\rho = \rho_0 + u/c^2$ is the total mass density, which includes contributions from both the rest mass density, ρ_0, and the internal energy density, u. The enclosed gravitational mass, $\tilde{m}$, is given by

$$\tilde{m}(r) = \int_0^r 4\pi r'^2 \rho \, dr'. \tag{3.9}$$

We further have

$$\Gamma^2(r) = 1 - \frac{2G\tilde{m}(r)}{rc^2}. \tag{3.10}$$

Comparing Equations (3.7) and (3.8), and neglecting the contribution of the internal energy density to the total mass density, the Newtonian potential Φ_{1D}^N can be replaced by

$$\Phi_{1D}(r) = G\int_\infty^r \left[\frac{\tilde{m}}{r^2}\left(1 + \frac{4\pi r^3 P}{\tilde{m}c^2}\right)\frac{1}{\Gamma^2}\left(1 + \frac{P}{\rho_0 c^2}\right)\right]\mathrm{d}r', \tag{3.11}$$

in order to compute the source terms for the momentum and energy density in the Newtonian hydrodynamic equations. Equation (3.11) is integrated numerically. In case of two-dimensional models the required pressure and density are averaged over angle. Furthermore, two-dimensional Newtonian corrections are added to $\Phi_{1D}(r)$ in order to approximately account for the asphericity of the potential. For this purpose Poisson's equation is solved first with an angle-averaged density in order to obtain the one-dimensional Newtonian potential Φ_{1D}^N. Subsequently, the two dimensional Newtonian potential Φ_{2D}^N is computed with the algorithm described in Müller & Steinmetz (1995). The final gravitational potential in the two-dimensional case is then obtained from

$$\Phi_{2D} = \Phi_{1D} + (\Phi_{2D}^N - \Phi_{1D}^N). \tag{3.12}$$

The asphericity corrections given by the terms in brackets were, however, small. Using this potential, the accretion shock from Bruenn's model showed only a slight adjustment to our numerical procedures, which was confined to its steepening into a sharp discontinuity of only about two zones in width, due to the higher resolution of discontinuities obtained with PPM. In particular the shock remained at its initial radius of 130 km during the first tens of milliseconds of evolution until neutrino heating had become efficient enough to push the shock outward in our exploding models.

3.6   Explosive nucleosynthesis

Except for a possible r-process which may occur in the high-entropy neutrino driven wind from the proto neutron star (Woosley et al. 1994; Takahashi et al. 1994), explosive nucleosynthesis in core collapse supernovae can be divided into five basic types of thermonuclear "burning", according to the temperatures that are attained in the shock-heated material within about the first second of shock propagation. These are

1. Explosive silicon burning with complete silicon exhaustion ("complete silicon burning"): $5 \times 10^9 \, \text{K} \leq T < 7 \times 10^9 \, \text{K}$[1].

2. Explosive silicon burning with incomplete silicon exhaustion ("incomplete silicon burning"): $4 \times 10^9 \, \text{K} \leq T < 5 \times 10^9 \, \text{K}$

3. Explosive oxygen burning: $3.3 \times 10^9 \, \text{K} \leq T < 4 \times 10^9 \, \text{K}$

4. Explosive neon burning: $2.1 \times 10^9 \, \text{K} \leq T < 3.3 \times 10^9 \, \text{K}$

5. Explosive carbon burning: $1.9 \times 10^9 \, \text{K} \leq T < 2.1 \times 10^9 \, \text{K}$

It should be noted that this classification depends only on the temperature and *not* on the initial composition, i.e. the available "fuel", although the names already indicate which zones of the presupernova will usually be affected. A detailed description of each of these types of burning and their most important products can be found e.g. in the review of Thielemann et al. (1998). With present supercomputer technology, detailed predictions of the abundance patterns resulting from these processes are only feasible within the framework of one-dimensional hydrodynamic calculations. There are two main reasons for this fact: i) the numerical diffusion inherent to Eulerian hydrodynamic schemes and ii) the complex physics of silicon burning.

Silicon burning is complicated by the fact that it is not characterized by a few heavy ion reactions as e.g. carbon or oxygen burning (where the main reactions are $^{12}\text{C} + {}^{12}\text{C} \rightarrow \text{A} + \text{B}$ and $^{16}\text{O} + {}^{16}\text{O} \rightarrow \text{C} + \text{D}$, respectively, and A–D represent the variety of possible products, Arnett 1996). Instead, and especially in matter which has undergone substantial neutronization, a complex network including photodisintegrations through the reactions (γ, p), (γ, n), (γ, α) and subsequent light particle captures as e.g. (p, n), (p, α), (n, α) and their inverse reactions on a multitude of nuclei is involved which leads to either complete or incomplete "photodisintegration rearrangement" of the initial (usually ^{28}Si-rich) composition to nuclei of the iron group. While under conditions of complete silicon burning nuclear statistical equilibrium (NSE) obtains (Clayton 1983) and the nuclear abundances follow from a set of Saha equations, NSE cannot be attained within the explosion time scale of about $1\,\text{s}$ if the temperature drops below 5×10^9 K (Thielemann et al. 1998). Thus a proper calculation of the energy release and composition changes over time requires the solution of a nuclear reaction network with hundreds of isotopes (see Appendix A.2).

In one-dimensional computations it is nowadays possible to solve reaction networks consisting of a few hundred species online with the hydrodynamics (Woosley & Weaver 1995). However, this is seldomly done. Instead it is customary to solve only an approximation to Eq. (A.13) coupled to the hydrodynamics, i.e. to use a "reduced" nuclear reaction network, in order to obtain an approximate energy generation rate. The detailed chemical composition is then computed after the hydrodynamic calculation in a post-processing step. This is facilitated by the Lagrangian nature of nearly all one-dimensional codes employed for explosive nucleosynthesis calculations. In these codes, the grid moves with the fluid, and therefore it is trivial to record the temperature and density evolution of specific fluid elements (i.e. Lagrangian zones) and thus to obtain the necessary input for the post-processing calculations.

---

[1]Usually no maximum temperature is given for this type of burning since for temperatures greater than 5×10^9 K nuclear statistical equilibrium (NSE) holds. The maximum temperature listed above is only meant to indicate that the NSE composition will switch from nuclei of the Fe-group to α particles.

In contrast, most multidimensional hydrodynamics schemes are of Eulerian type. Lagrangian methods, usually lead to severe grid distortions in multidimensional calculations, when shear and vortex flows are encountered (see the discussion in Müller 1998). Alternatively the Smoothed Particle Hydrodynamics (SPH) method, a gridless Lagrangian method, might be used. However, due to its Monte-Carlo nature, the level of noise inherent to SPH is intolerably high for problems involving hydrodynamic instabilities. Being left with Eulerian schemes in the multidimensional case, the numerical diffusion inherent in these methods poses problems for an accurate computation of the nucleosynthesis which are difficult to solve. Furthermore, within an Eulerian framework post-processing approaches are not straightforward. Such a method has been adopted in the only previous study of multidimensional nucleosynthesis in core collapse supernovae. Nagataki et al. (1997) distributed 500 marker particles along the progenitor's Si and O shells, and advected them with the flow in the course of their Eulerian calculations while recording their density and temperature "history" in order to obtain the necessary input for postprocessing nucleosynthesis calculations. This approach has, however, some severe drawbacks. Most importantly, in the case of shear and vortex flow as e.g. in convective instabilities during delayed neutrino-driven explosions, it is hardly possible to control the accuracy of the results. Depending on the local flow velocities, the separation between marker particles might vary widely in different regions of the computational domain and may even become comparable to or even larger than the local temperature scale height. Resolving the temperature distribution accurately is, however, essential. The strong temperature dependence of the reaction rates will otherwise lead to considerable errors in the abundances. To put it another way, there is nothing gained in solving a network including hundreds of isotopes when the temperature is only known to an accuracy of several 10%. Adding more particles does not necessarily cure the resolution problem (unless a really huge number of particles is used) since it does not allow to exert direct control upon the spatial resolution by keeping the particles' separation below some threshold value throughout the course of the computation.

In the framework of Eulerian hydrodynamic calculations the only satisfactory approach for a computation of the nucleosynthesis remains the advection of separate fluid components with the flow, which represent the single nuclear species, and the online solution of the nuclear network with the hydrodynamics. For this purpose the hydrodynamic equations have to be augmented by additional continuity equations for each nucleus which is included in the reaction network (see Appendix A for a more detailed discussion of the equations of self-gravitating, reactive fluid flow). In this case, the attainable accuracy can be controlled by the spatial resolution of the underlying Eulerian grid, though this may require the use of a high resolution in order to reduce the numerical diffusion of the scheme to acceptable limits. The major drawback, however, is, that besides the CPU time, also the memory required to store all the nuclear species in a high-resolution multidimensional calculation becomes quickly prohibitive and one is forced to use networks of small to moderate size which can only approximately follow the nucleosynthesis in cases of appreciable neutronization.

Given the current constraints and the main goal of this study, which is a reliable computation of the spatial distribution of the most important nuclei, ^{56}Ni, ^{28}Si and ^{16}O and *not* the derivation of accurate yields for trace isotopes, we have decided to incorporate a small nuclear network into HERAKLES. We have evolved this network in a "co-processing" approximation, i.e. the network is solved online with the hydrodynamic

equations but any feedback to the dynamics is not considered. This means in particular that the equation of state is computed with the same approximations as in Janka & Müller (1996), i.e. with only four species in nuclear statistical equilibrium. The same holds for the energy release due to the recombination of nucleons and α-particles under conditions of NSE with temperatures as low as $\sim 7 \times 10^9$ K. The energy release from silicon, oxygen, neon and carbon burning is neglected. These approximations are not as crude as they might appear at first glance and still give a reliable spatial distribution of the burning products. Concerning the equation of state, the contribution of the nuclei to the pressure represents only a small correction to the terms arising from radiation, degenerate electrons and electron-positron pairs. The energy release due to explosive nucleosynthesis is strongly progenitor-dependent and will be discussed below.

Provided that the electron fraction Y_e takes on values above ~ 0.49, the smallest reaction network which can describe explosive nucleosynthesis from helium up to silicon burning with a fair degree of accuracy is the α-chain including the 13 α-nuclei from ^{4}He to ^{56}Ni where besides the 3α reaction

$$2\alpha(\alpha,\gamma)^{12}\text{C} \tag{3.13}$$

and the heavy ion reactions

$$^{12}\text{C}\left(^{12}\text{C},\alpha\right){}^{20}\text{Ne} \tag{3.14}$$
$$^{12}\text{C}\left(^{16}\text{O},\alpha\right){}^{24}\text{Mg} \tag{3.15}$$
$$^{16}\text{O}\left(^{16}\text{O},\alpha\right){}^{28}\text{Si}, \tag{3.16}$$

the only links between the nuclei are provided by (α,γ) and (γ,α) reactions. However, for its application to core collapse supernovae, modifications are needed. Since the simple α-network consisting only of nuclei with $Z = N$ cannot account for the effects of neutronization it will lead to grossly overestimated ^{56}Ni yields when the innermost zones of the ejecta will start to recombine. Depending on the progenitor model and the ratio of the ν_e and $\bar{\nu}_e$ luminosities from the proto neutron star, these layers will consist of deleptonized matter of the presupernova's iron core and in addition might suffer strongly from deleptonization due to neutrino-heating during the explosion. Since we evolve Y_e in the simulation we have a means to approximately correct for the wrong nucleosynthesis in deleptonized zones. By adding a "switch" to the α-network we can replace the ^{56}Ni production by an additional species when Y_e drops below a threshold value. This is readily done since the only reaction which produces ^{56}Ni in our α-network is

$$^{52}\text{Fe}(\alpha,\gamma)^{56}\text{Ni}. \tag{3.17}$$
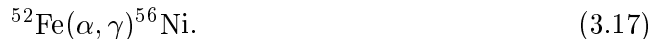
The purpose of this additional nucleus, which we will denote with X in the following, is solely to trace the neutronized material. Otherwise, all of its properties are set to be identical to those of ^{56}Ni. This means in particular that we assume identical reaction rates for reaction

$$^{52}\text{Fe}(\alpha,\gamma)\text{X} \tag{3.18}$$

which we set to replace reaction (3.17) if $Y_e < Y_{e,\text{crit}}$. Correspondingly the photodisintegration rate for the inverse reaction of (3.18) is also identical to that of the inverse of (3.17), namely $\lambda(^{56}\text{Ni})$ (see Appendix A.2). The necessary modifications to the network equations can then be written in terms of the functions G defined in Eq. (A.18). The

original G's of the α-network for ^{4}He, ^{52}Fe and ^{56}Ni are replaced by

$$
\begin{aligned}
\hat{G}(^4\mathrm{He}) \;=\;& G(^4\mathrm{He}) \\
& - \left(\rho N_A \left\langle ^4\mathrm{He}, {}^{52}\mathrm{Fe} \right\rangle Y(^4\mathrm{He}) Y(^{52}\mathrm{Fe}) - \lambda(^{56}\mathrm{Ni}) \, Y(^{56}\mathrm{Ni}) \right) \\
& + \; s_2 \, \rho N_A \left\langle ^4\mathrm{He}, {}^{52}\mathrm{Fe} \right\rangle Y(^4\mathrm{He}) Y(^{52}\mathrm{Fe}) \\
& + \; s_4 \, \rho N_A \left\langle ^4\mathrm{He}, {}^{52}\mathrm{Fe} \right\rangle Y(^4\mathrm{He}) Y(^{52}\mathrm{Fe}) \\
& - \; s_1 \, \lambda(^{56}\mathrm{Ni}) \, Y(^{56}\mathrm{Ni}) \\
& - \; s_3 \, \lambda(^{56}\mathrm{Ni}) \, Y(\mathrm{X}),
\end{aligned}
\tag{3.19}
$$

$$
\begin{aligned}
\hat{G}(^{52}\mathrm{Fe}) \;=\;& G(^{52}\mathrm{Fe}) \\
& - \left(\rho N_A \left\langle ^4\mathrm{He}, {}^{52}\mathrm{Fe} \right\rangle Y(^4\mathrm{He}) Y(^{52}\mathrm{Fe}) - \lambda(^{56}\mathrm{Ni}) \, Y(^{56}\mathrm{Ni}) \right) \\
& + \; s_2 \, \rho N_A \left\langle ^4\mathrm{He}, {}^{52}\mathrm{Fe} \right\rangle Y(^4\mathrm{He}) Y(^{52}\mathrm{Fe}) \\
& + \; s_4 \, \rho N_A \left\langle ^4\mathrm{He}, {}^{52}\mathrm{Fe} \right\rangle Y(^4\mathrm{He}) Y(^{52}\mathrm{Fe}) \\
& - \; s_1 \, \lambda(^{56}\mathrm{Ni}) \, Y(^{56}\mathrm{Ni}) \\
& - \; s_3 \, \lambda(^{56}\mathrm{Ni}) \, Y(\mathrm{X}),
\end{aligned}
\tag{3.20}
$$

and

$$
\begin{aligned}
\hat{G}(^{56}\mathrm{Ni}) \;=\;& \dot{Y}(^{56}\mathrm{Ni}) \\
& + \; s_1 \, \lambda(^{56}\mathrm{Ni}) \, Y(^{56}\mathrm{Ni}) \\
& - \; s_2 \, \rho N_A \left\langle ^4\mathrm{He}, {}^{52}\mathrm{Fe} \right\rangle Y(^4\mathrm{He}) Y(^{52}\mathrm{Fe}),
\end{aligned}
\tag{3.21}
$$

and the following equation for the tracer nucleus is added

$$
\begin{aligned}
\hat{G}(\mathrm{X}) \;=\;& \dot{Y}(\mathrm{X}) \\
& + \; s_3 \, \lambda(^{56}\mathrm{Ni}) \, Y(\mathrm{X}) \\
& - \; s_4 \, \rho N_A \left\langle ^4\mathrm{He}, {}^{52}\mathrm{Fe} \right\rangle Y(^4\mathrm{He}) Y(^{52}\mathrm{Fe}).
\end{aligned}
\tag{3.22}
$$

The first terms on the right-hand side of Eqs. (3.19) and (3.20) are the original terms of the unmodified network which have to be corrected by the second terms in order to be able to introduce the switches s_i for the terms arising from Eqs. (3.17) and (3.18). In order to switch between reactions (3.17) and (3.18) as discussed above, one has to set

$$
s_i = 1 \quad \text{for } i = 1, 2 \qquad s_j = 0 \quad \text{for } j = 3, 4,
\tag{3.23}
$$

if $Y_\mathrm{e} > Y_\mathrm{e,crit}$ and

$$
s_i = 0 \quad \text{for } i = 1, 2 \qquad s_j = 1 \quad \text{for } j = 3, 4
\tag{3.24}
$$

otherwise. This does, however, not take into account that material with high Y_e that has already formed ^{56}Ni and is advected into hotter, deleptonized layers, can be photodissociated again. Similarly material with low Y_e that is advected into hot material with high electron fractions could also not be photodisintegrated. We therefore set

$$
s_i = 1 \quad \text{for } i = 1, 2, 3 \qquad s_4 = 0,
\tag{3.25}
$$

if $Y_\mathrm{e} > Y_\mathrm{e,crit}$ and

$$
s_i = 1 \quad \text{for } i = 1, 3, 4 \qquad s_2 = 0
\tag{3.26}
$$

otherwise. Having separated the ^{56}Ni distribution that an unmodified α-network would produce into two species in this way, for which we solve also separate continuity equations, we can get approximately correct ^{56}Ni yields and monitor the distribution of the neutrino-heated, neutron-rich material. We have chosen to set $Y_{e,crit} = 0.49$. It should be noted that the explosive nucleosynthesis results of Thielemann et al. (1996) show that for $Y_e < 0.4989$ the abundance of ^{56}Ni starts to decrease in favor of ^{58}Ni. For $Y_e = 0.4915$ the abundances of both isotopes become comparable, while ^{56}Ni ceases to be synthesized as the dominant nucleus in the iron group once $Y_e < 0.49$. Of course, in a full network calculation this occurs gradually and so our simple approximation will still tend to overestimate the ^{56}Ni yield. As we will show in Sections 3.7 and 3.9 these errors are rather small.

The reaction rates are taken from the rate library of Thielemann (e.g. Thielemann et al. 1998). Photodisintegration rates are computed from the principle of detailed balance. The network is solved for all zones with temperatures between 10^8 K and 8×10^9 K. For temperatures higher than 8×10^9 K the abundances are set to their NSE values (i.e. to a pure α-particle composition in case of our α-network). Under conditions typical in core collapse supernovae, temperatures this high are only attained for high densities and thus it is safe to assume that NSE will hold in these zones (see Aufderheide et al. 1991).

The network solver has been optimized to run efficiently on vector computers as proposed by Müller (1986). In this approach, explicit advantage is taken of the sparse character of the Jacobian by using a matrix solver generated by the GIFT program package. This package outputs FORTRAN code for the optimal Gaussian elimination given a specific sparsity pattern of the matrix, by deleting all unnecessary operations involving zeroes. This also allowed us to efficiently vectorize the problem by solving the network in parallel for all zones on the grid in which the temperatures are in the required range. We note that by using this small network, the CPU time required for a 2D simulation with a resolution of 400×180 zones increased already by a factor of three compared to a run without nuclear burning and amounted to 250 hours on one processor of an NEC SX-4B, with the fully vectorized code running at a sustained speed of 600 MFlops.

Some remarks on possible future improvements appear to be appropriate here. It has long been known (Bodansky et al. 1968; Woosley et al. 1973) that during silicon burning certain groups of nuclei form, which are internally in equilibrium under the exchange of photons, protons, neutrons and α-particles. These quasi equilibrium (QSE) groups remain out of equilibrium with respect to other QSE groups until the reactions representing the "bottleneck" links between the different groups have had sufficient time to establish the final equilibrium (i.e. NSE). This behavior can in principle be exploited to lower the computational load of silicon burning in hydrodynamic calculations by designing "reduced" reaction networks in which only a fraction of the reactions and isotopes needs to be followed time-dependently. Recent work by Hix & Thielemann (1996), Hix & Thielemann (1999) and C. Freiburghaus & F.-K. Thielemann (private communication) shows that results comparable to a full network calculation involving about 300 nuclei can be obtained with only ~ 70 nuclear species. Though this progress is very encouraging, given our timings from above, the resulting computational load appears to be currently still beyond the limit of what one can afford in multidimensional simulations and further reductions of the number of species and reactions are still required. Nevertheless, in the future, a combination of specially designed reaction

Model	Resolution	$L^0_{\nu_e,52}$	$L^0_{\nu_x,52}$	ΔY_L	$\Delta\varepsilon$	$E_{\mathrm{exp},51}$	t_{expl}
O240	400	2.400	2.027	0.0755	0.0539	–	–
O245	400	2.450	2.069	0.0762	0.0544	0.44	178
O260	400	2.588	2.185	0.0805	0.0575	0.94	122
O310	400	3.094	2.613	0.0963	0.0688	1.59	70
O310/800	800	3.094	2.613	0.0963	0.0688	1.59	71
O310/1600	1600	3.094	2.613	0.0963	0.0688	1.58	71
O310/3200	3200	3.094	2.613	0.0963	0.0688	1.58	71
O310/6400	6400	3.094	2.613	0.0963	0.0688	1.58	71
T240	400×192	2.400	2.027	0.0755	0.0539	0.76	92
T245	400×192	2.450	2.069	0.0762	0.0544	0.88	88
T260	400×192	2.588	2.185	0.0805	0.0575	1.13	82
T310	400×192	3.094	2.613	0.0963	0.0688	1.77	62
T280*	400×180	2.813	2.375	0.0875	0.0625	1.48	61
T310*	400×180	3.094	2.613	0.0963	0.0688	1.83	48

Table 3.1: Initial electron and heavy lepton neutrino luminosities in units of 10^{52} erg/s, ($L^0_{\nu_e,52}$ and $L^0_{\nu_x,52}$, respectively) energy loss and lepton loss parameters of the inner iron core (see Janka & Müller 1996) and explosion energies, $E_{\mathrm{exp},51}$, (in units of 10^{51} erg) for our one-dimensional and two-dimensional explosion models, O240 – O310 and T240 – T310, respectively. The explosion time scale t_{expl} (given in ms) is defined as the time after the start of the simulation when the explosion energy exceeds 10^{48} erg. Models with a star (*) showed "odd-even decoupling".

networks, faster algorithms and massively parallel computers appears to be promising in order to obtain a more accurate description of the explosive nucleosynthesis.

3.7 One-dimensional models

We begin with a discussion of the general features of our one-dimensional explosion models before we will examine multidimensional effects in Section 3.9. In Table 3.1 we have summarized all one and two-dimensional models which we have computed for the discussion in this chapter. The models are characterized by the initial values of the electron and heavy lepton neutrino luminosities ($L^0_{\nu_e,52}$ and $L^0_{\nu_x,52}$, respectively) and the energy loss and lepton loss parameters of the inner iron core, which together determine the luminosity of antielectron neutrinos as well as the characteristic time scale for the decay of the luminosities, t_L, which is of the order of $500 - 700$ ms (see Janka & Müller 1996).

Although our models are generally comparable to those of Janka & Müller (1996), we did not obtain explosions for any value of the neutrino luminosities given in the latter work. This is caused by our use of general relativistic corrections to the gravitational

potential. The shock has to overcome a deeper potential well than in the Newtonian case, while due to its smaller stagnation radius also the volume of the gain region and therefore the amount of neutrino heated material is initially significantly smaller than in the models of Janka & Müller (1996). The neutrino luminosities which are required for an explosion are therefore higher. For instance our model O240 failed to explode, even though its neutrino luminosities were higher than those in the most energetic model of Janka & Müller (1996) by 7%. Similarly, higher neutrino luminosities are needed if a given final explosion energy[2] is to be obtained. This can be seen for example when comparing our low-energy models O245 and O260 with models O2c and O3c of Janka & Müller (1996). The latter two were computed with $L^0_{\nu_e,52} = 2.200$ and $L^0_{\nu_e,52} = 2.225$ and exploded with an energy of 0.49×10^{51} ergs (or 0.49 "foes"[3]) and 0.95 foes respectively. In our case, model O245 exploded with an energy of 0.44 foes and model O260 with an energy of 0.94 foes, so that in order to get comparable explosion energies our luminosities had to be larger by $\gtrsim 11\%$ and $\sim 16\%$ respectively. The luminosities quoted here should only be taken as a rough indication of what might be required to get explosions in fully consistent models with detailed neutrino transport. It appears, however, that general relativistic effects are important and should not be neglected. This has also been emphasized by de Nisco et al. (1998) and Mezzacappa et al. (1998b). The reader is referred to these works for more detailed discussions.

As is the case for the calculations of Janka & Müller (1996), with the adopted values of the initial neutrino luminosities and the prescription of their evolution in time, we do not find long shock stagnation times for models which finally succeed to explode. Instead, the shock starts to move out of the iron core without noticeable delay. Yet, its propagation speed shows a clear dependence on the neutrino luminosities. To illustrate matters we show spacetime plots of the evolution of the density with time for models O245, O260 and O310 in Figures 3.1 a to 3.1 c, respectively. Additionally, in Figs. 3.2 and 3.3 we depict the evolution of the most important hydrodynamic and thermodynamic quantities for models O245 and O310 as a function of radius. Evolutionary times are given with respect to the start of our calculations. We will adhere to this convention throughout the following discussion. The time after bounce can be obtained by adding 20 ms to the quoted times.

The shock is visible as the outermost discontinuity in Figures 3.1 a to 3.1 c. In model O245 it has reached radii of $\sim 10^8$ cm and $\sim 3.8 \times 10^8$ cm, at $t = 300$ ms and $t = 800$ ms, respectively. This yields a mean shock velocity of only 5600 km/s while the corresponding velocities for models O260 and O310 are 16 000 km/s and 19 000 km/s, respectively. The evolutionary differences between models O245 and O310 can also be noted when comparing Figure 3.2 to Figure 3.3. In both figures, the initial post-collapse data is plotted with heavy lines, and the Si/O interface can be discerned by the associated jump in density at $\log r \; [\text{cm}] = 8.8$. For both models one can easily recognize the transition of the accretion shock to an outwardly propagating shock, the rarefaction generated by the explosion, as well as the contraction and deleptonization of the outer layers of the proto neutron star. These show negative entropy and electron fraction gradients, which are unstable to Ledoux convection. The neutron star itself

---

[2]We define the explosion energy as in Janka & Müller (1996) as the total energy, i.e. kinetic plus internal plus gravitational energy, of all zones of the grid where this sum of energies is positive. Note that one still has to subtract from this energy the binding energy of the outer envelope, in order to obtain the (observable) explosion energy at infinity.

[3]In the following we will often use the terminology of G. Brown, in which 0.49 "foes" correspond to 0.49 times ten to the fifty one ergs.
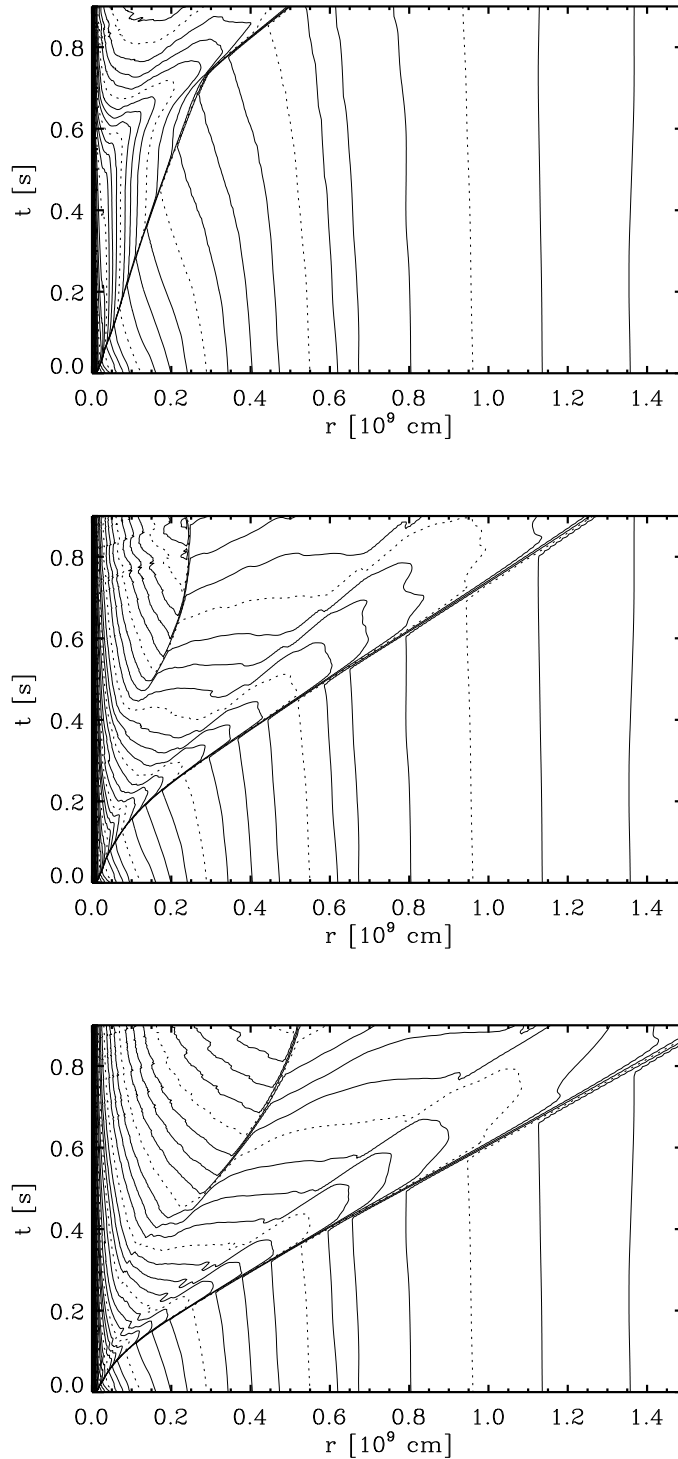
Figure 3.1: Spacetime plots for the evolution of the logarithm of the density for the one-dimensional explosion models. From top to bottom: a) model O245, b) model O260 and c) model O310. The time is given with respect to the start of the calculations. The time after bounce can be obtained by adding 20 ms to the given values. The supernova shock is visible as the outermost discontinuity which extends diagonally in each plot. Note the different expansion velocities of the shock for models with different neutrino luminosities. Around 450 ms a reverse shock forms in the inner ejecta of models O260 and O310 which separates the ejecta from the neutrino driven wind.
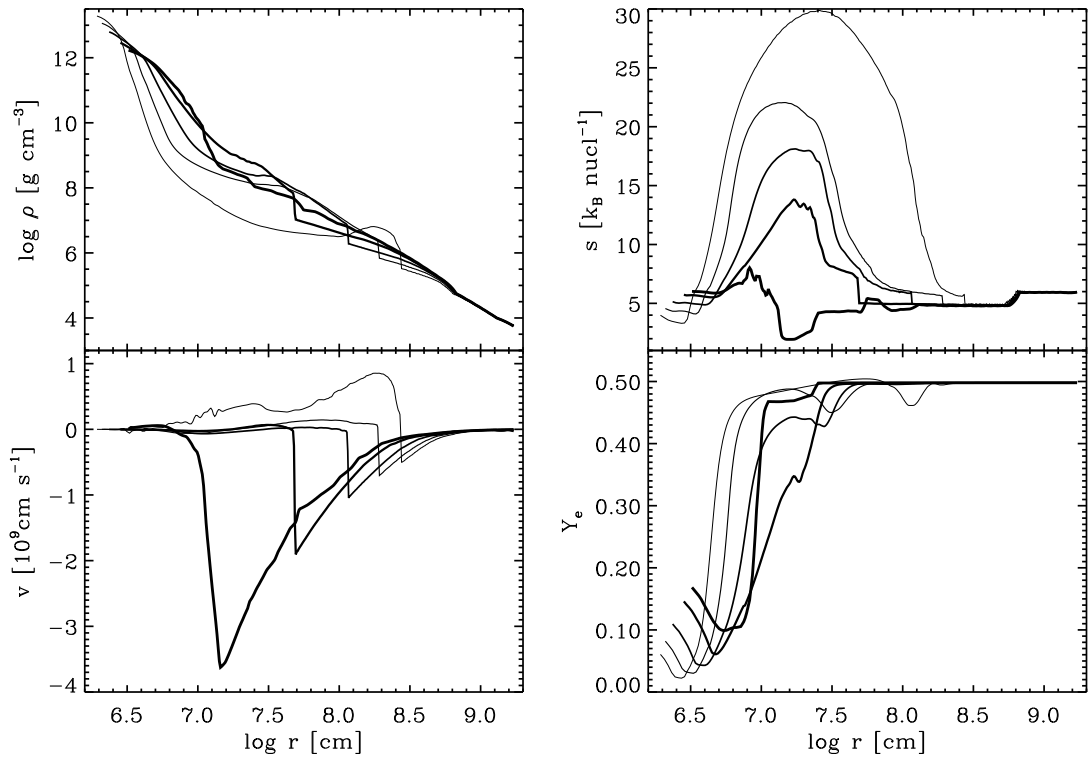
Figure 3.2: Evolution of density, entropy, velocity and electron fraction in model O245 for times of 0 ms (i.e. 20 ms after core bounce, heaviest line), 100 ms, 300 ms, 500 ms and 700 ms.

shrinks from its initial radius of 60 km, to 20 km at the end of the calculations. Despite these similarities it is evident, however, that the post-shock velocities in model O245 are rather small (a few 1000 km/s). Owing to the slow expansion in this model, the shock has not crossed the Si/O interface even after 800 ms and the densities at this time are higher than in model O310 by a factor of more than ten. Despite higher densities, the entropies during the late evolution in the inner ejecta of model O245 are higher than in O310 and reach values around 30 k_B/nucl. This is caused by higher temperatures due to the weaker expansion cooling of model O245.

Different from model O245, in model O310 neutrino energy deposition has led to the formation of a fast tenuous outflow, the neutrino driven wind, which is blown off the surface of the proto neutron star. The interaction zone of the accelerating wind and the slower moving ejecta steepens into a strong reverse shock in the flow around 450 ms after the start of the calculations (Fig. 3.3). From then on, both shocks mark the boundaries of a dense shell which contains most of the ejecta mass. This shell shows considerable substructure. Especially interesting is the formation of a narrow high-density region right behind the supernova shock in model O310 (as well as model O260) which is not visible in model O245 (Figs. 3.2 and 3.3). The trajectory of its inner boundary can be discerned in Figures 3.1 b and 3.1 c between the forward and the reverse shock. The occurrence of this high-density shell is *one of the most important features* in the models that we present in this thesis. It is in these stellar layers where explosive nucleosynthesis takes place and where convection as well as Rayleigh-Taylor instabilities must be expected to grow.
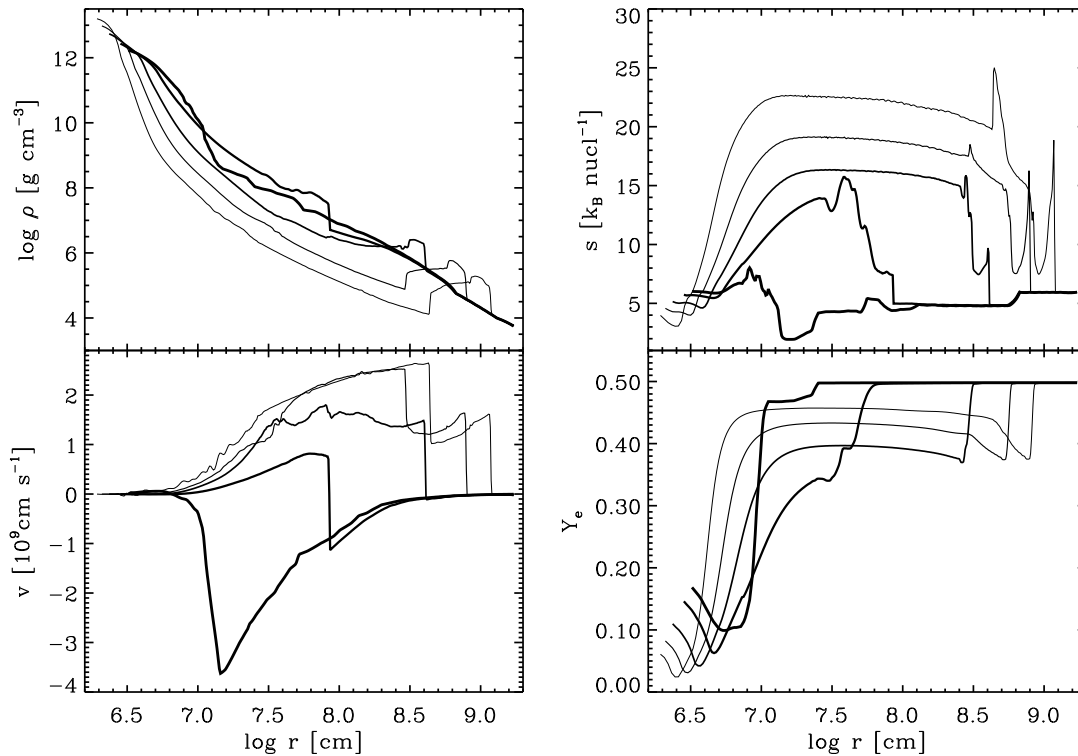
Figure 3.3: Evolution of density, entropy, velocity and electron fraction in model O310 for times of 0 ms (i.e. 20 ms after core bounce, heaviest line), 100 ms, 300 ms, 500 ms and 700 ms.

Initially, the high-density region is bounded at its outer edge by the supernova shock. However, the slight acceleration and subsequent deceleration that the shock experiences around 500 ms after core bounce, when it crosses the density step at the Si/O interface, results in a slight compression of the post-shock layers. A density "hump" is thereby left behind by the shock, whose outer boundary coincides with the Si/O interface and shows a pronounced negative density gradient. This negative density gradient is accompanied by a positive pressure gradient (Fig. 3.4), a state which is unstable to the Rayleigh-Taylor instability.

Of crucial importance for the synthesis of iron group elements are the processes which take place at the *inner* boundary of the hump. Figure 3.5 shows the density and temperature for model O310 as a function of the enclosed (baryonic) mass and time, and thus depicts the evolution in the frame comoving with the matter. It can be noted, that the inner edge of the density hump is stationary in this frame and can be found at a mass coordinate of $M_r \approx 1.27\,M_\odot$ (Fig. 3.5). By comparing its location with Fig. 3.6, which shows the evolution of the electron fraction, it is found that this mass shell marks the border between low and high-Y_e material in the expanding ejecta for times $t \geq 100$ ms. This means that symmetric nuclei, like ^{56}Ni, cannot be synthesized in regions with mass coordinates $< 1.27\,M_\odot$ and will thus be *confined to the density hump*. Further consequences for nucleosynthesis can be expected due to the fact that near the Y_e interface at $1.27\,M_\odot$ the entropy starts to rise steeply when one moves inward (Figs. 3.6 and 3.3), and reaches a maximum in the neutrino heated layers near the gain radius. This negative entropy gradient is sustained throughout the entire evolution
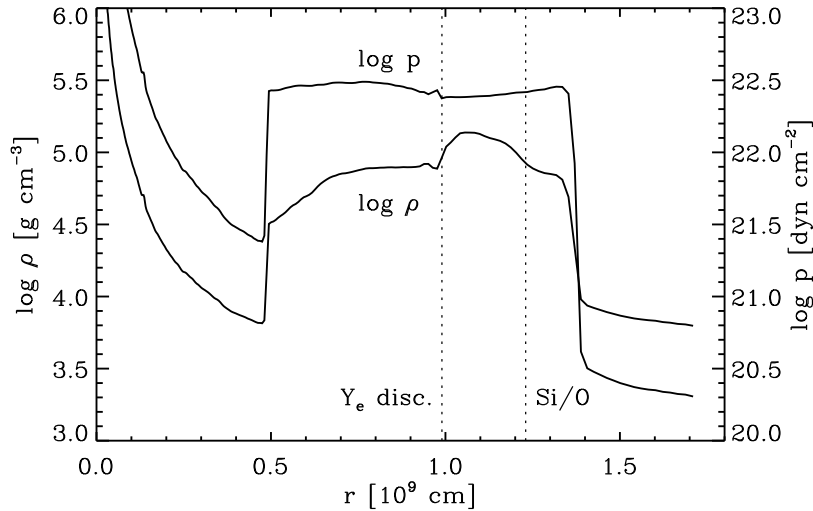
Figure 3.4: Density and pressure profiles of model O310 at $t = 800\,\mathrm{ms}$. The position of the Y_e discontinuity as well as the Si/O interface are also indicated. Note the density hump at $r \approx 10^9\,\mathrm{cm}$ and the density and pressure gradients of opposite sign for $1.05 \times 10^9\,\mathrm{cm} \leq r \leq 1.35 \times 10^9\,\mathrm{cm}$.

within the first 800 ms. It will tend to drive convective motions in this region which, in contrast to the one-dimensional situation, will mix high entropy (low Y_e) matter from the deeper layers of the iron-core with lower entropy (high Y_e) material of the outermost iron core and the silicon shell. We will discuss the implications of this (neutrino driven) convection in more detail in Section 3.9.

It must be pointed out, that the confinement of nuclei with $Z = N$ to the outer ejecta, which we discussed above, may not hold in general. As Figure 3.6 indicates, neutrino-matter interactions may potentially change the electron fraction in the inner ejecta to an extent, that Y_e values ≥ 0.49 may be attained. In order to discuss this question in more detail, a close inspection of Y_e in the initial model is required. As Figure 3.6 shows, in the post-collapse model of Bruenn (1993) the interface between material with low and high electron fractions is originally located at a mass coordinate of $\sim 1.25\,\mathrm{M_\odot}$. Outside this mass shell, this model shows Y_e values of ~ 0.498 while interior to it, the electron fraction decreases to 0.47 before it rapidly drops toward the electron neutrino sphere. Furthermore, the Y_e discontinuity coincides only roughly with the Fe/Si interface of the star at $1.32\,\mathrm{M_\odot}$ (Table 3.2), i.e. the outermost $0.07\,\mathrm{M_\odot}$ of the iron core show an electron fraction which is nearly identical to the one in the Si shell of 0.498 (compare Woosley & Weaver 1995, for a discussion). It is worth noting that pre-supernova models of different authors differ largely in their Y_e values for these stellar layers. The high electron fraction of the Woosley et al. (1988) progenitor in the silicon shell indicates that this model did not strongly suffer from electron captures during core-oxygen burning, as e.g. the models of Nomoto & Hashimoto (1988) which have a Y_e as low as 0.4915 in these zones.

Within the first few 100 ms of evolution, as the gas is heated by absorbing ν_e and $\bar{\nu}_e$ from the nascent neutron star, the Y_e-profile in the iron core is substantially modified. Already 100 ms after the start of the simulation, material between mass coordinates of
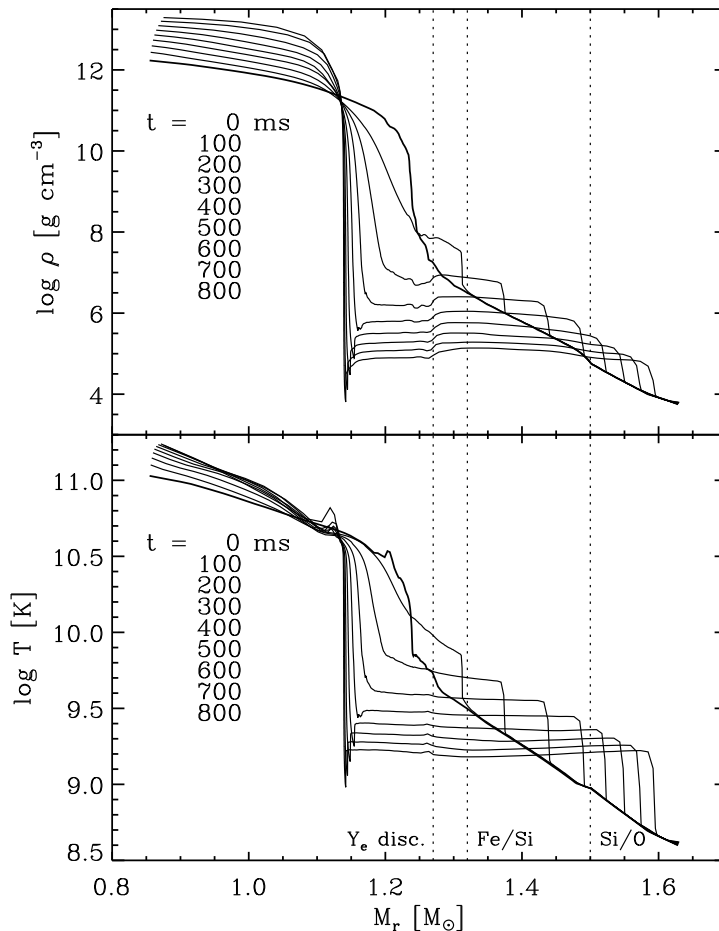
Figure 3.5: Evolution of the logarithms of density and temperature as a function of the enclosed mass for model O310 with a resolution of 400 radial zones for times between $t = 0$ ms and $t = 800$ ms. The positions of the Fe/Si and Si/O interfaces of the presupernova as well as the Y_e discontinuity (see text) are also indicated.

1.22 $M_\odot$ and 1.27 $M_\odot$ has been significantly deleptonized. The electron fraction within these zones has decreased to values as low as ~ 0.34. Correspondingly, the Y_e interface has shifted outwards, from 1.25 $M_\odot$ to 1.27 $M_\odot$, the value quoted above, where it remains throughout the subsequent evolution. In contrast, Y_e has substantially *increased* for zones between 1.14 $M_\odot$ and 1.22 $M_\odot$. In order to understand this behavior, a consideration of the delicate balance between the important charged-current reactions

$$\nu_e + n \; \rightleftharpoons \; e^- + p \qquad (3.27)$$

$$\bar{\nu}_e + p \; \rightleftharpoons \; e^+ + n \qquad (3.28)$$

is required. The neutronization of the neutrino-heated medium is a result of the competition of these four weak interaction processes. Positron capture on neutrons and ν_e absorption by neutrons tend to increase Y_e by making the matter more proton rich. On the other hand, the inverse processes of electron capture on protons and $\bar{\nu}_e$ absorption by protons tend to make the matter more neutron rich. This already indicates that Y_e in the ejecta will depend sensitively on the temporal evolution of the ν_e and $\bar{\nu}_e$ luminosities and energies. A dependence on the difference of the neutrino energies
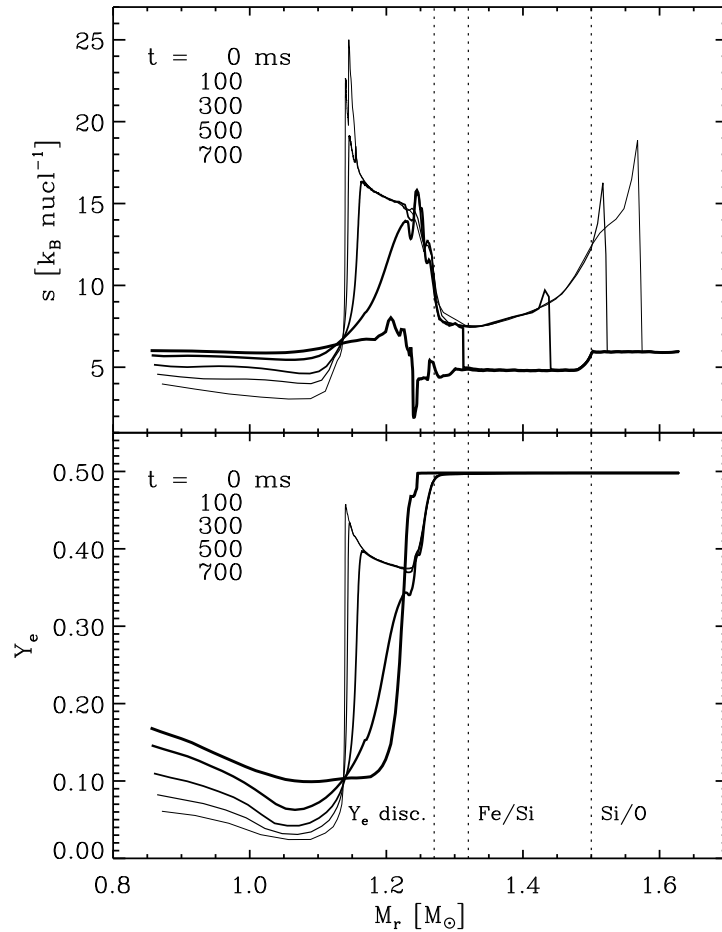
Figure 3.6: Evolution of the electron fraction and entropy as a function of the enclosed mass in model O310 for times of 0 ms (i.e. 20 ms after core bounce, heaviest line), 100 ms, 300 ms, 500 ms and 700 ms. The positions of the Fe/Si and Si/O interfaces of the presupernova as well as the Y_e discontinuity are also indicated.

is expected due to the fact that $\bar{\nu}_e$ captures on protons are hampered by an energy threshold, since the neutron is heavier than the proton by ≈ 1.293 MeV. On the other hand the capture of ν_e by neutrons is a reaction for which no energy threshold must be overcome. The importance of this threshold grows as the ν_e and $\bar{\nu}_e$ energies as well as the difference $\epsilon_{\bar{\nu}_e} - \epsilon_{\nu_e}$ decrease.

Taking into account that material in the innermost expanding zones is ejected at later times than matter which is located farther out in radius (or mass), Figures 3.3 and 3.6 indicate that in an early phase of our models, conditions are favorable for neutronization. However, the situation changes after some time and the balance of reactions (3.27) and (3.28) tips to the proton rich side, thus increasing Y_e. Yet, the electron fraction remains ≤ 0.46 even in the inner ejecta of model O310 up to the end of the simulation. A similar behavior is seen in nearly all of our one and two-dimensional models. The only exception was model O245, which showed an increase of Y_e above 0.5 in some of its inner ejecta (Fig. 3.2). Consequently, ^{56}Ni formation in model O245 took place in two different sites, separated by the low-Y_e material that is visible for $\log r$ [cm] ≈ 8.2 in Fig. 3.2. We will comment further on such effects in our discussion

of the two-dimensional models in Sections 3.9 and 3.10.

In the following we will make use of the simple model of a radiation dominated bubble with a constant density and pressure distribution behind the shock (Fig. 3.5) (Weaver & Woosley 1981; Thielemann et al. 1996), in order to infer simple estimates of the nucleosynthetic yields, the radii where freezeout of nuclear reactions will occur and the total energy release due to explosive nucleosynthesis in the Woosley et al. (1988) progenitor. Subsequently, we will discuss our actual numerical results focusing on model O310. As we noted above, the latter model gives a more representative picture of the phenomena that we generally see in successful explosion models than does model O245.

To obtain expressions for the freezeout radii of explosive nucleosynthesis, r_{fr}, one usually equates the supernova explosion energy E_{exp} with the radiation energy inside the radius r of the shock front

$$E_{\mathrm{exp}} = \frac{4\pi}{3} r^3 a T(r)^4 \qquad (3.29)$$

and inserts the minimum temperatures, T_{min}, which are required for the single types of burning:

$$r_{\mathrm{fr}} = \left(\frac{3 E_{\mathrm{exp}}}{4\pi a T_{\mathrm{min}}^4} \right)^{1/3} \qquad (3.30)$$

(e.g. Thielemann et al. 1996). However, in model O310 ($E_{\mathrm{exp}} = 1.59 \times 10^{51}$ ergs), only part of the explosion energy is in the form of internal energy during the first $\sim 500\,\mathrm{ms}$ of evolution (the typical time scale for the occurrence of explosive nucleosynthesis), and one should therefore replace E_{exp} by the temporal average of the internal energy which equals about 10^{51} ergs. For this energy, we summarize in Table 3.3 the critical minimum temperatures T_{min} and the freezeout radii r_{fr} for complete and incomplete silicon burning as well as oxygen and neon burning (see Thielemann et al. 1996). The mass coordinates corresponding to the different r_{fr} in the case of the Woosley et al. (1988) progenitor are also listed. These mass coordinates should be compared to Table 3.2, which gives the locations of the composition interfaces for this model. It is obvious from both tables, that we can expect at most

$$M_{\mathrm{r}}(\text{compl. Si-burning}) - M_{\mathrm{r}}(\text{Fe/Si}) = (1.42 - 1.32)\,\mathrm{M_\odot} = 0.10\,\mathrm{M_\odot} \qquad (3.31)$$

of silicon fuel to experience explosive silicon burning with complete silicon exhaustion. Since the electron fraction in these layers remains larger than 0.49 during the explosion (Fig. 3.6) this material will end up mostly as ^{56}Ni (e.g. Woosley & Weaver 1995; Thielemann et al. 1996; Thielemann et al. 1998).

	"iron core"	Fe/Si interface	Si/O interface	(C+O)/He interface
r [km]	260	1376	6043	29800
M_{r} [M$_\odot$]	1.25	1.32	1.50	1.68

Table 3.2: Radii and mass coordinates of the iron core and the composition interfaces of the 15 M$_\odot$ progenitor of Woosley et al. (1988). The radii are taken from the post-collapse data of Bruenn (1993), 20 ms after core bounce. Note that for the "iron core", the radius and mass coordinate of the Y_{e} discontinuity (see text) do *not* coincide with those of the Fe/Si interface.

	compl. Si-burning	incompl. Si-burning	O-burning	Ne-burning
$T_{\min}\,[10^9\,\mathrm{K}]$	5	4	3.3	2.1
$r_{\mathrm{fr}}\,[\mathrm{km}]$	3700	4980	6430	11,750
$M_{\mathrm{r}}\,[\mathrm{M_\odot}]$	1.42	1.47	1.50	1.57

Table 3.3: Minimum temperatures and freezeout radii for explosive silicon burning with complete and incomplete silicon exhaustion, explosive oxygen and neon burning. A total internal energy of 10^{51} ergs is assumed, and mass coordinates corresponding to the freezeout radii are given for the case of the $15\,\mathrm{M_\odot}$ progenitor model of Woosley et al. (1988).

From Tables 3.2 and 3.3 one can also infer that in the Woosley et al. (1988) progenitor, explosive nucleosynthesis will be mostly confined to the silicon shell. While there is some admixture of oxygen in the outer silicon shell, both ^{16}O and ^{20}Ne are abundant only for mass coordinates between $1.50\,\mathrm{M_\odot}$ and $1.68\,\mathrm{M_\odot}$. Explosive oxygen and neon burning, however, will freeze out when the shock has reached mass coordinates of only about $1.50\,\mathrm{M_\odot}$ and $1.57\,\mathrm{M_\odot}$, respectively. Thus the oxygen core of the star will remain largely unaffected by explosive nucleosynthesis, a result which depends only weakly on the (internal) energy of the explosion due to the $E^{1/3}$ dependence of r_{fr} (Eq. 3.30).

Our numerical models show that the post-shock temperatures have fallen below $5 \times 10^9\,\mathrm{K}$, $4 \times 10^9\,\mathrm{K}$, $3.3 \times 10^9\,\mathrm{K}$ and $2.1 \times 10^9\,\mathrm{K}$ in model O310 after 200, 250, 350, and 600 ms, respectively (Fig. 3.5). Thus, complete silicon, incomplete silicon, oxygen and neon burning have frozen out when the shock has reached mass coordinates of 1.37, 1.40, 1.46 and $1.55\,\mathrm{M_\odot}$, respectively (Fig. 3.5). These results are in fair agreement with the simple estimates given above. Figures 3.7 and 3.8 demonstrate that the oxygen core of the star was indeed hardly affected by explosive burning. This is of particular importance for the energy release from thermonuclear reactions. As we alluded to in Section 3.6, we neglect the resulting heating in our hydrodynamic calculations. This is motivated by the following estimate: According to Eq. (A.23) the energy release from explosive nucleosynthesis can be written as

$$\Delta\epsilon = -9.644 \times 10^{17} \sum_i \Delta M_i \frac{\Delta X_i}{A_i} \ [\mathrm{ergs/g}]. \tag{3.32}$$

Assuming complete silicon burning of $0.10\,\mathrm{M_\odot}$ of ^{28}Si to ^{56}Ni (this mass is by a factor of more than 2 larger than the one which is actually burned in model O310) one obtains an energy of

$$
\begin{aligned}
E(\text{compl. Si-burning}) &= -1.919 \times 10^{50} \left(\frac{\Delta M_{^{56}\mathrm{Ni}}}{A_{^{56}\mathrm{Ni}}} - \frac{\Delta M_{^{28}\mathrm{Si}}}{A_{^{28}\mathrm{Si}}} \right) \ \mathrm{erg} \tag{3.33} \\
&= 3.7 \times 10^{49} \ \mathrm{ergs} \tag{3.34}
\end{aligned}
$$

where we have inserted $\Delta M_{^{56}\mathrm{Ni}} = -53.903$ and $\Delta M_{^{28}\mathrm{Si}} = -21.492$, the mass excesses of ^{56}Ni and ^{28}Si in MeV. The $\sim 0.01\,\mathrm{M_\odot}$ of oxygen that were burned in model O310 will release at most another 1.3×10^{49} ergs so that the total energy gain is $\sim 5 \times 10^{49}$ ergs. Compared to the explosion energy of typically $(1-2) \times 10^{51}$ erg this energy is negligible, and therefore we do not expect nuclear energy release to have an appreciable effect on
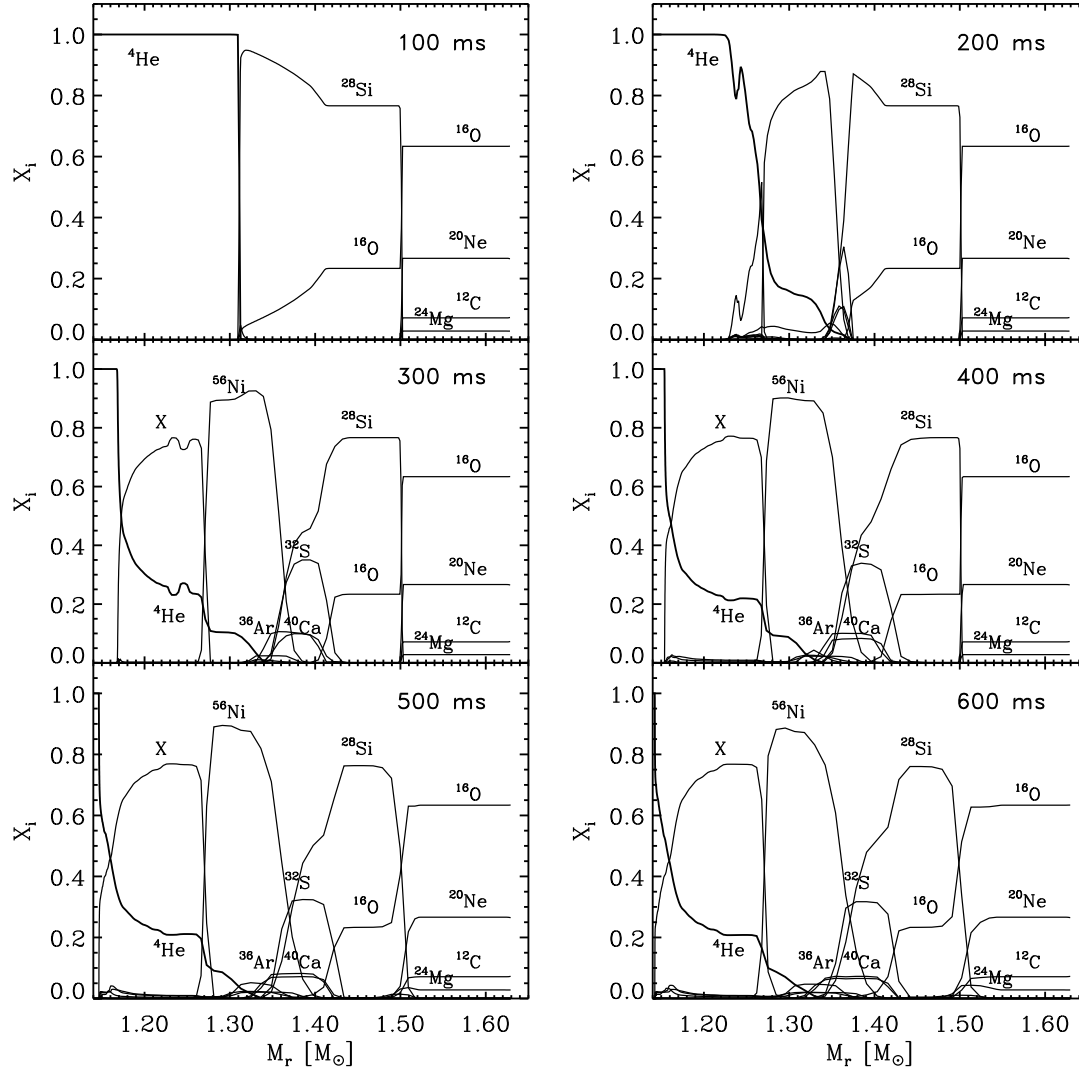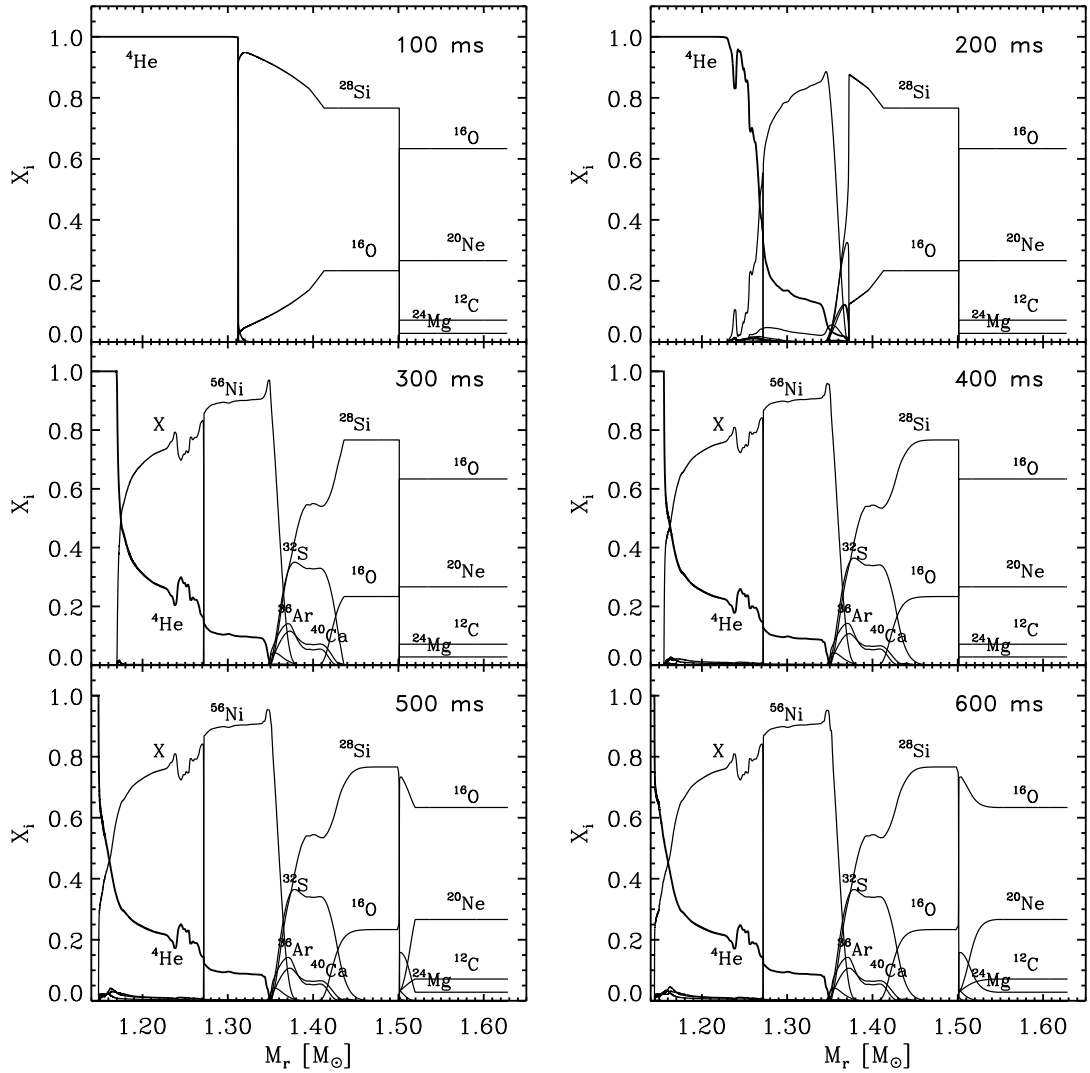
Figure 3.7: Explosive nucleosynthesis exterior to the proto neutron star in model O310 using a radial resolution of 400 zones. Snapshots of the chemical composition from $t = 100$ ms to $t = 600$ ms in steps of 100 ms are shown. Note that the inner boundary of the presupernova's silicon shell was initially located at $1.32\,M_\odot$ and that therefore only $0.04\,M_\odot$ of ^{28}Si is burned to ^{56}Ni. The remaining $0.04\,M_\odot$ stem from the recombination of photo-dissociated iron core matter with high electron fractions. Interior to $1.27\,M_\odot$ about $0.08\,M_\odot$ of material freezes out with electron fractions smaller than 0.49 and ends up in our tracer nucleus (denoted with X).

Figure 3.8: Explosive nucleosynthesis exterior to the proto neutron star in model O310 using a radial resolution of 6400 zones. Snapshots of the chemical composition from $t = 100\,\mathrm{ms}$ to $t = 600\,\mathrm{ms}$ in steps of 100 ms are shown. Compare the distribution of the elements with Fig. 3.7.

the dynamics in the case of the Woosley et al. (1988) progenitor except, possibly, for models which are just at the verge to non-explosion and end up with very low explosion energies around 5×10^{50} ergs. The situation may change, however, for different progenitors. As test calculations show, this is e.g. true for more massive models of the SN 1987 A progenitor computed by Woosley et al. (1997). In these, a substantial fraction of the oxygen core of the star attains temperatures in excess of 3.3×10^9 K and might even be burned to elements of the iron group.

Focusing now on the evolution of the abundances, one can recognize from Figure 3.7 that for temperatures above 7×10^9 K, which prevail for $t \leq 100$ ms, the photodisintegration rates are so large that NSE favors the lightest nucleus in our network, ^{4}He. Only 100 ms later, about $0.08\,M_\odot$ of ^{56}Ni have been synthesized in the deeper post-shock regions. Interestingly, about half of this mass stems from recombined material of the outermost layers of the iron core while the rest is due to complete silicon burning in the innermost regions of the silicon shell. With the decrease of the temperatures below 5×10^9 K in the layers immediately behind the shock at $t = 200$ ms, NSE cannot be sustained any more and silicon is burned only incompletely to ^{56}Ni, while a significant abundance of ^{32}S as well as ^{36}Ar and ^{40}Ca is built up. Explosive oxygen burning $(3.3 \times 10^9\,\mathrm{K} \leq T < 4 \times 10^9\,\mathrm{K})$ freezes out around 350 ms, and produces mainly ^{28}Si and ^{32}S but also some ^{36}Ar and ^{40}Ca. Concurrently deeper layers of the ejecta, between mass coordinates of $1.17\,M_\odot$ and $1.27\,M_\odot$ have cooled sufficiently and with decreasing photodisintegration rates the α-rich composition reassembles to heavier nuclei. Since these zones are substantially deleptonized, with a $Y_e < 0.49$, our modified α-network has not allowed ^{56}Ni to be synthesized in these layers and redirected the flow from the ^{52}Fe(α, γ) reaction into our neutronization tracer nucleus. The reassembly of the α-particles in these zones takes place at densities which are smaller by a factor of ~ 10 as compared to the conditions during ^{56}Ni synthesis in the region with mass coordinates between $1.27\,M_\odot$ and $1.37\,M_\odot$. This freezeout in high-entropy material leaves behind a large abundance of α particles. Finally, after 400 ms all types of nuclear burning except for explosive neon and carbon burning, which result only in insignificant changes in the ^{12}C, ^{16}O, ^{20}Ne, ^{24}Mg and ^{28}Si abundances, have frozen out.

3.8 A one-dimensional resolution study

One of the greatest problems in Eulerian calculations of reactive flows is numerical diffusion. The extensive study of Fryxell et al. (1989) as well as the recent work of Plewa & Müller (1999), have shown that diffusion of the composition can significantly influence the nucleosynthesis in Eulerian calculations if coarse zoning is used. Moreover, as both of these works demonstrate, even the best Eulerian methods can yield inaccurate results despite the use of fine zoning if no care is taken in order to exactly fulfill the requirement of local mass conservation, i.e. the sum of the mass fractions must remain equal to unity (up to machine accuracy) in each zone of the grid and at any given time. This is generally *not guaranteed* when a high-order advection scheme is used. Lower-order schemes usually lead to a better local mass conservation, but are unfortunately also more diffusive.

Plewa & Müller (1999) have performed a study of the numerical accuracy which can be achieved with codes that are based on the direct Eulerian formulation of the Piecewise Parabolic Method (PPM) for the problem of thermonuclear burning in core collapse supernovae. They demonstrate that when using their Consistent Multifluid

Advection method, which is implemented in our HERAKLES code, the yield of ^{44}Ti is essentially converged in their calculations when a grid with a radial resolution of 40 km is used. The more diffusive multifluid advection scheme proposed by Fryxell et al. (1989) needs a resolution which is higher by a factor of up to 4 or more in order to yield results of comparable quality. In their simulations, which employed uniform spherical grids and the same progenitor model which is used in the present work, the explosion was initiated by an ad hoc deposition of thermal energy into the innermost zones of the Si shell and the iron core of the star was omitted. Our neutrino-driven explosion models differ from these simplified models in several respects. The revival and early propagation of the shock is taken into account consistently (though for prescribed neutrino luminosities). In order to adequately resolve the flow near the neutron star, a moving, logarithmic radial grid is used, in which the radial resolution decreases with increasing radius. The differences in both approaches necessitated a separate resolution study for the calculations presented in this work. Unfortunately, this can only be accomplished in one spatial dimension. Doubling the resolution in both grid directions for the two-dimensional case increases the total CPU requirements for the hydrodynamic part of the calculations already by a factor of 8 and the number of burning zones at least by a factor of 2 (due to the twofold increase in angular resolution, if one assumes that only the first row of zones behind the shock is burned during a single hydrodynamic time step, which is a good approximation). Due to a better resolution of the shock, the post-shock temperatures will also be higher and therefore the burning time scales will be shorter. This in turn increases the number of time steps that have to be taken by the network solver in order to cover the hydrodynamic time step. All this increases the CPU time by at least a factor of 4, to 1000 CPU hours on one processor of an NEC SX-4B for a calculation with "only" $\sim 800 \times 400$ zones. We can therefore only give some indication of the errors which are expected to occur in two-dimensional models judging from the errors present in one-dimensional models with the same radial resolution.

For this purpose, we have varied the number of (radial) zones for model O310 from 400 to 6400 (compare Table 3.1) which corresponds to cell widths, Δr, of $1.2 \leq \Delta r/\text{km} \leq 200$ and $1.2 \leq \Delta r/\text{km} \leq 5$ in the 400 and 6400 zone runs, respectively. Figure 3.8 shows the distribution of the mass fractions in the 6400 zone calculation and should be compared to Fig. 3.7 which shows the same quantities for our "standard" run with 400 zones. It can be seen that numerical diffusion is substantially reduced in the high resolution calculation and that all composition interfaces are much sharper even for times as late as 600 ms. Considerably more fine structure is visible, e.g. in the ^{4}He, ^{36}Ar, and ^{56}Ni mass fractions, which show local maxima that are either completely absent or gradually smoothed with time in the lower resolution run. Due to the better resolution of the temperature profile behind the shock, explosive neon burning is calculated much more accurately and the characteristic local peak of e.g. the oxygen mass fraction caused by the photodisintegration reaction ^{20}Ne$(\gamma, \alpha)^{16}$O is clearly present at a mass coordinate of $1.5\,\text{M}_\odot$ while it is not visible in the low-resolution run.

In Figure 3.9 we plot for each run that we have performed for model O310, the relative deviation of the total yield of each species as compared to the results of our highest resolution simulation with 6400 zones. It can be noted that for ^{44}Ti, ^{48}Cr and ^{52}Fe, all products of the α-rich freezeout, the errors are large and amount to more than 150%, 63% and 25%, respectively. The abundance of ^{44}Ti is not fully converged even in the highest resolution calculation. Figure 3.10 shows the temporal evolution of the ^{44}Ti yield for different resolutions and suggests that an error of about 6% has
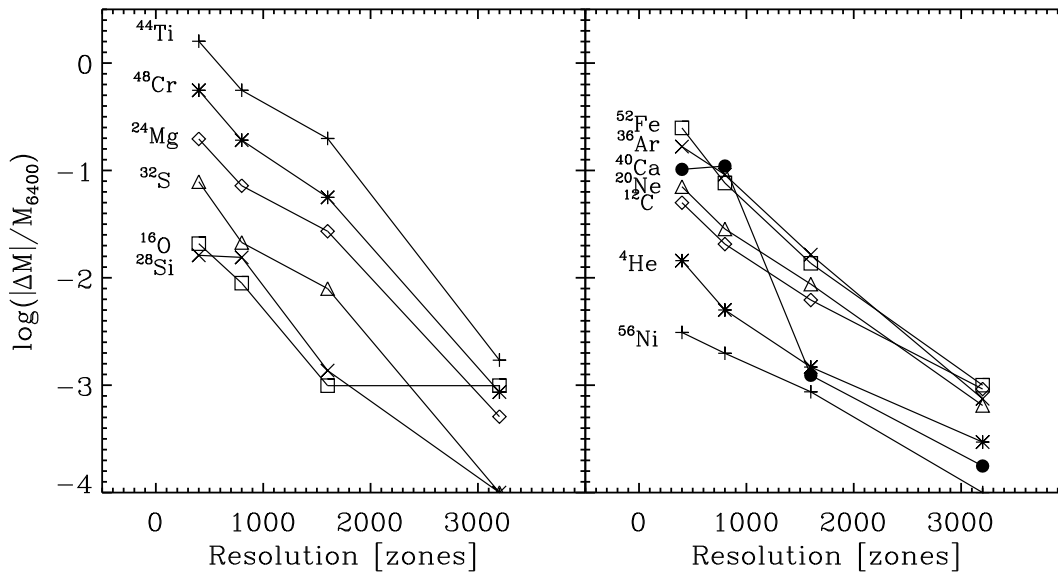
Figure 3.9: Deviations, $|\Delta M|/M_{6400}$, of the total yields of the α-nuclei for different resolutions relative to the yields of the 6400 zone calculation for model O310. The time is $t = 800\,\mathrm{ms}$ and a logarithmic scale is used.

still to be expected for the 6400 zone run. Plewa & Müller (1999) have shown that the strong dependence of the ^{44}Ti mass on the spatial resolution can be understood in terms of its formation site. ^{44}Ti is known to be synthesized mainly in the layers of α-rich freezeout close to the collapsed core (Woosley & Weaver 1995; Thielemann et al. 1996). Furthermore, in the calculations of Woosley & Weaver (1995), a small fraction of the total ^{44}Ti mass is synthesized in the regions of incomplete silicon burning which are abundant in ^{40}Ca. This second site of ^{44}Ti formation may already be affected to some extent by numerical diffusion in calculations with Lagrangian finite-difference codes that employ rezoning and an artificial viscosity in order to suppress numerical post-shock oscillations. In an Eulerian calculation, numerical diffusion presents an even bigger problem, even if it is as small as in the PPM scheme. Numerical diffusion of α-particles from the zones of α-rich freezeout ($1.15 \leq M_r/\mathrm{M_\odot} < 1.35$; Fig. 3.11), into regions which experience incomplete silicon burning leads to a smeared interface between ^{4}He and ^{40}Ca in which α-captures on ^{40}Ca can synthesize ^{44}Ti much more efficiently than given the small ^{40}Ca abundances in deeper layers. This build-up of ^{44}Ti causes the broad peak in the ^{44}Ti mass fraction of the 400 zone run (Fig. 3.11), which is much narrower in the 6400 zone calculation, though it did not vanish completely. It should be noted that the errors result almost exclusively from this region. The abundances in zones interior to $\sim 1.26\,\mathrm{M_\odot}$ are well represented, even in the 400 zone run. In absolute terms, we find $1.6 \times 10^{-3}\,\mathrm{M_\odot}$ of ^{44}Ti in the nearly converged 6400 zone calculation for model O310, a value which is by a factor of 3 and a factor of 8 larger than the one obtained by Plewa & Müller (1999) and Woosley et al. (1988), respectively, who used somewhat different explosion energies, however. This may indicate, that (due to neutrino heating) our entropies are higher than in calculations which adopt an ad hoc energy deposition.

Deviations $\geq 10\%$ between the yields of the lowest and the highest resolution calculation can be seen for ^{32}S, ^{36}Ar and ^{40}Ca, the products of explosive oxygen and
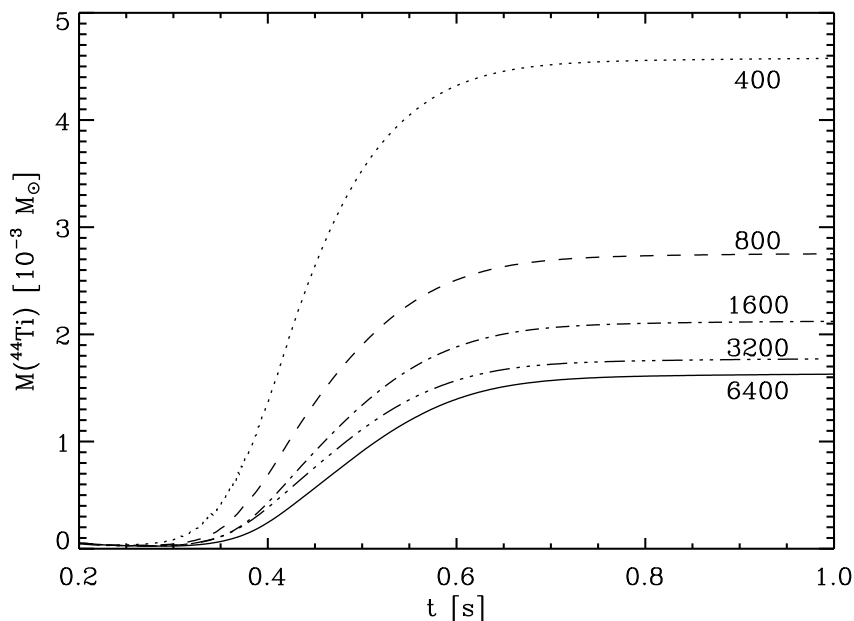
Figure 3.10: Evolution of the ^{44}Ti mass for model O310 computed with 400, 800, 1600, 3200 and 6400 radial zones.

incomplete silicon burning and up to 20% for the nuclei ^{12}C, ^{20}Ne and ^{24}Mg which are affected by explosive neon and carbon burning. These differences are caused by a loss of spatial resolution in the outermost parts of the computational domain due to the use of a logarithmic grid. Although they appear to be large, for the case of ^{12}C, ^{20}Ne and ^{24}Mg the errors for the total yields of these nuclei are insignificant, because a negligible mass of our progenitor model is affected by explosive neon and carbon burning (most of the C+O-core of the star is not even covered by our grid in the calculations presented in this chapter). It should be noted that, assuming the 6400 zone run is converged, about 3000 radial zones are needed in order to reduce all errors to the level of a few percent.

While caution has to be exercised when extrapolating these results to the two-dimensional case, the accuracy of the low-resolution one-dimensional models indicates that our two-dimensional calculations have sufficient resolution in order to predict the spatial distribution and the yields of the important nuclei ^{12}C, ^{16}O, ^{28}Si and ^{56}Ni with confidence. For ^{32}S, ^{36}Ar and ^{40}Ca, the errors may be as large as a few 10%, while for the products of α-rich freezeout deviations from a converged solution up to more than a factor of 2 must be expected. These errors do not take into account uncertainties in nuclear reaction rates as well as the neutronization of matter in zones experiencing an α-rich freezeout. Hence, great care is needed when performing Eulerian nucleosynthesis calculations. In particular it is very difficult to *reliably* determine the yield of ^{44}Ti in current multidimensional core collapse supernova simulations since it appears that extremely fine zoning is required. This is very unfortunate, because ^{44}Ti is of significant importance for observational γ-ray astronomy and could be used as a probe for hydro-dynamic instabilities during the explosion, due to its production site near the collapsed core. This has led Nagataki et al. (1998a) to propose that the overabundance of ^{44}Ti relative to ^{56}Ni observed in Cas A argues in favor of strong asymmetries during the
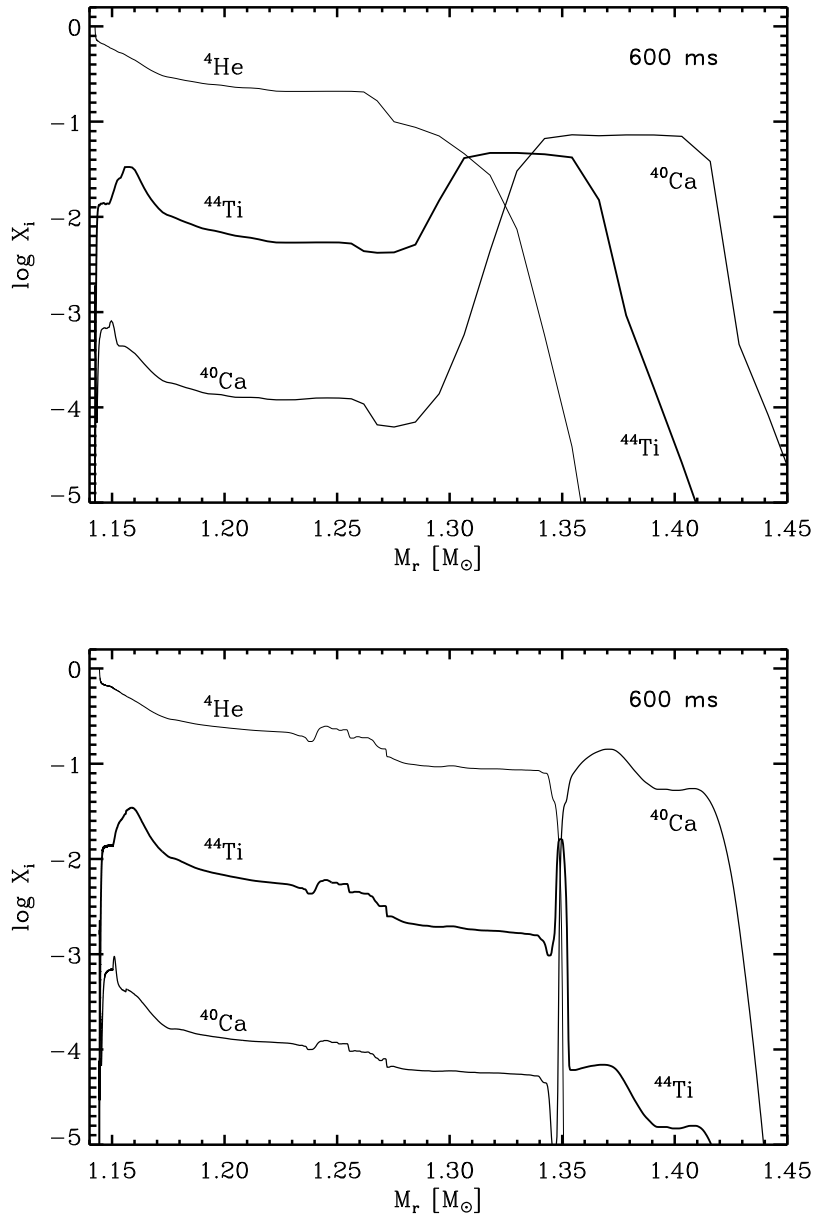
Figure 3.11: Logarithm of the mass fractions of ^{4}He, ^{40}Ca and ^{44}Ti over the enclosed mass in model O310 for a resolution of 400 (top) and 6400 zones (bottom), at $t = 600$ ms.

explosion. These authors base their hypothesis on the observation that due to higher entropies in the polar compared to the equatorial regions of their (jet-like) axisymmetric explosion models, their ^{44}Ti yields are higher than the ones obtained in spherically symmetric explosive nucleosynthesis calculations by a factor of ~ 3. We think that given the problems of numerical diffusion in Eulerian calculations, the claims of Nagataki et al. (1998a) cannot be supported on grounds of present day multidimensional nucleosynthesis calculations. In Section B.3 of the Appendix we describe an adaptive mesh refinement code which is able to minimize numerical diffusion and which we will use in future multidimensional nucleosynthesis calculations.

3.9   Two-dimensional models

As the one-dimensional models have shown, unstable stratifications of the electron fraction and entropy are sustained within the first second of the explosion in the zones below the electron neutrinosphere as well as in the gain region. Of these, the region between gain radius and shock is particularly interesting. Convective overturn in this zone might lead to large-scale anisotropies in the spatial distribution of the nucleosynthetic products and might further influence the explosion energy. We have therefore carried out six two-dimensional runs with the same setup, radial resolution and initial neutrino luminosities as in our one-dimensional calculations in order to study the effect of neutrino-driven convection on the energetics and the nucleosynthetic yields. Their characteristic parameters are summarized in Table 3.1.

Models T280* and T310* suffered from "odd-even decoupling". We have included these models in Table 3.1 in order to illustrate the adverse effects of numerical noise on the nucleosynthetic yields and the character of neutrino-driven convection in Section 3.11. Models T240, T245, T260 and T310 were computed using the multidimensional artificial viscosity discussed in Appendix B and do not exhibit this problem.

Before we will focus on a detailed discussion of two representative two-dimensional models, it is instructive to gain a general overview by considering the differences in the explosion energies as compared to the one-dimensional case. As one can note in Figure 3.12 these differences are significant for low energy models while they are only minor for the high-energy explosions. The most extreme case is our failing one-dimensional model O240. Compared to our exploding one-dimensional model with the lowest neutrino luminosities (i.e. model O245), model O240 had neutrino luminosities which were smaller by only 2% and failed to explode in one dimension. However, the increased efficiency of neutrino heating due to neutrino driven convection turned this model into a successful explosion in the two-dimensional calculation T240 (though with a rather low explosion energy of 0.76 foes). Significant boosts in the final explosion energy are also seen for model T245 which exploded with an energy of 0.88 foes, i.e. twice the energy as in the 1D calculation, and with an explosion time scale which is shorter by a factor of 2 (Table 3.1). It must be emphasized, though, that, as in the calculations of Janka & Müller (1996), such drastic deviations between the one and two-dimensional models are *only* observed within a narrow window of neutrino luminosities close to the critical luminosity required for an explosion. For the more energetic models O260 ($E_{\mathrm{exp}} = 0.94$ foes) and O310 ($E_{\mathrm{exp}} = 1.59$ foes) the gain in explosion energy in two dimensions is only about 20% and 11%, respectively.

Taking models T245 and T310 as representatives of a low and a high energy explosion, respectively, we now turn to a detailed description of their evolution. It should
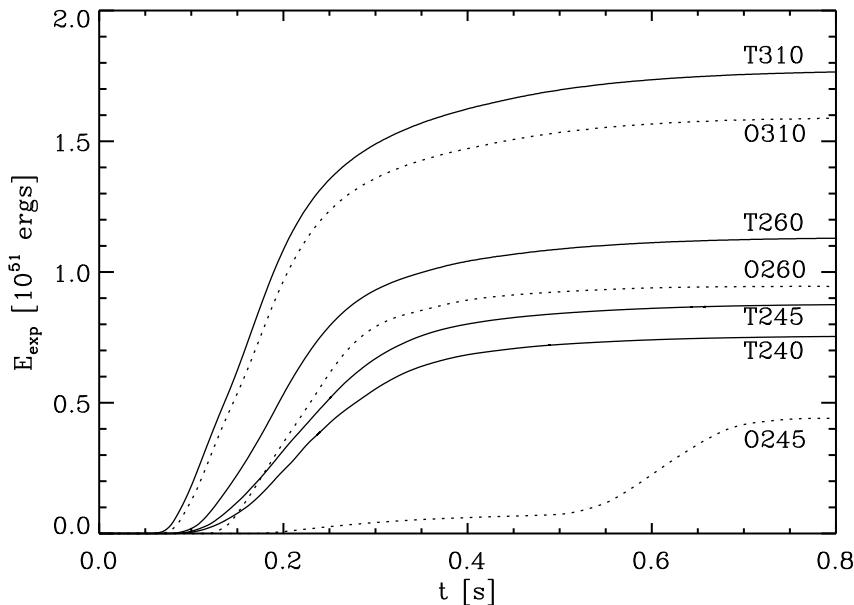
Figure 3.12: Evolution of the explosion energy for 2D models T310, T260, T245, and T240 and their exploding one-dimensional counterparts O310, O260 and O245. The one-dimensional version of model T240 failed to explode and is therefore not included (see also Table 3.1).

be noted that model T310 ($E_{\mathrm{exp}} = 1.77\,\mathrm{foes}$) is somewhat above the upper limit of the (1.15 ± 0.35) foes and (1.0 ± 0.4) foes deduced for the explosion energy of SN 1987A by the light-curve modeling of Woosley (1988) and Shigeyama & Nomoto (1990), respectively, while model T245 ($E_{\mathrm{exp}} = 0.88\,\mathrm{foes}$) is rather close to the lower limit.

Focusing first on the evolution of model T245 we find that convective activity sets in already about 20 ms after the start of the calculations in the unstable regions beneath the neutrinosphere. These can most easily be seen near the coordinate center in Figures 3.13 a and 3.13 b, below the dark blue concentric region, which marks the location of the local minimum in the Y_{e} trough. Concurrently, convection between gain radius and shock develops, while a stable intermediate layer separates the two unstable regions (Figures 3.13 and 3.14). Note that the computational domain has been rotated counterclockwise by 90° in Figures 3.13 and 3.14. This includes the cylindrical grid, which is indicated in these plots, and to which the data was mapped for plotting. The same holds for most of the following figures which depict quantities of the 2D models. In these figures the symmetry axis extends horizontally. Regions with $0 \leq \theta \leq \pi/2$ are visible in the left half, while regions with $\pi/2 \leq \theta \leq \pi$ occupy the right half of the plots. The projection of the equatorial plane ($\theta = \pi/2$) coincides with the vertical axis.

At $t = 40\,\mathrm{ms}$, mushrooms of high entropy material with an angular size of about $5° - 10°$ have formed in the neutrino heated layers and start to rise toward the shock in the surrounding lower-entropy gas (see Fig. 3.14 a). Already 80 ms after the start of the calculation these small-scale structures have merged with each other, and produced larger high-entropy blobs with angular sizes of about 30° (Fig. 3.14 b).

As one can also note in Figs. 3.13 b and 3.14 b, the bubble visible near the symmetry axis at $\theta \approx \pi$ has grown much faster than the other structures. It already extends to a
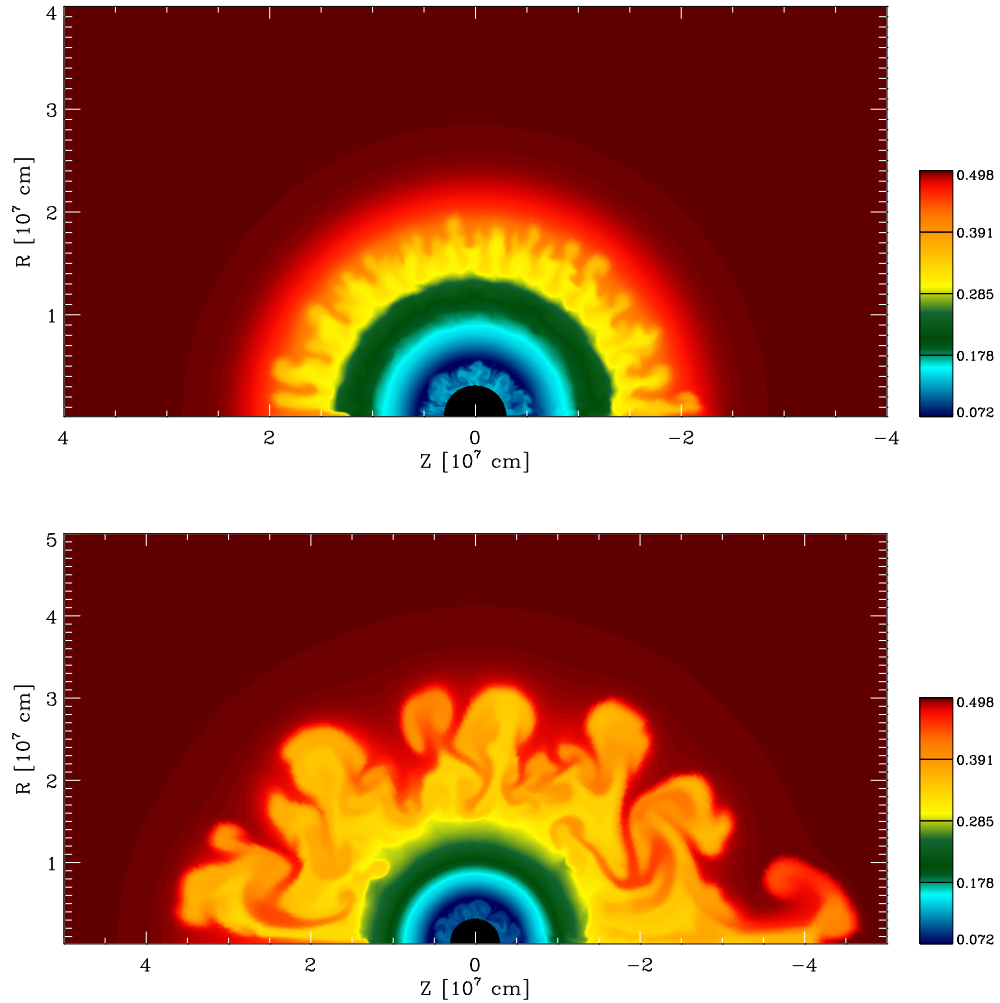
Figure 3.13: Distribution of the electron fraction in model T245. From top to bottom: a) $t = 40\,\text{ms}$. b) $t = 80\,\text{ms}$. Given are (R, Z) coordinates of the cylindrical grid which was used for plotting. The calculations have been carried out using spherical coordinates.

radius of $\sim 4.6 \times 10^7$ cm while the blobs which have formed in the equatorial region have reached radii around $\sim 3 \times 10^7$ cm. The faster growth of the structure along the symmetry axis is a numerical artifact which is caused by the interaction of several effects. In contrast to the "bubbles" found far from the pole, which are in fact axisymmetric tori, the structures protruding along the polar axis are genuine (3D) mushrooms. The growth rates of both objects differ because of the different drag that they experience owing to their different geometries (Kane et al. 2000). This effect, however, is strongly enhanced by the interaction of the flow with the reflecting boundaries along the axis. The vortices which form near the boundaries lead to a redistribution of lateral into radial momentum since the fluid, not being able to penetrate through the boundary, must either flow outwards or inwards along the axis. The latter effect can be seen for angles $\theta \approx 0$ in the left parts of Figs. 3.14 and 3.15.

In our discussion of the one-dimensional models in Section 3.7 we have already pointed out that the rising high-entropy material in the bubbles should be substantially
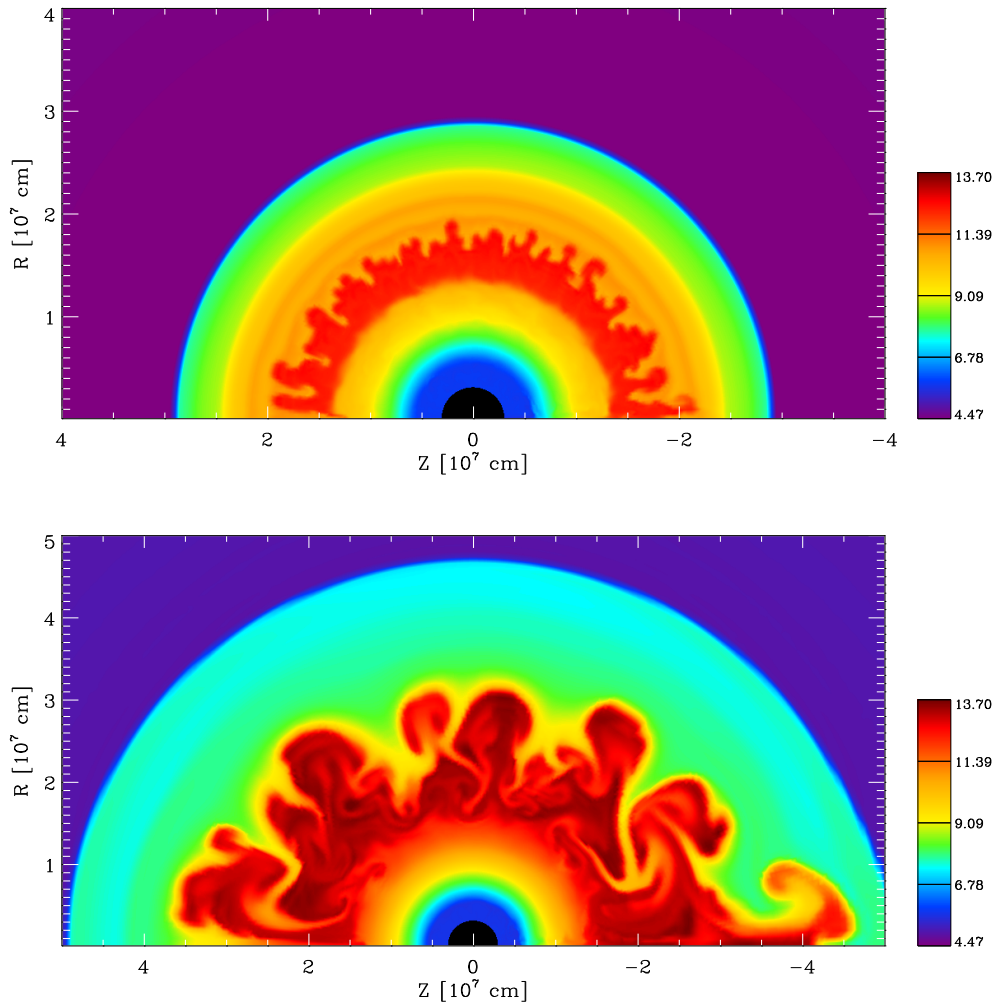
Figure 3.14: Distribution of the entropy (in k_B/nucleon) in model T245. From top to bottom: a) $t = 40\,\mathrm{ms}$. b) $t = 80\,\mathrm{ms}$.

deleptonized. In contrast to the 1D models, the mixing resulting in two dimensions not only transports the deleptonized material outwards, but also enhances neutronization by cycling high-Y_e material through the regions near the gain radius. Between the bubbles, low-entropy gas is visible in Fig. 3.14 b which penetrates in narrow, bent, finger-like downflows towards the deeper layers of the core. These fingers exhibit the typical mushroom heads caused by Kelvin-Helmholtz instabilities and start to meander around the gain radius where they are distorted by vortex motions. As long as the gas in these fingers does not reach the regions of maximum neutrino heating, it does not experience large $\bar{\nu}_e$ and ν_e interaction rates and therefore most of this material has a Y_e which is close to its original value of 0.498. However, after penetrating into the strongly heated layers just outside the gain radius, the gas is substantially deleptonized because at this time the ν_e and $\bar{\nu}_e$ fluxes from the proto neutron star favor neutronization. Subsequently, some of this matter rises toward the shock and mixes with the material of the bubbles. All these effects lead to Y_e values in the bubbles as low as $0.35 - 0.4$ (Fig. 3.13).
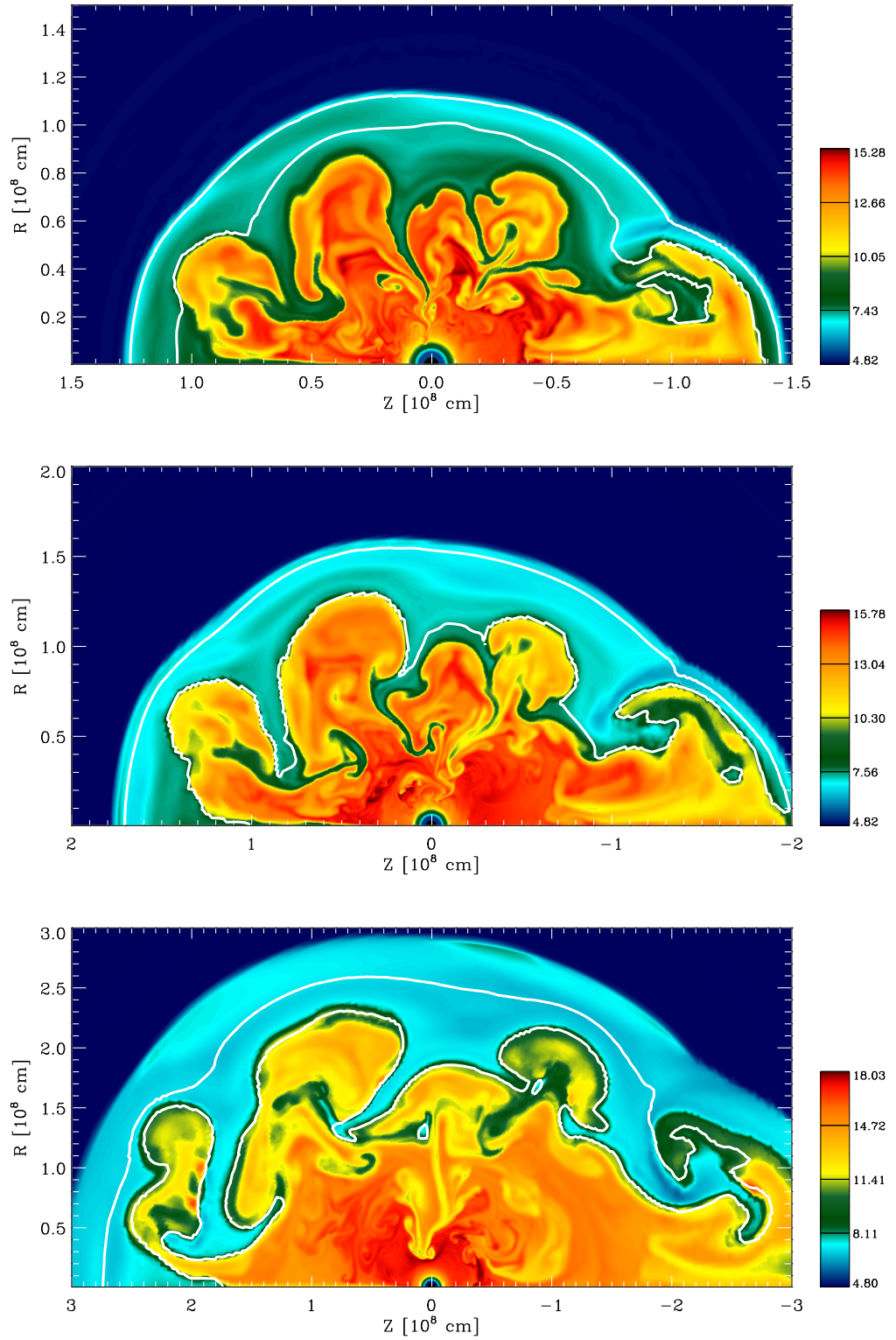
Figure 3.15: Distribution of the entropy (in k_B/nucleon) in model T245. The white line encloses the region in which the ^{56}Ni mass fraction is $\geq 20\%$. From top to bottom: a) $t = 160$ ms. b) $t = 200$ ms. c) $t = 300$ ms.

At $t = 120\,\text{ms}$ the shock reaches the Fe/Si interface, which has meanwhile fallen from its initial radius of $r = 1.36 \times 10^8\,\text{cm}$ to a radius of $7.5 \times 10^7\,\text{cm}$. At this time the post-shock material is still in nuclear statistical equilibrium (NSE) and is composed mainly of α-particles and nucleons. However, with the ongoing expansion, temperatures *right behind* the shock drop below $7 \times 10^9\,\text{K}$, after $t \approx 130\,\text{ms}$ and NSE starts to favor the formation of heavier nuclei (the temperature gradient between the radius of maximum neutrino heating and the shock is negative, i.e. the temperature has a minimum in the immediate post-shock region (see Fig. 3.5); deeper layers of the ejecta will cool below this temperature only after some time).

As we have stressed in Chapter 2, the question to which extent neutrino driven convection influences the distribution of the products of explosive nucleosynthesis is of crucial importance for an understanding of the observations of SN 1987 A. In order to illustrate this, we show the evolution of the entropy, the electron fraction and the mass fraction of ^{56}Ni between $t = 160\,\text{ms}$ and $t = 300\,\text{ms}$ in Figures 3.15, 3.16 and 3.17, respectively. From Fig. 3.15 one can recognize that during this time-span the post-shock flow is dominated by five "balloon-like" bubbles of high-entropy material, with angular extents between $30°$ and $45°$, which have formed out of mergers of the somewhat smaller structures visible in Fig. 3.14 b. These bubbles have risen close to the shock wave and distorted it appreciably. This is most easily seen in case of the large "mushroom" which has formed near the symmetry axis.

We recall from our discussion in Section 3.7 that the synthesis of ^{56}Ni requires i) temperatures in the range $(5 - 7) \times 10^9\,\text{K}$ and ii) electron fractions $Y_e > 0.49$. Since the deleptonized bubbles themselves have a $Y_e \leq 0.4$ (see Figs. 3.13 and 3.16) ^{56}Ni will not form within them. Instead, as Figs. 3.15 a to 3.17 a show, ^{56}Ni synthesis starts in the thin filamentary shell between the bubbles and the shock, where Y_e takes on values of ~ 0.497. As the expansion proceeds, also the inner regions of the flow start to cool to temperatures where formation of iron-group nuclei is favored by NSE. Yet, the only sites where ^{56}Ni synthesis can proceed in these layers are (the outer parts of) the narrow downflows which separate the deleptonized bubbles (Figures 3.15 b to 3.17 b). The downflows themselves show an electron fraction gradient. Near their (outer) edges, favorable Y_e values for ^{56}Ni formation of ~ 0.496 are found. However, the parts which have protruded deepest into the neutrino heated layers show Y_e values as low as 0.4 (see above and compare also Figs. 3.15 b and 3.16 b). Hence, the inner boundary of the ^{56}Ni shell closely traces the contours of the low-entropy (high-density) material in the convective region, except for the very narrow parts of the tongues which reach down to the gain radius (Figs. 3.15 b and c). On the other hand, the outer boundary of the ^{56}Ni shell coincides with the aspherical shock wave as long as the post-shock temperatures have not dropped below $5 \times 10^9\,\text{K}$ (Figs. 3.15 a and b). When this happens and complete silicon burning freezes out at $t \approx 250\,\text{ms}$, a "bent" nickel shell is left behind while the shock continues moving outward. Together with the anisotropies introduced by convection and the deleptonization of the neutrino-heated material this leads to a highly inhomogeneous nickel distribution at $t = 300\,\text{ms}$ (Figs. 3.15 c to 3.17 c).

By comparing Figure 3.16 with Figure 3.17 one can also judge the accuracy that can be achieved in the two-dimensional case with our simplified treatment for ^{56}Ni nucleosynthesis. As one can note in Figure 3.16, there exists always a sharply defined boundary between material which did not experience significant ν_e and $\bar{\nu}_e$ captures and thus has a $Y_e \geq 0.496$, which is close to its original value of 0.498, and the material in the strongly deleptonized bubbles. In particular, the amount of gas with $0.49 < Y_e \lesssim$
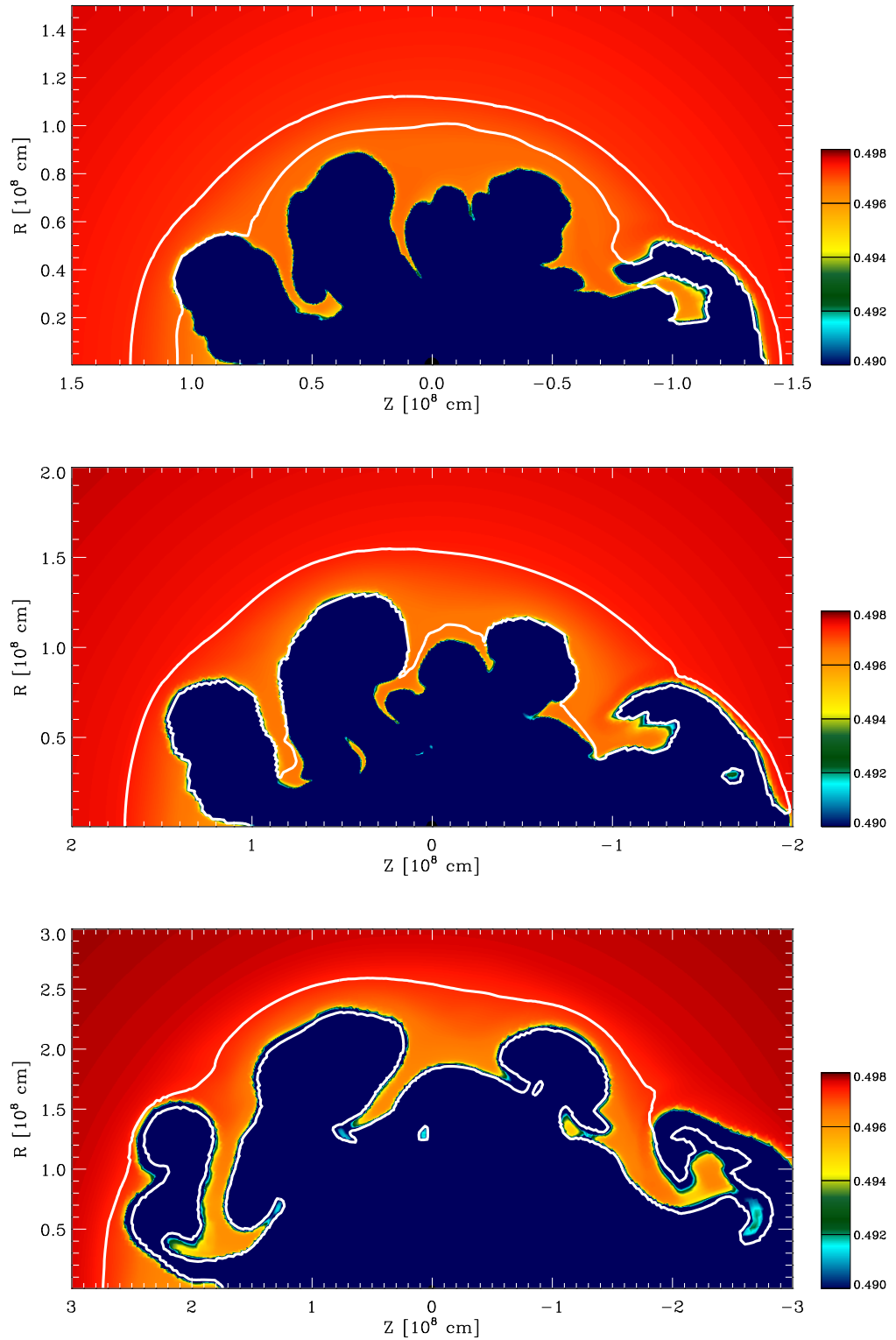
Figure 3.16: Distribution of the electron fraction in model T245. Only values of $Y_e \geq 0.490$ are displayed in order to show the variation of Y_e in the low-entropy fingers. The white line encloses the region in which the ^{56}Ni mass fraction is $\geq 20\%$. Note the sharp separation between the fingers and the deleptonized bubbles ($Y_e \leq 0.490$, dark blue regions). Also note that the amount of material with $Y_e \lesssim 0.496$ in the fingers is negligible. From top to bottom: a) $t = 160$ ms. b) $t = 200$ ms. c) $t = 300$ ms.
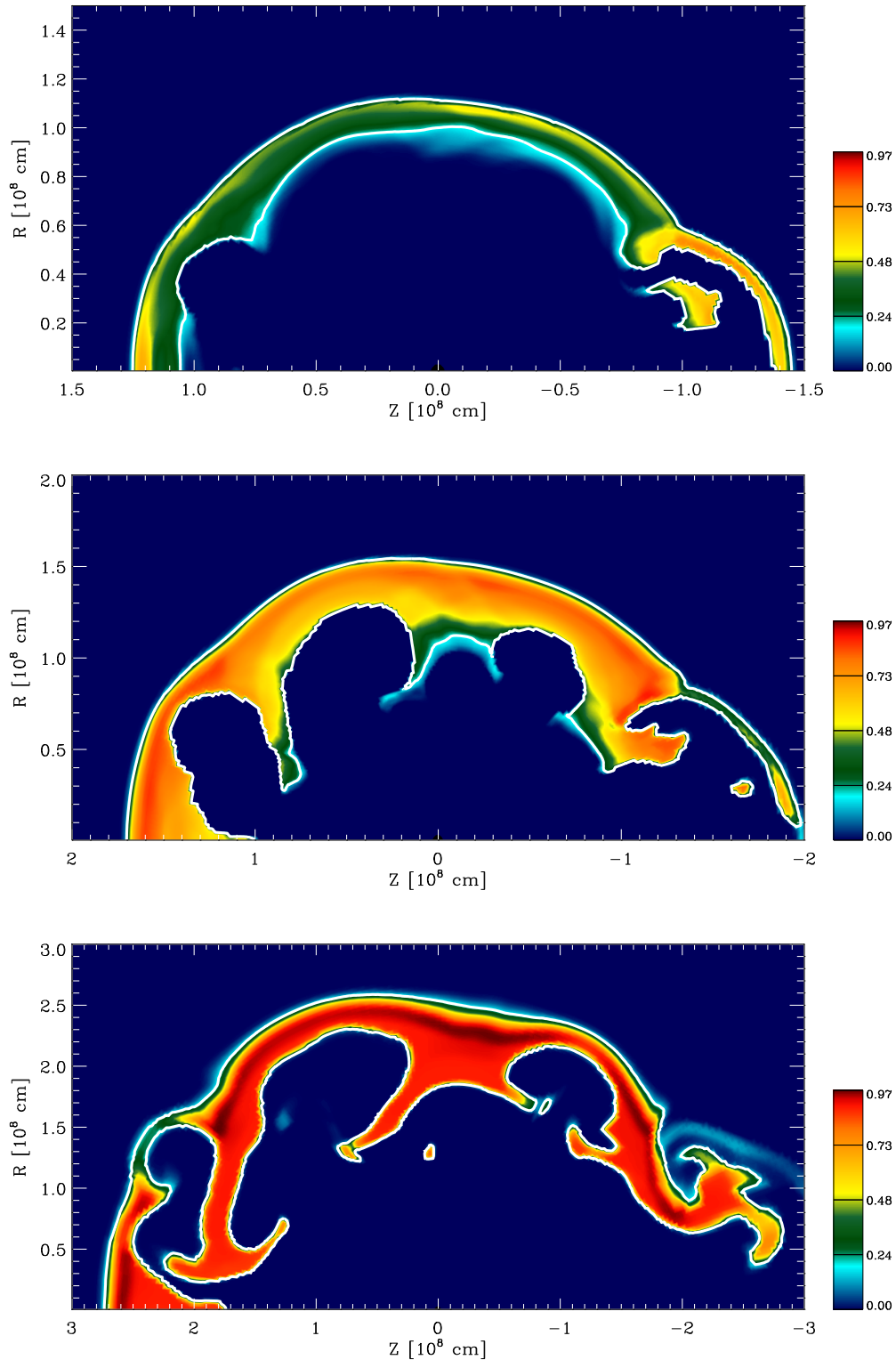
Figure 3.17: Distribution of the ^{56}Ni mass fraction in model T245. Overlaid is the contour line for a mass fraction value of 20%. From top to bottom: a) $t = 160$ ms. b) $t = 200$ ms. c) $t = 300$ ms.

0.496 is negligible. Since this is the range of electron fractions where our modified α-network is expected to result in somewhat overestimated ^{56}Ni yields (see the discussion in Sect. 3.6), the errors introduced by our approximation are small and we are able to track the yield and the spatial distribution of ^{56}Ni with satisfactory accuracy.

A much more severe problem of our current models is that the strong deleptonization of the bubbles will result in the synthesis of large amounts of (neutron-rich) nuclei with neutron numbers $N = 50$ and mass numbers $A \approx 90$, as ^{88}Sr, ^{89}Y and ^{90}Zr, which are incompatible with the elemental abundances observed in the solar system (Woosley et al. 1994; Witti et al. 1994). If ejected during the explosion, this material will also be at odds with chemical evolution models of the Galaxy (Hoffman et al. 1996; Thielemann et al. 1996; Herant et al. 1994, and the references therein). It must be emphasized, that a strong deleptonization of the neutrino heated ejecta is a common problem in all multidimensional supernova models and that late-time fallback of this material onto the neutron star has been proposed to lower the discrepancy to observed elemental abundances (e.g. Woosley et al. 1994; Herant et al. 1994; Burrows et al. 1995; Janka & Müller 1996). On the other hand, Hoffman et al. (1996) have shown that the overproduction problem of $N = 50$ nuclei disappears when the electron fraction during freezeout takes on values $\gtrsim 0.484$. In their calculations with $Y_e = 0.485$ and entropies around $50 \, k_B$/nucleon the large yields of ^{88}Sr, ^{89}Y and ^{90}Zr are replaced by ^{70}Ge, and ^{74}Se, ^{78}Kr, ^{84}Sr and ^{92}Mo in about their solar abundances. Indeed, very recent one-dimensional supernova simulations employing a full solution of the Boltzmann equation for neutrino transport (Mezzacappa et al. 2000; Rampp & Janka 2000) concur in predicting that Y_e in a significant part of the neutrino heated ejecta takes on values *above* 0.5! If confirmed in future (especially multidimensional) studies this result would prove that the overproduction of neutron-rich nuclei in all current multidimensional hydrodynamic models results from overly simplified descriptions of neutrino transport, which yield unrealistic $\bar{\nu}_e$ and ν_e luminosities and mean energies. Moreover, the nucleosynthesis problems just discussed would be cured, and ^{56}Ni formation could proceed also in the neutrino heated bubbles and would not be confined to a shell exterior to this material, as we have found above! Thus, a proper treatment of the problem definitely requires multidimensional calculations which include Boltzmann neutrino transport. Once such simulations will be available, it might be possible, though, to obtain relations for the temporal evolution of the $\bar{\nu}_e$ and ν_e luminosities and spectra which could be used in much less expensive light-bulb calculations, in order to study the resulting nucleosynthesis. This would, in any case, be preferable to nucleosynthesis calculations which employ an ad hoc initiation of the explosion. We finally note, that even if Boltzmann neutrino transport solves the problems connected to the low Y_e of the ejecta, uncertainties in the neutrino opacities and the equation of state at high densities still remain, which might have a significant impact on the nucleosynthesis since the properties of the neutrino field sensitively depend on them. See Janka & Müller (1996) for a discussion of these issues.

The aspherical shock wave, imprints an asphericity onto the layers which undergo incomplete silicon and oxygen burning. Therefore aspherical shells containing the products of these burning stages form outside the nickel-enriched region, behind the outward sweeping shock (Fig. 3.19). The post-shock temperature has dropped to 2×10^9 K (i.e. below the minimum temperatures for explosive oxygen and neon burning) at $t = 600$ ms, when the shock encounters the Si/O interface. Thus only negligible amounts of oxygen and neon are burned in model T245 as well as in all other two-dimensional models.
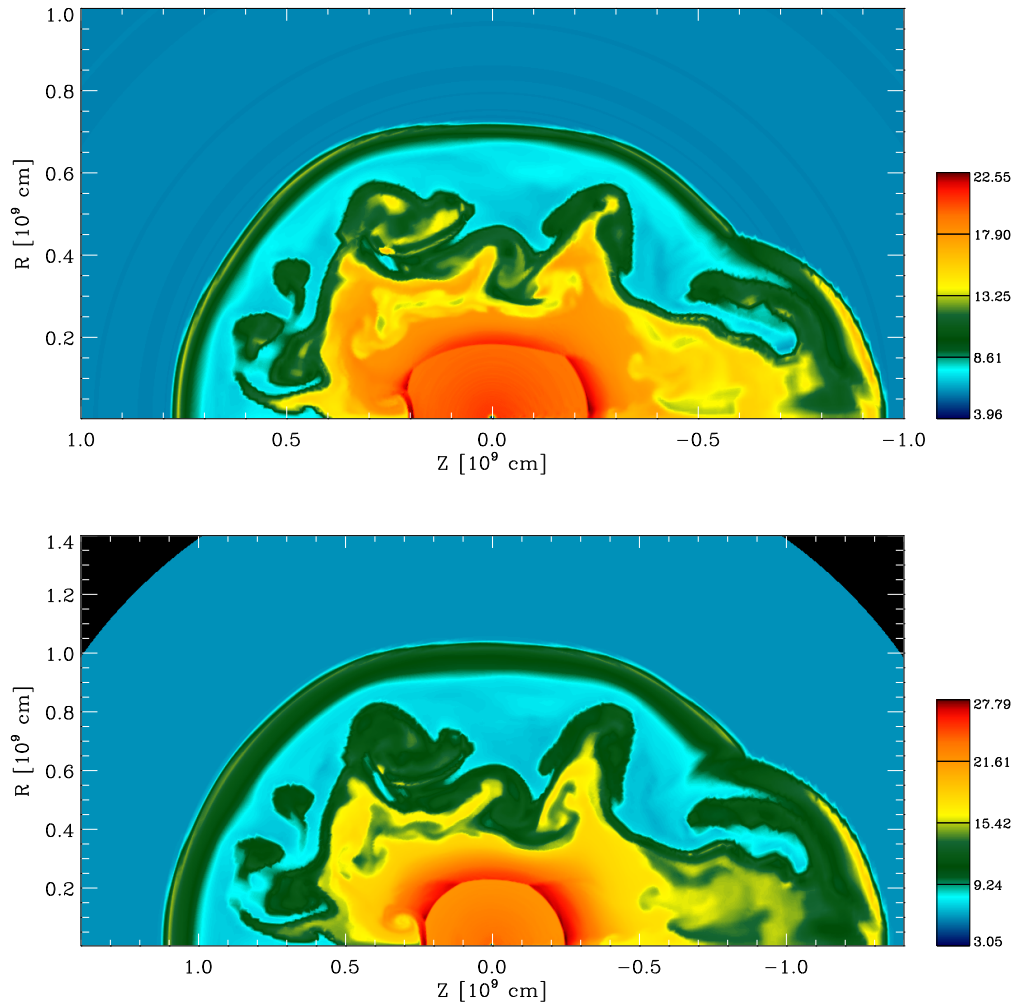
Figure 3.18: Distribution of the entropy (in k_B/nucleon) in model T245. From top to bottom: a) $t = 600$ ms. b) $t = 800$ ms.

This is caused by the specific structure of the progenitor model of Woosley et al. (1988) and the weak dependence of the radii for freezeout of the different nuclear reactions on the explosion energy (see Section 3.7).

A general feature of our models is that (weak) convective motions are still present for some time after nuclear reactions have frozen out and continue to distort the layers which contain the products of explosive nucleosynthesis. As Fig. 3.18 a shows, convection ceases only after $t \approx 600$ ms in model T245. Only then, the flow pattern becomes frozen in and the entire post-shock region expands nearly self-similarly (Fig. 3.18 b).

It is interesting to compare model T245 to its 1D analogue O245 at this evolutionary stage. As already mentioned, a major difference between these models is the explosion energy, which is twice as high in the two-dimensional calculation. This is a direct consequence of the higher efficiency of neutrino heating due to neutrino driven convection in the two-dimensional case. Consequently in model T245 the shock expands to radii of $\sim 3.5 \times 10^8$ cm and $\sim 1.2 \times 10^9$ cm after 300 ms and 800 ms, respectively (Figures 3.15 c and 3.19). This translates to a mean shock velocity of 17 000 km/s. The corresponding
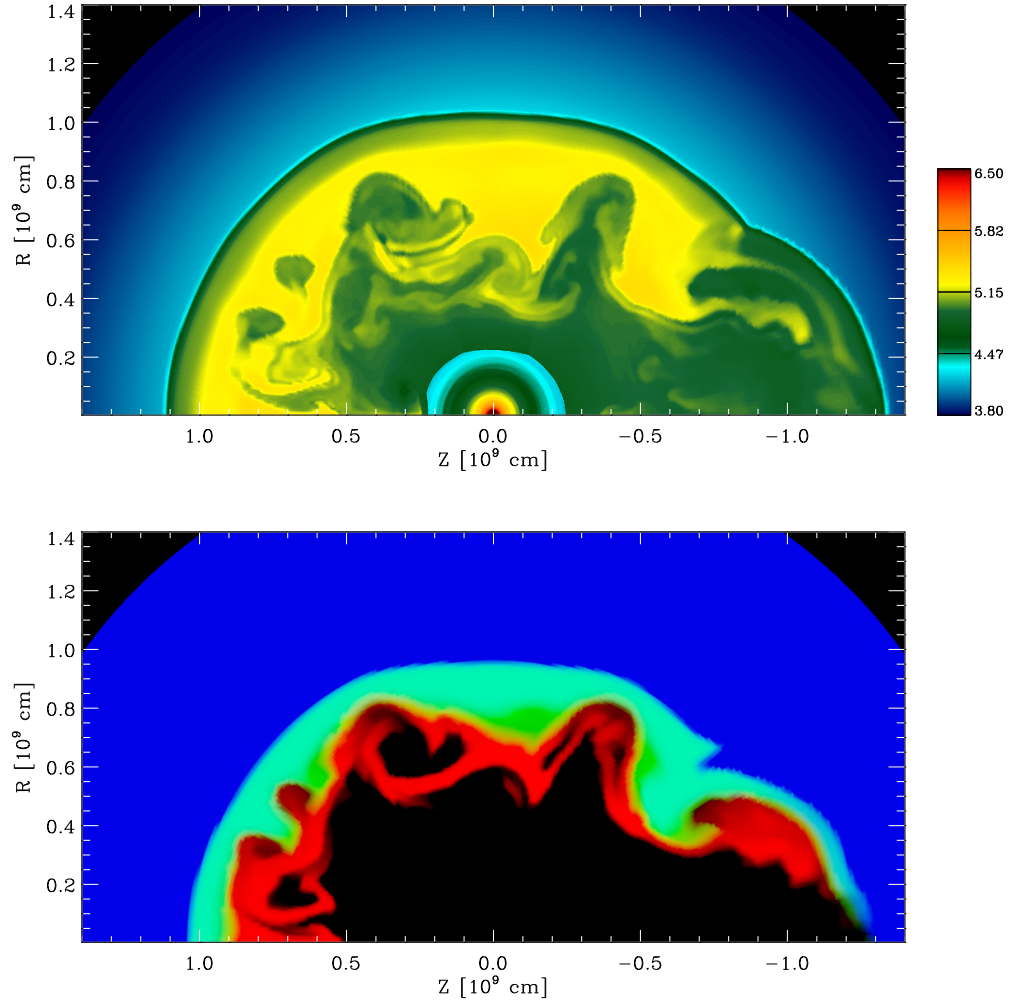
Figure 3.19: Spatial distributions of nickel, oxygen and silicon as well as the mass density in model T245 for $t = 800$ ms. From top to bottom: a) Logarithm of the density. Only regions with $\log_{10} \rho \, [\mathrm{g \, cm^{-3}}] < 6.5$ are shown. b) Logarithm of the mass fraction of ^{56}Ni (red), ^{28}Si (green) and ^{16}O (blue). Note that in this plot regions which are populated by more than one element are coded with a mixture of the colors assigned to the single nuclei. E.g. the inner edge of the region which experienced incomplete silicon burning and contains ^{28}Si as well as some ^{56}Ni appears yellow.

velocity for model O245 was only 5600 km/s. A second important difference between models T245 and O245 is the formation of a wind-driven hot bubble in model T245 which is not visible in the one-dimensional case even for times as late as $t \approx 900$ ms. In contrast, starting at $t \approx 400$ ms a fast wind is blown from the surface of the proto neutron star in the two-dimensional model. By interacting with the slower and denser convective shell, the wind has created a reverse shock in the flow at $t = 600$ ms (visible at radii of about 2×10^8 cm in Fig. 3.18 a) which is initially aspherical but looses its asphericity with time. The occurrence of a neutrino driven wind phase and the formation of the associated reverse shock are also visible in one-dimensional models but require higher neutrino luminosities (or more precisely, larger explosion energies and smaller explosion time scales) than the ones of model O245 (compare Figure 3.1 for the evolution of one-dimensional models with varying neutrino luminosities).

As we have just shown, multidimensional effects are very important in the lower part of the range of explosion energies derived for SN 1987 A and influence both the energetics and the nucleosynthesis. In what follows we will demonstrate that for models near the upper end of this range the deviations from spherical symmetry are minor. For this purpose we compare our high-energy model T310 to model T245. Figures 3.20 a and 3.20 b, respectively, show the entropy and ^{56}Ni distribution in model T310 after 300 ms. These should be compared to Figures 3.15 c and 3.17 c, which show the same quantities for model T245. Striking qualitative differences can clearly be seen between the high energy explosion T310 and the low energy model T245. The asphericities introduced by neutrino driven convection are either less pronounced or totally absent in model T310. The supernova shock is perfectly spherical and is hardly influenced by the convection beneath it. Owing to the significantly shorter explosion time scale of model T310 compared to model T245 (62 ms versus 88 ms), neutrino driven convection does not develop into a large-scale overturn and the convective elements are confined to angular sizes of around $20°$. In contrast to model T245, no balloon-like bubbles or narrow downflows can be observed in model T310 and the convective activity, never having been particularly vigorous, comes to an end already after about 250 ms. As is to be expected from the larger explosion energy, the mean shock velocity is also larger in model T310, and amounts to 19 000 km/s compared to 17 000 km/s in case of model T245. What is more important, however, is that this value is identical to the mean velocity computed for the one-dimensional model O310, again demonstrating the similarity of the overall evolution between the two-dimensional and the one-dimensional case.

^{56}Ni synthesis occurs in a contiguous shell in model T310 which is only moderately deformed by small-scale convective mushrooms at its base and does not exhibit the filamentary structure found in the low-energy model T245 (compare Fig. 3.20 to Fig. 3.17). Due to the spherical symmetry of the shock wave and the weakness of the convective flows, the distribution of nuclei which are synthesized during incomplete silicon and oxygen burning is also almost spherically symmetric.

From what has been said above it might appear that models with high explosion energies are less suited than lower-energy explosions in order to explain the large-scale mixing processes observed in SN 1987 A. We wish to emphasize, however, (and will prove this in Chapter 4) that although the multidimensional effects occuring in high-energy models seem dwarfed compared to those found in the low-energy case, already such small deviations from spherical symmetry *are crucial* for the later evolution of the supernova. With an outlook to this late evolution, we show the distribution of
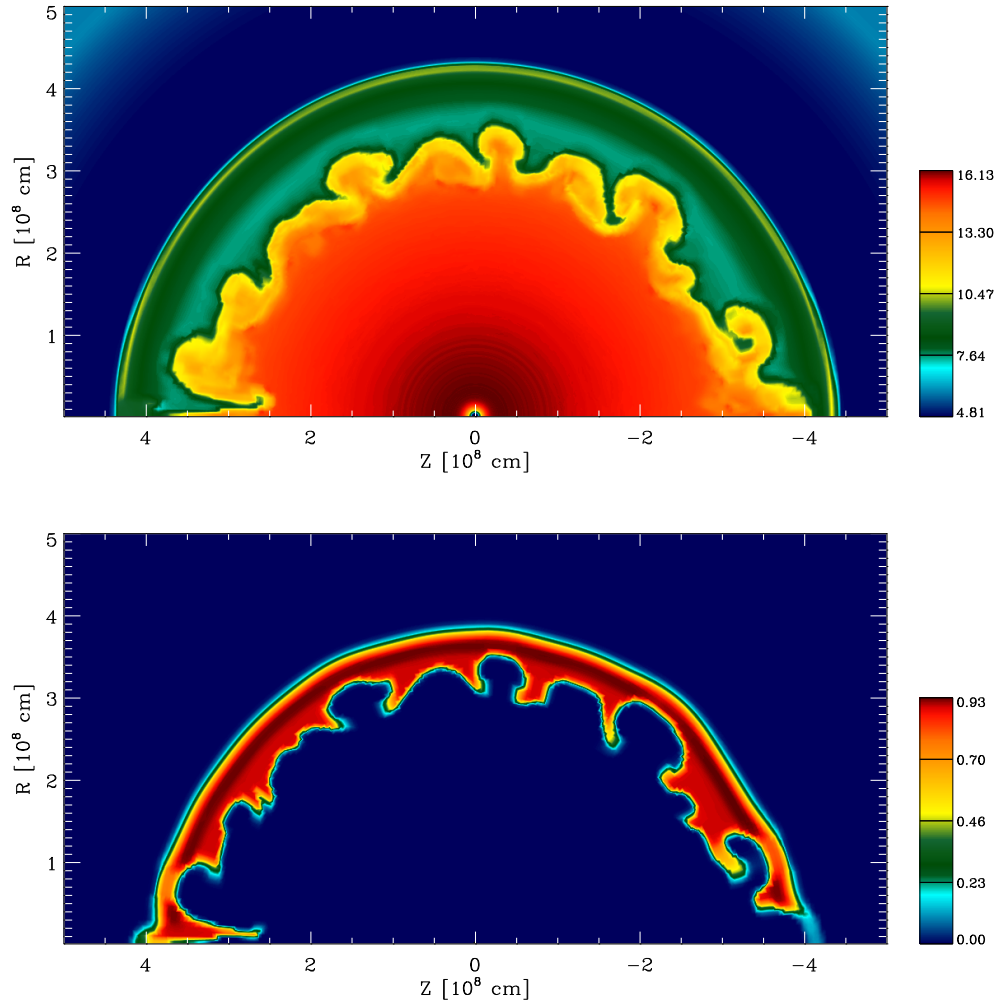
Figure 3.20: Distribution of the entropy and the mass fraction of ^{56}Ni in model T310 for $t = 300$ ms. From top to bottom: a) Entropy (in k_B/nucleon). b) ^{56}Ni mass fraction.

the logarithms of the mass density and the mass fractions of ^{56}Ni, ^{28}Si and ^{16}O in Figure 3.21, shortly before we stopped our calculations at $t = 800$ ms. At this time the shock is already propagating through the oxygen shell. One can recognize that the entire silicon shell and the layers which experienced incomplete silicon burning as well as complete silicon burning under conditions with $Y_e > 0.49$ (and therefore produced ^{56}Ni) are confined to a high-density shell which can be discerned just outside the deleptonized material in the low-density mushrooms. As in the 1D models (see Fig. 3.4), a positive pressure and a negative density gradient (the latter can be seen at the position of the Si/O interface in Figure 3.21 a) exist between this dense shell and the shock. It will turn out in Chapter 4, where we will use model T310 as initial data for our subsequent calculations, *that Rayleigh-Taylor instabilities at the Si/O interface, seeded by the perturbations due to neutrino driven convection, grow within only a few minutes after core bounce and destroy the onion shell structure of the star.*
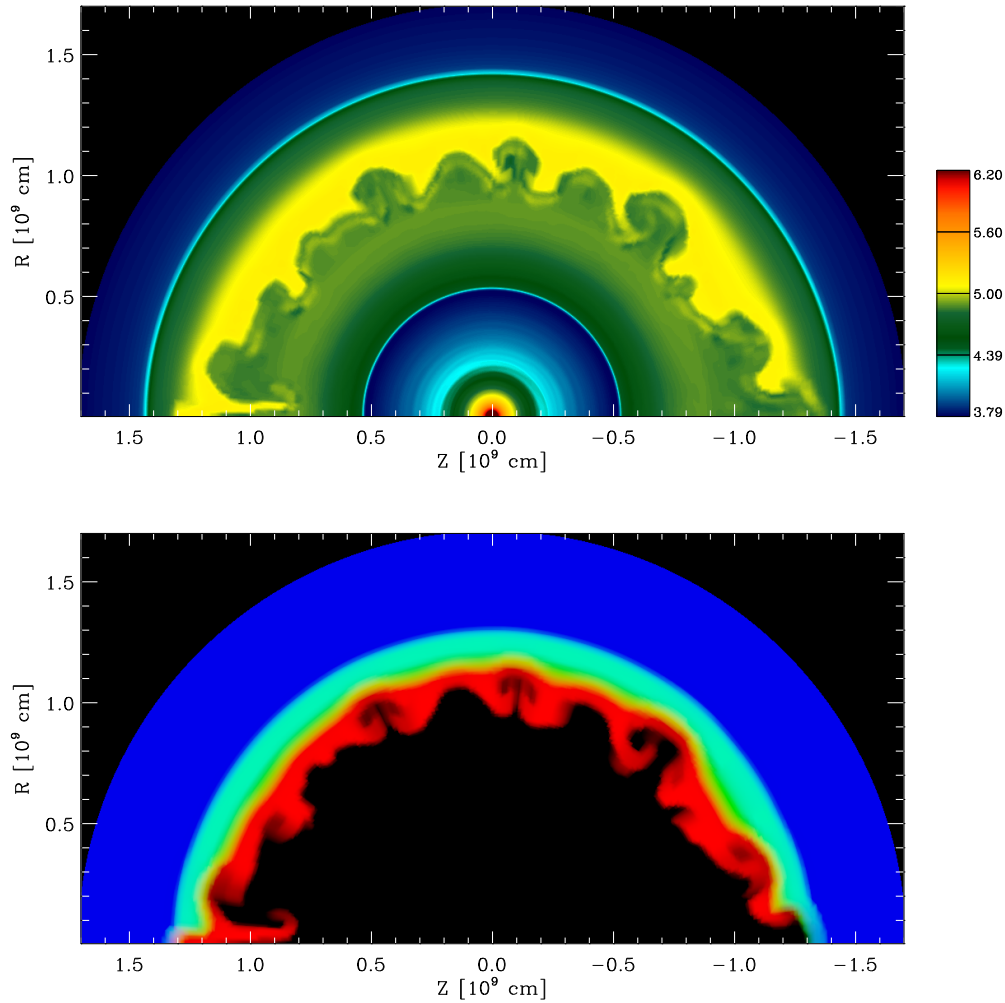
Figure 3.21: Spatial distributions of nickel, oxygen and silicon as well as the mass density in model T310 for $t = 800$ ms. From top to bottom: a) Logarithm of the density. Only regions with $\log_{10} \rho$ [g cm^{-3}] < 6.2 are shown. b) Logarithm of the mass fraction of ^{56}Ni (red), ^{28}Si (green) and ^{16}O (blue).

3.10 Yields

Since nearly all studies of explosive nucleosynthesis in core collapse supernovae that have been performed up to date have assumed spherical symmetry, and given the fact that their results are in wide-spread use for models of galactic chemical evolution, it is especially interesting to investigate deviations of the nucleosynthetic yields of our two-dimensional models as compared to the one-dimensional case.

Table 3.4 summarizes the final absolute yields (neglecting the effects of fallback) for all nuclei included in our two and one-dimensional calculations. Astonishingly, except for a few (though very important) elements the yields do *not* deviate strongly between the two and the one-dimensional case, *provided that a healthy explosion is obtained*. The largest differences are observed in case of models T245 and O245. Here the yields of nuclei with $A \leq 40$ differ by up to a factor of 2 while for nuclei with $40 < A \leq 56$ this factor is as large as 5. However, with increasing neutrino luminosities and smaller differences in the explosion energies between two and one-dimensional models the yields become insensitive to the dimensionality of the calculation and differ only at a level of $\lesssim 8\%$ for nuclei with $A \leq 40$ and $\lesssim 25\%$ for $40 < A \leq 56$. This can be readily understood in case of model T310, which showed only minor deviations from spherical symmetry (see Section 3.9). However, it is somewhat surprising in case of model T260, which shows much more pronounced anisotropies and inhomogeneities and resembles model T245 in this respect. Judging from the comparison of models O260/T260 and O310/T310, the large discrepancies found in models O245/T245 must be attributed mainly to the anemic explosion in case of O245 rather than to multidimensional effects.

As a closer inspection of Table 3.4 further shows, the α-nuclei can be divided into three groups. The first group is made up of nuclei with $4 \leq A \leq 32$ whose yields are insensitive to multidimensional effects in our calculations. Note that among these nuclei are ^{12}C, ^{16}O, ^{20}Ne and ^{24}Mg which are hardly affected by explosive nucleosynthesis in the Woosley et al. (1988) progenitor. Their yields therefore reflect the composition of the pre-supernova model. It has to be emphasized that this must not hold for other progenitors and that we therefore cannot give reliable estimates on how multidimensional effects will affect the synthesis of ^{12}C, ^{16}O, ^{20}Ne and ^{24}Mg in those cases. ^{32}S is interesting since, as it is formed by oxygen and incomplete silicon burning, the primary multidimensional effect which should influence its yield is the asphericity of the shock wave. Yet, hardly any differences can be seen in the final ^{32}S masses between one and two-dimensional models.

The products of incomplete silicon burning ^{36}Ar and ^{40}Ca make up the second group of nuclei. Their yields in models O245/T245 differ by factors of ~ 2 while in all other models their abundances are comparable between the one-dimensional and the two-dimensional case. Finally, the third group is occupied by nuclei with $A \geq 44$ whose yields depend sensitively on the explosion mechanism and thus on the dimensionality of the calculation. These are the products of the α-rich freezeout (^{44}Ti, ^{48}Cr and ^{52}Fe) as well as ^{56}Ni and the material subsumed in our neutronization tracer, which will be made up mainly of nuclei with $N = 50$ and $A \approx 90$ in case $Y_e \approx 0.46$. Since we have already commented earlier on the sensitivity of the α-rich freezeout on the entropy (which may vary strongly between one and two-dimensional models) we will now focus on the ^{56}Ni mass.

From our discussion in Sections 3.7 and 3.9 one might anticipate that with the description of the neutrino physics adopted in this work, convection will tend to reduce
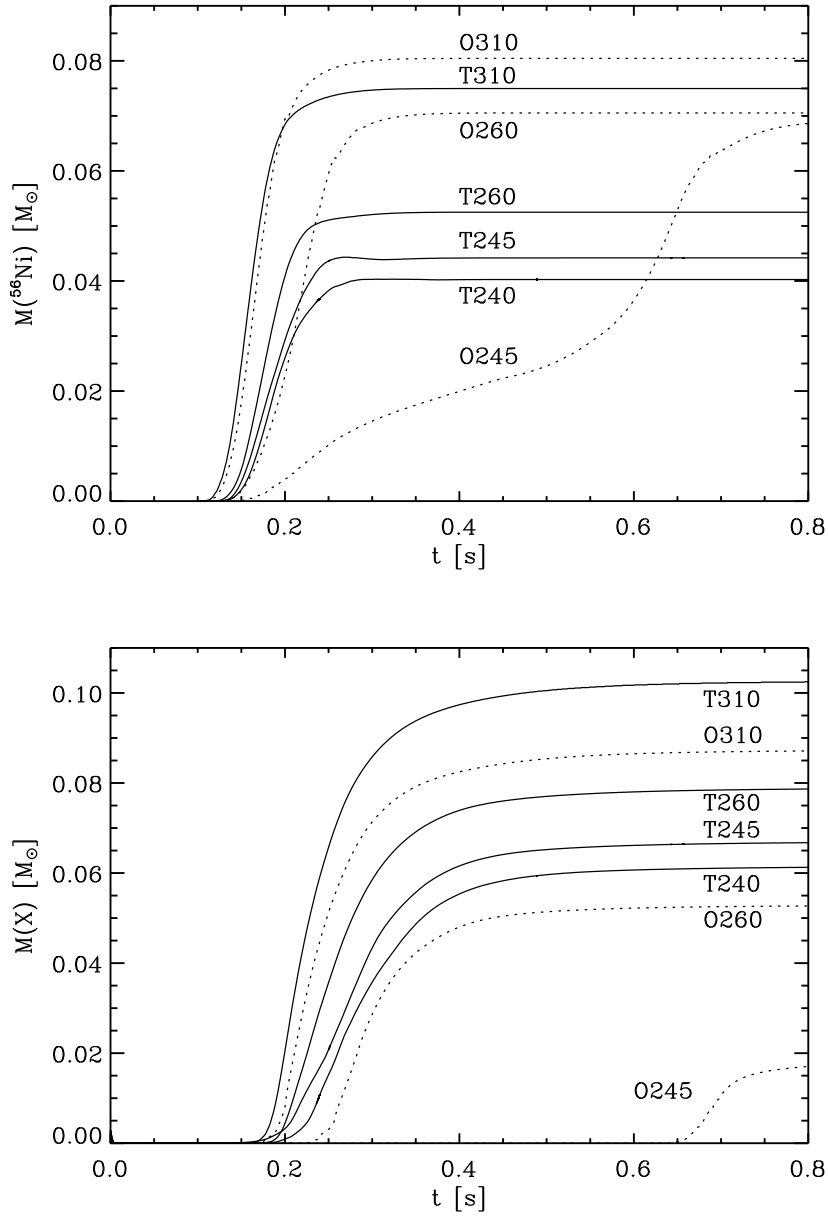
Figure 3.22: Evolution of the ^{56}Ni mass and the mass concentrated in our tracer nucleus X for the 2D models T310, T260, T245, and T240 and the corresponding one-dimensional models O310, O260 and O245 (compare also with Table 3.4). Note the anticorrelation between the yields of the two species in the 1D and 2D models. For all models, the final ^{56}Ni mass is smaller in the 2D than in the 1D case, while the reverse is true for the amount of neutronized material.

Nucleus	T240	T245	T260	T310	O245	O260	O310
^{4}He	5.4(+0)	5.4(+0)	5.4(+0)	5.3(+0)	5.4(+0)	5.4(+0)	5.3(+0)
^{12}C	1.2(-1)	1.2(-1)	1.2(-1)	1.2(-1)	1.2(-1)	1.2(-1)	1.2(-1)
^{16}O	2.0(-1)	2.0(-1)	1.9(-1)	1.9(-1)	2.0(-1)	1.9(-1)	1.9(-1)
^{20}Ne	4.7(-2)	4.7(-2)	4.6(-2)	4.5(-2)	4.9(-2)	4.6(-2)	4.5(-2)
^{24}Mg	5.1(-3)	5.1(-3)	5.3(-3)	6.1(-3)	5.2(-3)	5.2(-3)	5.9(-3)
^{28}Si	1.0(-1)	9.8(-2)	9.3(-2)	8.5(-2)	9.7(-2)	9.3(-2)	8.6(-2)
^{32}S	1.7(-2)	1.6(-2)	1.9(-2)	2.3(-2)	1.6(-2)	2.0(-2)	2.2(-2)
^{36}Ar	4.8(-3)	4.9(-3)	5.5(-3)	6.6(-3)	3.1(-3)	5.1(-3)	6.2(-3)
^{40}Ca	4.5(-3)	4.9(-3)	5.5(-3)	6.5(-3)	2.7(-3)	5.1(-3)	6.2(-3)
^{44}Ti	2.8(-3)	3.5(-3)	3.2(-3)	5.0(-3)	7.5(-4)	2.8(-3)	4.6(-3)
^{48}Cr	2.3(-3)	2.8(-3)	2.7(-3)	3.9(-3)	7.4(-4)	2.2(-3)	3.6(-3)
^{52}Fe	2.4(-3)	2.7(-3)	3.0(-3)	4.0(-3)	1.1(-3)	2.6(-3)	3.7(-3)
^{56}Ni	4.0(-2)	4.4(-2)	5.2(-2)	7.5(-2)	6.9(-2)	7.1(-2)	8.0(-2)
X	6.1(-2)	6.7(-2)	7.9(-2)	1.0(-1)	1.8(-2)	5.3(-2)	8.7(-2)

Table 3.4: Final elemental yields (in $M_{\odot}$) for the 2D models T240, T245, T260, and T310 and the one-dimensional models O245, O260 and O310. The time is $t = 800\,\mathrm{ms}$ for all models except for O245, where the abundances are given at $t = 1.6\,\mathrm{s}$ due to the later freezeout of nuclear reactions. Note that the numbers given have not been corrected for the effects of an eventual fallback onto the neutron star.

the final yield of ^{56}Ni in a two-dimensional model as compared to the one-dimensional case, by advecting post-shock material with a high electron fraction toward deeper layers where deleptonization is significant. On the other hand, strong convective activity can boost the explosion energy and thereby increase the mass which experiences complete silicon burning. The competition of both effects tends to make the ^{56}Ni yield a non-trivial function of the neutrino luminosities (and energies). Figure 3.22 indicates, however, that the effect of mixing-enhanced neutronization is dominant. The final ^{56}Ni masses in all two-dimensional models are *smaller* than in their one-dimensional counterparts. That the "missing" ^{56}Ni mass in the 2D models is indeed lost to neutronization is confirmed by the final yields of our neutronization tracer nucleus. These show the reverse trend between 2D and 1D models, i.e. the yields are larger in the 2D simulations than in their 1D analogues.

The largest deviations of the ^{56}Ni yields are found for the low energy models O245/T245 and amount to $\sim 40\%$ (with the spherically symmetric case being the reference) while in case of the high energy explosions O310/T310 the difference is about 6%. We consider these deviations to be significant. The recent one-dimensional supernova calculations with Boltzmann neutrino transport (Rampp & Janka 2000; Mezzacappa et al. 2000) either do not yield explosions or result in low-energy explosions comparable to model O245. However, we have to emphasize that with the high electron fractions $0.5 \leq Y_{e} \leq 0.6$ that are found for the neutrino heated gas in these calcula-

tions, the trends that we have found above might even be reversed. The ^{56}Ni yields in 2D calculations might thus end up being *larger* than in the spherically symmetric case, especially for progenitor models with very low Y_e values in the silicon shell (e.g. Nomoto & Hashimoto 1988). However, detailed explosive nucleosynthesis calculations for conditions with $0.5 \leq Y_e \leq 0.6$ remain to be carried out and therefore neither the absolute ^{56}Ni yields nor the deviations between 2D and 1D models can currently be regarded to be very reliable. Thus our considerations should only be taken as an illustration of what might happen if two-dimensional effects are neglected.

Finally, it is interesting to note in Figure 3.22 that, regardless of the dimensionality of the calculations, the yields of ^{56}Ni as well as our neutronization tracer grow with increasing neutrino luminosities due to the growth of the mass of the gas which is heated by the shock to temperatures $> 5 \times 10^9$ K.

3.11   "Odd-even decoupling" and the role of numerical noise

Quirk (1994) (see also Quirk 1997 for a reprint of this work) has reported on a subtle flaw in a number of Riemann-solvers (these are at the heart of Godunov-type hydrodynamics schemes as PPM) which becomes evident when calculating multidimensional flows with strong, grid-aligned shocks. He has dubbed this failure, which he considers to be "the [by far] most insidious failing that we have come across", the "odd-even decoupling" phenomenon.

The problem shows up only if a sufficiently strong shock is either fully or nearly aligned with one of the coordinate directions of the grid, and if, in addition, the post-shock flow is slightly perturbed. This can be due to either perturbations intentionally introduced in order to study *physical* instabilities, as in the present work, or due to perturbations caused by other flow features or simply by rounding errors. Many Riemann solvers, especially the less diffusive ones, show the tendency to allow these perturbations to grow without limit along the direction of shock alignment. Thus a numerical instability is triggered which manifests itself in a strong rippling of the shock as well as the post shock state. The density, pressure, and velocity profiles along such a shock exhibit variations between odd and even numbered zones akin to a sawtooth-profile (thus the term "odd-even decoupling"). Quirk (1994) shows that for calculations of a planar shock propagating down a duct, the perturbations become indeed so strong that the shock is finally completely disrupted if the approximate Riemann solver of Roe (1986) is used.

Though we do not see effects of this magnitude in two-dimensional supernova simulations that we have conducted using the exact Riemann solver implemented in HERAKLES and PROMETHEUS, the numerical instability clearly showed up in two of our explosion models (i.e. models T280* and T310*) and had adverse effects on their results. In order to demonstrate that the failure is indeed introduced during the solution of the hydrodynamic equations, we show results of a test calculation in Fig. 3.23 which employed spherical coordinates and a resolution of 400 radial and 180 angular zones. For this test, the gravity, neutrino source term and nuclear burning modules of the code were all switched off. We therefore relied solely on the pressure gradient to initiate an explosion in the post-bounce model of Bruenn (1993). The calculation was further divided into two steps. Without adding any seed perturbations, the evolution
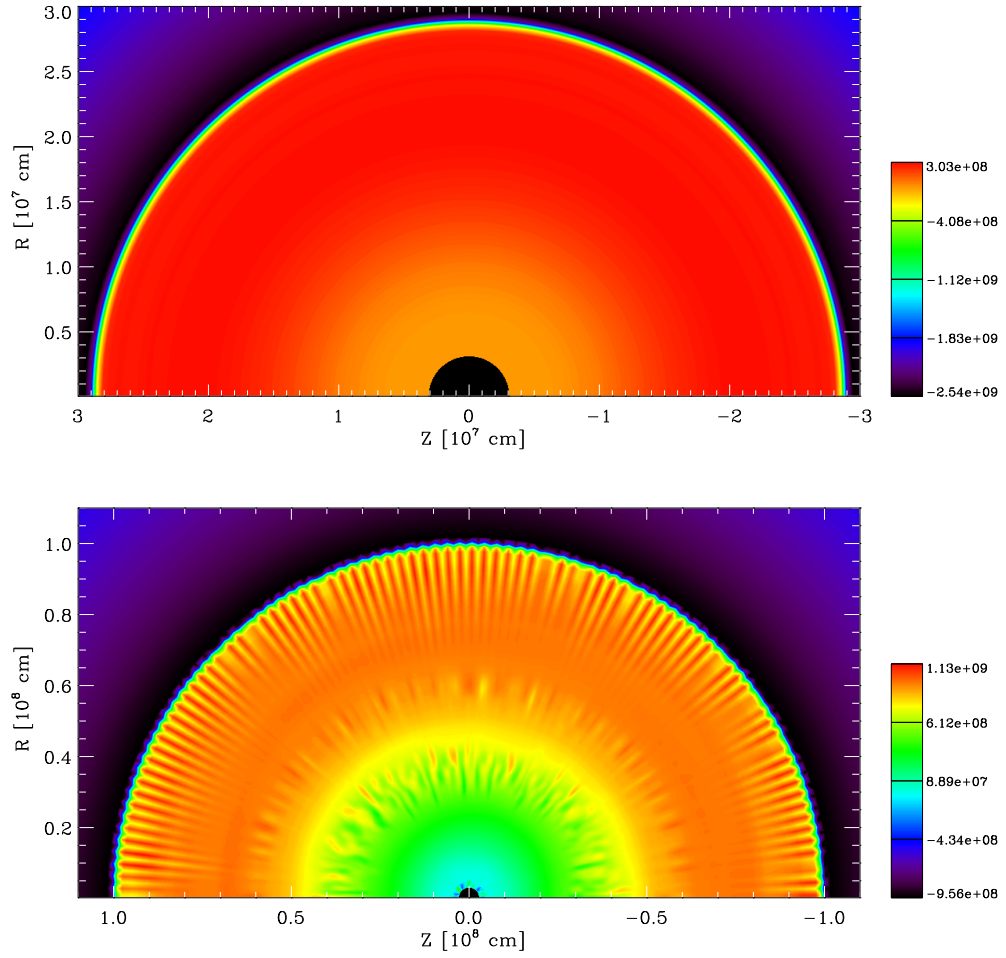
Figure 3.23: Odd-even decoupling in the test calculation (see text). Note that while (R, Z) coordinates of the cylindrical grid which was used for plotting are indicated in the Figure, the calculations have been performed in spherical coordinates. From top to bottom: a) Radial velocity (in cm/s) of the unperturbed model, at $t = 30\,\mathrm{ms}$. b) Radial velocity at $t = 108\,\mathrm{ms}$, after seed perturbations have been added to the model shown in a).

was initially followed in two dimensions up to a time of 30 ms, when the resulting shock wave had propagated out to a radius of $2.9 \times 10^7\,\mathrm{cm}$. The radial velocity at $t = 30\,\mathrm{ms}$ is shown in Fig. 3.23 a. It has to be emphasized that up to this time (which took more than 3600 time steps to compute) the code had maintained perfect spherical symmetry of the computed solution, i.e. the lateral velocity, v_θ, remained exactly zero on the entire grid. Subsequently, perturbations to the velocity field with a modulus of 10^{-3} of the radial velocity were added to the post-shock region and the calculations were continued. Figure 3.23 b shows the results for $t = 108\,\mathrm{ms}$. A regular pattern of radial streaks is visible behind the shock which reaches down to the two convectively unstable layers visible for radii around $6 \times 10^7\,\mathrm{cm}$ and $4 \times 10^7\,\mathrm{cm}$ and adds strong perturbations to the radial velocity. Figure 3.24, which depicts (part of) a meridional slice at a radius of $9.7 \times 10^7\,\mathrm{cm}$ for the radial velocity field shown in Fig. 3.23 b, demonstrates that the amplitude of these perturbations is about 20%, clearly a large effect.
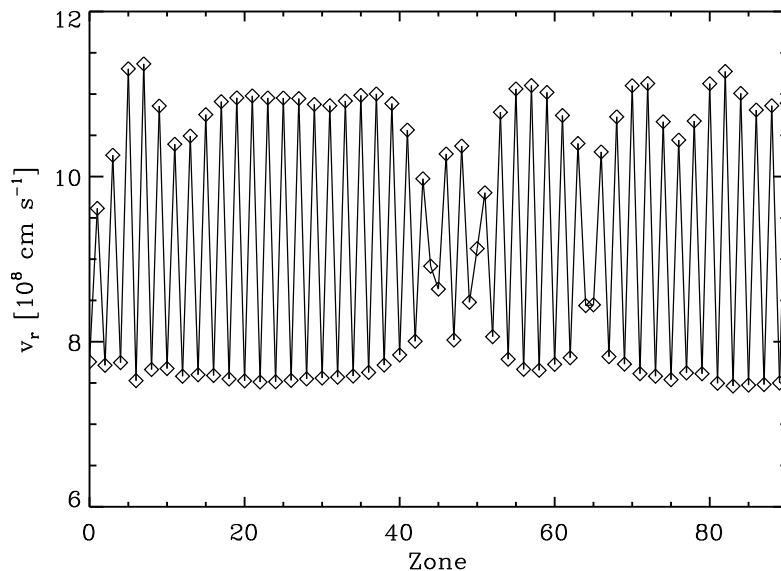
Figure 3.24: Meridional slice of the radial velocity field shown in Fig. 3.23 b, for a radius $r = 9.7 \times 10^7$ cm and angles $0 \leq \theta \leq \pi/2$. The abscissa is labeled with the (angular) zone number in order to show that the wavelength of the perturbation is two zones wide.

According to Quirk (1994), odd-even decoupling "has gone largely unnoticed [in the numerical hydrodynamics literature] simply because it is only exposed by very high-resolution simulations". While the simulation presented in Fig. 3.23 b, which clearly shows the failure, is not exactly a "high-resolution" one, the "ripples" become much stronger if the resolution is significantly increased. In low-resolution calculations, though present, they are often simply overlooked because the amplitude of the perturbations is smaller and the variations occur over a larger fraction of the computational domain. Thus the problem is not as conspicuous as in the high-resolution case. Although this failure should be very common to computations performed with Godunov-type schemes, to our knowledge the only author who has reported on it in the context of astrophysical calculations is Walder (1993).

The numerical instability is not observed for shocks which propagate with some inclination angle relative to the grid. However, if the shock is curved and locally tangent to one of the grid lines it will show a protrusion, which is known in the literature as the "carbuncle" phenomenon (see Quirk 1994; LeVeque 1998, and the references therein). This behavior makes it even more difficult to note the problem in "production calculations" and to disclose its deeper nature. It is therefore not surprising that a significant number of published multidimensional supernova models, which were obtained with computer codes that are based on the PPM and other Godunov-type schemes, are affected by this numerical flaw. Among these are, for instance, calculations of the Rayleigh-Taylor instability. In simulations of Müller et al. (1991a) which made use of a spherical grid, odd-even decoupling along the entire extent of the shock wave seems to have occurred. Similar effects have marred one of our adaptive mesh refinement simulations, which is discussed in Kifonidis et al. (2000) as well as Chapter 4. In calculations employing cylindrical grids, a spherical shock is aligned with the coordinate lines only

near the symmetry axis and in the direction perpendicular to it. Thus, in this case, the problem is less severe and limited to an appearance of the carbuncle phenomenon. Yet, this can be clearly seen in the calculations of Hachisu et al. (1992) (their Figure 2 d), Hachisu et al. (1994) (e.g. their Figure 1) and Iwamoto et al. (1997) (their Figures 5 a and 5 b) who have all used a Roe-type scheme, as well as in data of Müller et al. (1991a), which we have consulted for comparison. The carbuncle phenomenon is also present in multidimensional models of the explosion itself which were computed by Burrows & Fryxell (1993) (along the diagonals in their Figure 1b), Burrows et al. (1995) (their Figures 22 and 24) and Janka & Müller (1996) (see the radial velocity plot in their Figure 20) and were all obtained with the direct Eulerian version of PPM. It appears to affect also calculations of Mezzacappa et al. (1998b) who used a code that is based on the Lagrangian with a remap formulation of the PPM scheme.

To demonstrate the impact of odd-even decoupling on the results, we show in Figure 3.25 the evolution of the ^{56}Ni yield and explosion energy in models T310* and T280*. The relevant quantities of model T310, which did not show the numerical instability, are also depicted for comparison. The only differences of model T310 as compared to T310* were the slightly higher angular resolution (192 compared to 180 zones) and the use of the multidimensional artificial viscosity which is discussed in Appendix B and which cured the failure. As one can note, the ^{56}Ni mass in model T310* is 4.8×10^{-2} M$_\odot$ which is $\sim 36\%$ smaller than in T310. This can be understood from Figure 3.26 which shows that owing to the strong noise in model T310* the mixing is much more efficient than in T310. More material with high electron fractions is thereby exposed to the neutrino fluxes, deleptonized, and therefore lost for ^{56}Ni synthesis. Figure 3.25 shows that due to the latter effect, not even the correct trend of the dependence of the ^{56}Ni yield on the neutrino luminosities can be recovered! Model T280*, which according to the relation found in Section 3.10 should produce *less* ^{56}Ni than T310* because of its lower luminosities, actually shows a final ^{56}Ni mass which is *higher* than the one of model T310* by 10%.

The situation might be even more problematic than the different ^{56}Ni yields suggest. The strong perturbations introduced by odd-even decoupling may potentially enhance neutrino driven convection to such an extent, that owing to a more efficient convective energy transport, even the qualitative outcome of a simulation (explosion/non-explosion) may be altered. That the explosion energies are indeed increased by this effect can be seen in Fig. 3.25 for models T310 and T310*. In this high energy case, the difference in explosion energies is about 5%. Since we have not computed a flawed low-energy model, we cannot give estimates to which extent odd-even decoupling may affect shock revival in low-energy explosions. The present calculations already illustrate, however, that

i) great care is needed when applying Godunov-type schemes to the modeling of convective instabilities and explosive nucleosynthesis in core collapse supernovae

ii) the level of numerical noise in *any* numerical scheme applied to these problems must be extraordinarily low in order to obtain reliable results.

The dependence of the size of the convective blobs on the amplitude of numerical noise, that can be seen in Figure 3.26, may also explain why groups employing SPH hydrodynamics find very large scale flows and very efficient convective energy transport (and therefore "robust explosions") in their multidimensional simulations, while other groups do not. The Monte-Carlo nature of SPH leads to a rather high intrinsic level
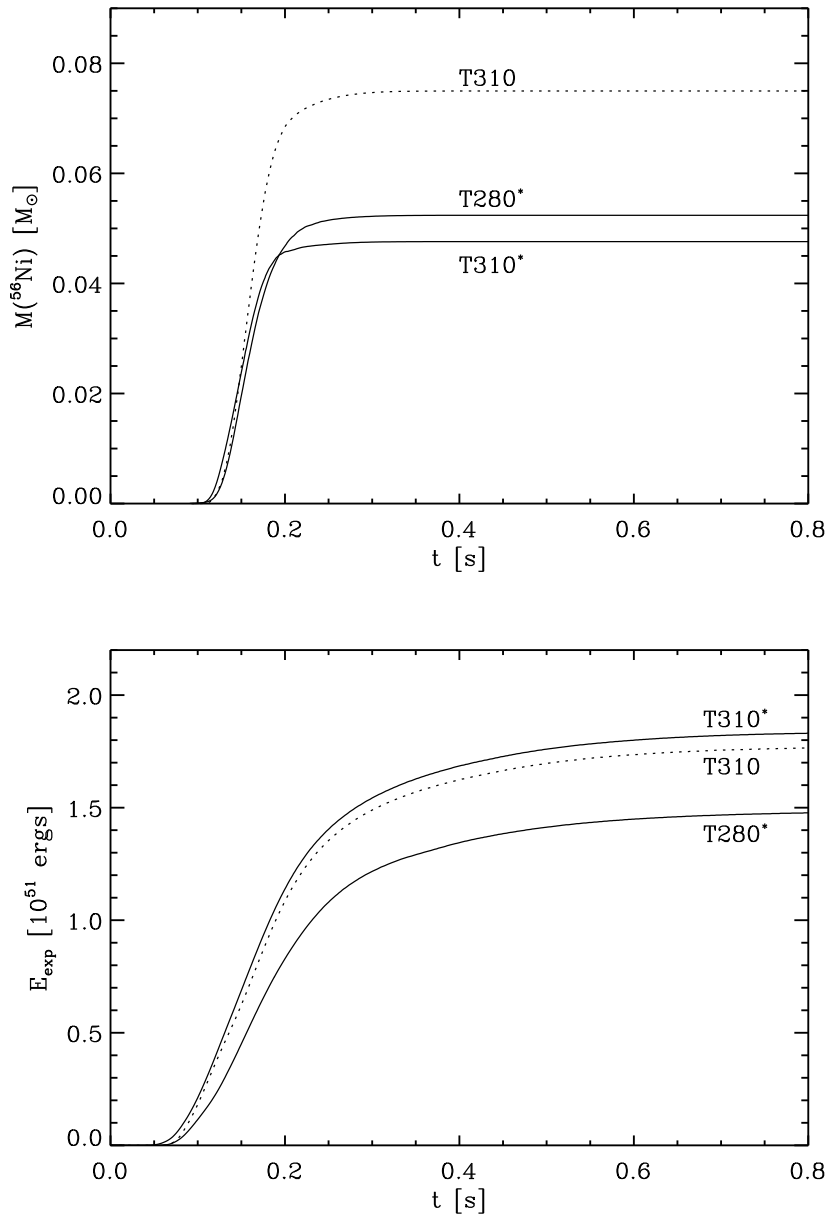
Figure 3.25: Evolution of the ^{56}Ni yields (top) and explosion energies for 2D models T310* and T280*, which suffered from odd-even decoupling, compared to model T310.
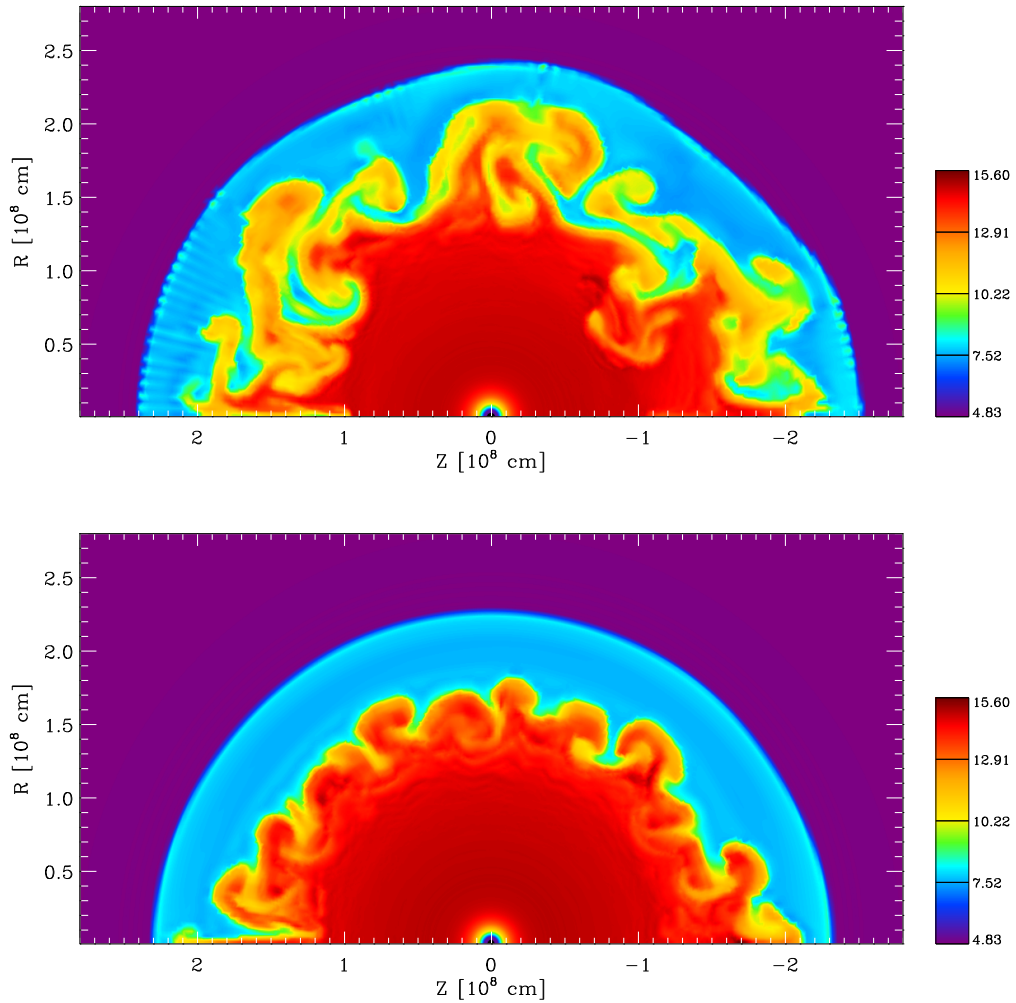
Figure 3.26: Entropy distribution (in k_B/nucleon) at $t = 188$ ms in models T310* (top) and T310 (bottom). Note the different sizes of the convective bubbles and the deformation of the shock in T310*.

of noise of this method. This has also been recognized by Shimizu (1995) who has criticized the calculations of Herant et al. (1994) in this respect.

Finally, our results also indicate that a strong dependence of the wavelength of the convective modes on the amplitude of the initial seed perturbation exists. We have proven this in a parameter study, where we have varied the amplitude of the initial seed perturbation for model T310. In these calculations only the velocity field behind the shock was perturbed. As the amplitude of the seed perturbation was increased from values of 0.1% to 10% of the local sound speed, the angular size of the convective blobs in model T310 grew from about $10°$ for the former, to $30° - 40°$ for the latter value at $t = 120$ ms. The corresponding mean shock radii were 1150 km and 1250 km, the latter being larger due to the stronger deformations that the larger blobs incurred on the shock. Though this result *qualitatively* agrees with earlier observations of Miller et al. (1993), we do not see the large *quantitative* effects of the amplitude of the seed perturbation on shock expansion which were found in the latter work. It is likely that this is due to the different treatment of the neutrino physics in both approaches.

3.12   Velocity distributions of the elements

Of crucial importance for an understanding of the evolution of the supernova beyond the first second is the distribution of the elements in velocity space. Ultimately, this information should be compared to observations after the modeling has been carried to an evolutionary age consistent with the epoch for which spectroscopic data has been obtained.

In Figure 3.27 we show for model T310 as a function of the radial velocity v_r and time, the fraction of the total mass of ^{16}O, ^{28}Si, ^{44}Ti and ^{56}Ni which is contained within the velocity interval $[v_r, v_r + \mathrm{d}v_r]$ of width $\mathrm{d}v_r = 350\,\mathrm{km\,s^{-1}}$. Figure 3.28 depicts the same quantities for model T280*. Since our adaptive mesh refinement calculations (cf. Chapter 4) make use of these two models as initial data and because the information contained in these plots results from a convolution of many effects, we will exemplarily discuss Figure 3.27 in some detail.

At $t = 100\,\mathrm{ms}$, as the shock beats its way through the outermost layers of the iron core, substantial amounts of material from the silicon and oxygen shells are either still at rest or falling towards the shock. This causes the peak and the wings of the mass distribution for theses elements at vanishing and negative velocities. As the post-shock temperatures are beginning to drop to values which allow for the formation of iron-group elements, reassembly of the α-particles starts in the immediate post-shock region and leads to initially small abundances of ^{44}Ti and ^{56}Ni, the bulk of which can be seen for velocities around 8×10^3 km/s. Since the shock has a finite width of about two zones, there is also a second weaker component of these elements visible at $v_r \approx 0$.

Only 100 ms later ($t = 200\,\mathrm{ms}$) as the explosion gains momentum and the shock propagates through the silicon shell it encounters substantially smaller infall velocities. This leads to a cutoff of the high velocity wings of silicon and oxygen at $v_r \approx -3 \times 10^3$ km/s. Furthermore, at this time nickel synthesis is about to freeze out immediately behind the shock while in somewhat deeper layers silicon burning has not yet been completed and thus a small abundance of ^{44}Ti has built up. The neighborhood of both nuclei is reflected in their distribution in velocity space which shows that their masses both peak around 1.35×10^4 km/s. However, in contrast to ^{56}Ni, some ^{44}Ti has also formed in the rising convective blobs which at this stage show the highest velocities on the grid (Fig. 3.29). This causes the broad wing in the velocity distribution of ^{44}Ti which chops off only at 1.7×10^4 km/s while maximum ^{56}Ni velocities of about 1.55×10^4 km/s are observed.

At an age of 400 ms the supernova's explosion energy is still increasing and has led to maximum ^{56}Ni velocities as high as 1.65×10^4 km/s while substantial amounts of silicon have also been accelerated. A stratification of these elements is beginning to emerge in velocity space because the positive velocity gradient behind the shock (see Fig. 3.3) results in higher velocities of material which is located immediately behind the shock as compared to gas in the deeper layers of the ejecta. Meanwhile, the neutrino driven wind has also formed and attained velocities in excess of 2.0×10^4 km/s. Traces of ^{44}Ti in this material, which is dominated by α-particles and neutron-rich nuclei, can be seen at these velocities.

The distribution of ^{44}Ti in velocity space is somewhat uncertain. As we have stressed earlier, with the spatial resolution used in the two-dimensional models, the bulk of ^{44}Ti is synthesized between 400 ms and 700 ms at the ^{4}He/^{40}Ca interface at $M_r = 1.35\,\mathrm{M_\odot}$ between the regions of α-rich freezeout and incomplete silicon burning (Figs. 3.10 and
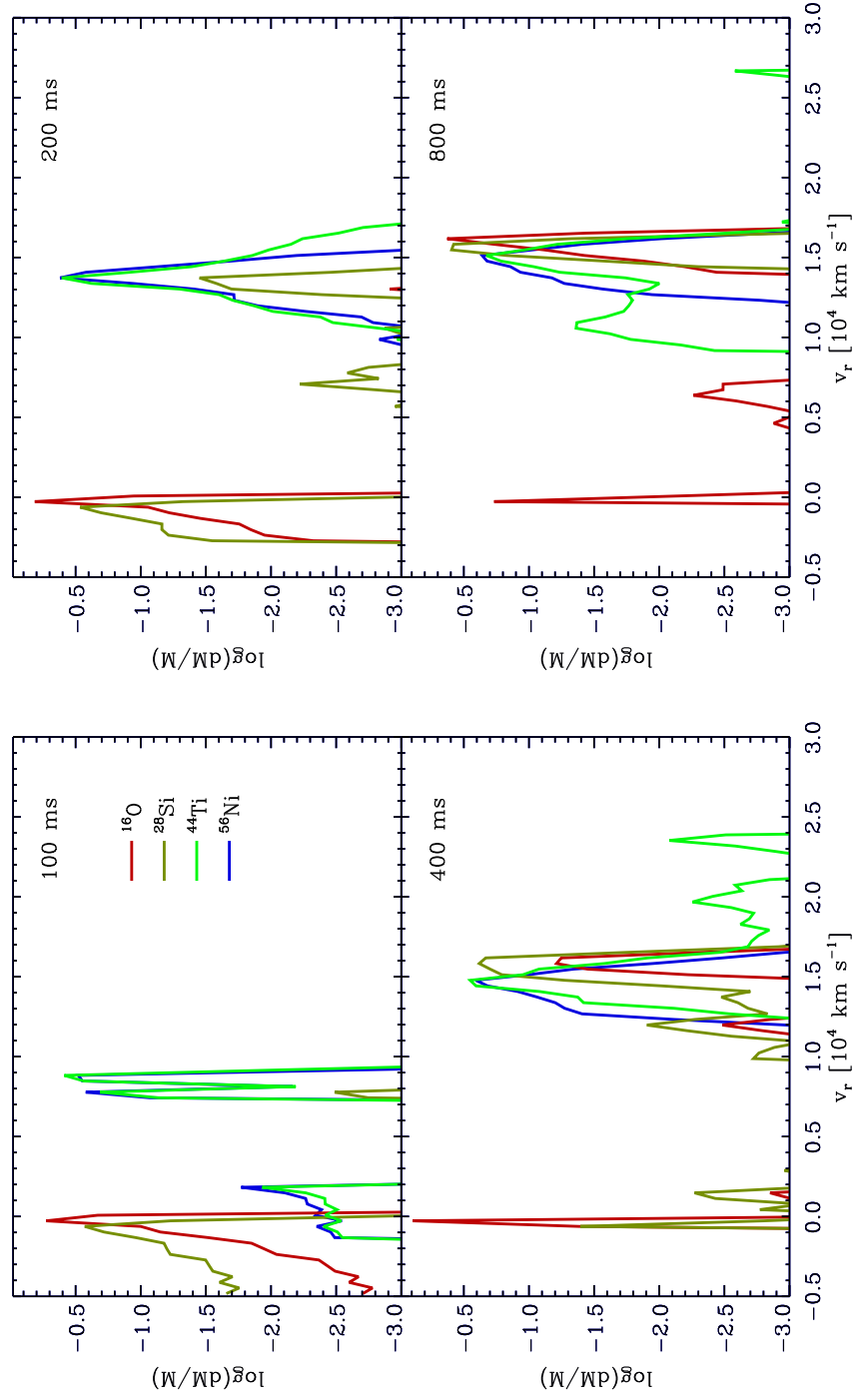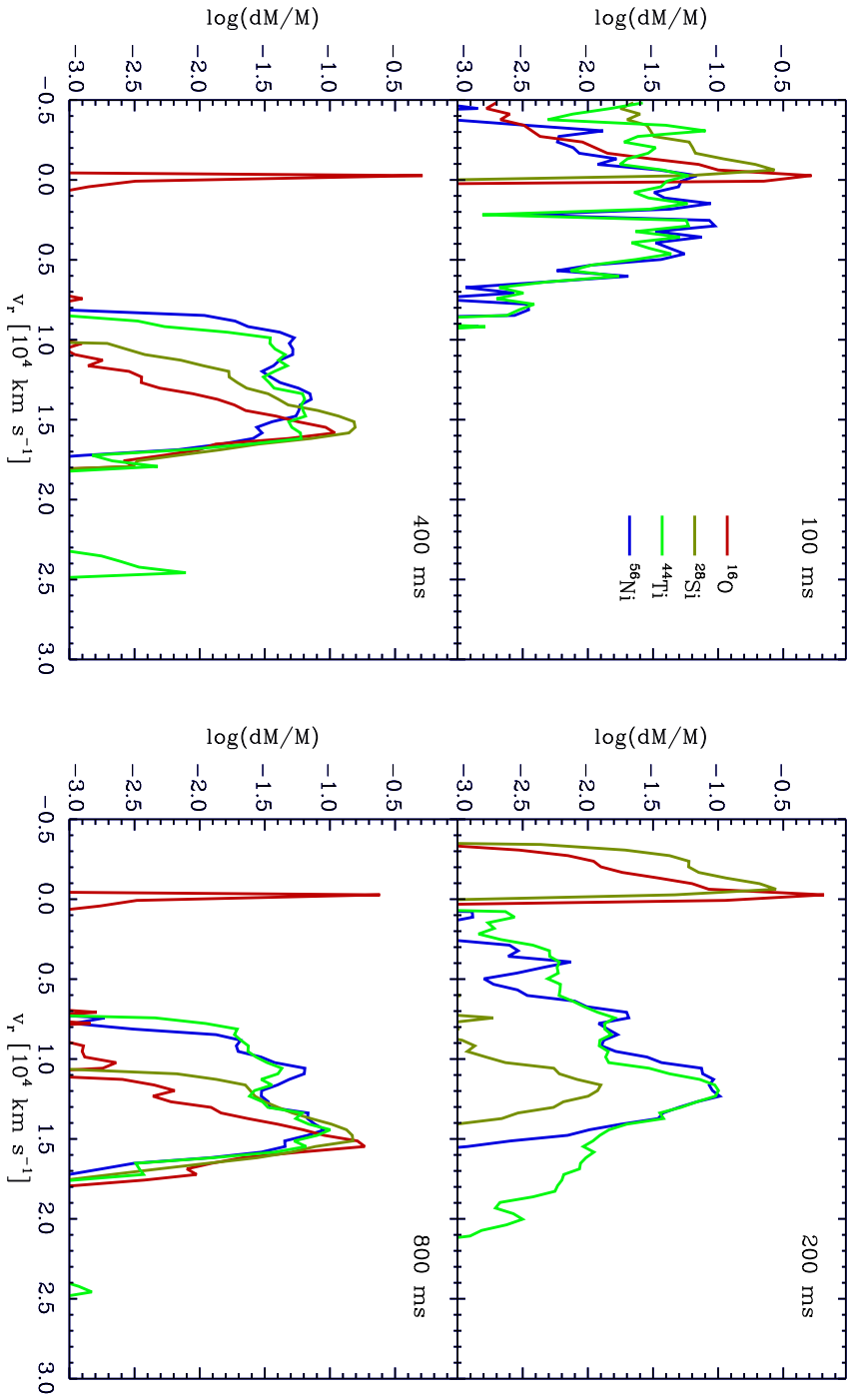
Figure 3.27: Fractional element mass contained within the velocity interval $[v_r, v_r + dv_r]$ as a function of the radial velocity v_r in model T310. The resolution is $dv_r = 350 \, \mathrm{km \, s^{-1}}$.
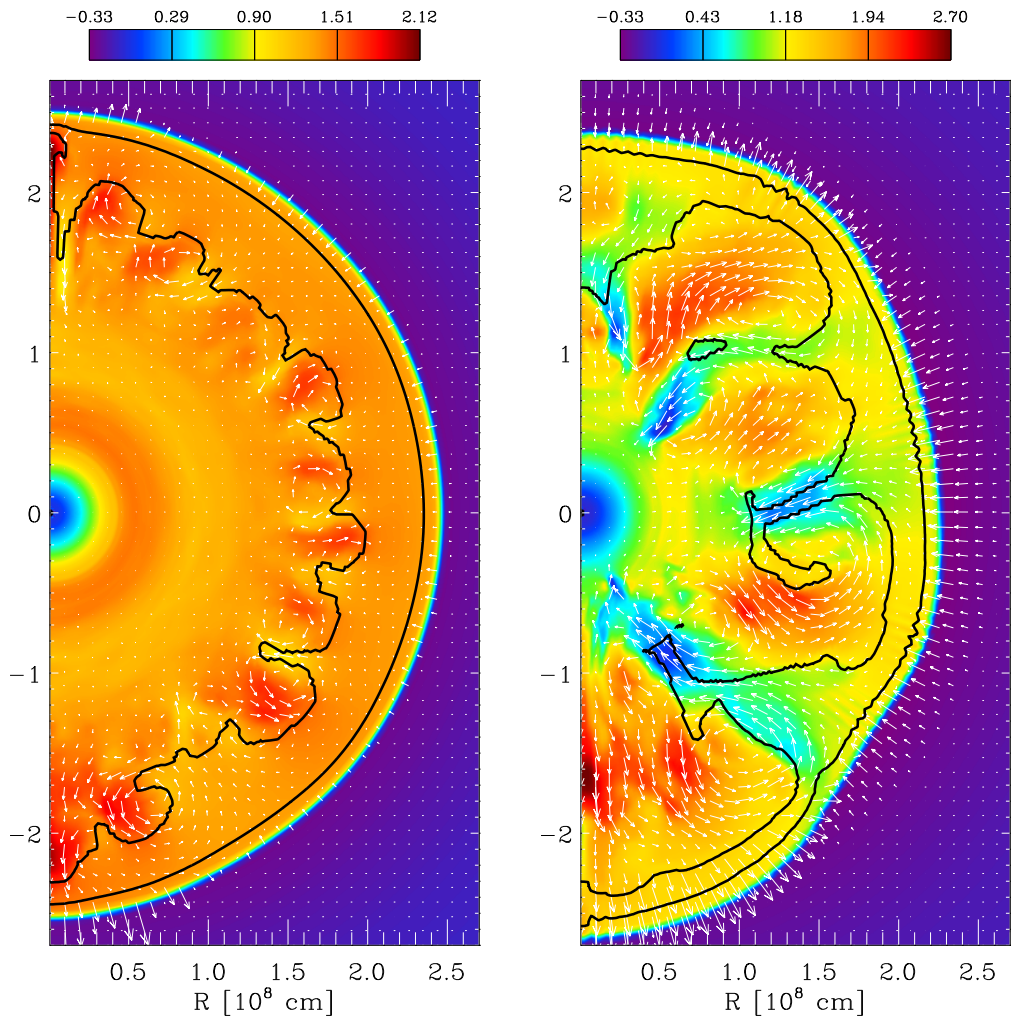
Figure 3.28: Fractional element mass contained within the velocity interval $[v_r, v_r + dv_r]$ as a function of the radial velocity v_r in model T280*. The resolution is $dv_r = 350\,\mathrm{km\,s^{-1}}$.

Figure 3.29: Radial velocity in units of 10^4 km/s in models T310 (left) and T280* (right). Overlaid are the 20% contour line of the ^{56}Ni mass fraction and the flow pattern, where the arrows show the difference of the velocity and the average radial velocity at each radius in units of 1000 km/s. The time is $t = 200$ ms.

3.11). The location of this interface coincides also with the maximum of the ^{56}Ni abundance (Figs. 3.7 and 3.8). Thus the peaks of both elements are found at comparable velocities of about 1.4×10^4 km/s in Fig. 3.27. We emphasize again, however, that the spatial distribution and the yield of ^{44}Ti are severely affected by numerical diffusion and that therefore the location of its peak for $t = 400$ ms in Fig. 3.27 is likely to be erroneous. It might actually occur at much lower velocities if ^{44}Ti synthesis due to numerical diffusion at the ^{4}He/^{40}Ca interface could be substantially reduced, since the contribution of the slower, deeper layers of the ejecta, which are close to the reverse shock, would then dominate. Indeed this material causes the second ^{44}Ti peak at 1.0×10^4 km/s in the plot for $t = 800$ ms.

The velocities of the fastest layers which contain ^{56}Ni, reach a maximum of 1.7×10^4 km/s around $t = 600$ ms and decrease slightly to 1.65×10^4 km/s at $t = 800$ ms. It is obvious, that these ^{56}Ni velocities are much larger than the ones observed in SN 1987 A and that some slow-down of this material must be expected to take place as

the nickel makes its way out of the stellar core. In fact, we will show in Chapter 4 that in contrast to all previous studies, which tried to explain the observations of SN 1987 A by *accelerating* the nickel to high velocities in making use of the Rayleigh-Taylor instabilities in the envelope, the main problem is to *avoid decelerating* this material during the subsequent evolution.

We close with some comments on the differences in the velocity distributions between models T280* and T310. The evolution proceeds qualitatively similar in both models, though the spread in velocities is much wider in model T280* than in T310, as a direct consequence of the more vigorous convection. For instance at $t = 200\,\mathrm{ms}$ the smallest radial expansion velocities of ^{56}Ni in model T280* are as low as $1000\,\mathrm{km/s}$ (Fig. 3.28), which is an order of magnitude smaller than in model T310 (Fig. 3.27). This can be explained by comparing the velocity plots in Fig. 3.29, which for model T280* show that some of the regions which contain ^{56}Ni and are colored in blue, expand much slower than with the average radial velocity. This effect is much weaker in model T310. In contrast to ^{56}Ni, the maximum ^{44}Ti velocities are by about 25% larger in model T280* as compared to T310, due to the higher velocities of the rising convective bubbles (dark red regions in Fig. 3.29). Similar effects can be seen for times of 400 and $800\,\mathrm{ms}$ in the velocity distributions in Figs. 3.27 and 3.28. Interestingly, the final ^{56}Ni velocities of $17\,000\,\mathrm{km/s}$ at $800\,\mathrm{ms}$ are somewhat higher than in T310 despite the smaller explosion energy of model T280*.

Chapter 4

The "outer problem": Shock propagation and Rayleigh-Taylor mixing

With the successful launch of the shock and the absence of physical processes which could transport the explosion energy to the stellar surface on a time-scale which is comparable to the shock propagation time through the star, the "outer problem" is governed solely by "simple hydrodynamics" and gravity. Yet, even though complex additional physics, as in case of the evolution during the first second, is not involved, the computations which are discussed in this chapter posed the greatest challenge for the studies presented in this thesis. The formidable range of spatial and temporal scales which had to be resolved in order to follow the interaction of the early convection with the later Rayleigh-Taylor instability resulted in a huge computational workload and required the use of a sophisticated and rather complex adaptive mesh refinement (AMR) hydrodynamics code. Even so, a *resolved* one-dimensional simulation of shock propagation from the first second until the first hours of the explosion still requires a few weeks of CPU time on a fast workstation-class machine. In two dimensions, about 1500 hours (i.e. 2 months) of computation on 16 processors of a dedicated CRAY J916 were required per simulation (compare this to the few hundred hours per simulation that were necessary for the calculations of Chapter 3; the sustained code performance was ~ 600 MFlops in both cases). This amount of computer time would have to be multiplied by a factor of about 5 if no effort had been undertaken to develop a code which is based on the AMR algorithm, and by an additional factor of 15 if this code would not have been parallelized to take full advantage of the architecture of this machine. In other words, the simulations would have been unfeasible, at least on the computer which was finally used. As a consequence of this computational load, we have been able to compute only two evolutionary sequences to date, so that conclusive studies with different progenitor and/or explosion models still remain to be carried out. Although we will concentrate the following discussion on features of the evolution which we presently consider to be insensitive to these issues, the reader is cautioned to regard the picture, which will be laid out in the following sections of this chapter, as being generic. We will try to point out the uncertainties, however, and to assess the differences between Type II and Type Ib explosions, for which our current Type II models can only give some indications.

4.1   The initial model

Since the adaptive mesh refinement calculations in this chapter are a continuation of
our shock revival models, we have made use of the same progenitor star as in Chapter 3
in order to follow the further propagation of the shock up to the stellar photosphere.
Unfortunately, however, the post-collapse model of Bruenn (1993), which was used as
initial data for the shock revival calculations of Chapter 3, extends only to layers within
the stellar He-core, and data from the original pre-collapse stellar model of Woosley
et al. (1988) is no longer available. We thus had to reconstruct the outer envelope of
the Woosley et al. (1988) star using a new $15\,\mathrm{M_\odot}$ blue supergiant model which was
kindly provided to us by S. E. Woosley. As the original progenitor of Woosley et al.
(1988), this new model was computed with the KEPLER code (Weaver et al. 1978)
and (whenever possible) with the same input physics (metallicity, convection algorithm,
opacities, nuclear reaction rates etc.). Although KEPLER has evolved over the years,
we have found that the density structure of the original star could be reproduced
remarkably well. The most noticeable differences between the two presupernova models
were their different radii, (2×10^{12} cm in case of the older Woosley et al. (1988) model
and 3.9×10^{12} cm for the new progenitor), which is due to a more extended hydrogen
envelope for the model calculated with the new version of KEPLER. Both values are,
however, still inside the range of radii that has been infered for the SN 1987 A progenitor
from pre-explosion photographic plates (Arnett et al. 1989a).

The initial data for our AMR simulations consisted of three different parts. Interior
to 17 000 km ($1.63\,\mathrm{M_\odot}$), data from our explosion models was used to interpolate the
density, pressure and velocities onto the AMR grid hierarchy. Exterior to this border,
data from Bruenn's 1D post-collapse model was used which fitted seamlessly to the
outermost zones of our explosion models which had not yet been reached by the shock.
Matched to Bruenn's model in turn was the new progenitor of Woosley. We were able to
fit these two models without introducing artifacts into the density profile by choosing a
fitting point at 8.4×10^9 cm ($M_r = 1.94\,\mathrm{M_\odot}$) which is well inside the He-core. Thus the
important density jump located at the C+O/He interface was taken over entirely from
Bruenn's post-collapse model, and the fitting took place in regions where the density
profile is rather flat. The chemical composition was taken over from Bruenn's data for
zones inside the fit radius. For zones between the fit radius and the small jump in
the He mass fraction at a mass coordinate of $2.9\,\mathrm{M_\odot}$ (compare Fig. 4.16), i.e. in the
inner He core, we have extrapolated the composition from the data of Bruenn (1993).
This was necessary in order not to introduce artificial discontinuities in the chemical
profiles, especially in case of the $^{12}\mathrm{C}$ mass fraction which depends sensitively on the
assumed $^{12}\mathrm{C}(\alpha, \gamma)^{16}\mathrm{O}$ reaction rate. Outside $2.9\,\mathrm{M_\odot}$, i.e. in the outer He core and in the
H envelope, all data was taken over unaltered from Woosley's new progenitor model.

Since the velocity of the supernova shock and the associated growth of the Rayleigh-
Taylor instability are very sensitive to the density profile, we have verified in a number
of one-dimensional test calculations that the "hybrid" stellar model so constructed had
no adverse effects on shock propagation. In these calculations we have cut out the iron
core of the star and induced the explosion artificially by depositing $\sim 10^{51}$ ergs in form
of thermal energy at the inner boundary of the silicon shell. This procedure enabled us
to compare the hydrodynamic evolution of our hybrid model with induced explosions
of new SN 1987 A progenitor models computed by Woosley et al. (1997) (for which no
collapse calculations including neutrino transport have been available at the time of

writing). The main evolutionary features were found to be comparable in all cases.

4.2 Hydrodynamics and equation of state

All adaptive mesh refinement calculations were performed with a version of the AMRA code (Plewa & Müller 2000) which is described in Section B.3 of the Appendix. AMRA ensures that the computational effort is concentrated in regions of the flow where it is really necessary. This is accomplished by a local refinement of the grid in critical regions which allows to avoid the use of a globally fine grid. Readers who are interested in details of the AMR algorithm as well as in the computational details of the calculations that are described in the following sections are advised to consult Appendix B and the references therein, before proceeding with the rest of this chapter.

The hydrodynamics solver which is used in AMRA is a specially adapted version of HERAKLES, the implementation of the piecewise parabolic method which we employed for the (single grid) calculations of Chapter 3. AMRA therefore offers the same capabilities for computing multifluid flows with general equations of state as (the standalone version of) HERAKLES. In addition a new nuclear burning module was integrated into the code which, however, was not used in the calculations which are described in this chapter since the post-shock temperature had decreased below 2×10^9 K when the AMR calculations were started and thus all nuclear reactions had already frozen out. The capability of AMRA to compute reactive flows will however be exploited in future high-resolution modelling of the explosion itself which will necessitate also a coupling of neutrino transport to the adaptive mesh hydrodynamics, a task which has not been attempted yet. Self-gravity is taken into account in the Newtonian limit by solving Poisson's equation in one spatial dimension with an angular average of the density. This approximation is adequate because once the shock has left the iron core and propagated out to a few thousand kilometers, general relativistic effects are negligible. In addition, in the models computed in this work, no large-scale asphericities develop, which would necessitate to take into account also higher-order terms in the multipole expansion of the potential.

The equation of state that we have used in our AMR calculations includes contributions from photons in thermodynamic equilibrium with the matter, nondegenerate, nonrelativistic electrons, ^{1}H and the 14 nuclei that are included in the nuclear reaction network that was discussed in Section 3.6 (i.e. the 13 α-nuclei from ^{4}He to ^{56}Ni and the neutronization tracer nucleus) as well as electron/positron pairs in the approximation of Witti et al. (1994). We have found, that for the range of thermodynamic conditions prevailing at a time of ~ 800 ms after bounce, when the mapping of an explosion model to the AMR code was performed, thermodynamic consistency of all state variables with an accuracy of a few percent could be achieved between the equations of state employed in our modeling of the shock revival phase and the one implemented in AMRA.

4.3   One-dimensional models

Although we will demonstrate later in this chapter that the late shock propagation phase *must* be treated in a multi-dimensional framework in order to obtain a realistic picture of the explosion, one-dimensional models are still valuable, since they already exhibit the gross evolutionary effects and allow one to interpret the much more complicated multidimensional results. Taken together, the results of simulations conducted in different spatial dimensions provide complementary information and thus reveal different facets of the problem which allows for a deeper understanding. In addition, one-dimensional simulations provide a quick overview of the location and number of unstable regions in case an entire palette of different stellar models has to be explored. This can be achieved by performing a linear stability analysis in the course of the calculations and we have done so in case of the Woosley et al. (1988) progenitor, where we will also contrast the one-dimensional findings with our two-dimensional results.

4.3.1   Computational setup

Even in one spatial dimension and with the speed-up offered by adaptive mesh refinement, the severe time step limitations imposed by the Courant-Friedrichs-Lewy stability condition make it impossible to follow the propagation of the shock up to the photosphere, if the collapsed stellar core is included in the computational domain. In setting up an AMR simulation we therefore had to cut out the innermost regions of an explosion model by placing the inner boundary of the AMR base level grid at a radius of 10^8 cm (i.e. 1000 km). The cutoff was thus introduced still inside the neutrino driven wind from the neutron star. The gravitational attraction of matter below the cutoff radius was taken into account by a central point mass, while free outflow was allowed for through the inner boundary. The assumption of a transmitting inner boundary is a crude approximation within about the first half minute of the explosion, since it leads to very early accretion (see below), but becomes more realistic for later times. The outer boundary of the computational domain was kept at the stellar radius of 3.9×10^{12} cm while transmitting boundary conditions were imposed also in this case.

In order to get the closest possible approximation to the energetics of the two-dimensional case, we have started the 1D calculations which are described in Section 4.3.2 from an angularly averaged version of our 2D explosion model T310 (compare Chapter 3), which we will henceforth refer to as model $\overline{\text{T310}}$. For this calculation, a very high effective resolution of 524 288 zones was used. The memory requirement was fairly modest and amounted to about 200 MBytes, most of which was used by the gravitational solver. In the current implementation, the latter does not operate on the AMR grid hierarchy but requires its own (fine) mesh. The rather low memory consumption is largely due to the fact that in one-dimensional simulations most of the features which need to be calculated with high resolution are sharply localized discontinuities. Thus, only a small fraction of the computational domain needs to be covered with fine grid patches. Note that the speed-up that can be obtained with AMR relative to a calculation which uses a uniform grid of the same effective resolution as the finest level of the AMR grid hierarchy is roughly given by

$$S = 1/f \tag{4.1}$$

where f is the fraction of the computational domain (the so-called "filling factor") which is covered by the finest level. Equation (4.1) expresses the fact that nearly all of

level	refin. factor	ϵ	$\epsilon_{\rho X}$	effect. res. (zones)	effect. res. (km)
1	4	10^{-2}	10^{-3}	512	76288
2	4	10^{-2}	10^{-3}	2048	19072
3	4	10^{-2}	10^{-3}	8192	4768
4	4	10^{-2}	10^{-3}	32768	1192
5	2	10^{-2}	10^{-3}	131072	298
6	2	10^{-2}	10^{-3}	262144	149
7	—	—	—	524288	75

Table 4.1: The refinement scheme which was used for model sequence $\overline{T310}$, our one-dimensional calculation of shock propagation through the stellar envelope. The different levels of the grid hierarchy as well as the refinement factors between levels are given in the first two columns. Columns three and four list the truncation error thresholds for the conserved variables $(\rho, \rho v_r, \rho E)$ and for the partial densities of nuclei, ρX_i, respectively. Zones on a given level were flagged for refinement, if either (i) the local truncation error estimate for these quantities was higher than the listed thresholds or (ii) density jumps $\geq 100\%$ were encountered between neighbouring zones.

the computational effort in an AMR calculation is spent in solving the system of partial differential equations on this finest level. The small filling factors in one dimensional simulations therefore result in a large speed-up relative to a uniform grid calculation. For our 524 288 zones run, which made use of the refinement scheme given in Table 4.1, we have measured speed-up factors as large as 10^3. Even so, keeping this refinement scheme (which corresponds to a linear resolution of 75 km) throughout the entire simulation, turned out to be too costly on one CPU of an IBM 7026-H70 workstation. Therefore, after 1870 s of evolution, the 7th level of the grid hierarchy was removed and thus the maximum resolution reduced to 149 km. This zoning was kept until $t = 4770$ s, when also level 6 was discarded and the rest of the evolution followed with a maximum resolution of 298 km. The computation was stopped at $t = 8500$ s post bounce, 1700 seconds after the shock had emerged from the photosphere.

4.3.2 General evolution

Figure 4.1 depicts the evolution of the density, pressure, velocity and sound speed in our 1D AMR simulation $\overline{T310}$. The locations of the Si/O, (C+O)/He, and He/H interfaces at the start of the calculation (i.e. 0.8 s after bounce) are also given. Note the various non-linear waves. The supernova shock is the conspicuous outermost discontinuity in each of the curves which display the hydrodynamic quantities for different times. Note also that the outer layers of the star remain in hydrostatic equilibrium until they are hit by the shock wave. The drop of the density in the immediate post-shock layers is enormous, and amounts to about eight orders of magnitude from the beginning to the end of the simulation.

In Fig. 4.2 we show the positions of the shock and of the composition interfaces as a function of time along with the evolution of the shock velocity. It can be noted
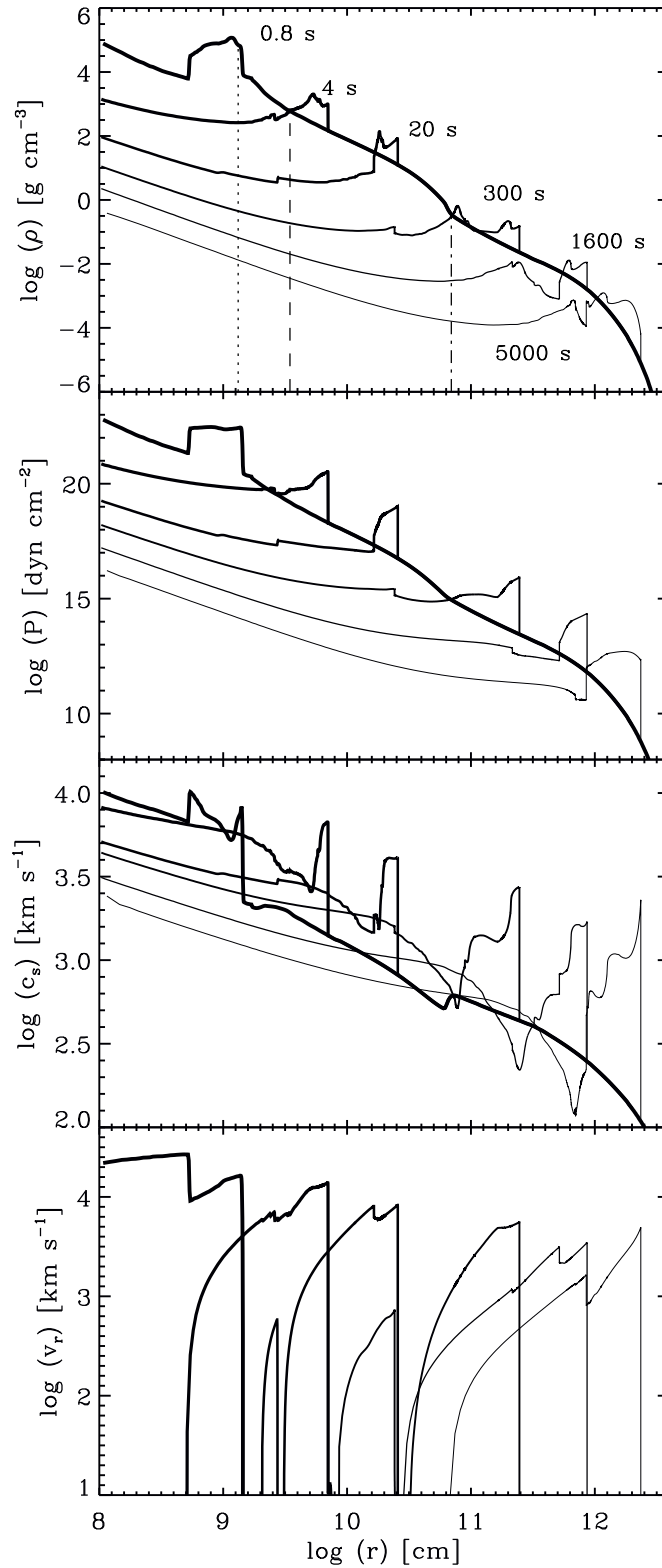
Figure 4.1: Evolution of the density, pressure, sound speed and velocity in our one dimensional adaptive mesh refinement simulation $\overline{\text{T310}}$. The dotted, dashed and dashed-dotted lines indicate the positions of the Si/O, C+O/He and He/H interface, respectively, at a time of 0.8 s after core bounce.
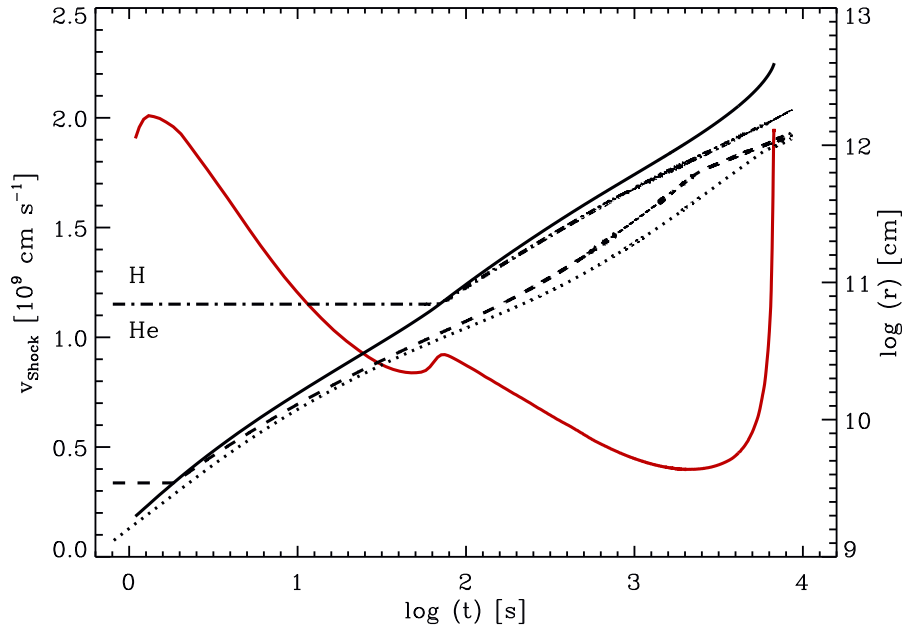
Figure 4.2: Evolution of the shock velocity (red line, left axis) and trajectories (right axis) of the shock (dark, solid line), as well as the Si/O (dotted), (C+O)/He (dashed) and He/H interface (dash-dotted) in model $\overline{\text{T310}}$. Note the deceleration of the shock after it has crossed the (C+O)/He interface at $\log(t/\text{s}) = 0.25$ and the He/H interface at $\log(t/\text{s}) = 1.85$. The steep increase of the shock velocity for times later than $\log(t/\text{s}) = 3.5$ is due to the pronounced drop of the density in the atmosphere of the star.

from this figure that around the time when the shock wave crosses the (C+O)/He interface ($t = 1.8\,\text{s}$) its propagation speed has reached a maximum of about $20\,000\,\text{km/s}$. Immediately thereafter, a rapid decrease of the shock velocity can be seen in Fig. 4.2. This indicates that the density profile in the He envelope falls off shallower than $\propto r^{-3}$ (see the discussion in Section 2.2). The deceleration endures until the wave has reached the rapid drop in density associated with the He/H interface (see Fig. 4.1) around $80\,\text{s}$ after core bounce. Then it temporarily accelerates to about $9000\,\text{km/s}$ (Fig. 4.2). Once the He/H interface has been passed, the evolution resembles again the situation after the wave had crossed the (C+O)/He interface. A gradual deceleration to propagation speeds as low as $4000\,\text{km/s}$ occurs, until the shock enters the atmosphere of the star and finally accelerates to more than $20\,000\,\text{km/s}$, while propagating off the numerical grid.

Every time the shock decelerates, a strong compression of the post-shock layers results, which must slow down as well. The shocked material thus piles up and forms a high-density shell. Note that since immediately behind the shock the flow is supersonic, information can only be mediated to deeper layers via supersonic motion, i.e. via a non-linear wave. Therefore, the deceleration of these zones occurs through a reverse shock, which forms at the inner boundary of the high-density shell and starts to propagate inwards in radius. The reverse shocks as well as the dense shells which form after the main shock has passed the (C+O)/He and He/H interfaces, respectively, can be clearly seen in the density structures for $20\,\text{s}$ and $1600\,\text{s}$ in Fig. 4.1. It is also apparent that the
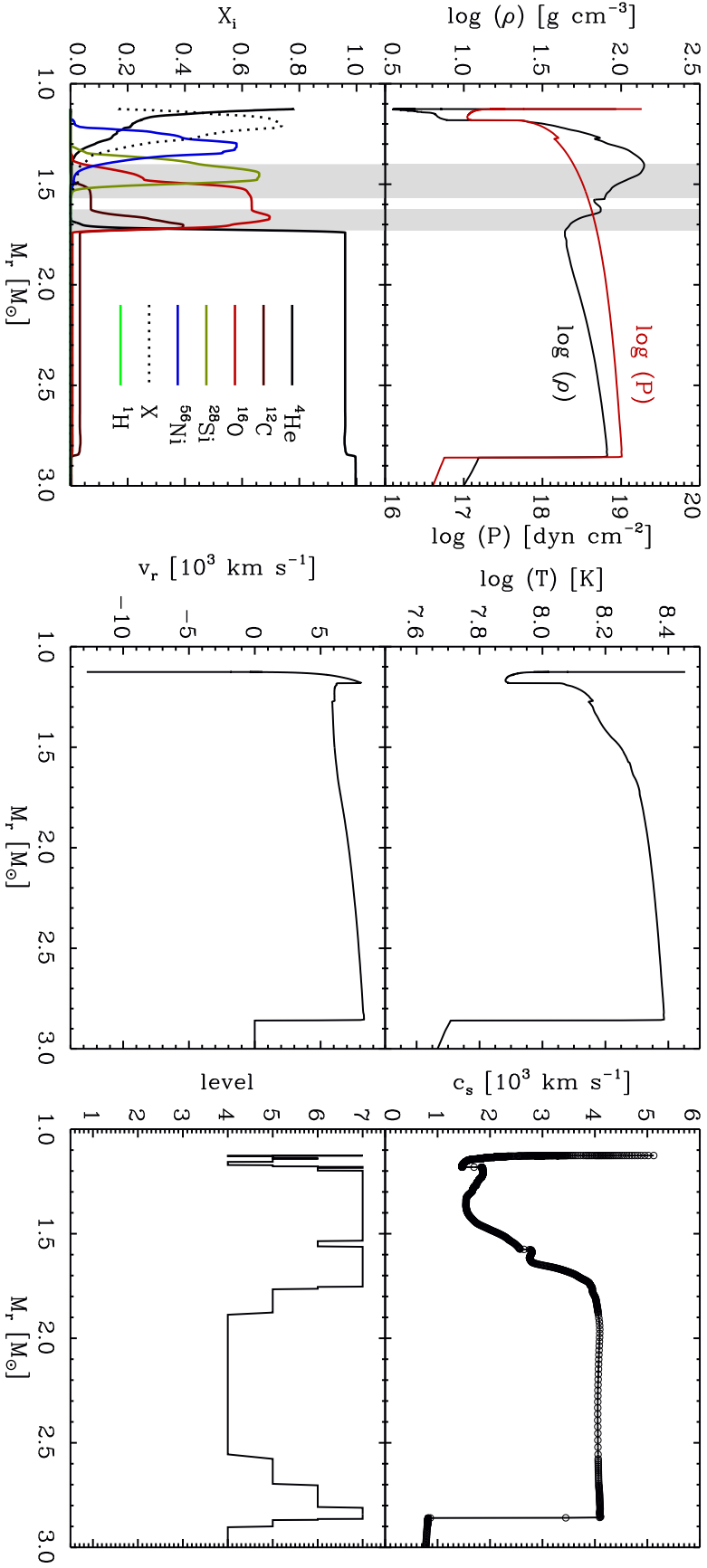
Figure 4.3: Structure of model T3l0, 20 s after bounce. Shown are (from top left to bottom right) the density, pressure, mass fractions, temperature, velocity and sound speed as a function of the enclosed mass. The distribution of the different levels of the AMR grid hierarchy is also shown for comparison. The spatial resolution can be judged from the data points which are shown in the plot of the sound speed. Note the two unstable regions (shaded in grey) with opposite density and pressure gradients near the Si/O and C+O/He composition interfaces. Note also that the code has concentrated the resolution in the steep features of the flow, e.g. near the supernova shock at 2.9 $M_\odot$, the reverse shock at 1.2 $M_\odot$ and the accreting matter which falls onto the proto neutron star at a mass coordinate of 1.15 $M_\odot$.
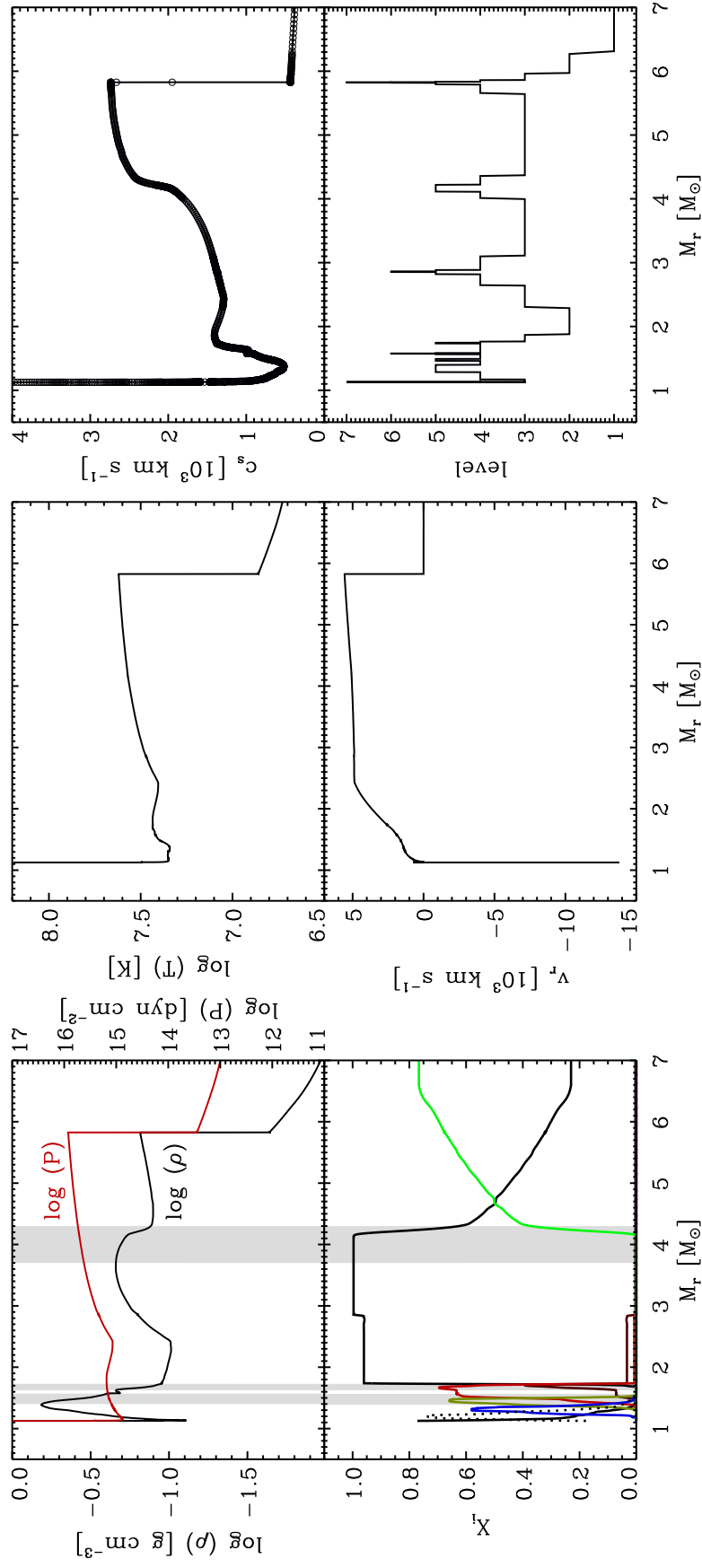
Figure 4.4: Same as Figure 4.3 but 300 s after core bounce. The entire metal core of the star ($M \leq 1.68\,M_{\odot}$) has been strongly compressed. Note the dense shell and the third unstable region which has been left behind by the shock at the He/H interface, as well as the high infall velocities at the inner grid boundary. See also the legend in the mass fraction plot of Fig. 4.3 for an identification of the composition.
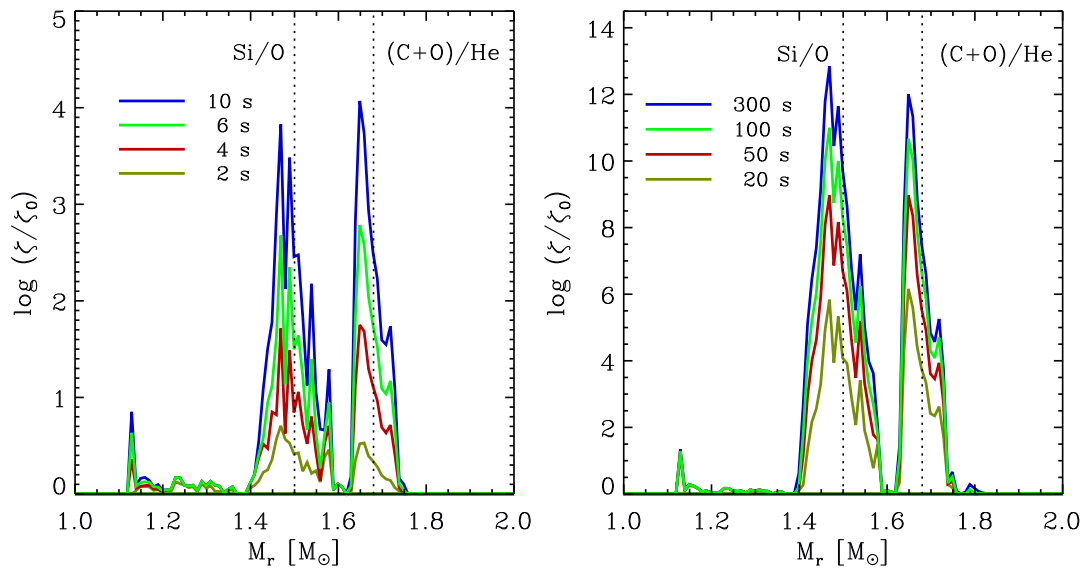
Figure 4.5: Logarithm of the total, time-integrated, growth rate in the unstable layers near the Si/O and (C+O)/He composition interfaces of model $\overline{\text{T310}}$ at different times. Note that the growth rates increase with time and reach amplification factors $\geq 10^{12}$ within the first 300 seconds (i.e. five minutes) of the explosion.

density profiles for these times show a striking similarity in the region which is bounded by the two shocks.

In a one-dimensional calculation, dense shells which have been swept up during earlier phases of the evolution do not vanish. We have already pointed out in Chapter 3 that already within the first 0.8 seconds the shock has left behind a density hump at the Si/O interface of the star. This can be seen in Figures 3.4 and 4.1, and more clearly in Fig. 4.3 which shows the most important flow quantities 20 s after core bounce as functions of the enclosed mass. Note that two high-density shells are visible at that time. The innermost is the one which we alluded to in Section 3.7. It contains the products of explosive silicon and oxygen burning. The outermost is the one which formed at the (C+O)/He interface. At the outer boundaries of these shells (shaded in gray in Fig. 4.3) negative density and positive pressure gradients exist, i.e. already at this early time, Rayleigh-Taylor instabilities must be expected to grow in these regions. This is also confirmed by a linear stability analysis. In Figure 4.5 we plot for these layers and for different times the total, time-integrated growth rate

$$\frac{\zeta}{\zeta_0} = \exp\left(\int_0^t \sigma dt\right), \tag{4.2}$$

i.e. the factor by which a perturbation with an initial amplitude ζ_0 would be magnified at time t. The growth rate of the instability, σ, is given by

$$\sigma = \sqrt{-\frac{P}{\rho}\frac{\partial \ln P}{\partial r}\frac{\partial \ln \rho}{\partial r}}, \tag{4.3}$$

(e.g. Müller et al. 1991b), where we have assumed an *incompressible* fluid. In the com-
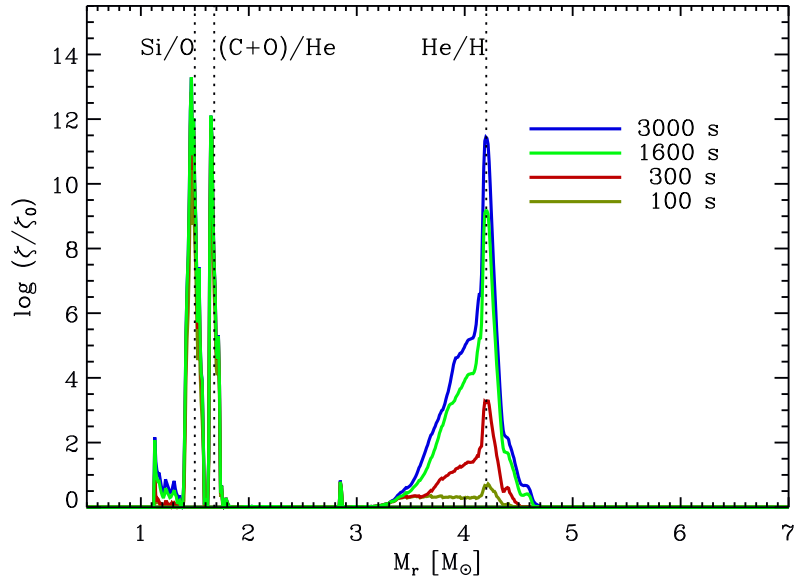
Figure 4.6: Logarithm of the total, time-integrated, growth rate in the unstable layers near the Si/O, (C+O)/He and He/H composition interfaces of model $\overline{T310}$ at different times. Compare the amplitudes of the growth rates at the Si/O and (C+O)/He interfaces with Fig. 4.5 and note that these have saturated after 300 s (in fact the curves for 300 s and 3000 s are not visible because they are identical, within plotting accuracy, to the one for 1600 s). Note also, however, that the rate for the instability at the He/H interface is still increasing between 300 s and 3000 s.

pressible case

$$\sigma = \frac{c_s}{\gamma}\sqrt{\left(\frac{\partial \ln P}{\partial r}\right)^2 - \gamma\frac{\partial \ln P}{\partial r}\frac{\partial \ln \rho}{\partial r}}, \tag{4.4}$$

holds. Both assumptions yield roughly comparable results, however. It can be noted that within only the first 20 s after bounce, the amplification factor has already grown to about 10^6 in both unstable regions, which are separated by a stable intermediate layer at $1.6\,M_\odot$. Furthermore, both growth rates are increasing up to a time of 300 seconds after bounce. Figure 4.4 displays the hydrodynamic state at this time and shows that the entire metal core of the star has been compressed to a high density zone which includes the two unstable interfaces. At this time the shock has also passed the He/H interface and a third unstable region has formed at the outer boundary of the density hump which the shock has left behind at the He/H interface. The evolution of the growth rate in this region is shown in Figure 4.6. At a time of 300 seconds after core bounce it is much smaller than the rates for the instability at the Si/O and (C+O)/He interfaces. However, while the latter reach their maximum at this time, the growth rate at the He/H interface still increases and reaches about the same level after 3000 seconds of evolution. This is an interesting result since it shows exactly the opposite behavior as the calculations of Müller et al. (1991b). These authors found that the instability should initially grow faster at the He/H interface and that only after some time should the growth at the (C+O)/He interface take over. As this result of Müller et al. (1991b) is almost certainly caused by the fact that they started their calculations only 300 s after core bounce, this underlines, *that a reliable calculation*

of the Rayleigh-Taylor growth must be started from the very earliest moments of the explosion. While quantitatively the results of the linear stability analysis are certainly invalid once non-linear growth has set in, the above conclusion will be substantiated by our two-dimensional calculations. It is also supported by results of Iwamoto et al. (1997) who find a similar behavior for the growth of the instability at the (C+O)/He and He/H interfaces of their models for SN 1993 J.

To our knowledge, no other work conducted to date has found a strong growth rate for Rayleigh-Taylor instabilities at the Si/O interface of a massive star. We suspect that this might be due to inconsistencies introduced into the hydrodynamic evolution by initiating the explosion using ad hoc energy deposition schemes, by the use of an insufficient numerical resolution, or by differences in the structure of the progenitor stars which were employed in these studies. Possibly, also a combination of the above effects could be involved and therefore conclusive high-resolution studies using the same hydrodynamic code and different progenitor models are urgently required. The reason why we belabor this point is that the instability at this interface *will turn out to be the most crucial one* in the two-dimensional models that we will discuss in Section 4.4.

As we mentioned earlier, our treatment of the inner boundary condition in the AMR calculation is not realistic during the first ~ 30 seconds of the explosion. Since we do not impose a continuous inflow of material from the neutrino driven wind into the computational domain, the strong reverse shock which separates the outermost regions of the wind from the ejecta and which is visible at $t = 0.8$ s in Fig. 4.1, is partially reflected at the inner boundary within the first 4 seconds of evolution. This gives rise to a series of weak non-linear waves which bounce back and forth between this boundary and the ejecta during the first ~ 20 seconds, while material near the boundary starts to be accreted onto the collapsed core. During this phase the wind is expected to operate still and though it weakens with time, it should prevent very early fallback of matter onto the compact object (H.-Th. Janka, private communication). Yet, we have found that even if a transmitting boundary is used throughout the entire simulation, only a very small amount of mass of $2 \times 10^{-3}\,\mathrm{M}_\odot$ falls back until $8500\,\mathrm{s}$ after core bounce for model $\overline{\mathrm{T310}}$. Furthermore, while a realistic modeling of the wind is important for the fallback, it is not necessary for a study of the Rayleigh-Taylor instabilities. We have implemented and tested a semi-analytic prescription for the wind which is based on the models of Janka (1993) (see also Witti et al. 1994) and found that though it has an influence on the mass cut, for realistic wind parameters (Witti et al. 1994) the energy and momentum fluxes are too small to influence the evolution in the outer ejecta.

The fate of the reverse shock which originates from the (C+O)/He interface is somewhat uncertain. Figure 4.1 shows that between $20\,\mathrm{s}$ and $300\,\mathrm{s}$ this shock detaches from its high-density shell and moves inwards to be reflected at the inner boundary. Subsequently it propagates back to larger radii and slightly compresses the inner ejecta. This (weak) reflected wave is visible at a radius of $\log(r/\mathrm{cm}) = 10.4$ in Fig. 4.1. Since our inner boundary is located at a radius of $1000\,\mathrm{km}$ it was not possible to follow the reverse shock down to the layers near the neutron star, and thus the reflection we see is a clear artifact. Physically, though, a reflection of this wave in the dense inner core is plausible and probably even inevitable.

4.4 Two-dimensional models

4.4.1 Computational setup

While performing a one-dimensional, high-resolution AMR calculation of shock prop-
agation as the one of Section 4.3.2 is rather easy, the task becomes significantly more
difficult in the multidimensional case, where finite computational resources are a much
more severe concern. A main problem in this respect is posed by the philosophy of
AMR to provide an adaptive framework in order to compute a solution with "a fixed
accuracy for a minimum cost" (see Berger & Colella 1989). One needs to realize that
the algorithm will try to do so *regardless of the resources that this might require*. In
practice, however, the task which has to be solved in astrophysical simulations is usu-
ally the reverse, namely one tries to calculate the most accurate solution for a fixed cost
(i.e. a given amount of memory and CPU time available on a supercomputer). Since the
adaptivity of AMR has *not* been designed to achieve the latter goal, substantial user
intervention is usually required in order to get the maximum out of existing hardware.

The problems that one faces in more than one spatial dimension are illustrated in
some more detail by the following considerations. In two and three-dimensional calcula-
tions, the occurrence of instabilities in the flow will usually require one to follow larger
fractions of the computational domain with high resolution than in a corresponding
one-dimensional calculation, where mostly shock waves and contact surfaces have to be
tracked. Thus, under unfavorable conditions, the filling factor, f, on the finest level of
the grid hierarchy might approach unity, and because of Equation (4.1) the advantage
of local mesh refinement as compared to a uniform grid calculation can be lost.

When using the algorithm for truncation error estimation as suggested by Berger &
Colella (1989) in order to flag points which need refinement, a large filling factor for a
given AMR level, l, can only result if the local truncation error estimate on level $l-1$ is
larger than the corresponding user-defined threshold throughout a significant fraction
of the computational domain. The occurrence of a large filling factor on the level with
the highest resolution of the grid hierarchy, $l_{\max}$, will therefore indicate that the flow
is rich in small-scale structure, which might not have been resolved yet. A continuous
increase of the resolution (i.e. adding more and more refinement levels) must at some
stage decrease the local truncation error of the solution on level $l_{\max} - 1$ below the
desired threshold[1]. Consequently regions of the flow where this is the case will not
have to be followed with (the even higher resolution of) level $l_{\max}$. The filling factor
on level $l_{\max}$ *must* therefore decrease once a specific accuracy has been attained, while
according to Equation (4.1) the speed-up will increase. Just *when* this will happen,
depends strongly on the problem one is trying to compute.

In practice, the possibility to increase the resolution is limited by the finite memory
and speed of the available computers. Thus even if AMR might offer substantial savings
for a specific problem in the limit of very high resolution, one may find oneself in
a situation where only modest gains can be obtained due to limits imposed by the
hardware. For instance, while we have demonstrated in Section 4.3 that a 1D calculation
of supernova shock propagation with an effective resolution of $\sim 10^6$ zones and measured
speedups of 10^3 can be done on a multiprocessor workstation, a 2D simulation with a
resolution of 10^{12} zones, which promises comparable gains in efficiency, is unfeasible. It

---

[1]Except for isolated discontinuities, like shocks, contact surfaces and material interfaces (see Berger
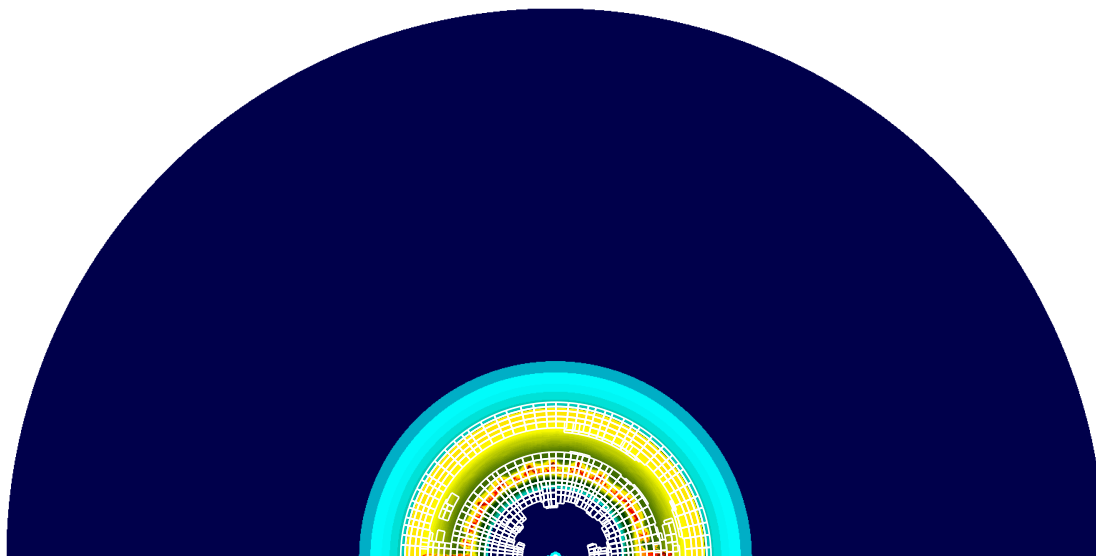& Colella 1989).

Figure 4.7: Distribution of the density and boundaries of grid patches in model T310 at $t = 50\,\mathrm{s}$. The entire computational domain of Run 3 from Table 4.2 is depicted while only patches of the highest level of the grid hierarchy are shown in order to illustrate the filling factor of the simulation during early stages. The code has concentrated these patches only in the regions near the supernova shock (yellow discontinuity), in the unstable layers (red and yellow) and near the reverse shock at somewhat smaller radii.

would require more memory and speed than the largest supercomputers can currently offer.

Indeed, the memory requirement turned out to be the most restrictive factor for our 2D calculations and forced us to follow a radically different computational strategy than in the one-dimensional case. Since it was impossible to sustain a very high resolution throughout a two-dimensional run using 3.4 GBytes of main memory on a CRAY J916, we have split the evolution into several substeps. In each of these steps we have followed the flow within a fraction of the stellar radius for some time using a pre-chosen refinement scheme and employing spherical coordinates (r, θ). The computational domain extended over $0 \leq \theta \leq \pi$ in angle and $r_{\mathrm{in}} \leq r \leq r_{\mathrm{out}}$ in radius. Reflecting boundary conditions were used at $\theta = 0$ and $\theta = \pi$ and transmitting boundaries at $r = r_{\mathrm{in}}$ and $r = r_{\mathrm{out}}$. Once the shock wave was about to reach r_{out} or the memory consumption became prohibitive for a continuation of the calculations (with the filling factor on the finest level approaching unity), a remapping procedure was applied. All hydrodynamic state quantities were mapped to a new grid hierarchy which (usually) employed the same refinement scheme but covered a radius which was twice or three times larger than in the previous run. Thus the effective resolution as well as the filling factor were reduced and the calculations could be continued. The new outer boundary was preferentially chosen in a way which would allow us to cover the region of the instability with zones whose aspect ratio $\Delta r / r \Delta \theta$ was close to unity. Figure 4.7 illustrates the grid distribution during the early stages in one of our sub-runs while Table 4.2 summarizes the entire remapping strategy.

In terms of efficiency, the speed-up that we have typically observed for a sub-run was found to be drastically smaller than in the one-dimensional calculation $\overline{\mathrm{T310}}$ and amounted to about a factor of 5. As we discussed above this is caused by moderately

Run	levels	t_i [s]	t_f [s]	$r_{\rm in}$ [10^8 cm]	$r_{\rm out}$ [10^{10} cm]	$N_r^{\rm Base} \times N_\theta^{\rm Base}$	$N_r^{\rm eff} \times N_\theta^{\rm eff}$	Δr [km]	$N_r^\star$
1	4	0.8	9.6	1	2	48×12	3072×768	65	599 985
2	4	9.6	34	10	6	48×12	3072×768	195	199 995
3	4	34	160	10	18	48×12	3072×768	586	66 550
4	4	160	310	30	36	48×12	3072×768	1172	33 275
5	4	310	780	80	100	48×12	3072×768	3255	11 980
6	4	780	1700	150	200	48×12	3072×768	6510	5990
7	4	1700	4800	280	390	48×12	3072×768	12604	3072
8	4	4800	34000	280	390	24×12	1536×768	25208	1536

Table 4.2: The computational setup which was used for the 2D AMR simulation of model T310. The number of refinement levels, the evolutionary times covered by each run, as well as the radii of the inner and outer grid boundaries are given in columns two to six. Columns seven and eight list the number of zones on the base level grid and the effective number of zones on the finest level, respectively. Column nine gives the radial resolution in km, while the last column lists the number of radial zones, $N_r^\star$, that would have been required to obtain the same radial resolution as in our AMR sub-runs, if the (base level) grid would have covered the entire star. Refinement factors of 4 between levels were used for each spatial dimension. Zones on a given level were flagged for refinement, if (i) the local truncation error estimate for the quantities $(\rho, \rho v_r, \rho v_\theta, \rho E)$ was larger than 10^{-2}, (ii) the local truncation error estimate for the partial densities of nuclear species was larger than 10^{-3}, or (iii) density jumps $\geq 100\%$ were encountered between neighbouring zones.

large filling factors and might indicate that features on even smaller scales may be found in even higher-resolution calculations. Yet, we are confident that we have been able to capture the essential features of the solution. Our spatial resolution is reasonably high during the initial growth phase of the instability. In addition, the flow structures are magnified with time by the expansion and thus extremely high resolution is not essential in order to calculate the very late stages of the explosion.

Altogether two evolutionary sequences were computed. The first of these made use of our two-dimensional explosion model T280* (see Sections 3.12 and 3.11) and neglected gravity. In all AMR calculations we have *not* applied any seed perturbations. However, during the course of the computations which were started from model T280* we have found that this shock revival model and also the subsequent AMR simulation were severely affected by the odd-even decoupling instability which was described in Section 3.11. The reason why we still discuss the results of this calculation in Section 4.4.3 is the fact that the neglect of gravity as well as the strong numerical noise due to odd-even decoupling, made this model rather optimistic regarding the energetics of the explosion and the efficiency of the mixing. It may therefore serve to illustrate the quality of results that can be obtained with rather "noisy" hydrodynamic schemes as SPH. Our second AMR model sequence was started from model T310. It includes gravity and the artificial viscosity algorithm that was already used to suppress odd-even decoupling in our shock revival models. We discuss its results in detail in the following section.

The feasibility of the simulations turned out to depend critically on the densities and temperatures that the gas attained near the inner boundary during the course of the computations. This was especially true in case of model T310 where due to the inclusion of gravity, accretion onto the compact object occurred. In one spatial dimension, the computational load was sufficiently small that the base level time step of about 3 s that resulted from the Courant-Friedrichs-Lewy condition due to the high infall velocities and sound speeds at the inner boundary, was not a significant concern. In two dimensions, however, the long-term evolution of models T280* and T310 could only be followed if the inner boundary was continually moved outwards toward smaller temperatures, densities and infall velocities in order to increase the time step. Table 4.2 lists the scheme that was used for this purpose in case of model T310.

4.4.2   Model T310

Having already discussed the main features of the evolution in the one-dimensional case we will now focus on multidimensional effects in the (late) evolution of model T310. In the following we show mainly plots of the density because this quantity already displays the main physics of the problem.

Figure 4.8 a shows the state of affairs 4 s after core bounce, when the supernova shock has already crossed the (C+O)/He interface of the star. The similarity of the structures that can be seen in this figure as compared to the state 800 ms after bounce which is shown in Fig. 3.21 is striking and indicates that within the first few seconds of the explosion the expansion has proceeded roughly self-similarly, at least in the low-density (high entropy) layers of the ejecta which were formerly heated by the neutrinos. However, it should be noted that outside the high-entropy mushrooms, and exactly as in the one-dimensional model $\overline{\text{T310}}$, material of the Si and C+O layers of the star is compressed to two dense shells, the outer one not being visible in Fig. 3.21. Ten
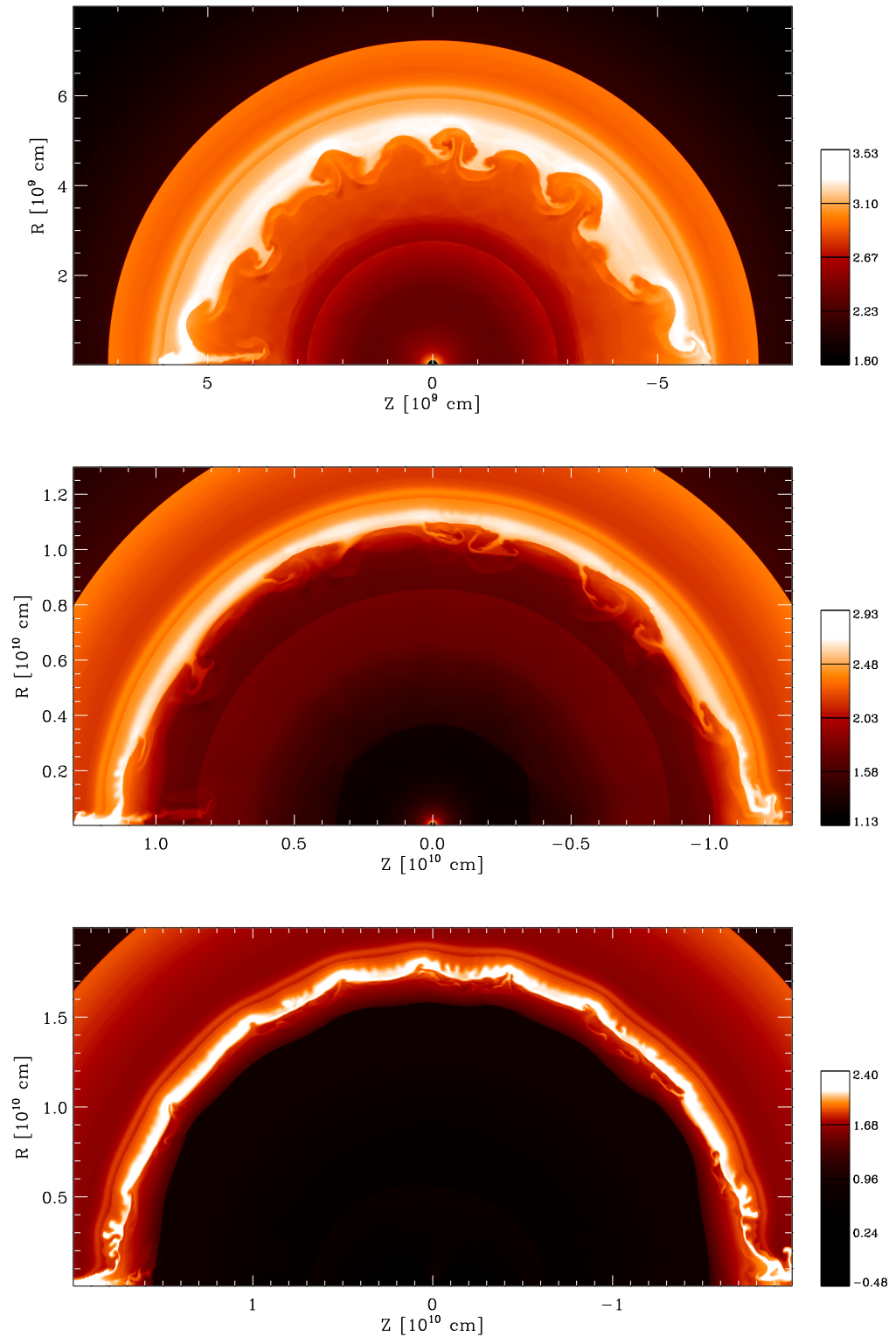
Figure 4.8: Logarithm of the density in model T310. From top to bottom: a) $t = 4\,\mathrm{s}$. b) $t = 10\,\mathrm{s}$. c) $t = 20\,\mathrm{s}$. Given are (R, Z) coordinates of the cylindrical grid which was used for plotting. The calculations have been carried out using spherical coordinates.
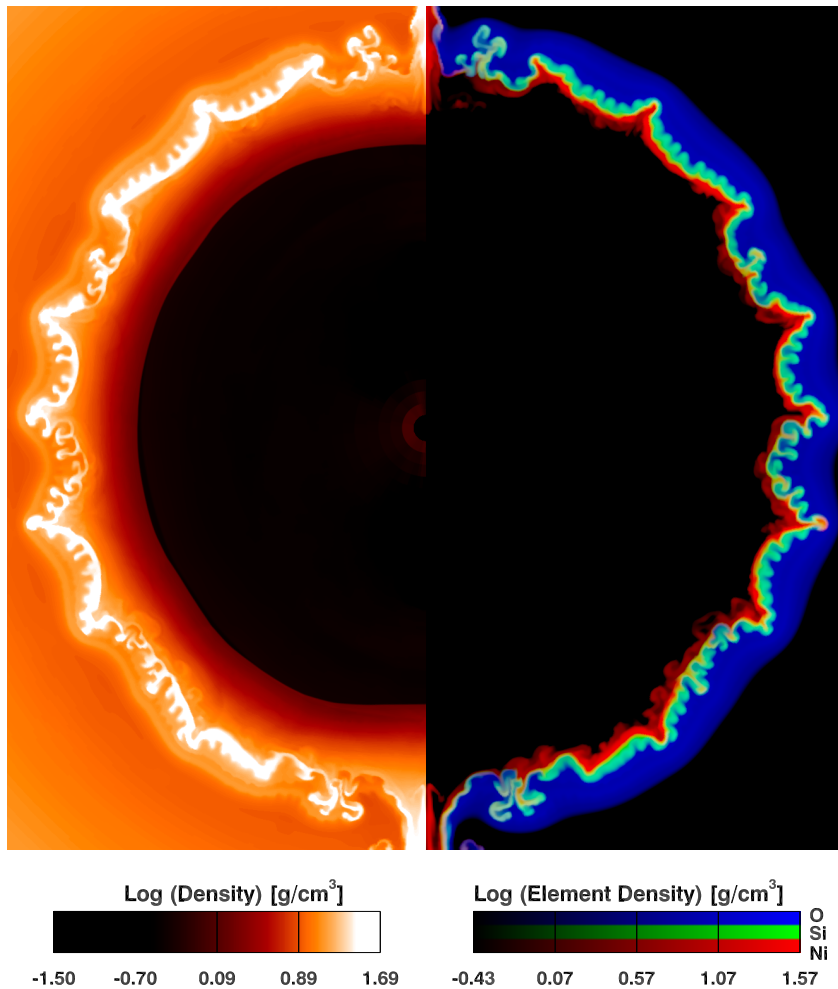
Figure 4.9: Logarithm of the density in model T310 (left panel) and distribution of the partial densities of ^{16}O, ^{28}Si and ^{56}Ni (right panel), 50 s after core bounce. The vertical extent of the figure corresponds to a diameter of 6.6×10^{10} cm.

seconds after core bounce (Fig. 4.8 b) the compression of the post-shock material has also affected the high-entropy gas, and the low-density mushrooms are "squeezed" into flat structures. Only 10 s later (Fig. 4.8 c) the compression has become so strong that the density field does not resemble the previous snapshots any longer. The strong reverse shock has formed, which is caused by the deceleration of the main shock in the He-core. It is visible as the dark discontinuity at a radius of 1.5×10^{10} cm in Fig. 4.8 c. The former convective mushrooms have imprinted a strong long-wavelength perturbation on the dense shell behind the Si/O interface as well as on the shell at the C+O/He interface farther out. Superposed upon this perturbation, small scale disturbances start to grow along the entire Si/O interface which also shows signs of about 10 developing cusps (not counting the features near the symmetry axis) which are separated by angles of about 20°. Interestingly, the locations of these cusps do *not* coincide with those of the former mushrooms which occupy the regions *between* the cusps. The cusps themselves form out of the material that constituted the former "downflows" which separated the mushrooms. It is exactly in these dense layers, where ^{56}Ni has formed during the first

250 ms of the explosion. Thus, although most of the ^{56}Ni is originally located in regions just interior to the unstable zone at the Si/O interface (see Fig. 3.21 and compare also the one-dimensional model Fig. 4.3), due to the larger momentum of the dense layers it cannot be slowed down to such small velocities as the neighbouring material, and thus penetrates outwards much further. This can be clearly seen in Fig. 4.9 which shows the logarithms of the total density and the partial densities of ^{16}O, ^{28}Si and ^{56}Ni at a time of 50 s after core bounce. The cusps already start to grow into separate fingers which strengthen the perturbation at the C+O/He interface farther out. Concurrently, the smallest scale perturbations that could still be resolved on our grid have grown to small mushrooms at the Si/O interface and start to mix predominantly ^{28}Si outwards while between them ^{16}O is mixed inwards.

At a time of 100 s after core bounce (Fig. 4.10 a) the instability at the Si/O interface, is fully developed and the fingers which carry the silicon and nickel already penetrate through the (C+O)/He interface. The (C+O)/He interface itself still shows only the long-wavelength perturbation which is imposed on it by the fingers from below. In the mean time the supernova shock has passed the He/H interface which is marked with the heavy white line in Fig. 4.10 a. Furthermore the reverse shock which originated near the C+O/He interface starts to propagate inwards in radius and to decelerate the innermost layers of the ejecta. Five minutes after bounce ($t = 300$ s, Fig. 4.10 b) this reverse shock has already been reflected at the inner boundary and moves outward as a forward shock, compressing the inner metal core of the star. The latter has been totally shredded by the instability. The original fingers have obtained the typical mushroom shape, which is caused by Kelvin-Helmholtz instabilities while they have also grown substantially in size. Material from the deep interior layers of the metal core has thus been flung through a substantial fraction of the He core (the region bordered by the two contour lines in Fig. 4.10 b). Figure 4.11, which shows a magnification of the inner region of Fig. 4.10 b together with the distribution of ^{16}O, ^{28}Si and ^{56}Ni, demonstrates that the density contrast between the densest parts of the mushrooms and the helium rich material outside the blue colored oxygen-rich regions is about a factor of 5. Note that between the fingers helium (the black-colored material outside the blue oxygen plumes) is mixed into the metal core in extended tongues. Furthermore a striking coincidence between the location of the densest "clumps" and the regions of high ^{56}Ni abundance (the red and pink regions in the right half of Fig. 4.11) can be observed.

The flow structures in the unstable layers of the inner core have become extremely complex 1600 seconds after bounce due to the interaction of the instabilities at the former Si/O and C+O/He interfaces as well as due to Kelvin-Helmholtz mixing (Fig. 4.10 c and Fig. 4.12). Interestingly, it took the C+O/He interface about 1000 seconds to show signs of growth of small-wavelength perturbations. The mixing has already become so strong that the composition is progressively homogenized. This can be seen from the large fraction of whitish regions in the right part of Fig. 4.12 which results from the superposition of the single colors which were assigned to the different elements.

While the instability is turning the inner core of the star inside out, a dense shell can be seen 1600 s after bounce at the border between helium core and hydrogen envelope in Fig. 4.10 c. It is the prominent shell that we have found also in the one-dimensional calculation $\overline{\text{T310}}$ as a result of the deceleration of the main shock in the hydrogen envelope. Note that as we have pointed out in the one-dimensional case, at the shell's inner edge a strong reverse shock has formed. In the one-dimensional calculation, the layers of the metal core lagged behind the inner edge of the shell and did not catch
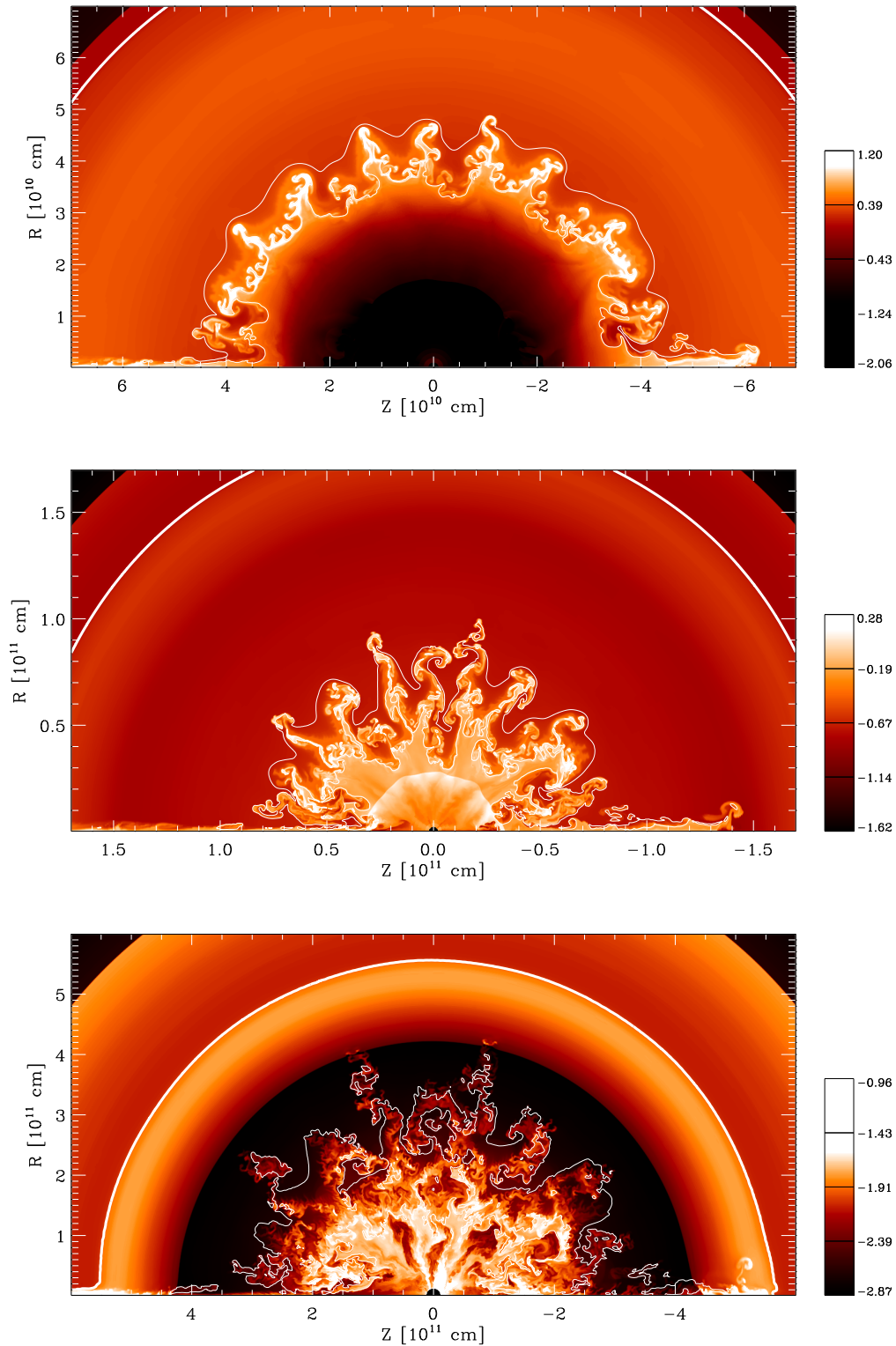
Figure 4.10: Logarithm of the density in model T310. From top to bottom: a) $t = 100$ s. b) $t = 300$ s. c) $t = 1600$ s. The overlaid contour lines indicate where the ^{1}H and ^{16}O mass fractions equal 20% (heavy and thin line, respectively). The region in between these lines is the stellar helium core.
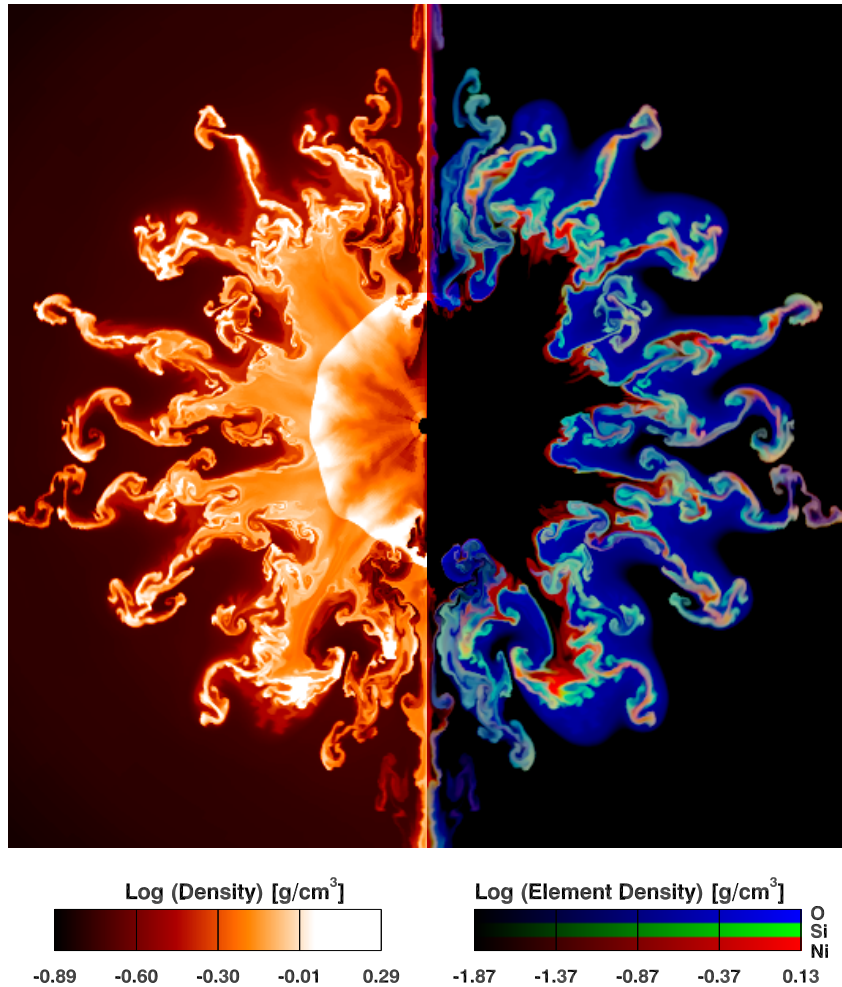
Log (Density) [g/cm^3]

-0.89   -0.60   -0.30   -0.01   0.29

Log (Element Density) [g/cm^3]

O
Si
Ni

-1.87   -1.37   -0.87   -0.37   0.13
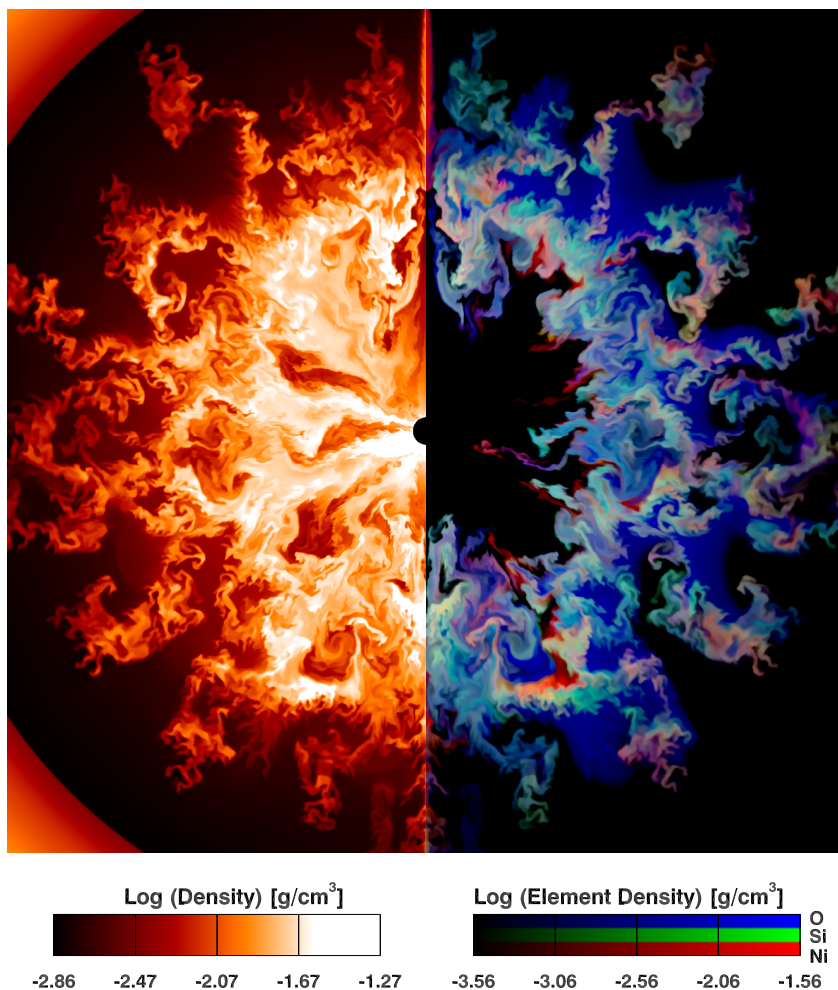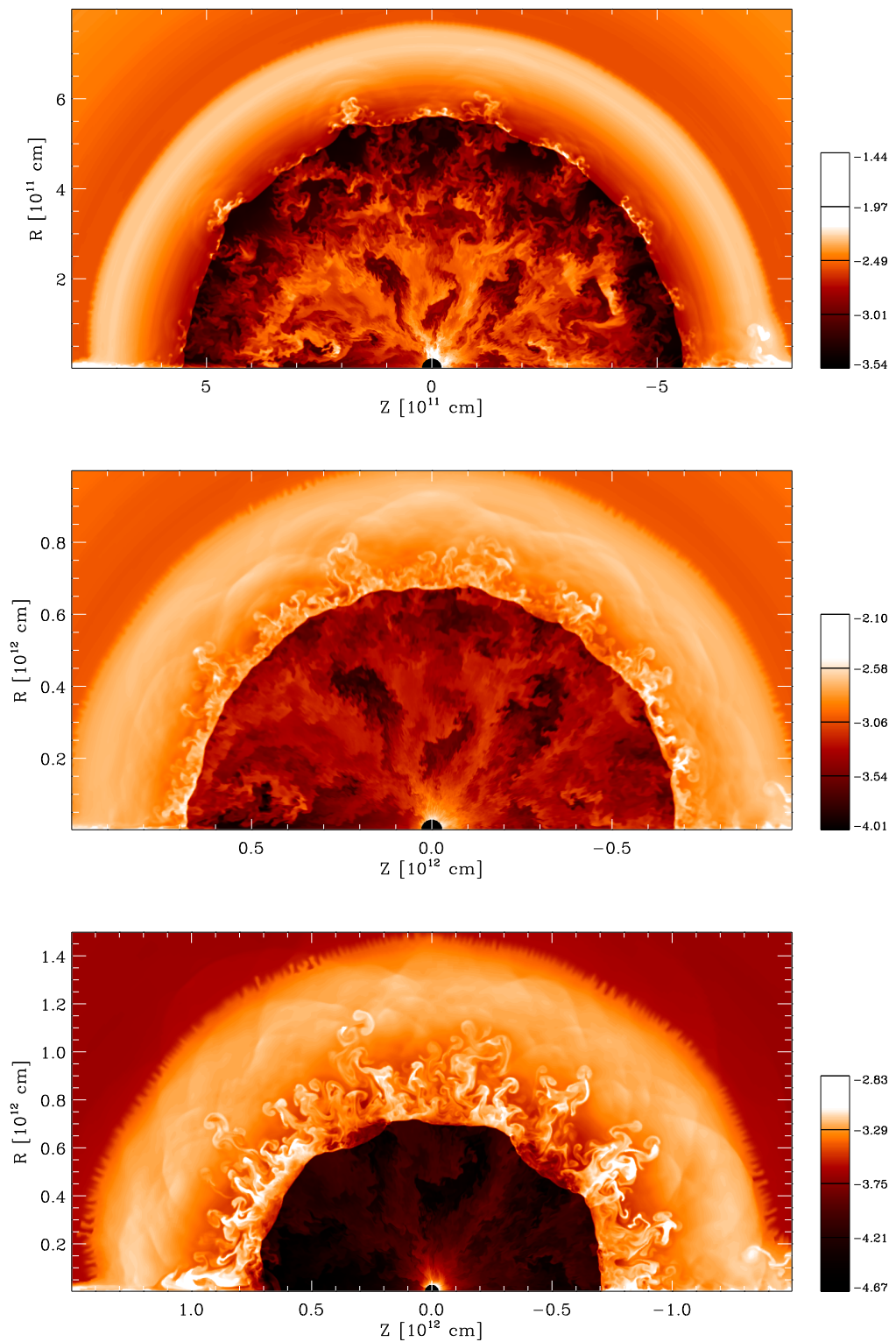
Figure 4.11: Same as Fig. 4.9 but showing a magnification of the central region of Fig. 4.10 b. The time is $t = 300$ s.

up with it at least as late as 5000 s after core bounce. In two dimensions, however, the fastest mushrooms already start to penetrate through the reverse shock around 1600 s after bounce (Fig. 4.10 c and Figs. 4.13 a to c). *This interaction of the metal-enriched clumps with the dense helium shell has not been reported in any previous calculation of Rayleigh-Taylor instabilities in Type II supernova progenitors. It is one of the most important effects that we see in our models and has direct and severe consequences for the velocity distribution of the elements because it leads to a strong deceleration of the clumps.* We will address this issue in more detail in Section 4.4.5. For the moment it is sufficient to note that after penetrating through the reverse shock, the clumps have to move supersonically through the high-density shell. As a result they are dissipating a large fraction of their kinetic energy in bow shocks and strong acoustic waves. The wave fronts can be seen in Figures 4.13 a to c which show the interaction of the clumps with the shell between 3000 s and 10 000 s after bounce as well as in Fig. 4.14 which shows a magnification of the central region of Fig. 4.13 c. The latter figure also indicates that during this interaction the composition within the clumps themselves is almost entirely homogenized. Furthermore, acting as a "wall"

Figure 4.12: Same as Fig. 4.9 but showing a magnification of the central region of Fig. 4.10 c. The time is $t = 1600\,\mathrm{s}$. The whitish spots in the right panel result from a superposition of the red, green and blue color channels which have been assigned to the different nuclei. Thus white coloring indicates a homogenization of the composition.

the shell has shielded the hydrogen envelope of the star from becoming enriched with freshly synthesized elements. This is a very interesting result, because it allows for some conclusions about the explosion mechanism and the structure of the progenitor star. Recall from our discussion in Section 2.2 that nearly all previous calculations of Rayleigh-Taylor mixing in Type II supernovae were started about 300 s after core bounce from one-dimensional explosion models making use of ad hoc seed perturbations. Therefore, these calculations did not allow one to probe the explosion mechanism by confronting the outcome of the simulations with observations. This, however, *is* possible with consistent multidimensional models.

The mixing between hydrogen envelope and helium core in SN 1987 A, is of crucial importance in this respect. Although, as we have shown by a linear stability analysis in Section 4.3.2 the He/H interface of the Woosley et al. (1988) star is Rayleigh-Taylor un-stable, in model T310 we did not find a strong growth of the instability at this interface which might have led to the required amount of mixing (but see also the discussion of

Figure 4.13: Logarithm of the density in model T310. From top to bottom: a) $t = 3000\,\text{s}$. b) $t = 5000\,\text{s}$. c) $t = 10\,000\,\text{s}$.
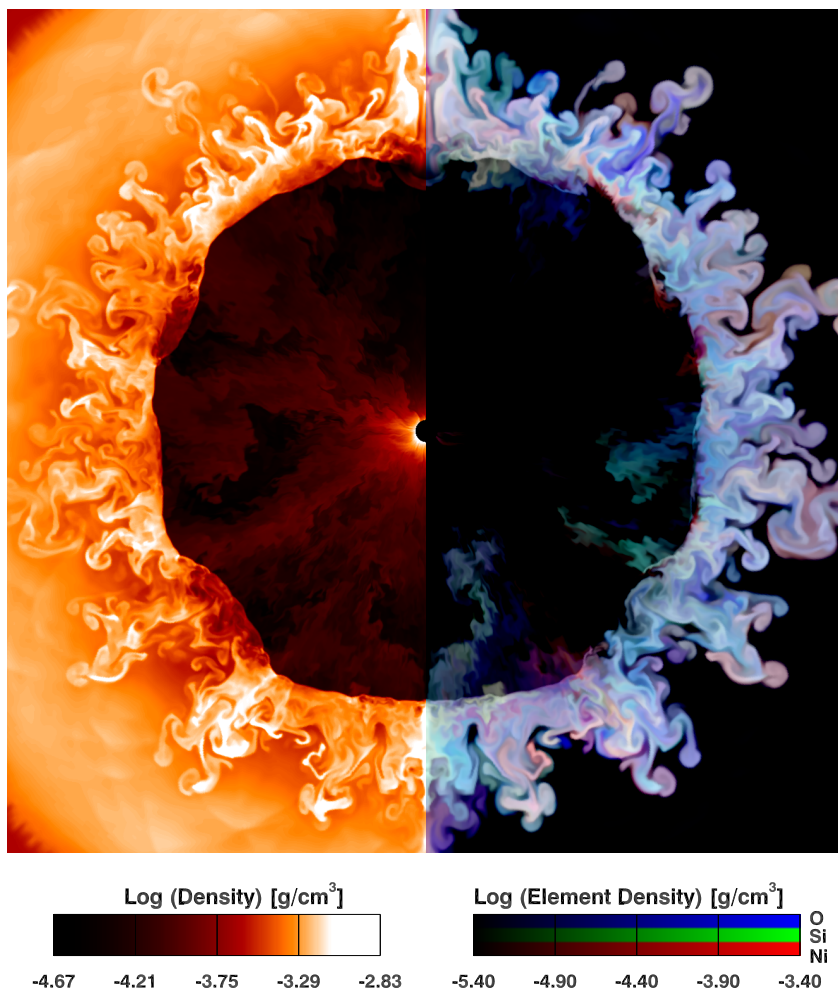
Figure 4.14: Same as Fig. 4.9 but showing a magnification of the central region of Fig. 4.13 c. The time is $t = 10\,000\,\text{s}$.

model T280* below regarding this point). Since the supernova shock is almost perfectly spherically symmetric when it crosses the He/H interface the evolution in these layers proceeds basically one-dimensionally. Only when the metal-enriched clumps reach the inner boundary of the dense shell behind the interface and start to dissipate their energy about 3000 s after bounce, are perturbations from spherical symmetry induced by the waves which are thereby excited. However, these perturbations encounter only a moderately unstable interface at this time. This is suggested by the linear stability analysis (Fig. 4.6) which shows that after 3000 s of evolution the temporal integral of the growth rate, σ, has ceased to grow. Therefore only small scale variations at the He/H interface can be seen up to the end of the simulation and the instability at this interface never enters the non-linear regime. It is likely that this result will also hold in case other progenitor models are used. Our current simulations therefore indicate, that *on its own neutrino driven convection is not able to provide the perturbations which are needed to induce strong mixing of the helium core and the hydrogen envelope.* Thus other sources for this mixing, which has been unequivocally observed in SN 1987 A, must be sought for. This might hint towards convective activity in these layers which

deviates markedly from mixing length theory, as found recently by Bazan & Arnett (1998) in case of the oxygen burning shell. It might also point towards a pronounced large scale asphericity of the shock wave as found in models of core collapse that include the effects of rotation. In addition, anisotropic neutrino emission and jet-like outflows might also be involved. We will discuss these issues further in Section 4.4.5.

4.4.3 Model T280*

The evolution of model T280* resembles in general that of model T310. However, there are three main features of this sequence which need to be noted in order to understand the differences in the extent of the mixing and the velocities of different nuclei which we will discuss below. First of all, gravity was neglected in the AMR computation which was started from the shock revival data of T280*, i.e. in this AMR run no gravitational binding energy had to be overcome. This was different in case of model T310, where gravity has been included in both, the shock revival as well as the AMR simulation. Thus although the explosion energy

$$E_{\text{expl}} = E_{\text{kin}} + E_{\text{int}} - |E_{\text{grav}}| \tag{4.5}$$

of model T280* was smaller than for T310 at a time of 0.8 s after bounce (see Table 3.1), due to

$$E_{\text{grav}}^{\text{AMR}}(\text{T280}^\star) \equiv 0 \tag{4.6}$$

in the corresponding AMR calculation, model T280* ended up with an explosion energy of $\sim 1.87 \times 10^{51}$ ergs which is *larger* than the final explosion energy[2] of model T310 by more than 20%. Therefore the overall expansion in model T280* was somewhat faster. Secondly, 0.8 s after bounce model T280* showed asphericities on much larger scales as compared to model T310 due to larger convective elements and supersonic convective velocities that resulted from the stronger neutrino driven convection in this model. Finally, also the shock wave itself was markedly deformed (see Fig. 3.29). This had two main consequences for the AMR calculation which was started from model T280*.

i) The asphericity of the shock led to an anisotropic perturbation of the He/H interface due to odd-even decoupling (see below).

ii) The asphericity of the dense shell which had formed near the Si/O interface resulted in a more uneven distribution of the inner ejecta by the Rayleigh-Taylor instability than in model T310

In particular, two strong outflows formed near the polar axis due to the effects which were discussed in Section 3.9. These can be seen in Fig. 4.15, while a comparison with Fig. 4.10 also shows that they are much more pronounced than the similar features that are observed for model T310.

As we already mentioned, model T280* was affected by odd-even decoupling throughout both the shock revival and AMR calculations. In the former simulation the shock was only locally aligned with the grid due to its large-scale asphericity and the numerical instability developed predominantly for angles $\theta \approx 135°$. Yet, we have found that after a few seconds of evolution in the subsequent AMR calculation, the shock

---

[2]Note that the values given for a time of 0.8 s in Table 3.1 are not corrected for the binding energy of the outer stellar layers.
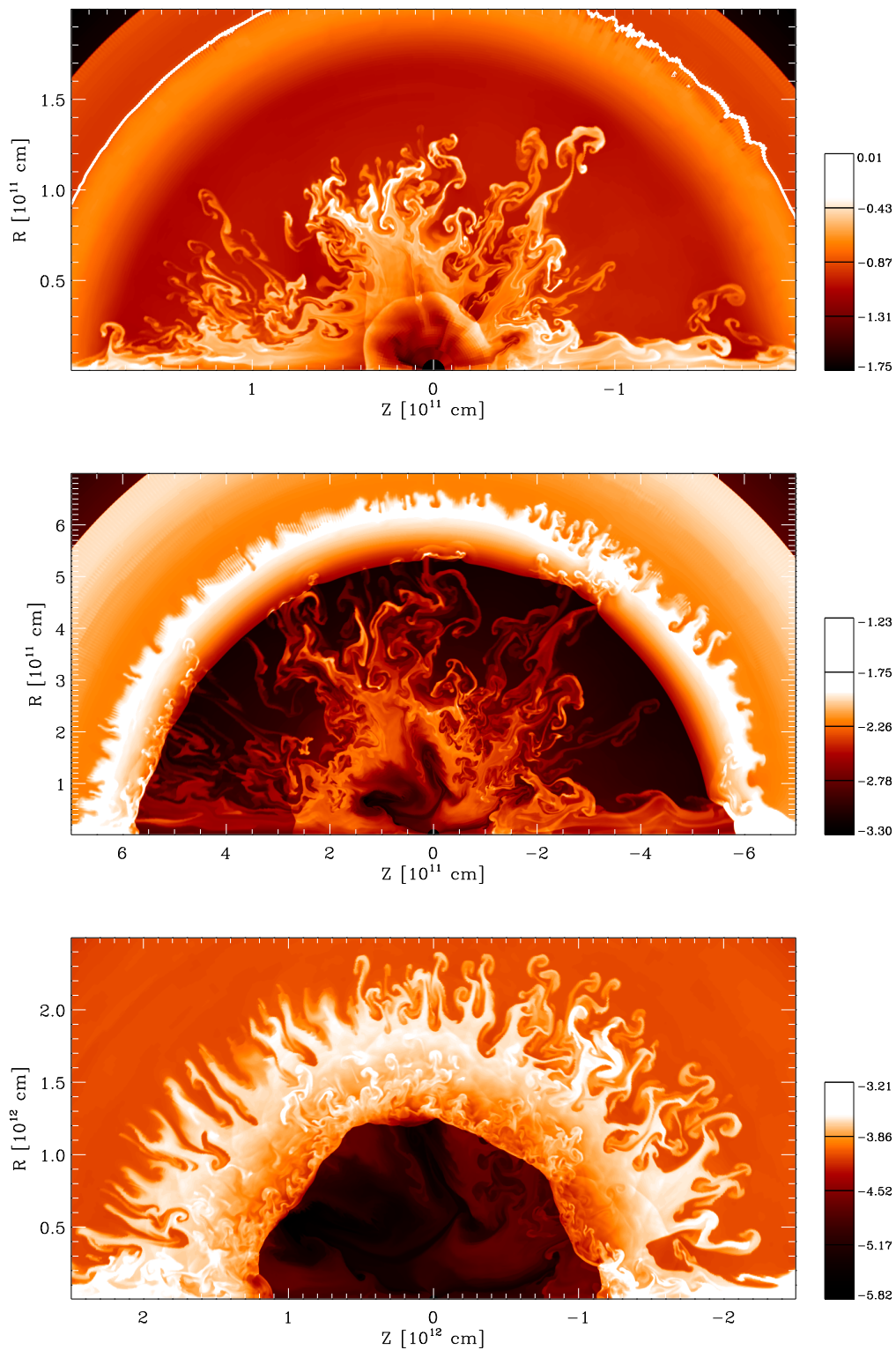
Figure 4.15: Logarithm of the density in model T280*. From top to bottom: a) $t = 300$ s. The white contour line marks the He/H interface. b) $t = 1600$ s. c) $t = 10000$ s.

had almost lost its initial asphericity. Only a small anisotropy remained at the time when the shock was about to cross the He/H interface. Therefore odd-even decoupling began to develop along the entire extent of the shock wave, starting at angles $\theta \approx 135°$ where the shock was aligned with the grid since the beginning of the calculation and subsequently spreading along the entire shock wave. Strong perturbations of a purely numerical origin were thus imposed on the flow, which in the immediate post-shock region amounted to about 20% of the radial velocity. As a result of this numerical noise the growth of Rayleigh-Taylor instabilities was artificially strongly enhanced, especially for angles $\theta \approx 135°$ which suffered strongest from the numerical defect. This explains why e.g. the prominent mushroom, which is visible along the diagonal in the right part of Fig. 4.15 a has grown faster than the surrounding features.

Furthermore, the strong ripples which were imposed on the velocity and density field, and which are responsible for the ragged appearance of the He/H interface in Fig. 4.15 a, led to an enormous growth of the Rayleigh-Taylor instability in these layers. This can be observed already at an epoch of 1600 s after bounce (Fig. 4.15 b). At a time of $t = 10\,000$ s (Fig. 4.15 c) large mushroom structures have formed and significant mixing of the helium core and hydrogen envelope is visible. Note also the asymmetry between the right and left part of the density image at this time, which is due to the stronger noise imposed for angles $\theta \approx 135°$ as compared to $\theta \approx 45°$ because of the reasons which were mentioned above. In the former case the instability has fully evolved into the non-linear regime with the Rayleigh-Taylor fingers being already capped by mushroom heads while in the latter only finger-like structures can be observed at that time.

The *qualitative* differences which can be seen when comparing Figs. 4.10 and 4.13 with Fig. 4.15 once more underscore the importance of using an excellent numerical scheme for a reliable calculation of this problem and the extraordinary care which is required even when state-of-the-art numerical methods are used. Numerical noise can completely bury the underlying physics and even lead to wrong conclusions. This is especially crucial in this case since the spectrum of perturbations in the helium cores and hydrogen envelopes of massive stars is still unknown. Being unaware of odd-even decoupling and given the results shown in Fig. 4.15 one might have concluded that the perturbations induced by neutrino driven convection could also cause strong mixing at the He/H interface. Actually, however, the results of Section 4.4.2, which are based on reliable numerics, suggest that this does not hold.

4.4.4 Implications of the mixing for observations

To facilitate a comparison of our two-dimensional models with one-dimensional work, upon which basically all attempts to reproduce observations are based, we summarize the extent of the mixing as a function of the enclosed mass and time for models T310 and T280* in Figures 4.16 and 4.17, respectively. The plots labeled with "0 s" show the distribution of the mass fractions for the original presupernova model. In these plots, the Si/O interface can be found at a mass coordinate of $1.50\,M_\odot$ while the C+O/He and He/H interfaces are located at $1.68\,M_\odot$ and $4.2\,M_\odot$, respectively. Note that already within the first 300 s of the explosion elements like ^{16}O and ^{28}Si, that made up the original metal core as well as the newly synthesized ^{56}Ni have been mixed almost homogeneously throughout the inner $2\,M_\odot$ and $2.3\,M_\odot$ in models T310 and T280*, respectively, i.e. throughout about the inner half of the helium core. In model

T310, the extent of mixing increases up to $2.7\,M_\odot$ at $10\,000\,\text{s}$ and is identical for the nuclei ^{28}Si, ^{16}O and ^{56}Ni as we have already seen above. The only species which are not mixed this far out in mass are ^{44}Ti and our neutronization tracer. These nuclei were synthesized in the innermost layers of the ejecta which were located very close to the collapsed core. In the right halves of Figs. 4.11, 4.12 and 4.14, i.e. in the plots of the element distributions, these nuclei occupy mostly the black innermost regions. The situation differs somewhat in model T280*. Figure 4.17 shows that $10\,000\,\text{s}$ after bounce our neutronization tracer nucleus has been mixed outward along with ^{28}Si and ^{56}Ni to mass coordinates as large as $4.5\,M_\odot$, i.e. up to the base of the hydrogen envelope. Note that the stronger the mixing of neutronized material into the hydrogen envelope is, the more of this material will *not* fall back to the central remnant as is required by nucleosynthetic studies (see e.g. Janka & Müller 1996; Herant et al. 1994). Responsible for the strong mixing in model T280* are

i) the pronounced anisotropy of the ejecta due to strong neutrino driven convection,

ii) the large perturbations imposed on the unstable regions by odd-even decoupling,

iii) the more energetic explosion, and

iv) the interaction of the instabilities which originated in the metal core with the one at the He/H interface.

The contributions of these effects are difficult to disentangle, however. Especially the importance of the first item in the list above remains unclear, because odd-even decoupling had affected model T280* already since the first seconds of its evolution. About 300 seconds after bounce the ^{28}Si and ^{56}Ni-enriched mushrooms are polluted with as much as $0.04\,M_\odot$ of neutronized material in this case. In model T310 a much stronger concentration of neutronized matter to the central regions of the ejecta is observed. However, it is not clear whether this must be mainly attributed to the suppression of odd-even decoupling in this model, or to the more isotropic distribution of the ejecta at the time when the AMR calculations were started (i.e. $t = 0.8\,\text{s}$). Yet, it is clear that the more energetic explosion in case of model T280* has ejected a few of the clumps close to the region near the He/H interface where they became engulfed in the Rayleigh-Taylor mixing of these layers.

The small amount of fallback (a few $10^{-3}\,M_\odot$) that we see in case of the $15\,M_\odot$ Woosley et al. (1988) star[3] does not support the hypothesis that the neutronized material must fall back to the central remnant. On the other hand, it is known (Woosley & Weaver 1995) that (for the same explosion energy) more massive stars have also more massive fallback. Thus our current results cannot be regarded to be conclusive in this respect. The recent one-dimensional shock revival calculations using Boltzmann neutrino transport (Rampp & Janka 2000; Mezzacappa et al. 2000) indicate, however, that a solution to the overproduction problem of $N = 50$ nuclei (see Section 3.9) must probably be sought in the explosion mechanism itself.

We have pointed out already that without very strong mixing at the He/H interface (as e.g. in model T280*) all heavy elements remain confined to the He core (as in our realistic model T310), and that thus mixing of ^{56}Ni into the outer hydrogen envelope of the star as observed in SN 1987 A by the early detection of γ-rays cannot be reproduced. However, models like T310 appear to be very promising in order to naturally explain the
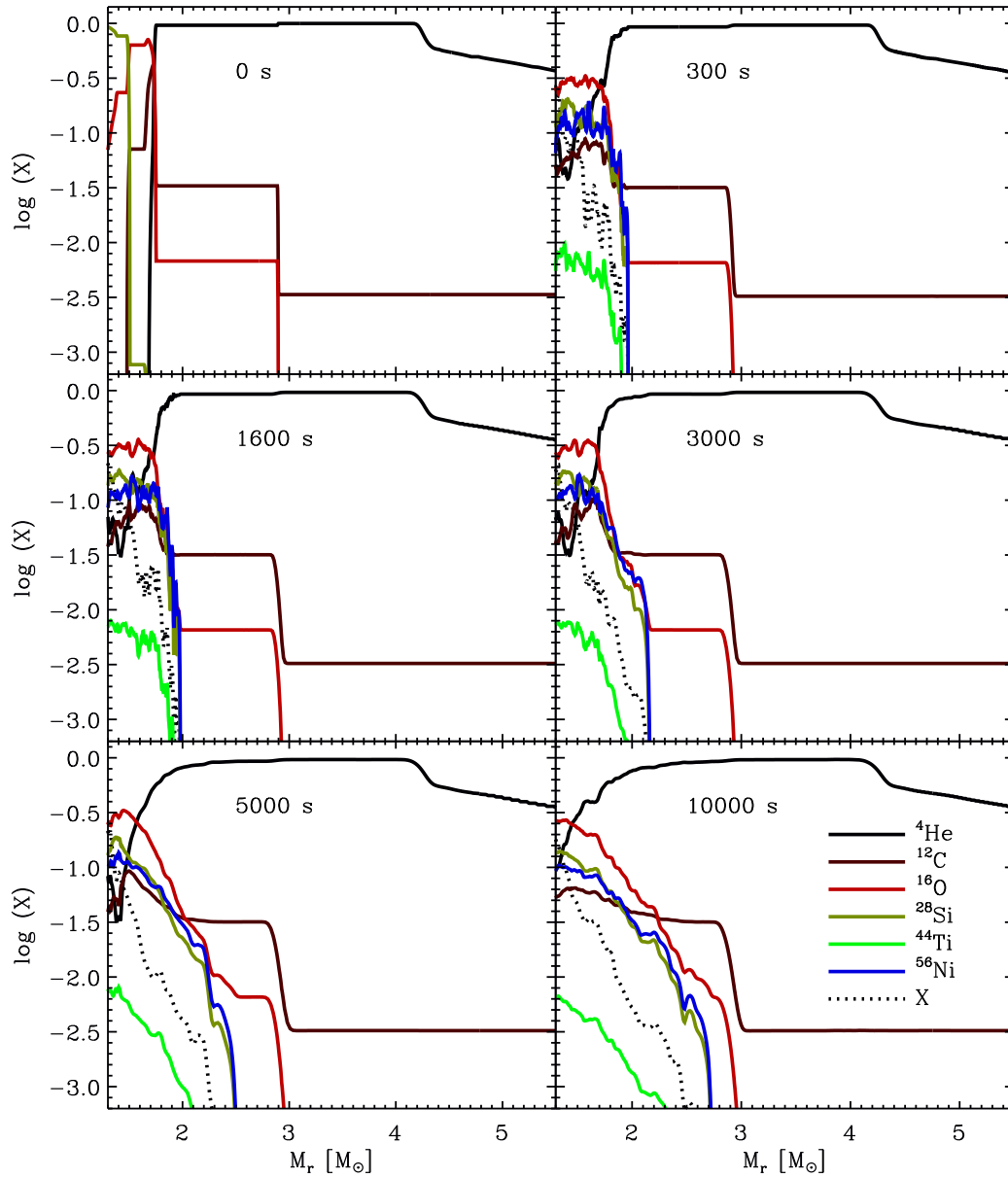
---

[3]using rather energetic explosion models, however

Figure 4.16: Evolution of the extent of the mixing in model T310. Note that all heavy elements are confined to the helium core (i.e. to the innermost $4.2\,M_\odot$ of the star) even for times as late as $10000\,s$ after bounce.
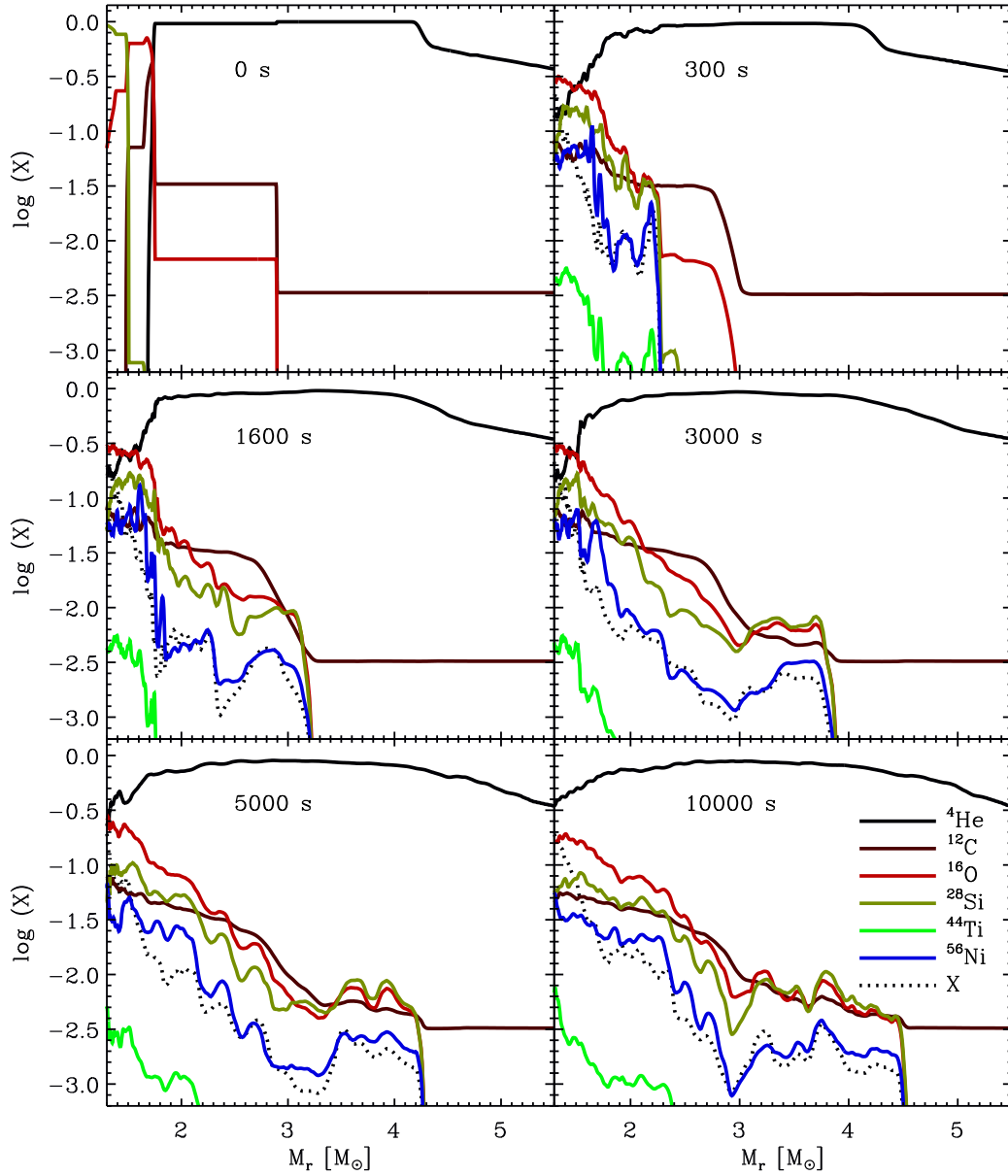
Figure 4.17: Evolution of the extent of the mixing in model T280⋆. Note the differences as compared to Fig. 4.16. While the bulk of the heavy elements is located at mass coordinates interior to $3\,M_\odot$ a small fraction of the metals has been mixed out to the base of the hydrogen envelope by the interaction of the instabilities originating in the metal core and at the He/H interface.
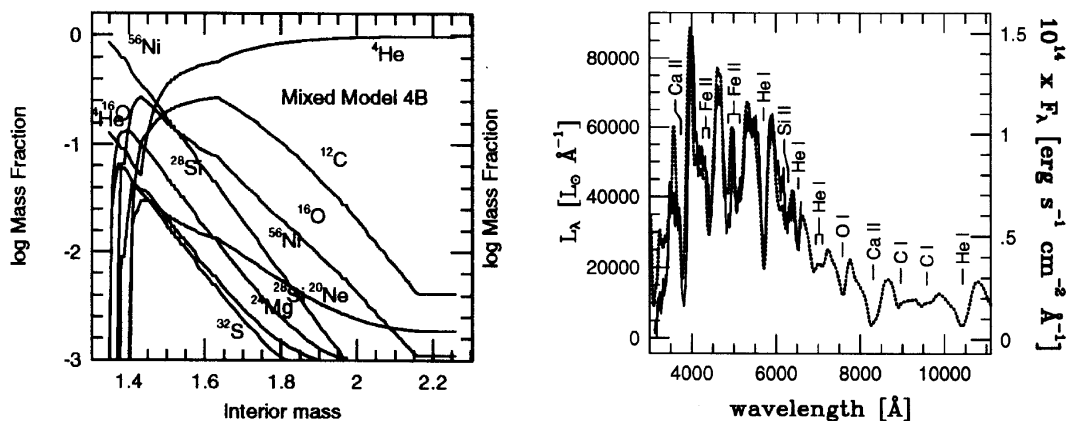
Figure 4.18: Left: Artificially mixed one-dimensional model of a $2.3\,M_\odot$ He core. Right: synthetic spectrum of this model + SN 1984 L data (dots). From Woosley & Eastman (1997).

mixing which has been inferred for several Type Ib explosions. Although the progenitors of Type Ib supernovae have not been unambiguously identified yet, one of the scenarios involves stars with a main sequence mass of around $15\,M_\odot$ which owing to a strong stellar wind or mass transfer in a binary system loose their entire hydrogen envelope prior to explosion. The collapse of the evolved iron core of the star then leads to an explosion within a stripped helium core. The hydrodynamic evolution in this scenario is identical to that of a Type II supernova until the time when the shock reaches the outer layers of the He core, i.e. within about the first minute of the explosion. Thus our models provide some insight also in this case. Differences in the hydrodynamics result only after this early stage, because the supernova shock will never encounter a thick hydrogen envelope in case of a Type Ib explosion and instead propagates down a steep density gradient when leaving the helium core of the star and entering the tenuous circumstellar medium.

The strong mixing that we have found to be triggered in case of the Woosley et al. (1988) model by the interaction of neutrino driven convection with Rayleigh-Taylor instabilities at the Si/O interface appears to solve a problem in the spectral modeling of Type Ib explosions that has puzzled several workers since Type Ib's were recognized as a separate class of supernovae in the late nineteen-eighties. In Section 2.1.2 we have already discussed the problems which are connected to the strength of the observed He I lines and which require a strong nonthermal source of heating in order to explain the spectra of these objects. Using a stripped $2.3\,M_\odot$ He core Woosley & Eastman (1997) have, for instance, computed synthetic spectra from one-dimensional explosion models and demonstrated that good fits to observed spectra of SN 1984 L could be obtained. However, this was only the case if they assumed a substantial amount of [56]Ni mixing into the helium envelope. The adopted element distribution for their "model 4B" is shown in the left panel of Fig. 4.18. Note the exponential decline of the [56]Ni mass fraction which decreases below 10^{-3} only at a mass coordinate of $\sim 2\,M_\odot$. The synthetic spectrum obtained from this model is shown in the right part of Fig. 4.18 together with data of SN 1984 L near maximum light. Clearly the quality of the fit is very good. Comparing our multidimensional model T310 (Fig. 4.16) with model 4B of Woosley & Eastman (1997) we find a flatter decrease of the [56]Ni mass fraction with mass for a time of $300\,$s after bounce (when effects due to the hydrogen envelope in our

Type II supernova model are not that pronounced yet). However, the outer boundary of the nickel enriched core coincides with that of the Woosley & Eastman (1997) model! Since this is the quantity which largely determines the flux of ionizing γ-photons in the He envelope, future hydrodynamic modeling which will include a consistent treatment of the explosion in two (and three) dimensions appears to be very promising in order to reproduce the spectra of Type Ib supernovae. That, in addition, the light curves might be reproduced as well is indicated by several publications (Shigeyama et al. 1990; Hachisu et al. 1994; Woosley & Eastman 1997). As pointed out by Hachisu et al. (1994) the main problem in this respect is the assumed amplitude of seed perturbations in multidimensional calculations of the Rayleigh-Taylor instability which must exceed 5% of the radial expansion velocity at the time the shock crosses the unstable interfaces in the metal core. Our models show that this is indeed the case if neutrino driven convection is taken into account!

The fact that convection seeds primarily Rayleigh-Taylor mixing at the Si/O interface of the star might also provide a natural explanation for the mixing observed in Type Ic supernovae. While (as with Type Ib) the progenitors of Type Ic explosions have not been unambiguously identified yet, at least one class of the proposed models assumes an explosion in a bare C+O core (Nomoto et al. 1997). Although there is no final consensus whether this is indeed a viable scenario for Type Ic's (see the discussion in Section 1.1) recent observations (Matheson et al. 2000) appear to support this hypothesis. Lacking a helium envelope and therefore also a C+O/He interface at which a strong Rayleigh-Taylor instability could develop, the mixing observed in these events could not be explained in the framework of bare C+O stars, unless jets and other large scale asphericities were invoked (Nakamura et al. 2000). Given the strong mixing that we find at the Si/O interface of our models, these assumptions are no longer necessary.

We therefore conclude that *the interplay of neutrino driven convection and Rayleigh-Taylor instabilities offers a natural explanation for the amount of mixing which is observed in Type Ib and Type Ic supernovae.*

4.4.5   Velocity distributions of the elements

The dynamics of the explosion is reflected in the distribution of the mass of the single isotopes in velocity space. Since the main hydrodynamic effects are the same for models T310 and T280* this distribution displays a similar behavior for both simulations over the entire evolution within the first 10 000 s, though the different explosion energies of the models lead to somewhat different quantitative results. In Fig. 4.19 we show the logarithm of the fractional mass which is contained within the velocity interval $[v_r, v_r + \mathrm{d}v_r]$ as a function of the radial velocity for model T310 and times from 2 s until 50 s after bounce. Fig. 4.20 shows the same quantities for model T280*. The most conspicuous feature which can be seen in these plots is the bulk deceleration of the material from velocities as large as $\sim 15\,000$ km/s at a time of 2 s after bounce to less than 5000 km/s after 50 s. This is purely a manifestation of the enormous deceleration that the shock, and with it the post-shock material, experience when propagating through the helium core of the star. Superimposed upon this main trend is a clear tendency of the mass distribution of ^{28}Si, ^{56}Ni and (to a weaker extent) ^{16}O to narrow down in velocity space. The original separation of the velocities of these elements that establishes within the first second of the explosion due to their spatial separation and the existence of a velocity gradient behind the shock (Section 3.12) is dissolved within
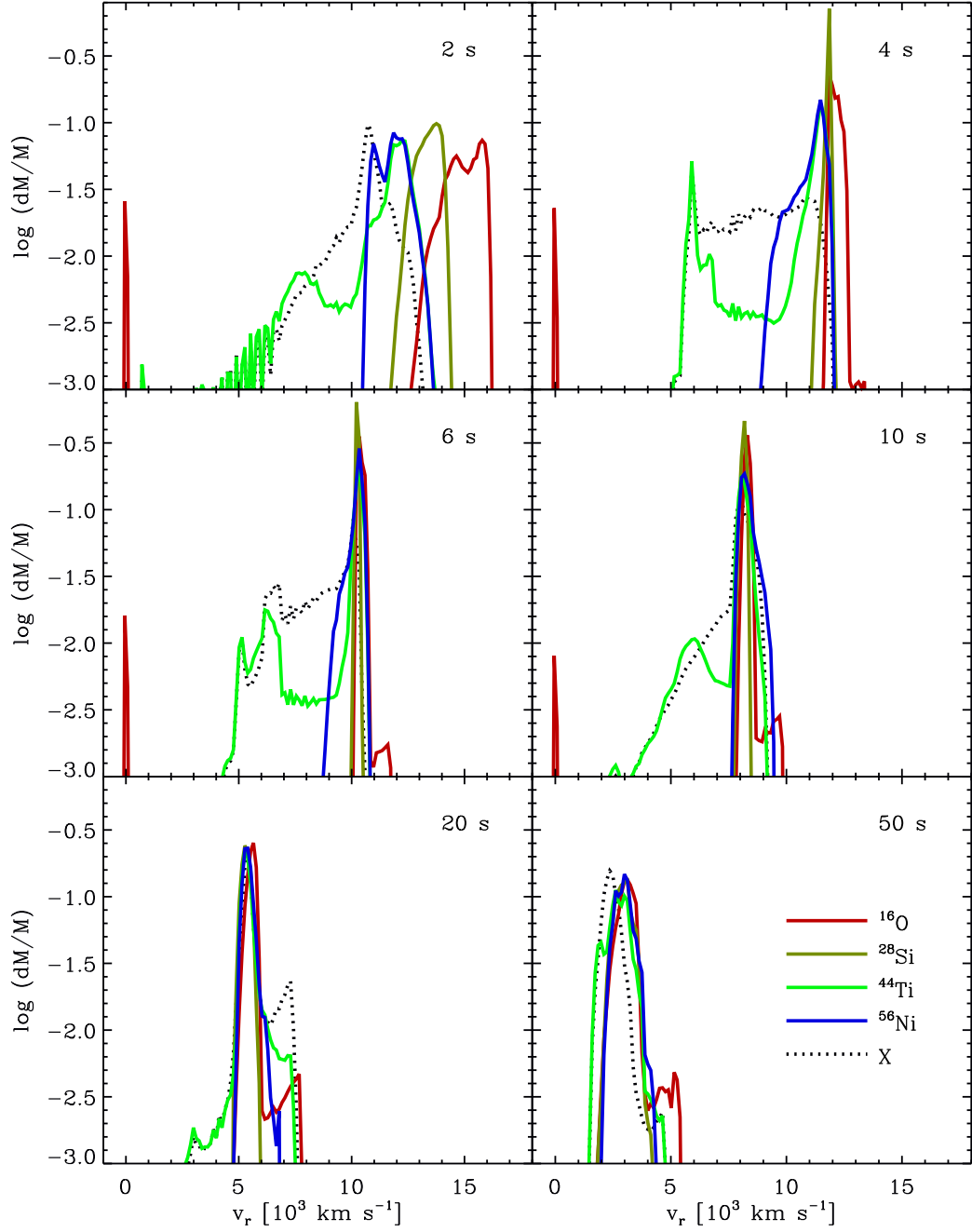
Figure 4.19: Logarithm of the fractional element mass which is contained within the velocity interval $[v_r, v_r + \mathrm{d}v_r]$ as a function of the radial velocity v_r in model T310 at various early epochs. The resolution is $\mathrm{d}v_r \approx 130\,\mathrm{km\,s^{-1}}$.
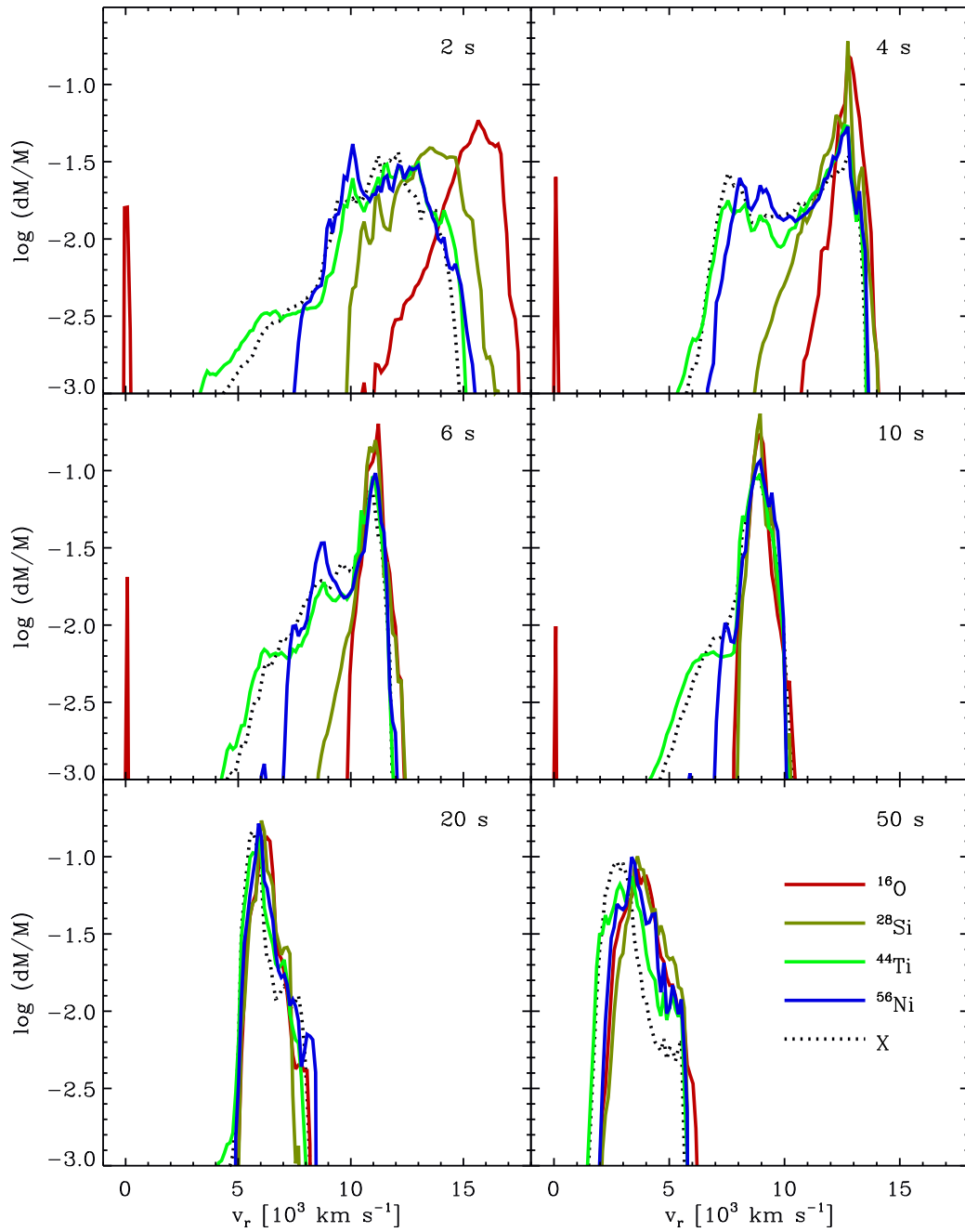
Figure 4.20: Same as Fig. 4.19 but for model T280⋆.

the first 20 s after bounce. The reason for this behavior is the strong compression that the post-shock layers experience after the supernova shock has crossed the C+O/He interface. Being squeezed into a very dense shell, ^{56}Ni and ^{28}Si are hardly separated in radius for times $\geq$ 10 s and thus both nuclei reflect the velocities that are prevailing in this shell. The bulk of ^{16}O is located only marginally farther out in radius and thus displays rather comparable velocities. All these effects lead to the narrow peak in the velocity distribution of these elements for times between 10 s and 50 s in Figs. 4.19 and 4.20. Being centered around 8000 km/s 10 s after bounce in model T310, this peak gradually recedes to velocities of $\sim$ 3000 km/s at $t = 50$ s. The maximum velocities for ^{56}Ni and ^{28}Si are higher than this value by about 1500 km/s, while a small fraction of ^{16}O is found at somewhat higher velocities, still. Elements that are not exclusively confined to the compressed shells (i.e. ^{44}Ti and our neutronization tracer) show somewhat broader distributions in velocity space during the first seconds of the explosion until the growth of the Rayleigh-Taylor instability at the Si/O interface also affects the spatial distribution of these nuclei and leads to a homogenization of all profiles in Fig. 4.19 around 50 s after bounce.

For the late evolution of models T310 and T280* which is depicted in Figures 4.21 and 4.22, respectively, we focus on the maximum ^{56}Ni velocity since this is the most interesting outcome of our simulations for a comparison with observations. Note that up to a time of 300 s in model T310 and 100 s in model T280*, when the instability is still developing, this velocity is steadily decreasing and reaches values of $\sim$ 2600 km/s in T310 and 4800 km/s in T280*. The maximum velocity is found in the mushroom caps of the Rayleigh-Taylor fingers. Since these "clumps" have to propagate through a rather dense medium in the early stages of their existence they are initially decelerated appreciably by their surroundings. At the times quoted above, however, the density contrast between them and their environment has grown substantially. The clumps thus "decouple" from the flow and start to move almost ballistically through the remaining part of the helium core. As a result, the maximum ^{56}Ni velocity remains constant for times between 300 s and 1600 s in model T310, and 300 s to $\sim$ 1000 s in model T280*. The latter times approximately coincide with the instants when the clumps penetrate through the strong reverse shock at the inner edge of the dense shell that has formed at the He/H interface. Having entered this shell they are decelerated strongly, with the velocities dropping to values of 1000 km/s and 2000 km/s in models T310 and T280*, respectively at a time of 10 000 s after core bounce. *These velocities are significantly smaller than the ones which have been observed in SN 1987 A.* Note that at least in the energetic model T280* the clump velocities *are in accordance* with the observations prior to the interaction of the clumps with the shell, i.e. *a good match to the observations is primarily prevented by the formation of the dense shell in the outer He core, which in turn is caused by the deceleration of the main shock due to the flat density profile in the (inner) hydrogen envelope.*

In order to understand why this deceleration is so strong one needs to investigate in some more detail the situation before and after the clumps hit the shell. The main points can already be illustrated by consulting the one-dimensional data which is plotted in Fig. 4.1. Consider e.g. the situation 300 s after bounce in Fig. 4.1 and for a radius of $\log(r/\text{cm}) = 11.0$, i.e. in the layers of the inner helium core just in front of the metal-enriched shell which fragments in the two-dimensional calculation. The sound speed in these layers takes on a value of about 1400 km/s ($\log(c_s/(\text{cm/s})) \approx 3.15$). The flow itself is expanding with $\sim$ 2400 km/s in these regions. Superimposed upon this
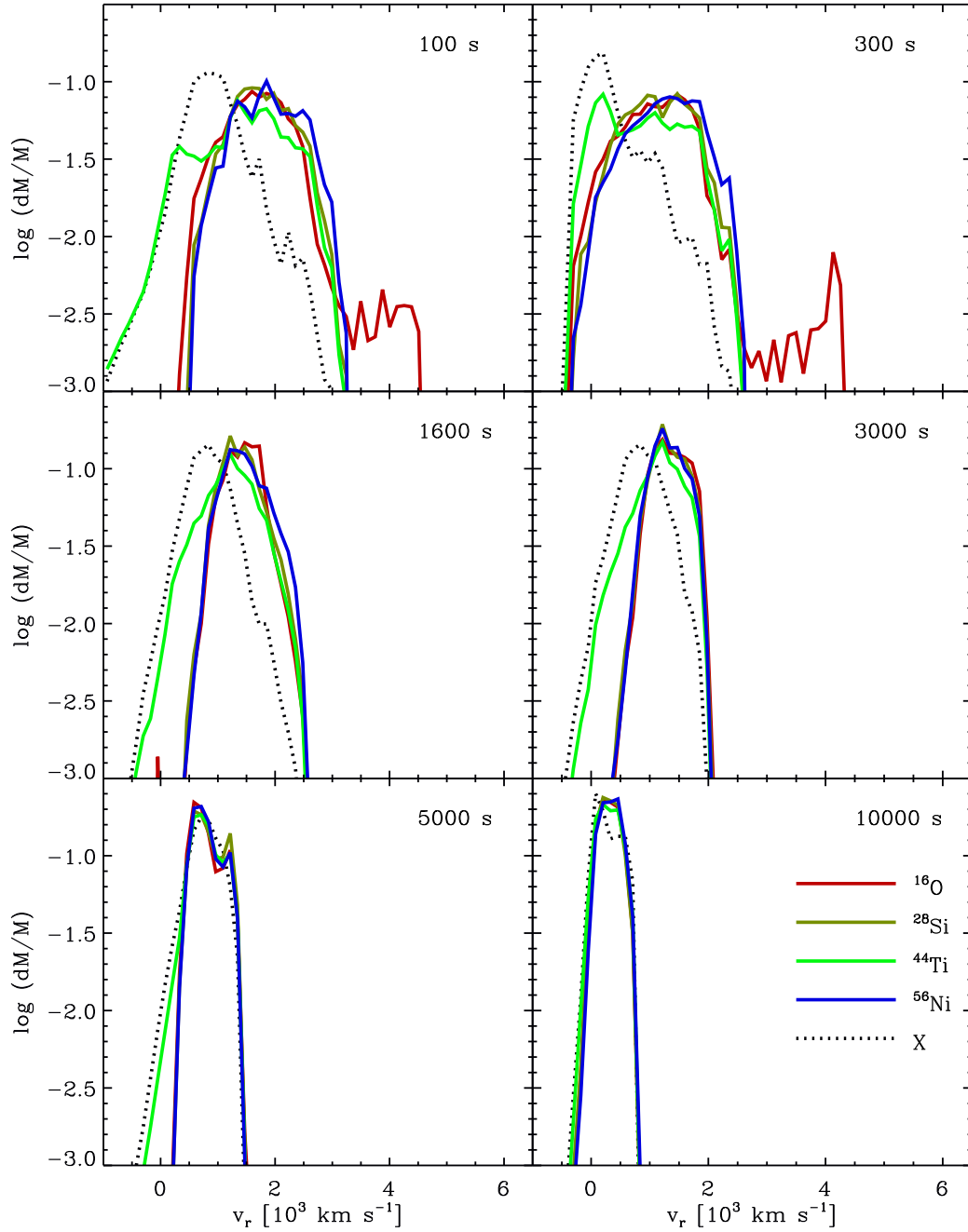
Figure 4.21: Logarithm of the fractional element mass which is contained within the velocity interval $[v_r, v_r + \mathrm{d}v_r]$ as a function of the radial velocity v_r in model T310 at various late epochs. The resolution is $\mathrm{d}v_r \approx 130\,\mathrm{km\,s^{-1}}$.
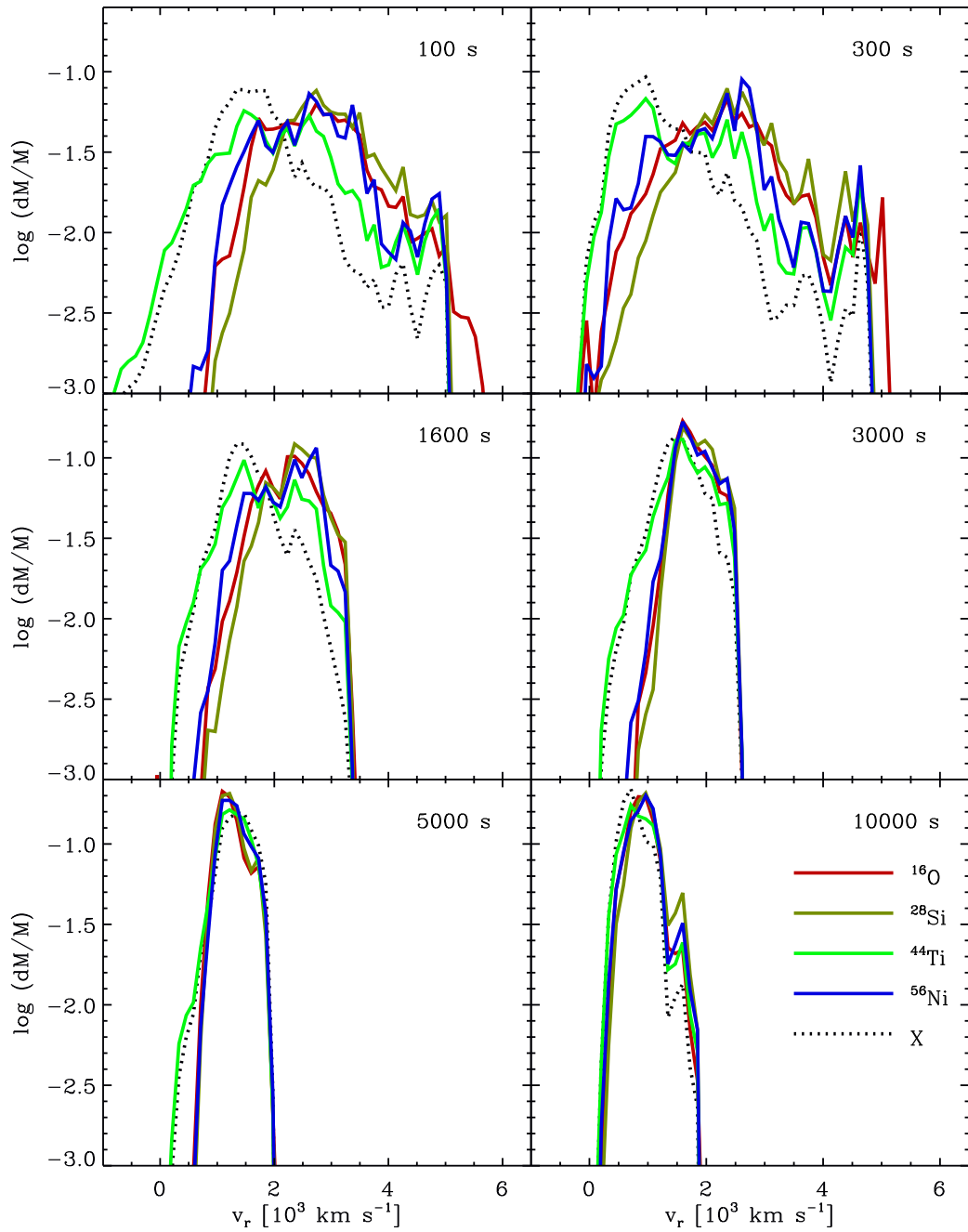
Figure 4.22: Same as Fig. 4.21 but for model T280*.

mean expansion is the propagation of the clumps in the two-dimensional case. At the considered epoch these have velocities of about 2600 km/s. Hence, the clumps move relative to the low-density layers of the inner He core, with only a few 100 km/s, i.e. their motion relative to the background is *subsonic*. Therefore, the drag they experience is rather small.

The situation changes, however, once the clumps penetrate into the shell. Recall that for model T310 this happens at a time around 1600 s after bounce. Since the clumps have to pass through a *reverse* shock they find themselves in an environment with a *smaller* mean expansion velocity than in the layers in front of the shock. Their velocity relative to the background is therefore *higher* than it was before they crossed the shock and at 1600 s amounts to about $600 - 700$ km/s. In addition, this velocity difference will tend to increase with time since the velocity behind the reverse shock *decreases* between 1600 s and 5000 s (Fig. 4.1). Considering the sound speed in the layers behind the shock at $t = 1600$ s, one can note that although there is a steep increase of this quantity due to the jump in pressure associated with the shock, its absolute value of 890 km/s is rather small. This is a result of the adiabatic cooling which is associated with the overall expansion decreasing the pressure and density with time. Since the expansion will continue to lower the sound speed in the dense shell, at some moment this must lead to *supersonic* motion of the clumps relative to their environment. The associated energy dissipation in this case is considerable[4]. In fact we have already pointed out in Section 4.4.2 that the entire dense shell is pervaded by bow-shocks and strong acoustic waves between times of 3000 and 10 000 s after core bounce.

During *no* phase of the evolution we do see an *acceleration* of material from the former metal core of the star. This is in contrast to the results of Herant & Benz (1992) who report to have obtained nickel velocities comparable to those observed in SN 1987 A provided that they "premixed" the ^{56}Ni in their SPH calculations throughout 75% of the metal core of their 20 M$_\odot$ progenitor. They claim that if the nickel is allowed to participate in the Rayleigh-Taylor instability at the He/H interface it can be accelerated to velocities in excess of 3000 km/s. We do not see any signs of such an effect in our calculations. Even in our "noisy" model T280* which showed strong mixing at the He/H interface the velocities of all elements are steadily *decreasing* throughout the first 10 000 s of evolution. The effects that we observe suggest that the occurrence of conditions which could give rise to the development of an instability at the He/H interface is actually *harmful* for the propagation of the clumps! Even if very strong perturbations are imposed upon the dense unstable shell which forms at this interface the instability is growing too slowly in order to shred this "wall" before the clumps will reach it. On the other hand, with a smoother density profile near the He/H interface, the dense shell might either not form at all or become at least less pronounced which might help the clumps to preserve most of their energy. This might hint towards uncertainties in current stellar evolutionary models, especially the treatment of convection and semiconvection, as being responsible for the discrepancy to the observations. A different density profile is also expected when the progenitor star of SN 1987 A was not the result of the evolution of a single star but a merger of two smaller stars. This is indeed supported by numerous other observations of the environment of the super-

---

[4]The same effect forces fighter aircraft pilots to engage their afterburners in order to attain supersonic speeds, and accounts for the largest fraction of the $10 000 bill that passengers of the Concorde have to pay for the round trip Paris–New York–Paris!

nova (see the "chain of evidence" presented in Podsiadlowski 1992). However, it is not clear whether such a scenario could solve all problems. After all, significant mixing of the He core and hydrogen envelope *has been observed* in SN 1987 A and is difficult to explain without strong Rayleigh-Taylor mixing (and thus strong shock deceleration in the hydrogen envelope what in turn implies dense shell formation).

The dimensionality of our simulations may also be a possible cause of the problem. The fingers found in two-dimensional calculations are in fact axially symmetric tori which also experience a larger drag when propagating outwards than genuinely three-dimensional mushroom structures. This may be crucial for the outcome of the interaction of the clumps with the dense shell. Clarifying this issue will be extremely difficult, though. Unfortunately an extension of the high-resolution calculations that we have presented in this thesis to three spatial dimensions will pose tremendous computational difficulties. Although first steps in this direction are currently being performed there is only little hope that with available hardware it will be possible to obtain results of comparable numerical quality as in two dimensions.

Finally, "missing physics" in the modeling of the explosion itself might be responsible for the small maximum nickel velocities that we obtain. On its own, the kind of small scale asphericities that we have found may not give an adequate description of the flow, if effects like rotation or anisotropic neutrino emission are important for the explosion mechanism. These may result in an additional *large scale* asphericity of the shock or even in jet-like outflows of the ejecta. Nagataki et al. (1998b) claim that when using almost "jet-like" shock waves it is possible to reproduce nickel velocities in excess of 3000 km/s. However, their calculations suffer from a lack of resolution and from rather unrealistic parameterized initial conditions and thus more elaborate calculations are required before definite conclusions can be drawn in favor of these effects.

Chapter 5

Summary and outlook

Having guided the reader through the first hours in the life of a model core collapse supernova in the last chapters, we can now summarize our main findings. In Chapter 3 we have presented multidimensional hydrodynamic calculations which covered about the first second of the evolution including the neutrino driven initiation of the explosion, the mixing due to convective instabilities between proto neutron star and shock as well as the explosive nucleosynthesis. Although these calculations were necessarily simplified in many respects and furthermore are based on a single ($15\,\mathrm{M}_\odot$) progenitor model, they allow to draw some first preliminary conclusions concerning the effects of multidimensional hydrodynamics and neutrino transport on the nucleosynthesis in core collapse supernovae.

In particular, our simulations indicate that the hitherto performed one-dimensional explosive nucleosynthesis studies appear to give reliable yields for the products of explosive *oxygen, neon and carbon burning*. The only multidimensional effect which influences the nucleosynthetic yields of these types of burning in our calculations is the possible asphericity of the shock wave. Its impact was found to be small. However, we have hopefully also conveyed that neutrino-matter interactions and multidimensional hydrodynamics conspire in complicating the problem of ^{56}Ni synthesis in core collapse supernovae to an extent, which has not yet been anticipated on grounds of one-dimensional calculations. We have argued that an accurate modeling of neutrino transport is indispensable in order to obtain an adequate description of the properties of the neutrino field, the degree of neutronization of the matter and the correct energetics of the explosion. Especially in case of low neutrino luminosities the latter is determined by a complex interplay with neutrino driven convection between gain radius and shock. The vigor of this convection determines the deviations of the thermodynamic conditions from spherical symmetry, the "stirring" of the post-shock gas and the amount of material which is exposed to the ν_e and $\bar{\nu}_\mathrm{e}$ fluxes from the proto neutron star. We have demonstrated that this in turn determines the yields and spatial distributions of the products of explosive silicon burning. Given the fact that the problem is further complicated by the impact prompt and neutron finger convection inside the neutron star have upon the electron neutrino and anti neutrino luminosities and spectra (these effects have been neglected in the present work) and our finding that even state-of-the-art hydrodynamic schemes are barely able to handle all the computational difficulties, substantial work is required until reliable ^{56}Ni yields from consistent multidimensional explosion models will be obtained.

Besides determining the nucleosynthetic yields, the first second of the explosion is

also crucial for the subsequent evolution of the supernova and our main results in this respect can be summarized as follows.

- The newly synthesized ^{56}Ni as well as the products of incomplete silicon and oxygen burning are confined to a high-density (low entropy) inhomogeneous shell that forms behind the outward sweeping shock.

- The outer boundary of this shell coincides with the Si/O composition interface and shows a negative density and a positive pressure gradient. This state is unstable to the Rayleigh-Taylor instability.

- Depending on the explosion time scale and the strength of neutrino driven convection the shell is either markedly or weakly deformed by deleptonized, rising, high-entropy material at its base.

- The wavelength of these perturbations is larger for large explosion time scales (or small explosion energies) and large initial seed perturbations.

- For explosion energies around 1.5×10^{51} ergs, ^{56}Ni is born with extremely high velocities, up to about $17\,000\,$km/s. These velocities are much larger than those observed in SN 1987 A, the closest supernova since centuries, and indicate that a substantial deceleration of this material must occur when it penetrates through the overlying layers of the star.

Indeed this was found to be the case in Chapter 4 where we presented results of the first calculations that were able to consistently follow the subsequent evolution of the supernova in two spatial dimensions until a few hours after core bounce. Of crucial importance in these simulations are Rayleigh-Taylor instabilities. When propagating through the envelope of the star the shock experiences short phases of acceleration when it crosses one of the composition interfaces and, subsequently, extended phases of deceleration when it enters regions where the density profile of the envelope falls off shallower than $\propto r^{-3}$. Every time the shock decelerates, a density inversion forms at the corresponding composition interface which is prone to Rayleigh-Taylor mixing. However, sufficiently large seed perturbations of a hitherto unknown origin must be present in these regions in order for the instability to grow and to reach the non-linear regime. Our calculations prove for the first time a hypothesis that has been proposed since the first multidimensional calculations of the explosion mechanism itself were performed in the 1990s: *Convective instabilities which develop during the first second of the explosion are able to provide the seed for significant Rayleigh-Taylor mixing.* In more detail we have found that

- Three Rayleigh-Taylor unstable regions develop in the model of Woosley et al. (1988): one at the Si/O interface, a second at the C+O/He interface and a third at the He/H interface of the star

- Seeded by the perturbations induced by neutrino driven convection, Rayleigh-Taylor mixing at the Si/O interface sets in already about 20 seconds after core bounce and leads to the formation of fingers of ^{56}Ni-enriched gas which distort also the C+O/He interface farther out

- Within only about five minutes after bounce the entire metal core of the Woosley et al. (1988) star is shredded

- Dense "bullets" and clumps of ^{56}Ni, ^{28}Si and ^{16}O-rich material decouple from the flow and start to propagate ballistically through the stellar helium core

- Depending on the energetics of the explosion, clump velocities as high as $4800\,\mathrm{km/s}$ are observed during this phase.

Up to this stage, our models are in excellent agreement with what has been observed in a number of extragalactic core collapse supernovae. In particular, the extent of the mixing is compatible with what has been inferred for the Type Ib SN 1984 L on grounds of spectral modeling studies. This result is very encouraging and indicates that the interaction of neutrino driven convection and Rayleigh-Taylor instabilities solves the problem of the origin of mixing in Type Ib events, which has been known from spectral studies for more than a decade. Moreover, since convection seeds primarily Rayleigh-Taylor mixing at the Si/O interface of the star, our calculations yield also a natural explanation for the mixing observed in Type Ic supernovae, which are presumably explosions in bare C+O cores. Given these results, at least in these two supernova types recourse to "non-standard" physics in the explosion mechanism appears to be unnecessary.

The ^{56}Ni velocities that we find during the first ~ 30 minutes of the explosion are as high as those measured in the Type II SN 1987 A and the Type IIb SN 1993 J. The main reason for this coincidence was found to be a subsonic ballistic motion of the ^{56}Ni clumps relative to the mean background flow. Therefore the clumps do not dissipate appreciable amounts of kinetic energy until they reach the outer helium core and encounter a dense (Rayleigh-Taylor unstable) shell which is left behind by the shock at the He/H interface. The concordance with observations of these Type II supernovae is, however, destroyed, when the clumps enter this dense shell and are decelerated to velocities $\leq 2000\,\mathrm{km/s}$ because their propagation in this new environment occurs *supersonically*.

It is somewhat disappointing that in the end our calculations yield ^{56}Ni velocities which do not deviate significantly from what has been predicted in earlier studies of Rayleigh-Taylor mixing in Type II supernovae. This is especially true since our simulations themselves indicate that, by neglecting clump formation within the first minutes of the explosion, all of these early investigations have been started from overly simplified initial conditions. Indeed the quality of the effects that we observe is in clear contrast to what has been reported previously.

- All earlier studies tried to *accelerate* the ^{56}Ni to velocities around $3000\,\mathrm{km/s}$ by making use of the instabilities at the composition interfaces.

- In contrast, in our calculations the ^{56}Ni velocities *are initially extremely high* (about $17\,000\,\mathrm{km/s}$) and the main difficulty is how to avoid to *decelerate* this material substantially during the later evolution.

Having missed essential parts of the physics of the problem, the predictions of ^{56}Ni velocities around $2000\,\mathrm{km/s}$ from the early investigations must therefore be regarded to be purely fortuitous.

Since the evolutionary effects that we see are so different from what has been reported previously, new ways out of the dilemma concerning the high nickel velocities in SN 1987 A must be sought. Uncertainties in stellar evolutionary models, especially the treatment of convection and semiconvection, might be the culprit here. Moreover,

considering the possibility that Sk $-69°\,202$ might have undergone a merger prior to explosion we are not even certain on observational grounds whether SN 1987 A was a "usual" event and its origin a single, isolated star, as assumed in all stellar evolutionary calculations. Yet, problems resulting from the restriction of our calculations to two dimensions and missing physics in the modeling of the explosion itself, as e.g. rotation and jets, might also be responsible for the discrepancy with the observations. All these issues need to be addressed in the future, but which of the above effects is the most important one is currently difficult to tell. In addition, we think that also the late time heating due to ^{56}Ni and ^{56}Co decay needs to be reexamined for its impact upon the velocities of iron group elements. This is especially important since the only previous study which has been done in this respect (Herant & Benz 1992) relied on numerical methods which we have found to be rather unsuited to treat the problem of Rayleigh-Taylor mixing in core collapse supernovae. The quality of numerical algorithms which is required for this purpose was a recurrent theme in the present work. We have attempted to convince the reader that even when using the best numerical schemes that are currently available for the solution of the "innocuous-looking equations of fluid mechanics" (Shu 1992) one needs to exercise extraordinary care. Failure to do so can lead to an overwhelming level of numerical noise and spurious solutions which may completely bury the underlying physics of the problem.

Taking only the observations of SN 1987 A as a measure, the reader might have gained the impression that the evolution and death of massive stars is currently less well understood than it appeared to be the case during the last decade. However, the present thesis has hopefully also shown, that despite existing deficiencies in reproducing specific observations, our physical understanding of the problem has considerably deepened during recent years.

Appendix A

The equations of reactive, self-gravitating fluid flow

A.1 Reactive, self-gravitating, neutrino hydrodynamics

The equations which govern astrophysical flows in the non-relativistic limit and in the absence of viscosity and magnetic fields are the well-known Euler equations of hydrodynamics which express the conservation of mass, momentum and energy of the fluid. Starting from moments of the Boltzmann equation of kinetic theory and closure relations obtained from the Chapman-Enskog procedure, the Euler equations can be derived under the assumption of a small collisional mean free path of the particles constituting the fluid as compared to typical macroscopic length scales of the problem (Shu 1992; Mihalas & Weibel Mihalas 1984). In case the flow comprises constituents with widely differing collisional mean free paths, e.g. matter (i.e. baryons and electrons) + radiation (i.e. photons or neutrinos) in the (semi-)transparent regime, the matter component can usually still be described by the Euler equations while the radiation component must be handled using a solution of the full Boltzmann equation. The coupling between matter and radiation field then leads to source terms for momentum and energy in the conservation laws for the matter component.

For the supernova problem the role of the "radiation" component is taken up by the different neutrino kinds since, due to the very high densities, photons have such small mean free paths that they attain thermodynamic equilibrium with the baryons and electrons and their effects are subsumed within the equation of state (see below). The Euler equations then read

$$\frac{\partial \rho}{\partial t} + \boldsymbol{\nabla} \cdot (\rho \mathbf{v}) = 0 \tag{A.1}$$

$$\frac{\partial \rho \mathbf{v}}{\partial t} + \boldsymbol{\nabla} \cdot (\rho \mathbf{v} \mathbf{v}) + \boldsymbol{\nabla} P = \rho \mathbf{g} + \rho \mathbf{f}_\nu \tag{A.2}$$

$$\frac{\partial \rho E}{\partial t} + \boldsymbol{\nabla} \cdot ([\rho E + P] \mathbf{v}) = \rho \mathbf{v} \cdot \mathbf{g} + \rho \dot{Q}_\nu + \rho \dot{Q}_{\mathrm{nuc}}, \tag{A.3}$$

where we have accounted for additional source terms due to gravity and nuclear reactions. In Equations (A.1) to (A.3) ρ, $\mathbf{v}$ and P have their usual meanings and $\rho \mathbf{v} \mathbf{v}$ is the momentum flux density tensor. With E we have denoted the total specific energy

$$E = \frac{1}{2} |\mathbf{v}|^2 + E_{\mathrm{int}} \tag{A.4}$$

which consists of the specific kinetic and specific internal energy of the fluid. The quantities $\mathbf{f}_\nu$ and $\dot{Q}_\nu$ are the acceleration due to neutrino momentum transfer and the specific net energy gain due to neutrino heating. In multidimensional calculations the last two quantities can currently only be calculated in some approximation since a concurrent solution of the full Boltzmann and the hydrodynamic equations is still unfeasible. The last source term in the energy equation, $\dot{Q}_{\mathrm{nuc}}$, is the specific net energy gain from nuclear reactions.

The gravitational acceleration $\mathbf{g}$ is obtained from the gravitational potential Φ by

$$\mathbf{g} = -\boldsymbol{\nabla}\Phi, \tag{A.5}$$

where Φ is computed by solving Poisson's equation

$$\Delta\Phi = 4\pi G\rho. \tag{A.6}$$

The occurrence of nuclear reactions in the flow requires that in addition to the basic Equations (A.1) to (A.3) a set of continuity equations for each nuclear species of the form

$$\frac{\partial\rho X_i}{\partial t} + \boldsymbol{\nabla}\cdot(\rho X_i\mathbf{v}) = \rho\dot{X}_i \tag{A.7}$$

must be solved, where the quantity ρX_i is the partial density of nucleus i, $\rho\dot{X}_i$ denotes the source term due to nuclear reactions and

$$X_i = \frac{n_i A_i}{\rho N_A} = \frac{n_i A_i}{\sum_i n_i A_i}. \tag{A.8}$$

is the mass fraction of that species. In the last equation A_i and n_i denote the atomic mass number and number density of nucleus i, while N_A is Avogadro's number, and the denominator gives the total density of baryons. Note that when Eq. (A.8) is summed over all nuclei one obtains

$$\sum_i X_i = 1, \tag{A.9}$$

i.e. the condition of baryon conservation. Equation (A.7) is usually rewritten in terms of the nuclear abundances Y_i as

$$\frac{\partial\rho Y_i}{\partial t} + \boldsymbol{\nabla}\cdot(\rho Y_i\mathbf{v}) = \rho\dot{Y}_i, \tag{A.10}$$

where the Y_i are defined as

$$Y_i = \frac{X_i}{A_i}. \tag{A.11}$$

The source terms $\rho\dot{Q}_{\mathrm{nuc}}$ and $\rho\dot{Y}_i$, which appear in Equations (A.3) and (A.10), respectively, have to be obtained from the solution of a nuclear reaction network and are discussed in more detail in the following section. To close this system of equations one finally needs to specify an equation of state. In the calculations which were described in the preceding chapters, this relation was given in terms of the temperature, T, and the internal energy density of the gas, e_{int},

$$P = P(\rho, T, X_i), \quad P = P(\rho, e_{\mathrm{int}}, X_i). \tag{A.12}$$

A.2 Nuclear reaction networks

A nuclear reaction network is defined by a system of first order differential equations in time for the nuclear abundances of the form

$$
\begin{aligned}
\dot{Y}_i \;=\;& \sum_j c_i(j)\lambda_j Y_j \\
+\;& \sum_{j,k} c_i(j,k)\rho N_A \langle j,k \rangle Y_j Y_k \\
+\;& \sum_{j,k,l} c_i(j,k,l)\rho^2 N_A^2 \langle j,k,l \rangle Y_j Y_k Y_l,
\end{aligned}
\tag{A.13}
$$

(e.g. Clayton 1983; Fryxell et al. 1989; Arnett 1996; Thielemann et al. 1998). The first term of Equation (A.13) describes changes of Y_i due to weak processes (β-decays and electron captures) and photo-disintegrations and so λ_j is the corresponding weak interaction rate or the photodisintegration rate. The second and third term of Equation (A.13) describe changes due to two and three-body reactions, respectively, so that $\langle j,k \rangle$ and $\langle j,k,l \rangle$ denote the thermally averaged products of the cross section, σ, and relative velocity, v, in the center of mass system for the two-body and three-body reactions, respectively. E.g. for a reaction between nuclei j and k this average has the form

$$
\langle j,k \rangle = \langle \sigma v \rangle_{j,k} = \left(\frac{8}{\mu\pi}\right)^{1/2} (kT)^{-3/2} \int_0^\infty E\sigma(E) \exp\left(-E/kT\right) dE,
\tag{A.14}
$$

where μ denotes the reduced mass of the system (j,k). The c_i are given by

$$
c_i(j) \;=\; N_i
\tag{A.15}
$$

$$
c_i(j,k) \;=\; \frac{N_i}{|N_j|!\,|N_k|!}
\tag{A.16}
$$

$$
c_i(j,k,l) \;=\; \frac{N_i}{|N_j|!\,|N_k|!\,|N_l|!}
\tag{A.17}
$$

where N_i, N_j, N_k, N_l are the numbers of particles of type i, j, k, l which are involved in the reaction. The sign of N is positive (negative) if the corresponding nucleus is created (destroyed). The denominators run over the species destroyed in the reaction and avoid double counting when identical particles react with each other. Note that the network equations fulfill the condition of baryon, or mass conservation Eq. (A.9).

Equations (A.13) are usually solved by transforming them into a non-linear algebraic system by a first-order accurate implicit discretization in time

$$
G_i = \frac{Y_i(t^{n+1}) - Y_i(t^n)}{\Delta t} - f_i(t^{n+1}) = 0.
\tag{A.18}
$$

Here $\Delta t = t^{n+1} - t^n$ is the time step, and $f_i(t^{n+1})$ denotes the right-hand side of Eq. (A.13) evaluated at time $t^n + \Delta t$. The nonlinear system (A.18) is then solved for the unknown $Y_i(t^{n+1})$ by linearization and Newton-Raphson iteration. In vector form Eq. (A.18) reads

$$
\mathbf{G}(\mathbf{Y}(t^{n+1})) = \frac{\mathbf{Y}(t^{n+1}) - \mathbf{Y}(t^n)}{\Delta t} - \mathbf{f}(t^{n+1}) = 0.
\tag{A.19}
$$

The Newton-Raphson procedure boils down to finding the zeroes of this equation by starting from a first guess for $\mathbf{Y}(t^{n+1})$:

$$\mathbf{Y}^0(t^{n+1}) \equiv \mathbf{Y}(t^n). \tag{A.20}$$

This guess is iteratively improved by applying a series of corrections $\delta\mathbf{Y}$, e.g. the l-th iteration step can be written as

$$\mathbf{Y}^{l+1}(t^{n+1}) = \mathbf{Y}^l(t^{n+1}) + \delta\mathbf{Y}^{l+1}. \tag{A.21}$$

The $\delta\mathbf{Y}^{l+1}$ are obtained from a solution of the matrix equation

$$\mathbf{J}^l\, \delta\mathbf{Y}^{l+1} = -\mathbf{G}(\mathbf{Y}^l), \tag{A.22}$$

where $\mathbf{J}^l$ is the Jacobian of $\mathbf{G}(\mathbf{Y}^l)$ with respect to $\mathbf{Y}^l$.

The time step Δt should be chosen in a way which guarantees that the iterates $\mathbf{Y}^l(t^{n+1})$ converge with a relative accuracy of about 10^{-6} after a small number of iterations (typically 3). The size of the time step is further restricted by constraints of accuracy. Typically, the changes in mass fractions during a nuclear time step should not be larger than a few percent. Similar constraints apply for the temperature which rises due to the energy release of

$$\Delta\epsilon = \dot{Q}_{\mathrm{nuc}}\,\Delta t = -9.644 \times 10^{17} \sum_i \Delta M_i \left(Y_i(t^{n+1}) - Y_i(t^n)\right) \; [\mathrm{ergs/g}] \tag{A.23}$$

resulting from the change of the abundances from time t^n to time t^{n+1}. Here ΔM_i is the mass excess of nucleus i.

Since the characteristic time scales for the different reactions vary widely, the system (A.13) and (A.23), which has to be solved in every zone of the grid with non-negligible nuclear activity, is extremely stiff and very robust methods are required for its solution. The first-order accurate, implicit discretization in time which is described above has proven to be stable, especially when combined with the method of Müller (1986) who proposes to solve Eqs. (A.13) and (A.23) together in a coupled Newton-Raphson iteration in case one has to compute into and out of the regime of NSE. Even so, it is difficult to follow the abundance changes during the first $\sim 200\,\mathrm{ms}$ of shock-propagation in a core collapse supernova by solving the network equations in the entire region between proto neutron star and shock. The very high temperatures that are encountered in these zones (up to a few $10^{10}\,\mathrm{K}$) and the exponential dependence of the reaction rates on temperature lead to time steps which are much smaller than typical dynamical times. Thus the network needs to be solved several tens of thousands or even hundreds of thousands of times per zone and per hydrodynamic time step (here assumed to be of the order of several $10^{-6}\,\mathrm{s}$, as in the computations described in Chapter 3) resulting in tens of billions or even thousands of billions of inversions of the matrix equation (A.22) throughout a one-dimensional or a two-dimensional hydrodynamic simulation, respectively. Even when taking advantage of the sparse character of typical Jacobians that result from nuclear networks (see, e.g. Timmes 1999), the computational load soon becomes prohibitive. It is therefore common practice to solve a set of Saha equations as long as NSE holds and to switch to Eq. (A.13) only when temperatures and densities have decreased to such values that NSE breaks down (Aufderheide et al. 1991). The difficulty with this approach, however, is to guarantee a smooth transition between the two regimes.

Appendix B

Numerical methods

B.1 The HERAKLES hydrodynamics solver

B.1.1 The basic algorithm

The HERAKLES hydrodynamics code solves the self-gravitating, reactive flow equations of Section A.1 in one, two or three spatial dimensions and in either Cartesian, cylindrical or spherical coordinates by making use of an extended version of the direct Eulerian PPM algorithm which is described in Colella & Woodward (1984). Since PPM has meanwhile become a rather "standard" numerical algorithm and sufficient details are given in the papers of Colella & Woodward (1984), Woodward & Colella (1984), Fryxell et al. (1989), Plewa & Müller (1999) and Fryxell et al. (2000) we will only give a general outline of the method below.

The core of the algorithm is a one-dimensional hydrodynamics solver which solves the (sub)set of equations

$$\frac{\partial U}{\partial t} + \frac{\partial (AF)}{\partial V} + \frac{\partial H}{\partial r} = G, \tag{B.1}$$

where

$$U = \begin{pmatrix} \rho \\ \rho u \\ \rho v \\ \rho w \\ \rho E \\ \rho X_i \end{pmatrix}, \quad F(U) = \begin{pmatrix} \rho u \\ \rho u^2 \\ \rho v u \\ \rho w u \\ \rho u E + u P \\ \rho u X_i \end{pmatrix}, \quad H(U) = \begin{pmatrix} 0 \\ P \\ 0 \\ 0 \\ 0 \\ 0 \end{pmatrix}, \quad G = \begin{pmatrix} 0 \\ \rho g \\ 0 \\ 0 \\ \rho u g \\ 0 \end{pmatrix}. \tag{B.2}$$

Here U is the vector of conserved quantities, $F(U)$ is the flux function and

$$V(r) = r^{\alpha+1}/(\alpha + 1), \qquad A(r) = r^{\alpha} \tag{B.3}$$

are volume and area coordinates with $\alpha = 0, 1, 2$ in case of planar, cylindrical or spherical symmetry, respectively. Note that the above equations are the one-dimensional Euler equations for a multi-component fluid *except* for the third and fourth equation which express a passive advection of the second and third component of the momentum vector $\rho \mathbf{v}$ with the first component of the velocity, u. This provision is required in order to solve the multidimensional hydrodynamic equations by applying the one-dimensional algorithm in a sequence of one-dimensional sweeps according to the second order accurate operator splitting procedure of Strang (1968).

The philosophy behind PPM is to introduce explicit non-linearity into the discretization of the hydrodynamic equations which mimics the physics of real flows as closely as possible. The solution is pieced together from solutions of suitably constructed Riemann problems at the interfaces between adjacent computational cells. For this purpose piecewise parabolic interpolation functions are constructed for the so-called "primitive variables" $(\rho, u, v, w, p, \gamma, \Gamma, X_i)$ using the cell averages of these quantities. These interpolation profiles are subject to monotonicity constraints, as well as steepening and flattening considerations in the vicinity of contact discontinuities and shocks, respectively. The latter two conditions are imposed in order to minimize and increase, respectively, the numerical dissipation of the scheme in critical regions of the flow. From these interpolation functions interface values of the primitive variables are constructed using a characteristics tracing step. This allows one to take into account the domains of dependence which can influence the state at the zone interface during the entire time step. The interface values so constructed are then used in the solution of the Riemann problem to compute the fluxes with which the conserved quantities are updated. We note that if multifluid problems are to be computed with PPM, the above algorithm will in general violate the condition of *local* mass conservation Equation (A.9). This problem and its solution, which requires an appropriate renormalization of the fluxes obtained from the Riemann solver, is described in detail in Plewa & Müller (1999).

Our HERAKLES implementation of PPM is based in parts on the older PROMETHEUS code which is discussed in Fryxell et al. (1989) as well as in Fryxell et al. (2000). However, it differs from its predecessor in the following respects: The algorithm for multifluid advection proposed by Fryxell et al. (1989) was replaced with the Consistent Multifluid Advection scheme of Plewa & Müller (1999). The computation of the input states for the Riemann solver follows closely the algorithm given in Colella & Woodward (1984). The enhanced version of the flattening algorithm for interpolation profiles given in the appendix of Colella & Woodward (1984) is adopted instead of the simpler algorithm employed in PROMETHEUS. Furthermore, the dissipation and shock detection algorithms of PROMETHEUS were replaced in order to cope with odd-even decoupling (see below).

As in PROMETHEUS the exact Riemann solver of Colella & Glaz (1985) is used, which allows for general, non-gamma law equations of state. After a hydrodynamic step is completed, source terms which may be due to nuclear reactions and/or neutrino-matter interactions are taken into account using operator splitting (see LeVeque 1998, for a discussion of the accuracy which can thus be obtained). The inclusion of gravity is more involved. In order to maintain as closely as possible the delicate balance between gravity and the pressure gradient in problems which are close to hydrostatic equilibrium, gravity should ideally be taken into account in the solution of the Riemann problem. PPM approximately accounts for this by making use of a predictor step, in which the input states to the Riemann problem are modified using the gravitational acceleration at the beginning of the time step. After a hydrodynamic sweep is completed, the new gravitational acceleration is determined and the time centered average of both values computed. This value is then used in a corrector step to compute the gravitational source terms in the energy and momentum equations.

B.1.2   Dissipation mechanisms

We have shown in Section 3.11 that the Riemann solver of Colella & Glaz (1985), while working very satisfactorily for a wide range of problems, suffers from the odd-even decoupling instability in case strong grid-aligned shocks have to be computed in multi-dimensional simulations. The method which we have used to cure this instability in the calculations of Chapters 3 and 4 is based on a modification of the dissipation algorithms which are described in Colella & Woodward (1984). PPM includes an artificial viscosity algorithm, which was proposed by Colella & Woodward (1984) in order to suppress post-shock oscillations behind nearly stationary shocks as well as a "multidimensional oscillation" which these authors noticed in calculations of the well known Mach 3 wind tunnel problem (see e.g. Woodward & Colella 1984). Indeed their description of the latter instability leaves little doubt that it must be identical to odd-even decoupling, and though not giving an entirely convincing discussion of the cause of the problem the authors already gave a recipe on how to minimize its effects. They proposed to add a viscous flux $F^{\mathrm{visc}}_{j+1/2}$ of the form

$$F^{\mathrm{visc}}_{j+1/2} = \nu_{j+1/2} \left(U_j - U_{j+1} \right) \tag{B.4}$$

to the fluxes computed by the Riemann solver, where $\nu_{j+1/2}$ is given by

$$\nu_{j+1/2} = K \max[-\left(\boldsymbol{\nabla} \cdot \mathbf{v}^n \right)_{j+1/2,k}, 0] \tag{B.5}$$

and where $\left(\boldsymbol{\nabla} \cdot \mathbf{v}^n \right)_{j+1/2,k}$ is an *unsplit* finite difference approximation of the divergence of $\mathbf{v}$ (In all above equations the standard notation is used in which upper indices represent time step values, lower integer indices denote zone centers and lower half integer indices denote cell interfaces). Note that the problem cannot be cured if the scheme is made more diffusive but the artificial viscosity algorithm is operating in one-dimensional sweeps. In this case, the viscosity term does not couple zones in the direction perpendicular to the sweep. This has already been emphasized by Colella & Woodward (1984).

   Colella & Woodward (1984) propose a value of the viscosity constant of $K = 0.1$. However, we have found that with this small amount of viscosity odd-even decoupling could not be suppressed efficiently and values as large as $K = 0.5$ were required in order to provide enough dissipation to reduce the noise in the simulations of Chapter 3 to a level which was about two orders of magnitude smaller than the seed perturbations which were applied to the velocity field. This poses a problem if the low viscosity of the PPM scheme is not to be compromised globally, since Colella & Woodward (1984) suggest to add the (small, i.e. $K = 0.1$) artificial viscosity flux to all zones of the grid (an approach which is also implemented in PROMETHEUS). Thus in HERAKLES we add the (extra large, i.e. $K = 0.5$) viscous flux only to zones which are detected to be located within shocks. For this purpose an appropriate *multidimensional* implementation of shock detection is required. If the shock detection is done in one-dimensional sweeps a shock aligned with e.g. the y-axis will not be "seen" in the hydrodynamic sweep along the y-direction and thus again no coupling of the zones along the shock will be introduced. Furthermore, the viscosity should only be increased in the direction of shock alignment in order not to unnecessarily smear the shock profile perpendicular to it. The latter can have severe consequences for the temperature profile, and thus for the computation of nuclear burning. Therefore, we compute the local direction of shock propagation, α, relative to our spherical grid. If α is found to be close to $0°$,

$90°$, $180°$ or $270°$, the shock is aligned with one of the coordinate lines. In this case we use a viscosity coefficient $K_{\text{aligned}} = 0.5$. Otherwise the standard value of $K = 0.1$ as suggested by Colella & Woodward (1984) is adopted.

With these modifications, the artificial viscosity method worked satisfactorily for the calculations of Chapters 3 and 4. However, it has the disadvantage of requiring parameters (i.e. the viscosity coefficients), which must be adjusted any time a new problem is to be computed. Furthermore, odd-even decoupling tends to become stronger with increasing resolution and thus these parameters are usually also resolution-dependent. Moreover, in cases of extremely high resolution the noise due to odd-even decoupling may in fact become so strong that it cannot be damped efficiently using reasonable values for K. Fortunately, a better solution to the problem appears to exist. Quirk (1994) has found that the relatively viscous HLLE Riemann solver of Einfeldt (1988), which is based on an approximate solution of the Riemann problem, does not exhibit odd-even decoupling. Quirk (1994) also gives an analysis of the problem considering the Roe and HLLE solvers and concludes that it is the way in which the numerical flux is calculated which determines whether a scheme will develop odd-even decoupling or not. This is also discussed in more detail in the recent study of Liou (2000). In order to cure the numerical instability while not suffering from the relatively large diffusivity of HLLE, Quirk (1994) suggested a hybrid method in which one uses a high-resolution method for most of the computational work but switches to the HLLE scheme in the vicinity of strong (grid-aligned) shocks. Very recent test calculations that we have performed for the supernova problem indicate that this method is indeed superior to an increase of the artificial viscosity. It yields results as accurate as if only an exact Riemann solver is used, eliminates odd-even decoupling entirely and works also in case of high spatial resolution without the need to adjust any parameters (Plewa, Kifonidis, Müller, in preparation).

B.2   Adaptive Mesh Refinement for multi-scale simulations

Many of the most interesting problems in astrophysics, like the evolution of core collapse supernovae, exhibit widely differing time and length scales and attempts to solve them with conventional numerical techniques soon stretch the limits of even the most powerful supercomputers. In these cases, progress in astrophysics is inevitably coupled to progress in numerical algorithm design and efficiency. Advances in these fields during recent years have led to adaptive numerical methods for the solution of the Euler equations, for which Adaptive Mesh Refinement (AMR) is an example.

AMR was suggested as an algorithm for the efficient solution of systems of time-dependent, hyperbolic partial differential equations by Berger & Oliger (1984). A re-worked version of the algorithm which is particularly suited for the conservative shock capturing schemes which are nowadays in use for solving the Euler equations of ideal, compressible flows has been discussed in Berger & Colella (1989). It is the basis for the algorithm implemented in the AMRA code of Plewa & Müller (2000), which served as a basic tool for the present work and is described in Section B.3. In what follows we will give only a basic description of the AMR technique. For an in-depth explanation and documentation of the entire algorithm, which is outside the scope of this thesis, we refer the reader to the original works cited above, as well as to Neeman (1996) and,
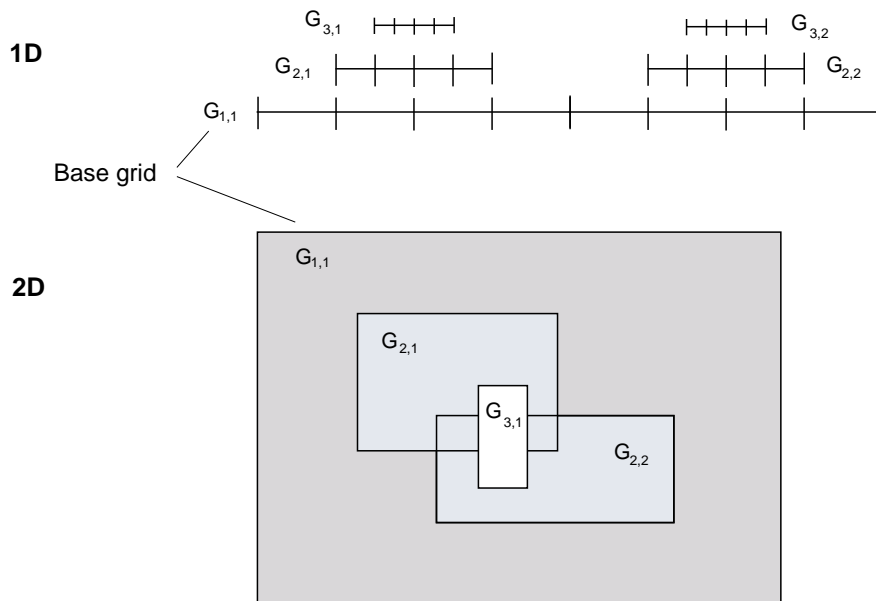
Figure B.1: Properly nested AMR grid hierarchies. The first index assigned to each grid patch depicted in this figure represents the grid level to which the patch belongs. The second index identifies the patch within that level. Patches within a given level of the hierarchy have the same spatial resolution.

above all, to the excellent discussion in Quirk (1991). The latter two references also give detailed hints for implementation on serial computer architectures.

B.2.1   Grid structure

The AMR algorithm of Berger & Colella (1989) has been designed in order to solve shock hydrodynamics problems with a fixed (user specified) accuracy while making use of a minimum amount of computer power. This goal is achieved by constantly monitoring the error of the evolving solution and by subsequently refining the computational grid *locally* where higher accuracy is required. Thereby it is often (but not always!) possible to avoid the use of a *globally* fine grid. The refinement has to be adaptive in space as well as in time in order to follow the evolving flow solution with a prescribed accuracy. This is achieved by generating a nested sequence of finer and finer grid patches on an underlying coarse grid, the so called base level grid, which covers the entire computational domain. The fine grid patches are not merged into the base level grid but represent single entities which make up an entire grid hierarchy (Fig. B.1). Different *levels* in this hierarchy consist of one or more grid patches with the same spatial resolution. The resolution changes between levels from lower (coarse) to higher (fine) levels by arbitrary (but integer) factors in each dimension. Patches forming a *single* level may partially overlap each other or may cover distinct regions of the computational domain. However, patches belonging to *different* levels must necessarily be "properly nested". This means that every patch on a given level must be entirely contained in one or more ("parent") patches which are located on the next coarser level of the grid hierarchy (see Fig. B.1).
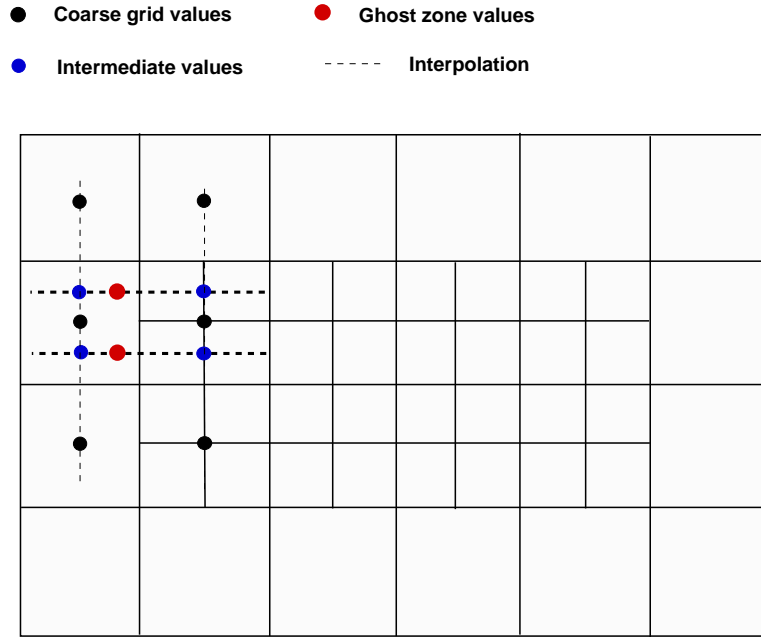
Figure B.2: Interpolation of boundary ("ghost zone") data for the integration of a fine patch from a coarser grid. Note that intermediate values need to be interpolated first, before data for ghost zones can be obtained.

B.2.2 Grid integration

AMR uses an integration scheme which (on a given refinement level, l,) refines in space as well as in time by the same mesh refinement factor, r_l. For instance in one space dimension, r_l is given by

$$r_l = \frac{\Delta x_l}{\Delta x_{l+1}}, \qquad (B.6)$$

where Δx_l is the spatial resolution on level l. Temporal refinement requires that also the time steps obey

$$r_l = \frac{\Delta t_l}{\Delta t_{l+1}}. \qquad (B.7)$$

Thus r_l times more (but smaller) time steps are used in order to integrate level $l+1$ to the same instant in time as level l. Note that in two dimensions and in case $\Delta x_l \neq \Delta y_l$, each spatial dimension has its own refinement factor and the maximum of both needs to be inserted in Eq. (B.7) (see Quirk 1991).

The integration of a given patch on a specific level of the grid hierarchy proceeds largely independent from other patches once suitable initial and boundary conditions are available. The base level grid can be readily integrated for one (base level) time step starting from the user-specified initial data and boundary conditions. However, (embedded) patches on higher levels of the hierarchy, which do not have to share the same boundaries as the base level grid, will in general require boundary data that must be obtained by interpolation from coarser levels. Figure B.2 illustrates this procedure. Note that due to the requirement of performing more integration steps on level l in order to reach the same time as on level $l-1$, also temporal interpolation might be needed in order to provide boundary data for level l.
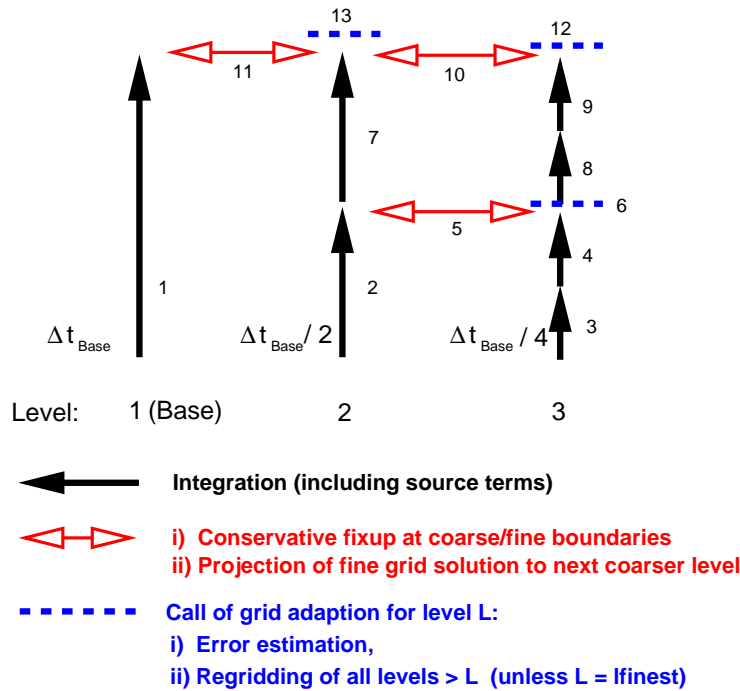
Figure B.3: Integration of the grid hierarchy over a single base level time step for 3 levels of refinement with a constant refinement factor $r = 2$. Note that grids at level $l + 1$ have to be evolved with time steps $\Delta t_l / r_l$. The numbers indicate the actual sequence of operations that has to be carried out. A regridding frequency of $K = 2$ was chosen in this example.

The various integrations of the different grid levels are recursively interleaved (Fig. B.3). This minimizes the span over which any temporal interpolation needs to take place. Once two adjacent levels have been evolved to the same time some amount of communication between the different levels is needed in order to obtain a consistent solution. This includes averaging of the solution obtained on fine patches and its projection down to parent patches. Furthermore, special attention is required at boundaries which separate coarse and fine grid cells. Numerical fluxes calculated with higher resolution will in general differ from fluxes calculated with lower resolution. To ensure global conservation a correction pass ("conservative fix-up") over all coarser grid cells abutting fine grid cells is needed once both grid levels have been integrated to the same time. We refer the reader to Berger & Colella (1989) for a detailed description of this procedure.

B.2.3   Error estimation and grid adaption

The grid hierarchy is constantly *recreated* to follow the interesting features of the flow. Every K time steps on a given level an error estimation procedure is invoked, which yields an estimate of the local truncation error of the solution. The regions where this value exceeds some predefined threshold, ϵ, are flagged and later covered with new grid patches of higher resolution. Regions which were formerly covered by fine patches but do not require to be followed with high resolution any longer are thus automatically "coarsened". Thereby flow features requiring high resolution like shocks, contact discontinuities or strong gradients are always followed with the higher level grids

while regions where the flow is essentially smooth are calculated at lower resolution. It is important to note in this context that newly created fine grids might have to be initialized with data that has to be obtained by interpolation from underlying coarser grids. This procedure may lead to serious numerical problems, especially for multi-component flows and we will discuss this in some more detail in Sections B.3.2 and B.3.3.

B.3   The AMRA code

The AMRA code of Plewa & Müller (2000) which represents a FORTRAN implementation of the concepts described in the last section provided the basic tool for the calculations of Chapter 4. AMRA allows for

- the solution of one, two, or three-dimensional problems,

- Cartesian, cylindrical or spherical coordinates,

- the high-order Godunov type PPM advection scheme of Colella & Woodward (1984)

- a general equation of state

- self-gravity

- an accurate treatment of multi-component and reactive flows, including a nuclear reaction network

- implicit and explicit conduction solvers

- portability and efficiency on a large number of serial and parallel (super)computing platforms. In particular a new memory layout was developed for the PPM based hydrodynamics solver HERAKLES which takes into account the special performance requirements of an AMR scheme (see Section B.3.4). This enables AMRA to take advantage of vector as well as scalar RISC based processor architectures.

Including HERAKLES and all of the physics modules AMRA consists of more than 200 subroutines and 30 000 code lines. The extensions necessary to apply AMRA to the problem of Type II supernovae incorporated the use of a realistic (non-gamma law) equation of state and a means to reduce artificial mixing of different fluid components by numerical diffusion to a minimum when dealing with multi-component flows (see Plewa & Müller 1999). These were prerequisites in order to couple a nuclear reaction network to the AMR based hydrodynamics. To our knowledge, the only other AMR tool where this has been successfully attempted for the extremely stiff nuclear rate equations is the FLASH code of the Accelerated Strategic Computing Initiative (ASCI) team (Ricker et al. 1999; Fryxell et al. 2000). Furthermore, the gravitational solvers had to be tested and problem specific initial and boundary conditions had to be implemented.

A rigorous test program has been and is continuously carried out as soon as new modules are added to the code. Moreover, the basic AMR part has been used with a number of different flow solvers and applied to many astrophysical and non-astrophysical problems. The latter include almost all known standard test problems in one and two dimensions and in different geometries, as e.g. Sod's simple shock tube or the much

more demanding colliding blast waves problem of Woodward & Colella (1984). On the astrophysical side, the code was applied to the modeling of relativistic and non-relativistic jets, supernova remnants and protoplanetary disks. This test program was absolutely essential in order to verify the correctness of the coding and through this approach we have been able to find a number of otherwise hardly detectable errors. We can therefore state that despite its complexity the code has been well tested and is able to handle even extreme situations.

B.3.1   Implementation of self-gravity in AMRA

The inclusion of self-gravity in AMRA is currently restricted to a solution of the one-dimensional Poisson equation. In two-dimensional problems in which a spherically symmetric gravitational potential is a good approximation, the density field is mapped from the AMR hierarchy to a separate uniform grid employing the same resolution as the finest level, and averaged over angle. Poisson's equation is then solved on this uniform grid and the potential mapped back to the grid hierarchy from where it is passed to the hydrodynamic solver.

B.3.2   Implementation of multi-species and reactive flow in AMRA

Two classes of problems are encountered when reactive flows are to be computed within an adaptive mesh refinement framework. The first is that the solution of the coupled system of hydrodynamic and nuclear rate equations Equations (A.1) to (A.3) and (A.7) necessitates an advection of the chemical composition within the hydrodynamic solver. In PROMETHEUS and its successor HERAKLES additional continuity equations for each fluid component are solved for this purpose, with the partial densities, ρX_i, as state variables. This extension of the basic Euler equations must be reflected within the AMR scheme in two ways. Firstly, the fixup procedure for fluxes at fine-coarse boundaries (Section B.2.2) has to be done in a similar way for the partial densities as for the other conserved quantities. Secondly, boundary data for the partial densities needs to be provided for the integration of fine patches as well as for the initialization of the interior of newly created fine patches. In AMRA *fractional masses* are interpolated for this purpose in order to maintain consistency between the masses of nuclear species on the parent and the child patch. However, problems may still arise *within* each fine zone thus initialized, due to the fact that when an interpolation scheme of second or higher order is used it is *not* guaranteed that the sum of partial densities will equal the total gas density in this cell after interpolation. One might expect that the magnitude of this problem will be large whenever the new patch is created in regions where the partial densities of nuclear species vary significantly. Furthermore, the degree of mismatch between the total and partial densities should decrease when the differences in the solution as seen on different refinement levels become smaller. This will depend on

 i) the refinement factors and

 ii) the truncation error estimator and truncation error thresholds which are used.

The latter must ensure that steep features in the partial densities of nuclear species will never escape from the higher level grids. We will demonstrate the importance of an appropriate error estimator in the next section.

The second class of problems is connected to the coupling of the nuclear reaction network itself to the AMR algorithm. As nuclear time scales in the supernova problem are much shorter than the hydrodynamic time scale, subcycling of the nuclear reaction network is required. Choosing an appropriate initial nuclear time step is crucial in this respect since too small a time step will result in a waste of computer time and too large a step will lead to non-convergence of the network. The usual solution to this problem employed in single grid codes is to save the last local nuclear time step that was used within a hydrodynamic step and to reuse this value for the first solution of the network within the next hydrodynamic time step. This is not possible within an AMR framework since there is no static grid which could be used to store the nuclear time steps with sufficient spatial resolution. Thus trial integrations of the network are needed every time the network solver is called anew on a given level, which must find the optimal nuclear time step within a minimum number of integrations. For an efficient implementation on parallel machines it is also important to gather all "burning" zones of a given level and to pass these to the network solver at once. Calling the network on each patch separately will usually result in severe load balancing problems due to varying numbers of "burning" cells between different patches. In addition, burning zones which are covered by grids on a finer level can usually be disregarded because the solution in these zones will be overwritten anyway with data from the finer grids.

B.3.3 Numerical tests

In the following one-dimensional test calculations are presented for an artificially induced supernova explosion in the $15 \, \mathrm{M_\odot}$ model progenitor of Woosley et al. (1988) which demonstrate the importance of a suitable truncation error estimator for the calculations which we discussed in Chapter 4. For this purpose AMRA was used in conjunction with the PROMETHEUS hydrodynamics solver. After removing the presupernova model's iron core the explosion was initiated by depositing 10^{51} ergs in form of thermal energy into the innermost region of the silicon shell. Five levels of refinement were used, with 256 zones on the base grid (level 1) and refinement factors of 2, 4, 6, and 8 for patches on levels 2, 3, 4, 5 respectively. This resulted in an effective resolution of $98\,304$ equidistant zones. The computational domain extended from 1.4×10^8 cm up to 3.8×10^{11} cm and thus covered about the inner $1/10$ th of the star. Besides ^{1}H, the 13 α-nuclei from ^{4}He to ^{56}Ni were included. The same equation of state as in Section 4.2 was used and gravity was taken into account.

In Fig. B.4 we show the results of 4 runs that were all done with this same setup but with varying trucation error thresholds and/or different truncation error estimators. Figure B.4 a displays the chemical profiles in case the truncation error was estimated only for $(\rho, \rho v_r, \rho E)$, i.e. only for a subset of the conserved quantities, disregarding the partial densities of nuclear species. A truncation error threshold $\epsilon = 0.1$ was used. Figure B.4 b was obtained with the same error estimator and a ten times smaller threshold $\epsilon = 0.01$. In both cases large errors in the distribution of nuclear species are visible. Using a smaller ϵ helps in resolving the outer edge of the silicon shell ($r \approx 1-2 \times 10^{10}$ cm), but some low-amplitude noise can still be seen at $r \approx 1.5 \times 10^{10}$ cm. However, the computed distribution of ^{28}Si in the core does not seem to be sensitive to this mild improvement in overall accuracy and in addition to low-amplitude noise a conspicuous undershoot is present at $r \approx 10^9$ cm for the $\epsilon = 0.01$ case. The quality of the solution improves significantly when in addition to the error estimation for $(\rho, \rho v_r, \rho E)$ we also estimate the truncation error for the partial densities (Fig. B.4 c). With $\epsilon = 0.1$
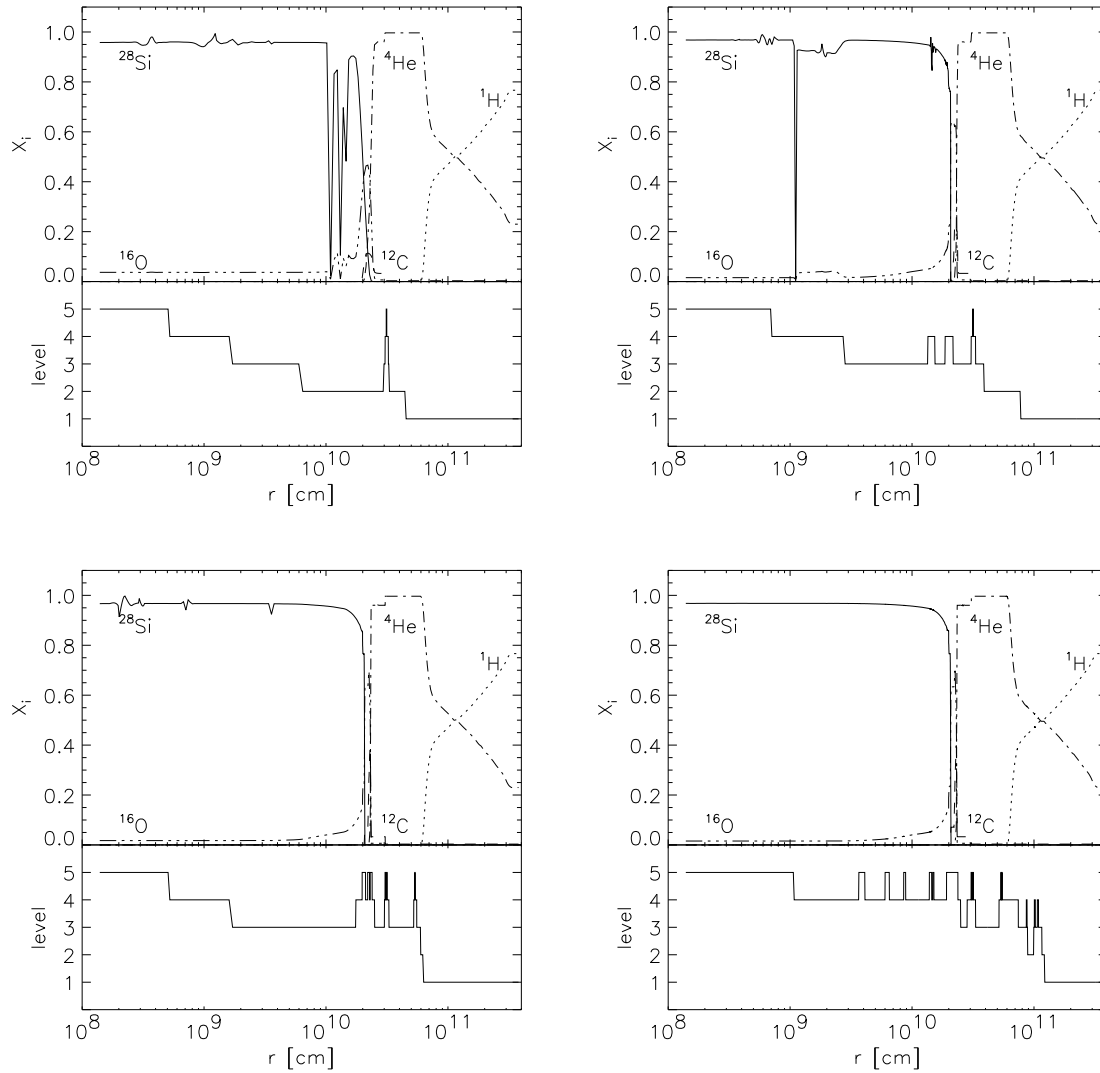
Figure B.4: Top left: a) Mass fraction profiles for our test problem after 34.9 s of evolution. By this time the shock has reached a radius slightly larger than 3×10^{10} cm and is tracked with a single level 5 patch. The error estimation algorithm was applied only to $(\rho, \rho v_r, \rho E)$ and a local truncation error of $\epsilon = 0.1$ was used. Large errors in mass fractions can clearly be seen in the central region of the grid. Top right: b) Same as left panel but with $\epsilon = 0.01$. In spite of the increased accuracy (by a factor of ten) the solution is still flawed. Bottom left: c) Same as top panels but with $\epsilon = 0.1$ for $(\rho, \rho v_r, \rho E)$ and additional flagging of the partial densities, ρX_i, with $\epsilon_{\rho X} = 0.1$. Bottom Right: d) Same as bottom left panel, but with $\epsilon = 10^{-3}$ and $\epsilon_{\rho X} = 10^{-2}$.
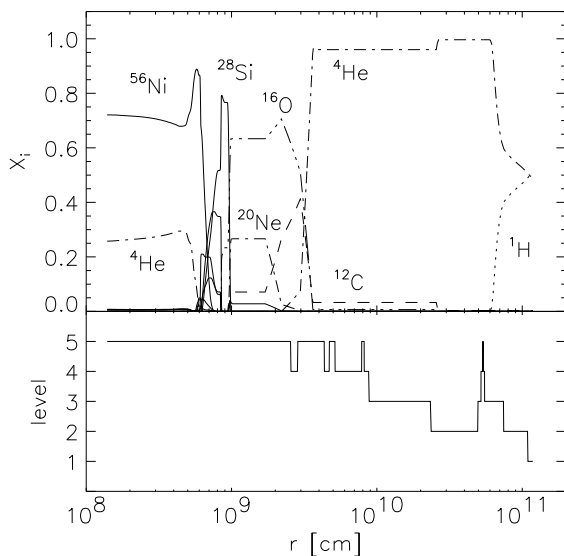
Figure B.5: Chemical composition at $t = 0.5\,\mathrm{s}$ for our run including nuclear burning (see text). Nucleosynthesis has taken place mainly in the former silicon shell. Note the products of complete and incomplete silicon burning. The C/O-core of the star is almost completely covered with the finest resolution ($\Delta r \approx 39\,\mathrm{km}$). The apparently coarse zoning in the outer oxygen core is a consequence of the coarse resolution of the initial model and does not reflect the (much higher) resolution of the AMR calculation.

and $\epsilon_{\rho X} = 0.1$ most of the material interfaces located just below the helium shell are resolved and no large errors in the silicon distribution are present. The small glitches which can still be seen in the silicon mass fraction finally vanish if error thresholds of $\epsilon = 0.001$ and $\epsilon_{\rho X} = 0.01$ are used (Fig. B.4 d). Note the changes in the distribution of grid patches between the different runs. The accuracy of the solution which has been attained in Fig. B.4 d has come at a cost of a larger number of patches on the finest level of the grid hierarchy. The latter now cover the entire inner region of the computational domain up to $r \approx 10^9$ cm as well as a larger fraction of the outer metal core of the star. This has led to an increase in the CPU-time which was required for this calculation by a factor of 5 and 3.6 as compared to the cases shown in Figs. B.4 a and b.

In Fig. B.5 we finally present results which were obtained with an α-chain network of 27 reactions for our 13 α-nuclei. The network was coupled to the hydrodynamics as described in Section B.3.2. The same explosion energy as for the other runs was also adopted for this setup. The computational domain extended from $r = 1.4 \times 10^8$ cm to $r = 1.2 \times 10^{11}$ cm. Five levels of refinement, 120 zones on the base grid and refinement factors of 2, 4, 4 and 8 were used. The truncation error thresholds were set to $\epsilon = 0.001$ and $\epsilon_{\rho X} = 0.01$. In addition flagging of density contrasts above 0.1 was employed. The obtained solution does not differ from a corresponding single grid model computed using 30 720 equidistant zones and demonstrates that with a cautious use of the AMR technique it is possible to obtain physically correct results.

B.3.4   AMRA and HERAKLES on parallel computers

Though substantial technological progress in recent years has provided researchers with ever more powerful computers, multidimensional supernova calculations like the ones presented in the preceding chapters are still restricted to the treatment of partial aspects of the "full problem" due to the persistent lack of adequate computer speed and memory. Especially global, highly resolved, three-dimensional computations will probably still remain out of reach of the supernova community for the next years to come. Furthermore, the most powerful computers available nowadays must employ parallelism of different kinds in order to meet their design goals and though relatively powerful ma-

chines may be available, the researcher is often confronted with a situation in which he cannot take immediate advantage of them. The difficulties in programming distributed memory, massively parallel systems and even traditional shared memory parallel vector computers ask for a substantial effort in order to make complex numerical algorithms (like AMR) run efficiently on these types of computers. The situation is even worse. Both of these computer architectures are basically incompatible to each other and techniques which are used to speed up the program on a system of a given kind will lead to a slowdown of the code for the other, thus making the design of portable code very difficult. This is the reason why special care has been given to the implementation of the HERAKLES version which is used as the standard hydrodynamics solver of AMRA. It provides for maximum performance of the code on a wide variety of different machine architectures. The implementation of the solver is crucial for the *single-processor* performance of AMR applications, especially if dimensional splitting is used to solve the multidimensional conservation laws in a sequence of one-dimensional sweeps.

Vector supercomputers, for instance, consist of one or more central processing units (CPUs) which rely on pipelining, i.e. parallelism at the level of the CPU's functional units. The arithmetic units in these processors consist of several pipelines which themselves are segmented into several subunits. Comparable to an assembly line, each subunit is assigned to perform one of the several suboperations required for e.g. a complete floating point addition, multiplication or division. Thereby, the subunits can concurrently work on different operands. In this way it is possible to generate one result per clock cycle and pipeline (Hockney & Jesshope 1988). To sustain this computational rate, however, it is necessary that the pipelines remain continuously filled. In order to meet this goal, the average length of the vectors, n, on which the numerical algorithm is operating has to be sufficiently large.

Most multidimensional hydrodynamics schemes (like PPM) utilize dimensional splitting to solve the multidimensional Euler equations in a sequence of one-dimensional sweeps. The performance with which these sweeps can be computed grows with the actual number of zones contained in each sweep. Within an AMR framework, the equations are usually solved on a number of small patches of the order of e.g. 48^2 zones in 2D or even 16^3 zones in 3D, so that the sweep length n equals only 48 or 16 elements, respectively. Many vector computers, however, usually yield nearly maximum performance only if n is substantially larger. Indeed, on most high-end machines $n \geq 128$ (CRAY T90) or $n \geq 256$ (NEC SX-4, SX-5) is required in order to obtain reasonable computational rates. Otherwise slowdown by a factor of 10 or more is incurred and there is no advantage concerning computational speed in moving from a workstation-class machine to a supercomputer.

In contrast, on many massively parallel computers, like the CRAY T3E, which consist of several hundred scalar CPUs (also called processing elements or PEs) the code's performance on a single PE is determined by the size of the program's instruction and data area which is accessed most frequently. If it can be stored in the PE's small cache memory and reside there for most of the execution time then access to this data is fast and the program does not spend excessive amounts of time in accessing the PE's much slower main memory.

At first glance optimizing the hydro solver to work efficiently for both types of architectures seems to be nearly impossible. HERAKLES solves this problem by adjusting the solver memory to the actual architecture. On vector computers several hydro sweeps are lumped together into a long contiguous vector in order to efficiently fill the registers

and vector pipelines of the processor, whereas on scalar CPUs the solver memory is made as small as necessary to fit into the CPU's cache memory. Unfortunately, this is only a part of the difficulties. The different arrangements of memory in distributed versus shared memory systems require the use of the message passing programming paradigm in order to obtain a parallel code which is portable between both types of machines. Even worse, the usually small communication bandwidths between different PE's on distributed memory machines may require an appropriate mapping of the patch hierarchy to processor space, in order to minimize communication overhead between different PE's. Additionally, an even partitioning of the workload among processors ("load balancing") has to be performed during runtime in order to avoid that PE's are idling. These problems are much less severe or are even completely avoided when a shared memory computer is used. Currently, a shared memory version of AMRA is available. It was used to perform the calculations presented in Chapter 4 and showed a parallelism of more than 99.5% for this problem on a CRAY J916. Work is currently under way to finish a message-passing version of the code which will allow for the use of large massively parallel systems in order to address the problem of nucleosynthesis and the interaction of the instabilities in three dimensions.

The problems which were discussed above may appear to most readers as beeing of "very technical" nature. Actually, however, they in fact determine whether a simulation is feasible or not. Attacking problems like the explosion of Type II supernovae without introducing unphysical assumptions and crude approximations requires enormous computer resources and consequently every effort in making the code as efficient as possible pays off, enabling one to treat the physics in greater realism and detail.

B.4 Assets and drawbacks of AMR

The savings in CPU time and memory that AMR may offer for a specific problem come at the cost of significant code complexity and a rather involved code maintenance. An efficient management of the complex data hierarchy within the simulation (and also within the later analysis of the data) poses challenging problems in computer science which are not common to conventional computational fluid dynamics (CFD) techniques. Although the basic algorithm was formulated more than 15 years ago, its efficient implementation, especially on distributed memory, massively parallel supercomputers, is still the subject of considerable research efforts in the CFD and computer science communities. For these reasons the AMR algorithm is still rather unpopular among researchers in CFD in general and astrophysical fluid dynamics in particular. Furthermore, in astrophysical problems considerable physics beyond hydrodynamics has to be taken into account. This may for instance necessitate a coupling of AMR to elliptic solvers in order to treat self-gravitating flows or to radiation transport schemes in order to solve radiation hydrodynamic problems. All this makes the development of efficient code even more difficult. Despite all these problems, the number of AMR implementations which are used in astrophysical research seems to be growing recently and in some cases also software is becoming publicly available. This is at least partly a consequence of the "Grand Challenge" projects in astrophysics as well as the US government's Accelerated Strategic Computing Initiative (ASCI). These projects involve large interdisciplinary collaborations consisting of dozens of scientists. The researcher interested in an application of the AMR method should note, however, that the performance of the algorithm is strongly problem-dependent. This fact is often ignored

in discussions of this method.

Bibliography

S. Amari, P. Hoppe, E. Zinner, R. S. Lewis (1992): *Interstellar SiC with unusual isotopic compositions - Grains from a supernova?*, ApJ, 394, L43

S. Amari, E. Zinner, R. S. Lewis (1995): *Large ^{18}O Excesses in Circumstellar Graphite Grains from the Murchison Meteorite: Indication of a Massive-Star Origin*, ApJ, 447, L147

M. C. Anderson, T. W. Jones, L. Rudnick, I. L. Tregillis, H. Kang (1994): *The dynamical and radiative evolution of clumpy supernova ejecta*, ApJ, 421, L31

W. D. Arnett (1987): *Supernova theory and supernova 1987A*, ApJ, 319, 136

W. D. Arnett (1988): *On the early behavior of supernova 1987A*, ApJ, 331, 377

W. D. Arnett (1996): *Supernovae and nucleosynthesis. An investigation of the history of matter, from the Big Bang to the present*, Princeton, NJ: Princeton University Press

W. D. Arnett, J. N. Bahcall, R. P. Kirshner, S. E. Woosley (1989a): *Supernova 1987A*, ARAA, 27, 629

W. D. Arnett, B. Fryxell, E. Müller (1989b): *Instabilities and nonradial motion in SN 1987A*, ApJ, 341, L63

B. Aschenbach, R. Egger, J. Trümper (1995): *Discovery of explosion fragments outside the vela supernova remnant shock-wave boundary*, Nature, 373, 587

M. B. Aufderheide, E. Baron, F.-K. Thielemann (1991): *Shock waves and nucleosynthesis in type II supernovae*, ApJ, 370, 630

W. Baade, F. Zwicky (1934): *Supernovae and Cosmic Rays*, Phys. Rev., 45, 138

R. Bandiera (1984): *Convective supernovae*, A&A, 139, 368

O. S. Bartunov, D. Y. Tsvetkov (1997): *Statistical Studies of Supernovae*, in: P. Ruiz-LaPuente, R. Canal, J. Isern, (Eds.) *Thermonuclear Supernovae*, Dordrecht: Kluwer

G. Bazan, W. D. Arnett (1998): *Two-dimensional Hydrodynamics of Pre–Core Collapse: Oxygen Shell Burning*, ApJ, 496, 316

J. F. Beacom (1999): *Neutrinos From the Next Galactic Supernova*, in: *Neutrinos in the Next Millennium. The 23rd Johns Hopkins Workshop on Current Problems in Particle Theory (Baltimore, June 1999)*

W. Benz, F.-K. Thielemann (1990): *Convective instabilities in SN 1987A*, ApJ, 348, L17

W. Benz, F.-K. Thielemann (1991): *Mixing in supernova 1987A*, in: S. E. Woosley, (Ed.) *Supernovae. The Tenth Santa Cruz Workshop in Astronomy and Astrophysics*, New York: Springer-Verlag

M. Berger, J. Oliger (1984): *Adaptive Mesh Refinement for Hyperbolic Partial Differential Equations*, Jour. of Comp. Phys., 53, 484

M. J. Berger, P. Colella (1989): *Local Adaptive Mesh Refinement for Shock Hydrodynamics*, Jour. of Comp. Phys., 82, 64

H. A. Bethe (1990): *Supernovae*, Physics Today, 43, 24

H. A. Bethe, J. R. Wilson (1985): *Revival of a stalled supernova shock by neutrino heating*, ApJ, 295, 14

R. M. Bionta, G. Blewitt, C. B. Bratton, D. Caspere, A. Ciocio (1987): *Observation of a neutrino burst in coincidence with supernova 1987A in the Large Magellanic Cloud*, Physical Review Letters, 58, 1494

D. Bodansky, D. D. Clayton, W. A. Fowler (1968): *Nuclear Quasi-Equilibrium during Silicon Burning*, ApJS, 16, 299

S. W. Bruenn (1985): *Stellar core collapse - Numerical model and infall epoch*, ApJS, 58, 771

S. W. Bruenn (1993): *Numerical Simulations of Core Collapse Supernovae*, in: M. W. Guidry, M. R. Strayer, (Eds.) *Nuclear Physics in the Universe*, Bristol: IOP

S. W. Bruenn, W. C. Haxton (1991): *Neutrino-nucleus interactions in core-collapse supernovae*, ApJ, 376, 678

S. W. Bruenn, A. Mezzacappa, T. Dineva (1995): *Dynamic and Diffusive Instabilities in Core-Collapse Supernovae*, Physics Reports, 256, 69

A. Burrows, B. A. Fryxell (1993): *A Convective Trigger for Supernova Explosions*, ApJ, 418, L33

A. Burrows, J. Hayes, B. A. Fryxell (1995): *On the Nature of Core-Collapse Supernova Explosions*, ApJ, 450, 830

R. A. Chevalier (1976): *The hydrodynamics of Type II supernovae*, ApJ, 207, 872

R. A. Chevalier, R. I. Klein (1978): *On the Rayleigh-Taylor instability in stellar explosions*, ApJ, 219, 994

N. N. Chugai (1994): *The oxygen mass in SN 1987A: Making use of fluctuations in the (O I) λλ 6300, 6364 profile*, ApJ, 428, L17

D. H. Clark, F. R. Stephenson (1977): *The Historical Supernovae*, Oxford: Pergamon Press

D. D. Clayton (1983): *Principles of stellar evolution and nucleosynthesis*, Chicago: University of Chicago Press

W. J. Cocke, M. J. Disney, D. J. Taylor (1969): *Discovery of Optical Signals from Pulsar NP 0532*, Nature, 221, 525

P. Colella, H. M. Glaz (1985): *Efficient Solution Algorithms for the Riemann Problem for Real Gases*, Jour. of Comp. Phys., 59, 264

P. Colella, P. R. Woodward (1984): *The Piecewise Parabolic Method for Gas-Dynamical Simulations*, Jour. of Comp. Phys., 54, 174

S. W. J. Colgan, M. R. Haas, E. F. Erickson, S. D. Lord, D. J. Hollenbach (1994): *Day 640 infrared line and continuum measurements: Dust formation in SN 1987A*, ApJ, 427, 874

S. A. Colgate, R. H. White (1966): *The Hydrodynamic Behavior of Supernovae Explosions*, ApJ, 143, 626

R. Courant, K. O. Friedrichs, L. H. (1928): *Über die partiellen Differenzengleichungen der mathematischen Physik*, Math. Ann., 100, 32

K. R. de Nisco, S. W. Bruenn, A. Mezzacappa (1998): *The effects of general relativity on core-collapse supernovae*, in: A. Mezzacappa, (Ed.) *Stellar Evolution, Stellar Explosions and Galactic Chemical Evolution, Proceedings of the 2nd Oak Ridge symposium on atomic and nuclear astrophysics*, Bristol: IOP

T. Dotani, K. Hayashida, H. Inoue, M. Itoh, K. Koyama (1987): *Discovery of an unusual hard X-ray source in the region of supernova 1987A*, Nature, 330, 230

T. Ebisuzaki, T. Shigeyama, K. I. Nomoto (1989): *Rayleigh-Taylor instability and mixing in SN 1987A*, ApJ, 344, L65

B. Einfeldt (1988): *On Godunov-type methods for gas dynamics*, SIAM Jour. Numer. Anal., 25, 294

R. I. Epstein (1979): *Lepton-driven convection in supernovae*, MNRAS, 188, 305

S. W. Falk, W. D. Arnett (1973): *A theoretical model for type II supernovae*, ApJ, 180, L65

A. Fassia, W. P. S. Meikle (1999): ^{56}Ni *dredge-up in Supernova 1987A*, MNRAS, 302, 314

A. Fassia, W. P. S. Meikle, T. R. Geballe, N. A. Walton, D. L. Pollacco, R. G. M. Rutten, C. Tinney (1998): ^{56}Ni *dredge-up in the type IIp supernova 1995V*, MNRAS, 299, 150

A. V. Filippenko, W. L. W. Sargent (1989): *Spectroscopic evidence for inhomogeneities in the ejecta of the Type Ib supernova 1985F*, ApJ, 345, L43

A. V. Fillipenko (1997): *Optical Spectra of Supernovae*, ARAA, 35, 309

B. Fryxell, E. Müller, W. D. Arnett (1989): *Hydrodynamics and Nuclear Burning*, MPA Preprint, 449, 1

B. Fryxell, E. Müller, W. D. Arnett (1991): *Instabilities and clumping in SN 1987A. I - Early evolution in two dimensions*, ApJ, 367, 619

B. Fryxell, K. Olson, P. M. Ricker, F. X. Timmes, M. Zingale, D. Q. Lamb, P. MacNeice, R. Rosner, J. W. Truran, H. Tufo (2000): *FLASH: An Adaptive Mesh Hydrodynamics Code for Modeling Astrophysical Thermonuclear Flashes*, ApJ, submitted

P. Goldreich, S. V. Weber (1980): *Homologously collapsing stellar cores*, ApJ, 238, 991

M. R. Haas, E. F. Erickson, S. D. Lord, D. J. Hollenbach, S. W. J. Colgan, M. G. Burton (1990): *Velocity-resolved far-infrared spectra of forbidden Fe II - Evidence for mixing and clumping in SN 1987A*, ApJ, 360, 257

I. Hachisu, T. Matsuda, K. I. Nomoto, T. Shigeyama (1990): *Nonlinear growth of Rayleigh-Taylor instabilities and mixing in SN 1987A*, ApJ, 358, L57

I. Hachisu, T. Matsuda, K. I. Nomoto, T. Shigeyama (1991): *Rayleigh-Taylor instabilities and mixing in the helium star models for Type Ib/Ic supernovae*, ApJ, 368, L27

I. Hachisu, T. Matsuda, K. I. Nomoto, T. Shigeyama (1992): *Mixing in ejecta of supernovae. I - General properties of two-dimensional Rayleigh-Taylor instabilities and mixing width in ejecta of supernovae*, ApJ, 390, 230

I. Hachisu, T. Matsuda, K. I. Nomoto, T. Shigeyama (1994): *Mixing in ejecta of supernovae. II. Mixing width of 2D Rayleigh-Taylor instabilities in the helium star models for type Ib/Ic supernovae*, A&AS, 104, 341

R. W. Hanuschik, J. Dachs (1987): *The H-alpha velocity structure during the first month of SN 1987a in the LMC*, A&A, 182, L29

R. W. Hanuschik, G. Thimm, J. Dachs (1988): *H-alpha fine-structure in SN 1987A within the first 111 days*, MNRAS, 234, 41P

R. P. Harkness, J. C. Wheeler, B. Margon, R. A. Downes, R. P. Kirshner, A. Uomoto, E. S. Barker, A. L. Cochran, H. L. Dinerstein, D. R. Garnett, R. M. Levreault (1987): *The early spectral phase of type Ib supernovae - Evidence for helium*, ApJ, 317, 355

M. Herant, W. Benz (1991): *Hydrodynamical instabilities and mixing in SN 1987A - Two-dimensional simulations of the first 3 months*, ApJ, 370, L81

M. Herant, W. Benz (1992): *Postexplosion Hydrodynamics of SN 1987A*, ApJ, 387, 294

M. Herant, S. E. Woosley (1994): *Postexplosion hydrodynamics of supernovae in red supergiants*, ApJ, 425, 814

M. Herant, W. Benz, S. Colgate (1992): *Postcollapse hydrodynamics of SN 1987A - Two-dimensional simulations of the early evolution*, ApJ, 395, 642

M. Herant, W. Benz, W. R. Hix, C. L. Fryer, S. A. Colgate (1994): *Inside the Supernova: A Powerful Convective Engine*, ApJ, 435, 339

W. Hillebrandt (1987): *Stellar collapse and supernova explosions*, in: F. Pacini, (Ed.) *High Energy Phenomena Around Collapsed Stars*, Dordrecht: Reidel

W. Hillebrandt, P. Höflich (1989): *The supernova 1987A in the Large Magellanic Cloud*, Rep. Prog. Phys., 52, 1421

K. Hirata, T. Kajita, M. Koshiba, M. Nakahata, Y. Oyama (1987): *Observation of a neutrino burst from the supernova SN1987A*, Physical Review Letters, 58, 1490

W. R. Hix, F.-K. Thielemann (1996): *Silicon Burning. I. Neutronization and the Physics of Quasi-Equilibrium*, ApJ, 460, 869

W. R. Hix, F.-K. Thielemann (1999): *Silicon Burning. II. Quasi-Equilibrium and Explosive Burning*, ApJ, 511, 862

R. W. Hockney, C. R. Jesshope (1988): *Parallel computers 2, Architecture, programming and algorithms*, Bristol: Hilger

R. D. Hoffman, S. E. Woosley, G. M. Fuller, B. S. Meyer (1996): *Production of the Light p-Process Nuclei in Neutrino-driven Winds*, ApJ, 460, 478

F. Hoyle, W. A. Fowler (1960): *Nucleosynthesis in Supernovae*, ApJ, 132, 565

J. P. Hughes, C. E. Rakowski, D. N. Burrows, P. O. Slane (2000): *Nucleosynthesis and Mixing in Cassiopeia A*, ApJ, 528, L109

K. Iwamoto, T. R. Young, N. Nakasato, T. Shigeyama, K. I. Nomoto, I. Hachisu, H. Saio (1997): *Instabilities and Mixing in SN 1993J*, ApJ, 477, 865

H.-T. Janka (1991): *Neutrino Transport in Type-II Supernovae and Protoneutron Stars by Monte Carlo Methods*, Dissertation, Technische Universität München

H.-T. Janka (1992): *Flux-limited neutrino diffusion versus Monte Carlo neutrino transport*, A&A, 256, 452

H.-T. Janka (1993): *Neutrinos from type-II supernovae and the neutrino-driven supernova mechansim*, in: F. Giovanelli, G. Mannocchi, (Eds.) *Frontier Objects of Neutrino Astrophysics and Particle Physics*, Bologna: Società Italiana di Fisica

H.-T. Janka, W. Keil (1997): *Perspectives of core-collapse supernovae beyond SN 1987A*, MPA Preprint, 1043, 1

H.-T. Janka, E. Müller (1996): *Neutrino Heating, Convection, and the Mechanism of Type-II Supernova Explosions*, A&A, 306, 167

J. Kane, W. D. Arnett, B. A. Remington, S. G. Glendinning, G. Bazán, E. Müller, B. A. Fryxell, R. Teyssier (2000): *Two-dimensional versus Three-dimensional Supernova Hydrodynamic Instability Growth*, ApJ, 528, 989

W. Keil (1997): *Konvektive Instabilitäten in entstehenden Neutronensternen*, Dissertation, Technische Universität München

W. Keil, H.-T. Janka, G. Raffelt (1995): *Reduced neutrino opacities and the SN 1987A signal*, Physical Review D, 51, 6635

W. Keil, H.-T. Janka, E. Müller (1996): *Ledoux Convection in Protoneutron Stars— A Clue to Supernova Nucleosynthesis?*, ApJ, 473, L111

K. Kifonidis, T. Plewa, H.-T. Janka, E. Müller (2000): *Nucleosynthesis and Clump Formation in a Core-Collapse Supernova*, ApJ, 531, L123

R. Kippenhahn, A. Weigert (1994): *Stellar Structure and Evolution*, Berlin: Springer

C. Kozma, C. Fransson (1998): *Late Spectral Evolution of SN 1987A. II. Line Emission*, ApJ, 497, 431

S. Kumagai, T. Shigeyama, K. I. Nomoto, M. Itoh, J. Nishimura, S. Tsuruta (1989): *Gamma rays, X-rays, and optical light from the cobalt and the neutron star in SN 1987A*, ApJ, 345, 412

M. I. Large, A. E. Vaughan, B. Y. Mills (1968): *A Pulsar Supernova Association?*, Nature, 220, 340

J. M. Lattimer, F. D. Swesty (1991): *A generalized equation of state for hot, dense matter*, Nucl. Phys. A, 535, 331

R. J. LeVeque (1998): *Nonlinear Conservation Laws and Finite Volume Methods*, in: O. Steiner, A. Gautschy, (Eds.) *Computational Methods for Astrophysical Fluid Flow*, Berlin: Springer

H. Li, R. McCray, R. A. Sunyaev (1993): *Iron, Cobalt, and Nickel in SN 1987A*, ApJ, 419, 824

M.-S. Liou (2000): *Mass Flux Schemes and Connection to Shock Instability*, Jour. of Comp. Phys., 160, 623

E. Livne, W. D. Arnett (1995): *Explosions of Sub–Chandrasekhar Mass White Dwarfs in Two Dimensions*, ApJ, 452, 62

L. Lucy (1991): *Nonthermal excitation of helium in type Ib supernovae*, ApJ, 383, 308

L. B. Lucy (1988): *Modelling the atmosphere of SN 1987A*, in: M. Kafatos, A. G. Michalitsianos, (Eds.) *Supernova 1987A in the Large Magellanic Cloud*, Cambridge: CUP

T. Matheson, A. V. Filippenko, R. Chornock, D. C. Leonard, W. Li (2000): *Helium Emission Lines in the Type Ic Supernova 1999CQ*, AJ, 119, 2303

S. M. Matz, G. H. Share, M. D. Leising, E. L. Chupp, W. T. Vestrand (1988): *Gamma-ray line emission from SN1987A*, Nature, 331, 416

O. E. B. Messer, A. Mezzacappa, S. W. Bruenn, M. W. Guidry (1998): *A Comparison of Boltzmann and Multigroup Flux-limited Diffusion Neutrino Transport during the Postbounce Shock Reheating Phase in Core-Collapse Supernovae*, ApJ, 507, 353

A. Mezzacappa, S. W. Bruenn (1993a): *A numerical method for solving the neutrino Boltzmann equation coupled to spherically symmetric stellar core collapse*, ApJ, 405, 669

A. Mezzacappa, S. W. Bruenn (1993b): *Type II supernovae and Boltzmann neutrino transport - The infall phase*, ApJ, 405, 637

A. Mezzacappa, A. C. Calder, S. W. Bruenn, J. M. Blondin, M. W. Guidry, M. R. Strayer, A. S. Umar (1998a): *The Interplay between Proto–Neutron Star Convection and Neutrino Transport in Core-Collapse Supernovae*, ApJ, 493, 848

A. Mezzacappa, A. C. Calder, S. W. Bruenn, J. M. Blondin, M. W. Guidry, M. R. Strayer, A. S. Umar (1998b): *An Investigation of Neutrino-driven Convection and the Core Collapse Supernova Mechanism Using Multigroup Neutrino Transport*, ApJ, 495, 911

A. Mezzacappa, M. Liebendörfer, O. E. B. Messer, W. R. Hix, F.-K. Thielemann, S. W. Bruenn (2000): *The Simulation of a Spherically Symmetric Supernova of a 13 $M_\odot$ Star with Boltzmann Neutrino Transport, and Its Implications for the Supernova Mechanism*, Physical Review Letters, submitted

D. Mihalas, B. Weibel Mihalas (1984): *Foundations of Radiation Hydrodynamics*, Oxford: Oxford University Press

D. S. Miller, J. R. Wilson, R. W. Mayle (1993): *Convection above the neutrinosphere in Type II supernovae*, ApJ, 415, 278

R. Minkowski (1941): *Spectra of Supernovae*, PASP, 53, 224

E. Müller (1986): *Nuclear-reaction networks and stellar evolution codes - The coupling of composition changes and energy release in explosive nuclear burning*, A&A, 162, 103

E. Müller (1998): *Simulation of Astrophysical Fluid Flow*, in: O. Steiner, A. Gautschy, (Eds.) *Computational Methods for Astrophysical Fluid Flow*, Berlin: Springer

E. Müller, M. Steinmetz (1995): *Simulating self-gravitating hydrodynamic flows*, Comp. Phys. Commun., 89, 45

E. Müller, W. Hillebrandt, M. Orio, P. Höflich, R. Mönchmeyer, B. A. Fryxell (1989): *Mixing and fragmentation in supernova envelopes*, A&A, 220, 167

E. Müller, B. Fryxell, W. D. Arnett (1991a): *High-Resolution Numerical Simulations of Instabilities, Mixing and Clumping in Supernova 1987 A*, in: J. Danziger, K. Kjär, (Eds.) *Supernova 1987 A and Other Supernovae*, Garching: European Southern Observatory

E. Müller, B. Fryxell, W. D. Arnett (1991b): *Instability and clumping in SN 1987A*, A&A, 251, 505

E. Müller, B. Fryxell, W. D. Arnett (1991c): *Two and three dimensional numerical simulations of instabilities and mixing in SN 1987 A*, in: F. Federini, J. Franco, F. Matteucci, (Eds.) *Elba Workshop on Chemical and Dynamical Evolution of Galaxies*, Pisa: ETS Editrice

M. Nagasawa, T. Nakamura, S. M. Miyama (1988): *Three-dimensional hydrodynamical simulations of type II supernova - Mixing and fragmentation of ejecta*, PASJ, 40, 691

S. Nagataki, M.-A. Hashimoto, K. Sato, S. Yamada (1997): *Explosive Nucleosynthesis in Axisymmetrically Deformed Type II Supernovae*, ApJ, 486, 1026

S. Nagataki, M.-A. Hashimoto, K. Sato, S. Yamada, Y. S. Mochizuki (1998a): *The High Ratio of $^{44}Ti/^{56}Ni$ in Cassiopeia A and the Axisymmetric Collapse-driven Supernova Explosion*, ApJ, 492, L45

S. Nagataki, T. M. Shimizu, K. Sato (1998b): *Matter Mixing from Axisymmetric Supernova Explosion*, ApJ, 495, 413

T. Nakamura, P. A. Mazzali, K. I. Nomoto, K. Iwamoto (2000): *Light curve and spectral models for the hypernova SN 1998bw associated with GRB980425*, ApJ, submitted

H. J. Neeman (1996): *Autonomous Hierarchical Adaptive Mesh Refinement For Multiscale Simulations*, Phd thesis, University of Illinois at Urbana Champaign

L. R. Nittler, S. Amari, E. Zinner, S. E. Woosley, R. S. Lewis (1996): *Extinct ^{44}Ti in Presolar Graphite and SiC: Proof of a Supernova Origin*, ApJ, 462, L31

K. I. Nomoto, M.-A. Hashimoto (1988): *Presupernova evolution of massive stars*, Physics Reports, 163, 13

K. I. Nomoto, T. Shigeyama, S. Kumagai, M.-A. Hashimoto (1988): *New developments in theoretical modelling of SN 1987A*, Proceedings of the Astronomical Society of Australia, 7, 490

K. I. Nomoto, T. Shigeyama, S. Kumagai (1991): *Model for Type Ib/Ic Supernovae and SN 1987 A: Nucleosynthesis, Mixing, and Light Curves*, in: J. Danziger, K. Kjär, (Eds.) *Supernova 1987 A and Other Supernovae*, Garching: European Southern Observatory

K. I. Nomoto, K. Iwamoto, T. Suzuki (1995): *The evolution and explosion of massive binary stars and Type Ib-Ic-IIb-IIL supernovae*, Physics Reports, 256, 173

K. I. Nomoto, K. Iwamoto, T. R. Young, N. Nakasato, T. Suzuki (1997): *Type Ib-Ic-IIb-IIL Supernovae: Common Envelope Evolution, Instabilities, and Circumstellar Interaction*, in: P. Ruiz-LaPuente, R. Canal, J. Isern, (Eds.) *Thermonuclear Supernovae*, Dordrecht: Kluwer

M. M. Phillips, S. R. Heathcote (1989): *Satellite emission features in the line profiles of SN 1987A*, PASP, 101, 137

M. M. Phillips, M. Hamuy, S. R. Heathcote, N. B. Suntzeff, S. Kirhakos (1990): *An optical spectrophotometric atlas of supernova 1987A in the LMC. II - CCD observations from day 198 to 805*, AJ, 99, 1133

P. A. Pinto, S. E. Woosley (1988a): *The theory of gamma-ray emergence in supernova 1987A*, Nature, 534

P. A. Pinto, S. E. Woosley (1988b): *X-ray and gamma-ray emission from supernova 1987A*, ApJ, 329, 820

T. Plewa, E. Müller (1999): *The Consistent Multi-fluid Advection method*, A&A, 342, 179

T. Plewa, E. Müller (2000): *Adaptive Mesh Refinement for Astrophysics*, Comp. Phys. Commun., in preparation

P. Podsiadlowski (1992): *The progenitor of SN 1987 A*, PASP, 104, 717

J. J. Quirk (1991): *An Adaptive Grid Algorithm For Computational Shock Hydrodynamics*, Phd thesis, Cranfield Institute of Technology, College of Aeronautics

J. J. Quirk (1994): *A contribution to the great Riemann solver debate*, Int. J. Num. Meth. Fluids, 18, 555

J. J. Quirk (1997): *A contribution to the great Riemann solver debate*, in: M. Yousuff Hussaini, B. van Leer, J. Van Rosendale, (Eds.) *Upwind and High-Resolution Schemes*, Berlin: Springer

M. Rampp, H.-T. Janka (2000): *Spherically Symmetric Simulation with Boltzmann Neutrino Transport of Core Collapse and Post-bounce Evolution of a 15 $M_\odot$ Star*, ApJ, submitted

S. Reddy, M. Prakash (1997): *Neutrino Scattering in a Newly Born Neutron Star*, ApJ, 478, 689

S. Reddy, J. Pons, M. Prakash, J. M. Lattimer (1998): *Neutrino opacities at high density and the protoneutron star evolution*, in: A. Mezzacappa, (Ed.) *Stellar Evolution, Stellar Explosions and Galactic Chemical Evolution*, Bristol: IOP

D. W. Richards, J. M. Comella (1969): *The Period of Pulsar NP 0532*, Nature, 222, 551

P. M. Ricker, B. Fryxell, K. Olson, F. X. Timmes, M. Zingale, D. Q. Lamb, P. MacNeice, R. Rosner, H. Tufo (1999): *FLASH: A Multidimensional Hydrodynamics Code for Modeling Astrophysical Thermonuclear Flashes*, in: *American Astronomical Society Meeting*, vol. 195

P. L. Roe (1986): *Characteristic-based schemes for the Euler equations*, Ann. Rev. Fluid Mech., 18, 337

L. I. Sedov (1959): *Similarity and dimensional methods in mechanics*, London: Infosearch

T. Shigeyama, K. I. Nomoto (1990): *Theoretical light curve of SN 1987A and mixing of hydrogen and nickel in the ejecta*, ApJ, 360, 242

T. Shigeyama, K. I. Nomoto, M. Hashimoto (1988): *Hydrodynamical models and the light curve of Supernova 1987A in the Large Magellanic Cloud*, A&A, 196, 141

T. Shigeyama, K. I. Nomoto, T. Tsujimoto, M.-A. Hashimoto (1990): *Low-mass helium star models for type Ib supernovae - Light curves, mixing, and nucleosynthesis*, ApJ, 361, L23

T. Shigeyama, K. Iwamoto, I. Hachisu, K. I. Nomoto, H. Saio (1996): *Instabilities and Mixing in Type II-P and II-b Supernovae*, in: R. McCray, Z. Wang, (Eds.) *Supernovae and supernova remnants. Proceedings of the International Astronomical Union Colloquium 145*, Cambridge; UK: Cambridge University Press

T. M. Shimizu (1995): *Explosion Mechanism of Supernovae with Rotation and Anisotropic Neutrino Radiation*, Phd thesis, University of Tokio

F. H. Shu (1992): *The physics of astrophysics. Vol.2: Gas dynamics*, Mill Valley, CA: University Science Books

J. Spyromilio (1991): *Supernova 1988A - Another clumped supernova*, MNRAS, 253, 25P

J. Spyromilio (1994): *Clumping and largescale anisotropy in supernova 1993J*, MNRAS, 266, L61

D. H. Staelin, E. C. Reifenstein (1968): *Pulsating Radio Sources near the Crab Nebula*, Science, 162, 1481

R. A. Stathakis, M. A. Dopita, R. D. Cannon, E. M. Sadler (1991): *AAT Observations of Supernova 1987A and Other Supernovae*, in: S. E. Woosley, (Ed.) *Supernovae. The Tenth Santa Cruz Workshop in Astronomy and Astrophysics*, New York: Springer-Verlag

G. Strang (1968): *On the construction and comparison of difference schemes*, SIAM, Jour. Num. Anal., 5, 506

R. Sunyaev, A. Kaniovskii, V. Efremov, M. Gilfanov, E. Churazov (1987): *Discovery of hard X-ray emission from supernova 1987A*, Nature, 330, 227

D. A. Swartz, A. V. Filippenko, K. I. Nomoto, J. C. Wheeler (1993): *Spectra of low-mass helium star models and the type IC supernova SN 1987M*, ApJ, 411, 313

K. Takahashi, J. Witti, H.-T. Janka (1994): *Nucleosynthesis in neutrino-driven winds from protoneutron stars II. The r-process*, A&A, 286, 857

F.-K. Thielemann, K. I. Nomoto, M. Hashimoto (1996): *Core-Collapse Supernovae and their Ejecta*, ApJ, 460, 408

F.-K. Thielemann, T. Rauscher, C. Freiburghaus, K. I. Nomoto, M. Hashimoto, B. Pfeiffer, K.-L. Kratz (1998): *Nucleosynthesis Basics and Applications to Supernovae*, in: *Neutrino Physics and Astrophysics*

F. X. Timmes (1999): *Integration of Nuclear Reaction Networks for Stellar Hydrodynamics*, ApJS, 124, 241

C. Travaglio, R. Gallino, S. Amari, E. Zinner, S. Woosley, R. S. Lewis (1999): *Low-Density Graphite Grains and Mixing in Type II Supernovae*, ApJ, 510, 325

V. P. Utrobin, N. N. Chugai, A. A. Andronova (1995): *Asymmetry of SN 1987A: Fast Ni-56 clump*, A&A, 295, 129

P. Vogel (1999): *What Might we Learn From a Future Supernova Neutrino Signal?*, in: *The 8th Int. Workshop on "Neutrino Telescopes", Venice, February 23-26, 1999*

R. Walder (1993): *Some Aspects of the Computational Dynamics of Colliding Flows in Astrophysical Nebulae*, Dissertation, ETH Zürich

P. T. Wallace, B. A. Peterson, P. G. Murdin, I. J. Danziger, R. N. Manchester, A. G. Lyne, W. M. Goss, F. G. Smith, M. J. Disney, K. F. Hartley, D. H. P. Jones, G. W. Wellgate (1977): *Detection of optical pulses from the VELA pulsar*, Nature, 266, 692

L. Wang, J. Hu (1994): *Blue-Shifted Oxygen Lines and the Clumpy Ejecta of Supernova 1993J*, Nature, 369, 380

T. A. Weaver, S. E. Woosley (1981): *Evolution and explosion of massive stars*, in: R. Ramaty, F. C. Jones, (Eds.) *Tenth Texas Symposium on Relativistic Astrophysics*, New York: New York Academy of Sciences

T. A. Weaver, G. B. Zimmerman, S. E. Woosley (1978): *Presupernova evolution of massive stars*, ApJ, 225, 1021

K. W. Weiler, R. A. Sramek (1988): *Supernovae and supernova remnants*, ARAA, 26, 295

J. C. Wheeler, R. P. Harkness (1986): *Physical models of supernovae and the distance scale*, in: B. F. Madore, R. B. Tully, (Eds.) *Galaxy Distances and Deviations from Universal Expansion*, Dordrecht: Reidel

J. R. Wilson (1985): *Supernovae and Post-Collapse Behavior*, in: J. M. Centrella, R. L. Bowers, (Eds.) *Numerical Astrophysics*, Boston: Jones and Bartlett

J. R. Wilson, R. W. Mayle (1988): *Convection in Core Collapse Supernovae*, Physics Reports, 163, 63

J. R. Wilson, R. W. Mayle (1993): *Report on the progress of supernova research by the Livermore group*, Physics Reports, 227, 97

J. R. Wilson, R. Mayle, S. E. Woosley, T. A. Weaver (1986): *Stellar Core Collapse and Supernova*, in: M. Livio, G. Shaviv, (Eds.) *Annals of the New York Academy of Sciences, Twelfth Texas Symposium on Relativistic Astrophysics*, vol. 470, New York: New York Academy of Sciences

P. F. Winkler, R. P. Kirshner (1985): *Discovery of fast-moving oxygen filaments in Puppis A*, ApJ, 299, 981

J. Witti, H.-T. Janka, K. Takahashi (1994): *Nucleosynthesis in neutrino-driven winds from protoneutron stars I. The α-process*, A&A, 286, 841

D. H. Wooden (1997): *Observational Evidence for Mixing and Dust Condensation in Core-Collapse Supernovae*, in: *Astrophysical Implications of the Laboratory Study of Presolar Materials*

P. R. Woodward, P. Colella (1984): *The Numerical Simulation of Two-Dimensional Fluid Flow with Strong Shocks*, Jour. of Comp. Phys., 54, 115

S. E. Woosley (1988): *SN 1987A - After the peak*, ApJ, 330, 218

S. E. Woosley, R. Eastman (1997): *Type Ib and Ic Supernovae: Models and Spectra*, in: P. Ruiz-LaPuente, R. Canal, J. Isern, (Eds.) *Thermonuclear Supernovae*, Dordrecht: Kluwer

S. E. Woosley, T. A. Weaver (1989): *The Great Supernova of 1987*, Scientifc American, August, 24

S. E. Woosley, T. A. Weaver (1994): *Sub-Chandrasekhar mass models for Type IA supernovae*, ApJ, 423, 371

S. E. Woosley, T. A. Weaver (1995): *The Evolution and Explosion of Massive Stars. II. Explosive Hydrodynamics and Nucleosynthesis*, ApJS, 101, 181

S. E. Woosley, W. D. Arnett, D. D. Clayton (1973): *The Explosive Burning of Oxygen and Silicon*, ApJS, 26, 231

S. E. Woosley, R. E. Taam, T. A. Weaver (1986): *Models for Type I supernova. I - Detonations in white dwarfs*, ApJ, 301, 601

S. E. Woosley, P. A. Pinto, L. Ensman (1988): *Supernova 1987A - Six weeks later*, ApJ, 324, 466

S. E. Woosley, J. R. Wilson, G. J. Mathews, R. D. Hoffman, B. S. Meyer (1994): *The r-process and neutrino-heated supernova ejecta*, ApJ, 433, 229

S. E. Woosley, A. Heger, T. A. Weaver, N. Langer (1997): *SN 1987A - Presupernova evolution and the progenitor star*, MPA Preprint, 1024, 1

A. Yahil (1983): *Self-similar stellar collapse*, ApJ, 265, 1047

A. Yahil, J. M. Lattimer (1982): *Supernovae for pedestrians*, in: M. J. Rees, R. J. Stoneham, (Eds.) *Supernovae: A Survey of Current Research*, Dordrecht: Reidel

S. Yamada, K. Sato (1990): *Global mixing in SN 1987A by the asymmetric shock wave*, ApJ, 358, L9

S. Yamada, K. Sato (1991): *Rayleigh-Taylor instability in the asymmetric supernova explosion*, ApJ, 382, 594

S. Yamada, H.-T. Janka, H. Suzuki (1999): *Neutrino transport in type II supernovae: Boltzmann solver vs. Monte Carlo method*, A&A, 344, 533

E. Zinner, S. Amari, C. Travaglio, R. Gallino, M. Busso, S. Woosley (1995): *The Isotopic Composition of Interstellar Graphite from the Murchison Meteorite: Evidence for Supernova Mixing*, in: *Lunar and Planetary Science Conference*, vol. 26

Acknowledgements

Curriculum Vitae

Name:	Konstantinos Kifonidis	
Date of Birth:	May 9th, 1971	
Place of Birth:	Berlin, Germany	
Nationality:	Greek	
Education:	1977–1983	German and Greek elementary school, Berlin/Tiergarten
	1983–1990	High-school (Heinrich-von-Kleist Gymnasium, Berlin/Tiergarten)
	1990–1996	Studies of Physics at the Technical University of Berlin (TU Berlin)
	Oct. 1992	"Vordiplom" in Physics
	1995–1996	Diploma thesis work at the Astrophysical Institute Potsdam (AIP) on "Radiation Gasdynamic Models of Planetary Nebulae with Rapidly Evolving Central Stars"
	Oct. 1996	Diploma in Physics at the TU Berlin
	March 1997 – Aug. 2000	PhD thesis work at the MPI für Astrophysik, Garching, on "Nucleosynthesis and Hydrodynamic Instabilities in Core Collapse Supernovae" under the supervision of Dr.-habil. E. Müller and Prof. W. Hillebrandt